Dissertation

submitted to the

Combined Faculty of Mathematics, Engineering and Natural Sciences

of Heidelberg University, Germany

for the degree of

Doctor of Natural Sciences

Put forward by

M.Sc. Simon Felix Steinmaßl

born in: Traunstein, Germany

Oral examination: 6th June, 2023

Probing particle acceleration in stellar binary systems using gamma-ray observations

Referees:

Prof. Dr. Jim Hinton
Prof. Dr. Stefan Wagner

Abstract

Only a few gamma-ray sources have been established as proton accelerators over the last decades, among them two extraordinary binary systems, the massive colliding wind binary Eta Carinae (η Car) and the recurrent nova RS Ophiuchi (RS Oph). In this thesis, the nature of acceleration processes up to TeV energies are probed in these systems using very-high energy (VHE; $\geq$ 100 GeV) gamma-ray data from the High Energy Stereoscopic System (H.E.S.S.) in conjunction with data from the Fermi Large Area Telescope (LAT).

To obtain reliable results from Imaging Atmospheric Cherenkov Telescopes like H.E.S.S., an accurate match between simulations and actual observations is crucial. Thus, in the first part of this thesis the successful validation of the simulations of the full 5-telescope H.E.S.S. array is presented. Based on this, the scientific verification of the monoscopic analysis was achieved using data from the large 28 m-telescope recently upgraded with a FlashCam prototype. The resulting spectrum of the Crab Nebula, the standard candle in the VHE regime, is found to be in good agreement with previous measurements by H.E.S.S. and other instruments.

Using this verified analysis configuration, the nova RS Oph was successfully detected during its 2021 outburst, making it the first nova with confirmed VHE emission. A detailed light curve was derived from the highly statistically significant gamma-ray signal observed with the full H.E.S.S. array. The combined properties of the H.E.S.S. measurements with simultaneous Fermi-LAT data clearly favor a common origin of the whole gamma-ray emission, implying efficient acceleration of hadrons at the external shock caused by the eruption.

η Car has been firmly established as a source of gamma-rays by Fermi-LAT and H.E.S.S. over the last decade. With its highly eccentric orbit lasting 5.5 years, the periastron passage of the two stars is extremely close, making it a particularly interesting phase range. The 2020 periastron passage was the first such event to be extensively monitored by H.E.S.S. In this thesis, the detection of a VHE signal from η Car during the 2020 periastron is presented, making use of a novel time-based image cleaning technique for the monoscopic analysis. In combination with simultaneous Fermi-LAT data, its spectral properties are characterized and together with previous and follow-up observations, for the first time, a VHE light curve spanning a full orbit is derived. At least some fraction of the accelerated particles traced by the gamma-ray emission likely escape from η Car, potentially interacting with target material on different spatial scales. With the detection of Fermi-LAT excess emission associated to molecular clouds in the Carina Nebula, this hypothesis is tested. Whereas the cosmic ray density profile is indicative of an origin of the interacting cosmic rays from η Car, a larger escaping flux than predicted by models or a contribution from other cosmic ray sources is needed to match the measured flux.

Kurzzusammenfassung

Nur einige wenige Gammastrahlenquellen konnten in den letzten Dekaden als Protonenbeschleuniger etabliert werden. Darunter sind zwei spezielle Doppelsternsysteme, zum einen das durch kollidierende Winde charakterisierte Eta Carinae (η Car) System und zum anderen die rekurrierende Nova RS Ophiuchi (RS Oph). Mit Hilfe von Gammastrahlungsbeobachtungen im sehr hohen Energiebereich ($\geq$ 100 GeV) durch das High Energy Stereoscopic System (H.E.S.S.) und Daten des Fermi Large Area Telescope (LAT) können dort Beschleunigungsprozesse bis zu TeV Energien studiert werden.

Um für H.E.S.S. eine robuste Analyse zu gewährleisten, muss eine präzise Übereinstimmung zwischen Simulationen und Daten sichergestellt werden. Dementsprechend wird im ersten Teil der Arbeit die erfolgreiche Validierung der Simulationen für alle fünf H.E.S.S. Teleskope behandelt. Das führte zu einer vollständigen wissenschaftlichen Verifizierung der monoskopischen Analyse des großen 28 m Teleskops, welches vor Kurzem mit einem FlashCam Prototypen ausgestattet wurde. Das resultierende Spektrum des Krebsnebels, die Standardkerze der Gammastrahlenastronomie, stimmte gut mit vorherigen Messungen von H.E.S.S. und anderen Instrumenten überein.

Mit Hilfe dieser verifizierten Analyse konnte die Nova RS Oph während ihrer Eruption im Jahr 2021 erfolgreich detektiert werden. Dadurch wurde sie zur ersten jemals detektierten Nova im hochenergetischen Gammastrahlungsbereich. Aus den Daten konnte eine detaillierte Lichtkurve extrahiert werden. Die Charakteristiken der Daten zusammen mit Daten des Fermi-LAT Experiments führten zur Schlussfolgerung eines hadronischen Ursprungs des Signals. Des Weiteren legen die Daten eine sehr effiziente Beschleunigung an der externen Schockfront nahe.

η Car war durch vorhergehende Observationen mit Fermi-LAT und H.E.S.S. bereits als Gammastrahlenquelle bekannt. Die Periastronpassage des Systems, welches eine sehr exzentrische 5,5 Jahre dauernde Umlaufbahn hat, ist durch den sehr kleinen Abstand der beiden Sterne von besonderem Interesse. Die Periastronpassage im Jahr 2020 war die erste, welche mit H.E.S.S. ausgiebig beobachtet wurde. In dieser Arbeit wird die signifikante Detektion durch H.E.S.S. während dieser Phase präsentiert, wobei ein neuer Algorithmus basierend auf der Zeitinformation zum Säubern der Bilder benutzt wurde. Zusammen mit Daten des Fermi-LAT Experiments wird das Spektrum beschrieben. Des Weiteren kann durch Archivdaten zum ersten Mal eine sehr hoch energetische Gammastrahlenlichtkurve des gesamten Orbits erstellt werden. Die beschleunigten Teilchen verlassen teilweise das System, um dann mit Material in der Umgebung zu interagieren. Mit Hilfe von Fermi-LAT Daten wird diese Hypothese getestet und signifikante Emission von nahen Molekülwolken entdeckt. Während das Dichteprofil der Teilchen für einen Ursprung von η Car spricht, bräuchte man jedoch einen höheren Fluss von η Car in der Vergangenheit oder zusätzliche Quellen, um das Signal vollständig zu erklären.

Contents

Chapter 1

Introduction

Astronomy is one of the oldest fields of science with the earliest known records dating back many millennia. However, up to the 19th century, the phenomena in the sky were exclusively observed in optical light. Only the discovery of wavebands invisible to the human eye and the subsequent technological advances opened up new windows to the universe. As our atmosphere has a wavelength-dependent opacity, only a few atmospheric windows exist, that allow direct ground-based observations. But with the emergence of satellites and advanced indirect detection techniques, most of the remaining frequency scales came within reach, allowing astronomers to observe the universe over a wide range of energy scales. Therefore, present-day astronomy consists of several subfields ranging from the low-energy radio regime to the highest-energy gamma-ray regime.

Astronomy in the gamma-ray regime was developed mainly in the last decades but has rapidly evolved. It is crucial for the detection of the highest energy phenomena of our universe by tracing radiation from some of the most extreme objects in the sky. Present-day gamma-ray astronomy offers a unique view into the universe providing a direct link to the acceleration of particles in the observed objects.

In this thesis, two particle acceleration laboratories are discussed with a focus on their gamma-ray emission. These are, on the one hand, the massive binary system Eta Carinae (η Car) possessing strong stellar winds and, on the other hand, RS Ophiuchi (RS Oph) and its eruptive nova outbursts. Special emphasis is laid on their detection with the High Energy Stereoscopic System (H.E.S.S.), which allows measurements of photons at energies between 100 GeV and 100 TeV. H.E.S.S. is an Imaging Atmospheric Cherenkov Telescope (IACT), using an indirect detection technique of gamma-rays via the atmosphere. To achieve reliable results with this technique a good description of the instrument in simulations as well as advanced analysis methods are needed.

This thesis is organized as follows:

- ♢ In Chapter 2 the mechanisms responsible for the acceleration of particles together with the basic properties of the accelerators and of the accelerated particles, the so-called cosmic rays (CRs), are introduced. Furthermore, the production of gamma-ray emission linked to the accelerators is discussed. Eventually,

η Car is introduced with a description of its properties as well as its surroundings. Additionally, particle acceleration from novae, in general, is discussed and the system RS Oph is characterized.

◊ In Chapter 3 the instrumental techniques used for the detection of gamma-rays are described with special emphasis on H.E.S.S. Moreover, the analysis principles and the reduction pipeline towards the final scientific products are outlined. Additionally, also the Fermi Large Area Telescope (LAT) instrument with its characteristics is described.

◊ Chapter 4 focuses on the end-to-end validation of the scientific results from H.E.S.S., which heavily rely on a good match between data and simulations. With this, the analysis of data from the recently installed FlashCam camera on the large telescope of H.E.S.S. is scientifically verified. Additionally, a new cleaning approach making use of the timing information of the events is investigated.

◊ The detection of RS Oph as the first nova at TeV energies is described in Chapter 5. This includes a combination of H.E.S.S. and Fermi-LAT data. Furthermore, the implications of this discovery are discussed.

◊ In Chapter 6, the gamma-ray data of observations of η Car over its orbit with special emphasis on its periastron passage is presented. This includes a light curve spanning over the full 5.5-year orbit, and a multiwavelength spectrum during its periastron passage. This is then compared to existing models of the gamma-ray emission from this system.

◊ Chapter 7 explores the escape of the CRs produced in η Car into its surroundings. Originating from this, potential gamma-ray emission from several surrounding features at varying distance scales is discussed. This is then linked with gamma-ray data from the Fermi-LAT instrument.

◊ A summary of the key findings of this thesis is presented in Chapter 8. An outlook on future questions arising from this thesis is given.

Most results presented in this thesis are retrieved from collaborative efforts. Throughout the thesis special emphasis was laid on my personal contributions but results derived by others are presented in a summarized form, where it is required to present a complete and comprehensible picture of the projects. Therefore at the beginning of each chapter, my personal contributions are declared and the contributions of others are clearly distinguished. Furthermore, at the beginning of each chapter, any publications including the presented work are stated, if the work has been published.

Chapter 2

Particle acceleration and gamma-ray emission from binary systems

The discovery of ionizing radiation at high altitudes in the atmosphere by Victor Hess in 1912 (Hess, 1912) can be seen as the origin of the field nowadays known as astroparticle physics. Hess made his discovery using electrometer measurements during balloon flights to measure the properties of the radiation at different altitudes. Subsequently, by contributions from several researchers, a terrestrial origin of this radiation could be ruled out. Instead, the radiation was found to originate from charged particles entering the atmosphere from above and interacting within it[1].

These charged particles, consisting of protons, electrons[2] and heavier nuclei, are typically referred to under the term cosmic rays (CRs). The characteristics of CRs have been measured in detail by several generations of instruments. Today these instruments employ both ground-based (Castellina, 2017) and balloon or space-based methods (Marrocchesi, 2017) to measure the properties over a wide range of energies reaching up to the EeV regime and beyond. To reach these high energies, charged particles must experience powerful acceleration mechanisms, making them tracers of unique laboratories. Due to their nature as charged particles, CRs are deflected by magnetic and electric fields along their path to Earth, resulting in an almost isotropic flux. Therefore, for observers on Earth, it is unfortunately almost impossible to trace CRs back to their sources. Currently, only hints at possible direct associations of CRs with specific source classes exist, but no clear evidence has been found yet (see e.g. Aab et al., 2018).

Complementary to cosmic ray experiments the origin of uncharged particles like photons and neutrinos can be investigated. These can be produced in interactions of cosmic rays with ambient magnetic and photon fields or with surrounding matter.

[1] A detailed review of the history of cosmic ray research can be found in e.g. Walter and Wolfendale (2012)

[2] For simplicity electrons will refer to both electrons and positrons in this thesis.

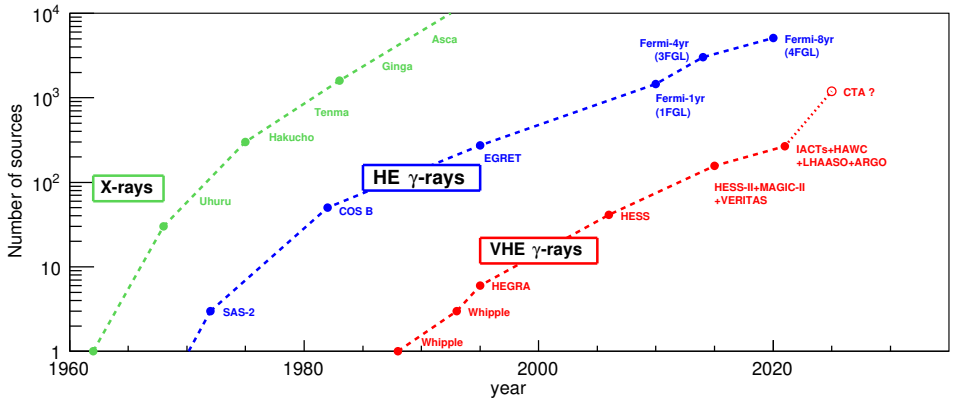

FIGURE 2.1: **Number of significantly detected X-ray and gamma-ray sources as a function of time**
The gamma-ray regime is split up into the high energy (HE) and the very-high energy (VHE) gamma-ray regime, which are defined as gamma-rays with energies below and above 100 GeV. The plot includes all sources detected until 2020 and predictions for the next generation instrument Cherenkov Telescope Array (CTA). The different telescopes are in more detail described in Chapter 3. Taken from de Naurois (2021).

The hottest objects in the universe, e.g. accretion disks around compact objects, extend only to energies of 10 keV in their thermal radiation, meaning that broadband gamma-ray emission above MeV energies must have a non-thermal origin. Carrying no charge, they can be traced back to their sources and provide important clues about cosmic rays and their origin. Whereas the field of neutrino astronomy has only recently claimed its first detected sources (IceCube Collaboration et al., 2018; IceCube Collaboration et al., 2022), gamma-ray astronomy has already provided several catalogs of sources up to the PeV regime.

Combining different detection techniques, both ground and space-based, gamma-ray astronomy offers a wealth of data spanning several orders of magnitude in energy. Typically the gamma-ray regime is subdivided into the high energy (HE) regime from ∼100 MeV to ∼100 GeV and the very-high energy (VHE) regime beyond 100 GeV based on the different observation techniques in the different regimes (discussed in more detail in Chapter 3). The catalog of significantly detected gamma-ray sources has steadily increased over time as shown in Figure 2.1, currently consisting of thousands of HE and hundreds of VHE sources.

This chapter summarizes the present-day knowledge about cosmic ray properties (Section 2.1) and introduces the current understanding of particle acceleration mechanisms (Section 2.1.1), the diffusion of CRs (Section 2.1.2) and potential accelerators (Section 2.1.3). Furthermore, the processes that produce gamma-rays are described in Section 2.2.1 and Section 2.2.2 together with an overview of known gamma-ray sources in Section 2.2.3 with special emphasis on gamma-ray binaries (Section 2.2.4). In the second part of this chapter two classes of binary systems are

introduced that provide a special environment for particle acceleration and subsequent gamma-ray radiation. First in Section 2.3, the massive colliding binary system Eta Carinae is characterized together with its surroundings in the Carina Nebula. Then in Section 2.4, nova outbursts from binary systems consisting of a white dwarf (WD) with a companion star are described. Further detail is provided on the recurrent nova RS Ophiuchi. These two systems and their surroundings will be the prominent examples of gamma-ray emitting binaries further discussed in this thesis.

For more extensive descriptions with further details on astroparticle physics and gamma-ray astronomy, I would like to point the reader to the literature, e.g. to the books by Gaisser et al. (2016), Longair (2011), and Aharonian (2004) and the detailed reviews on gamma-ray astronomy by, e.g. Hinton and Hofmann (2009), Funk (2015), and De Angelis and Mallamaci (2018). η Car is described in great depth in the book by Davidson and Humphreys (2012), whereas further details on novae can be found in, e.g. the review article by Chomiuk et al. (2021).

2.1 Cosmic rays

The CR differential flux, denoted as $\mathrm{d}N/\mathrm{d}E$ in the following, has been measured by many different instruments sensitive to different energy ranges. Combining the different measurements a broadband CR spectrum over the energy range from $\sim$1 GeV to $\sim$100 EeV can be obtained. For all energies E, the flux from protons and heavier nuclei is the main component of the CR flux with only a negligible contribution by electrons. As it can be seen in Figure 2.2, the CR spectrum shows a remarkable uniformity following a power law of the form $\mathrm{d}N/\mathrm{d}E \propto E^{-\alpha}$ with a spectral index of $\alpha \sim 2.7$ for large parts of the energy range. However, some spectral features can be noticed and are quantified by a change in the spectral index. These features have been named *knee* and *ankle* after their position in the CR spectrum.

As CRs consist of several particle species and heavier nuclei, the exact composition, charge and mass number is energy dependent (e.g. Aab et al., 2017). The largest mass number with a significant contribution to the overall CR flux is iron, which is the heaviest particle produced via fusion processes. The changing composition, the available accelerators and the confinement of charged particles need to be taken into account to explain the observed features. Below GeV energies, the magnetic field of the solar winds shields most of these low-energy CRs coming from outside the solar system, causing the apparent drop off below these energies.

Up to the *knee*, the large majority of CRs is believed to be of Galactic origin. The *knee* feature occurs at $\sim$1 PeV and is characterized by a spectral softening to $\alpha \approx 3.1$. It is proposed that above this energy, the dominant acceleration sites within our galaxy, supernova remnants, show a cut-off in their produced CR spectrum (see e.g. Bell et al., 2013). The exact location of this cut-off depends on the particle species and their respective charge with the cut-off for protons happening at lower energies than

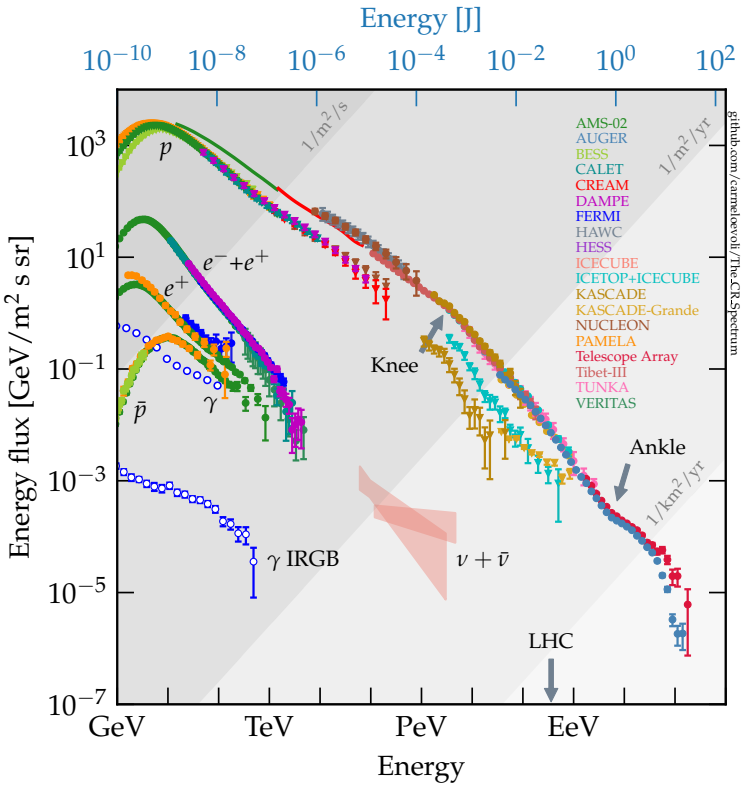

FIGURE 2.2: **The broadband cosmic ray spectrum**
Collection of measurements above GeV energies of several earth-based and space-borne experiments. The measured spectra of protons (and heavier nuclei), electrons, gammas and neutrinos are shown. The proton and heavier nuclei spectrum is the dominating component for all energies. The two main features, the *knee* and the *ankle*, are highlighted with arrows and particle rates are indicated by grey bands. Figure taken from Evoli (2020).

for iron nuclei. The range from PeV up to EeV energies is widely believed to be the transition regime between galactic and extragalactic CRs (Bell, 2013), even though no firm observational evidence for this exists yet.

At $\sim$5 EeV the spectrum hardens again, returning to a value of $\alpha \approx 2.6$. This spectral break is called the *ankle*. At this energy and beyond the origin of CRs is assumed to be dominantly extragalactic, as the CRs are not confined within our galaxy anymore (Bell, 2013). At $\sim$100 EeV a hard cut-off of the flux is observed. This can be explained by either a cut-off in the spectra of cosmic ray sources or by the Greisen–Zatsepin–Kuzmin effect (Greisen, 1966; Zatsepin and Kuzmin, 1966). These authors described the interaction of CRs with the cosmic microwave background, which severely limits the maximum distance the most energetic CRs can travel unhindered. Thus, it would be impossible for CRs above $\sim$100 EeV to reach Earth from an extragalatic origin.

Highly energetic cosmic rays with $\sim$10 EeV are extremely rare with rates of 1 per km^2 per year and lower. To still accumulate sufficient statistics in this regime detectors with effective areas of several hundred or thousand km^2 are needed. This

is achieved by present-day ground-based detectors such as the Pierre Auger Observatory and the Telescope Array.

2.1.1 Particle acceleration mechanisms

As the most energetic cosmic rays ever measured have energies up to 300 EeV (Bird et al., 1995), extreme environments to accelerate cosmic rays must exist in the universe. The accelerators need to exist in many different forms and on many different scales to produce the remarkably smooth spectrum of cosmic rays over a wide range of energies. An overview about the most important potential acceleration mechanisms and their detailed derivation can be found for example in Longair (2011). A widely considered acceleration mechanism to produce high energy CRs is the Fermi acceleration postulated by Enrico Fermi (1949). The basic concept used by Fermi has been extensively described and expanded (see e.g. Bell, 2013; Longair, 2011) and is only sketched in the following.

Based on the energy gain with regard to the flow velocity of the physical environment causing the acceleration, one can distinguish between two types of Fermi acceleration: The first-order Fermi acceleration at shocks and second-order Fermi acceleration in the environment of, e.g. moving magnetized gas clouds.

Second order Fermi acceleration The original idea for the Fermi acceleration process comes from the acceleration of particles by collisions in moving clouds. One can assume a cloud of ionized gas moving with velocity U into a certain direction. If a charged particle enters the cloud it will diffuse through it by elastic scattering on the turbulent magnetic fields inside the cloud until it exits the cloud again. The particle can gain energy in a head-on encounter or lose energy in a tail-on encounter depending on the direction in which the particle enters and exits the cloud relative to its direction of movement. On average, a particle will however gain energy as head-on collisions are more frequent. The resulting average energy gain is proportional to $(U/c)^2$. Nevertheless, typical velocities of such clouds in the Milky Way are rather small and collisions with these clouds are rare, making this process an unlikely acceleration mechanism to account for the majority of cosmic rays. Furthermore, there is no obvious reason why with such a process a global power law with an exponent between 2 and 3 as indicated by observations would follow. Additionally to the described process in moving gas clouds, there are also other second order Fermi acceleration processes with a $(U/c)^2$ energy gain, such as shear acceleration.

First order Fermi acceleration In the diffusive shock acceleration, the most prominent example of a first order Fermi acceleration process, particles move repeatedly back and forth across a shock, gaining energy each time. If one assumes a shock sweeping an ambient medium with a high velocity U, much faster than the speed of sound in the upstream medium, one can look at the relative velocities in different rest frames. In the following the shock is assumed to be non-relativistic and thin,

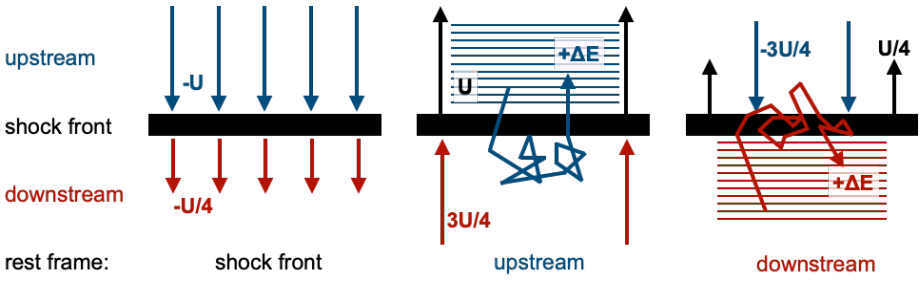

FIGURE 2.3: **Schematic description of diffusive shock acceleration in different rest frames**
The respective velocities of the shock and the upstream and downstream medium are shown for the three main rest frames. On the left, the shock is at rest, in the middle the upstream medium and on the right the downstream medium. For each reference frame, the relative velocities are depicted assuming an ideal gas description as described in the text. The crossing and scattering of a particle are shown in both the upstream and downstream reference frame leading to an energy gain of ΔE after crossing the shock twice. Taken from Ruiz Velasco (2021) adapted from Funk (2005).

which means the shock is much smaller than the gyro radius of the particles considered. The gyro radius or Larmor radius R_g for a relativistic particle with energy E and charge Ze, moving in a magnetic field with strength B perpendicular to its velocity is defined as:

$$R_g = \frac{E}{ZeB} \tag{2.1}$$

The different rest frames of the shock, the upstream and the downstream medium are sketched in Figure 2.3. Upstream denotes in this case the medium ahead of the shock and downstream the medium which has already been swept by the shock.

In the shock reference frame, the upstream gas flows towards the shock with a velocity $v_u = U$ and after crossing the shock moves away from the shock with a velocity v_d. With the continuity equation, one can derive the velocity ratio,

$$\frac{v_u}{v_d} = \frac{\rho_d}{\rho_u}, \tag{2.2}$$

with the densities ρ_u and ρ_d of the upstream and downstream medium, respectively. Assuming conservation of energy and momentum for an ideal gas with adiabatic index $\Gamma = 5/3$, one can find a compression ratio $r = \frac{\rho_d}{\rho_u} = \frac{\Gamma+1}{\Gamma-1} = 4$, which in turn implies $v_d = \frac{1}{4}v_u = \frac{1}{4}U$. In the rest frame of the upstream medium the shock approaches with velocity U and the shocked gas in the downstream then with $\frac{3}{4}U$. In the downstream rest frame, the shock moves away with $\frac{1}{4}U$ and the upstream gas approaches with $\frac{3}{4}U$.

With this, it becomes clear that a particle will gain energy each time it crosses the shock, as in both directions, the particles in the region it is crossing into will move toward the crossing particle. A test particle can undergo a cycle consisting

of 4 qualitative steps. Before its injection into the acceleration cycle the test particle is part of the upstream medium and hence on average at rest within that medium. As the shock approaches it crosses the shock head-on into the downstream medium and consequently gains energy. In the downstream medium the particle will scatter on fluctuations in the magnetic field and in a random walk process keep its energy. Therefore, the particle becomes isotropic with respect to the downstream medium and will eventually recross the shock again, as the particle velocity is assumed to be much larger than the velocity of the receding shock in the downstream frame. The shock crossing will again lead to an energy gain. Afterward, the particle can once again randomize its direction and can start the described crossing cycle again until it eventually escapes the shock region.

The mean energy gain per cycle for a relativistic particle is:

$$\frac{\Delta E}{E} = \frac{4}{3}\frac{v_u - v_d}{c} = \beta - 1, \tag{2.3}$$

which can be expressed in terms of the fractional energy gain $\beta = \frac{E}{E_0}$ assuming a particle with initial energy E_0. Hence after a number of cycles k the particle has an energy of $E = \beta^k E_0$. To derive an energy spectrum, the probability P of the particle remaining in the shock region is needed additionally. This is connected to the probability P_{esc} of particles escaping downstream in the system, which is $P_{esc} = \frac{U}{c} = 1 - P$. Because of that, after k cycles the number of particles above an energy E is $N = P^k N_0$ with N_0 being the number of initial particles. One can now formulate the resulting differential energy spectrum of the particles as:

$$\frac{\mathrm{d}N}{\mathrm{d}E}\mathrm{d}E \propto E^{\frac{\ln P}{\ln \beta}-1}\mathrm{d}E \tag{2.4}$$

For the case of an ideal gas, this results in $\frac{\ln P}{\ln \beta} = -1$, returning a power-law with index 2. Therefore, the diffusive shock acceleration can naturally explain the observed power-law spectra from sources and the overall cosmic ray spectrum if further energy-dependent transport is taken into account. As it scales in first order with the shock velocity, it can also provide efficient acceleration.

Diffusive shock acceleration has been established since the 1970s (see e.g. Bell, 1978a; Bell, 1978b; Blandford and Ostriker, 1978) to explain the acceleration of cosmic rays. For further details also beyond this rather simple description a large number of extensive reviews (see e.g. Bell, 2013; Malkov and Drury, 2001) can be consulted.

2.1.2 Diffusion

To make the described acceleration at shocks feasible, particle transport in the medium via diffusive propagation is needed. The charged particles can for example be scattered on magnetic field fluctuations. In general, if the particles diffuse spherically symmetric with a diffusion coefficient D, there is the following relation between the residence time t of the particles and the corresponding radial distance r (Hinton and

Hofmann, 2009):

$$r^2 = 2Dt \tag{2.5}$$

The diffusion coefficient is a measure of the average magnetic field strength B and its degree of turbulence δB on length scales similar to the gyration radius R_g (see Equation 2.1). For the so-called Bohm diffusion, the mean free path of particles with a velocity close to c is assumed to be equal to the gyration radius. Often the diffusion coefficient is expressed relative to the Bohm regime with a parameter η. In this case, one can write (see e.g. Hinton and Hofmann, 2009),

$$D \approx \eta \frac{R_g c}{3} \text{ with } \eta \geq 1 \tag{2.6}$$

with the coefficient $\eta \approx \left(\frac{\delta B}{B}\right)^{-2}$ (Strong et al., 2007). The Bohm limit $\eta = 1$ corresponds to the slowest possible diffusion.

The diffusion of the CRs within the Milky Way can be modeled with simple leaky box models, in which the energy dependence of the diffusion coefficient has the following form:

$$D(E) = D_0 \times \left(\frac{E}{1\,\text{GeV}}\right)^{\delta} \tag{2.7}$$

In these models, typical values for diffusion within our galaxy are $\delta = 0.3 - 0.6$ and $D_0 \sim (3-5) \times 10^{28}\,\text{cm}^2\,\text{s}^{-1}$ (Strong et al., 2007).

2.1.3 Cosmic ray accelerators

The maximum energy achievable with potential accelerators can be either limited by the lifetime of the shock, the radiative losses or the size of the acceleration region.

In the case of a shock with a finite lifetime t and velocity U, the particles can only be accelerated as long as the shock exists. In the case of Bohm diffusion, this limits the maximum energies to (Hinton and Hofmann, 2009):

$$E_{max} \sim \left(\frac{U}{1000\,\text{km}\,\text{s}^{-1}}\right)^2 \frac{t}{1000\,\text{yr}} \frac{B}{\mu\text{G}}\,\text{TeV} \tag{2.8}$$

As usual, B denotes the magnetic field strength. In the case of faster diffusion an additional factor η^{-1} needs to be taken into account, as the shock crossing rate is proportional to $1/D$.

If the radiative or other energy loss time scales get shorter than the acceleration time, the maximum energy is determined by the energy where acceleration and energy loss times are equal to each other. This is often important for electrons. If synchrotron losses dominate, the maximum energy can be estimated as (Hinton and Hofmann, 2009):

$$E_{max} \sim 100 \frac{U}{1000\,\text{km}\,\text{s}^{-1}} \left(\frac{B}{\mu\text{G}}\right)^{-1/2}\,\text{TeV} \tag{2.9}$$

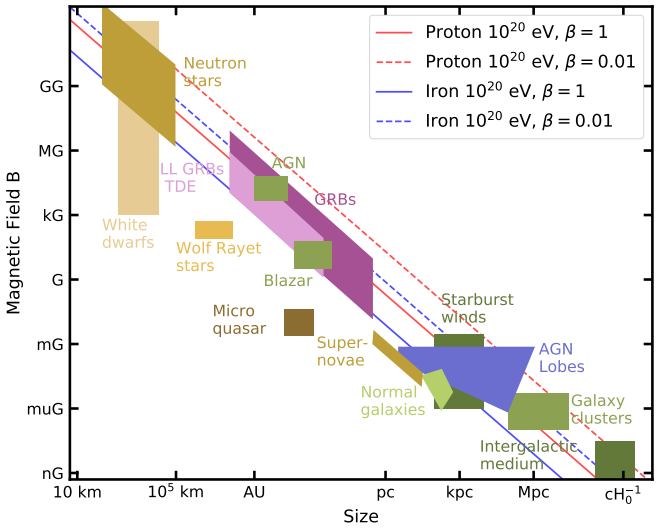

FIGURE 2.4: **Up-to-date version of the Hillas plot**
The plot relating magnetic field strength to accelerator size was originally produced by Michael Hillas (Hillas, 1984). The solid lines represent iron and proton CRs at energies of 10^{20} eV for a fast shock with $\beta = 1$ and the dashed lines for a slow shock with $\beta = 0.01$. Typical candidate sources for acceleration are compared. Adapted from Maier (2022).

In case the acceleration is limited by the size of the accelerator, the so-called Hillas condition named after its formulation by Michael Hillas (1984) can be set. A more general derivation of it can be found in e.g. Gaisser et al. (2016) and only the basic formulas are presented here. If the gyro radius R_g (see Equation 2.1) of an accelerated particle approaches the size of the accelerator R itself, the particle can not be confined by magnetic fields anymore. Hence it will escape the accelerator and further acceleration is impossible. This gives rise to a maximum energy $E_{max} < ZeBR$. In the case of smaller shock velocities $U < c$, a more general formulation for the maximum energy E_{max} with $\beta = U/c$ is:

$$E_{max} = \beta ZeBR \tag{2.10}$$

This relation on the maximum energy can be compared for potential accelerators on different size and magnetic field strength scales. With this visualization, typically referred to as Hillas plot (Hillas, 1984), one can find suitable astrophysical source classes for specific levels of maximum CR energy. An up-to-date version of the original Hillas plot is shown in Figure 2.4. From Equation 2.10 it becomes clear that the maximum energy depends not only on the product of B and R. Hence, several lines for the extreme cases of the charge of CRs (protons and iron nuclei) and for slow and fast shocks are shown, which would explain acceleration to energies of 10^{20} eV. This can potentially be achieved in a variety of source classes.

2.2 Gamma-rays

Non-thermal radiation is defined very broadly as any electromagnetic radiation emitted by particles through other means than their thermal energy. Whereas non-thermal radiation plays a role over the full electromagnetic spectrum, this section focuses on the processes relevant to high-energy photons in the gamma-ray regime. Naturally the particle population causing this radiation must have similar or higher energies to produce photons with high energies. Hence (very) high energy gamma-rays are closely connected to the existence of CRs of GeV energies and beyond.

Gamma-rays can be produced both via leptonic and hadronic processes. In both processes, high-energy leptons or hadrons interact with surrounding matter, magnetic or photon fields. The different processes are described in detail in e.g. Aharonian (2004) and in reviews such as Hinton and Hofmann (2009) and Funk (2015) and are outlined in the following

2.2.1 Leptonic radiation processes

For high-energy electrons three main radiative energy loss mechanisms exist: Bremsstrahlung, synchrotron radiation and inverse Compton scattering (see e.g. Blumenthal and Gould, 1970). Bremsstrahlung losses of electrons passing through a medium and experiencing acceleration or deceleration in the electric field of atomic nuclei are subdominant for potential HE and VHE gamma-ray production in most astrophysical objects and will hence not be discussed further. The electron population after experiencing an acceleration process can be considered to follow a cutoff power-law distribution with an index α_e and a potential cutoff E_c:

$$\frac{\mathrm{d}N}{\mathrm{d}E} \propto E^{-\alpha_\mathrm{e}} \exp\left(-\frac{E}{E_c}\right) \tag{2.11}$$

Synchrotron radiation In the presence of a magnetic field, charged particles are accelerated perpendicular to their motion. This results in a spiraling motion along the magnetic field lines and leads to an energy loss of the particle emitted via a photon. The energy loss via synchrotron radiation scales with m^{-2} for particles with mass m. Therefore, synchrotron emission is much more relevant for electrons compared to protons. For an electron with an energy in the TeV regime in a magnetic field with strength B the synchrotron radiation spectrum assuming an isotropic distribution of pitch angles peaks at (Funk, 2015):

$$E_{sy} = 0.2 \left(\frac{E_e}{\mathrm{TeV}}\right)^2 \frac{B}{10\,\mu\mathrm{G}}\,\mathrm{eV} \tag{2.12}$$

For a power law distribution of electrons with index α_e (see Equation 2.11) the differential synchrotron spectrum has the form of a power-law $\mathrm{d}N/\mathrm{d}E \propto E^{-\Gamma_{sy}}$ with index $\Gamma_{sy} = \frac{\alpha_\mathrm{e}+1}{2}$. An example of this is shown in Figure 2.5. From the overall

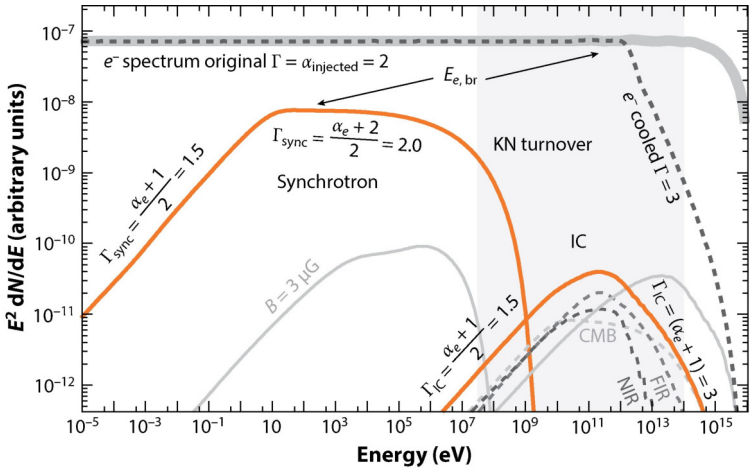

FIGURE 2.5: **Spectral energy distribution of synchrotron and inverse Compton emission from electrons**
The spectral energy distribution of electrons injected with $\alpha_e = 2$ is shown in grey with the state including cooling in a typical galactic source shown with the dashed line. Additionally, the resulting synchrotron and inverse Compton spectra are shown. The resulting spectral indices are marked. A magnetic field of 100 μG is assumed and the synchrotron radiation with 3 μG is shown for comparison. The inverse Compton spectrum was calculated for several target photon fields with far infrared (FIR), near-infrared (NIR) and cosmic microwave background (CMB) photons. The shaded gray region depicts the energy range observable by current gamma-ray detectors. Taken from Funk (2015).

synchrotron spectrum it becomes also evident, that very high electron energies are needed to produce HE gamma-rays via this process.

Inverse Compton emission The inverse Compton process describes the scattering of an electron off a low-energy photon, which results in an energy gain of the photon. This is in contrast to the classical Compton effect, where an electron gains energy from a photon. One prerequisite is hence the presence of a target photon field, which can be, e.g. ambient thermal radiation by stars and dust or the cosmic microwave background. There are two distinct regimes depending on the energy of the electron E_e and the photon E_{ph}: The Thomson limit where $4E_eE_{ph} \ll m_ec^2$ holds and the Klein Nishima regime with $4E_eE_{ph} \gg m_ec^2$.

For scattering off visible light the Thomson regime extends up to electron energies of 100 GeV, whereas for scattering off the cosmic microwave background it extends up to 500 TeV. The resulting distribution in the Thomson limit based on the electron and photon energy peaks at (Funk, 2015):

$$E_{IC} = 5 \times 10^9 \left(\frac{E_e}{\mathrm{TeV}}\right)^2 \frac{E_{ph}}{10^{-3}\,\mathrm{eV}}\,\mathrm{eV} \tag{2.13}$$

Assuming again that the electron spectrum follows a power law with index α_e (Equation 2.11), the resulting photon index shows the same relation as for the synchrotron

case $\Gamma_{IC} = \frac{\alpha_e+1}{2}$. In the Klein Nishima regime, however, the spectrum softens towards an index of $\Gamma_{IC} = \alpha_e + 1$ producing a spectral break. The spectral behavior with the pronounced spectral break is also clearly visible in Figure 2.5.

For inverse Compton processes in the Thomson regime, as well as for synchrotron processes, the energy loss time scale is $\propto E_e^{-1}$. Therefore, when electrons loose energy via these processes, the electron spectrum softens towards the index $\alpha_e + 1$ above energies, where the electrons had enough time to cool (see as well Figure 2.5). The energy at which this break occurs is approximately the energy at which the cooling time scale is similar to the age of the electron population within the system. For further details on this, the literature, e.g. Hinton and Hofmann (2009), can be consulted.

2.2.2 Hadronic radiation processes

Hadrons, such as protons and heavier nuclei, can produce gamma-rays through interactions with ambient matter. This target material can either be connected to the accelerator itself, e.g. through winds or shells of previous explosions or can be situated in the vicinity of the accelerator, e.g in dense molecular clouds. As the cross-section for a collision process of a proton with a hydrogen nucleus is only weakly energy dependent with a value of $\sigma \approx 35\,\mathrm{mb}$ for the VHE regime, the lifetime of VHE protons can be approximated depending on the number density n of the target material as (Hinton and Hofmann, 2009):

$$\tau_{pp} \sim 3 \times 10^7 \left(\frac{n}{\mathrm{cm}^{-3}}\right)^{-1} \mathrm{yr} \tag{2.14}$$

A typical collision results in a large number of pions and a few heavier hadrons, whereas ∼50 % of the energy of the primary is carried away by a leading nucleon. The inelastic scattering of a proton p can hence be expressed as:

$$\mathrm{p} + \mathrm{nucleus} \rightarrow \mathrm{p}' + \pi^{\pm} + \pi^0 + ... \text{ and } \pi^0 \rightarrow 2\gamma;\ \pi^{\pm} \rightarrow \mu^{\pm} + \overset{(-)}{\nu}_{\mu} \tag{2.15}$$

It can be assumed that roughly 1/3 of the remaining energy is carried away equally by neutral, positive and negative pions ($\pi^0, \pi^{\pm}$). Whereas the charged pions decay with high probability[3] into muons ($\mu^{\pm}$) and muon neutrinos ($\overset{(-)}{\nu}_{\mu}$), the π^0 will quickly[4] and with high probability[5] decay into two photons (γ). Therefore, the energy budget available for the production of gamma-rays is roughly 1/6 of the proton energy E_p. Assuming high gamma-ray energies larger than the rest mass of the neutral pion[6], $E_\gamma \gg m_{\pi^0}$, the distribution in gamma-ray energies is scale-invariant

[3] 99.99 % (Particle Data Group et al., 2022))
[4] The mean life time for π^0 is $(8.43 \pm 0.13) \times 10^{-17}$s (Particle Data Group et al., 2022).
[5] 98,8 % (Particle Data Group et al., 2022)
[6] The rest mass of the π^0 is 135 MeV (Particle Data Group et al., 2022).

with respect to $x = \frac{E_\gamma}{E_\mathrm{p}}$. The parameterization of the gamma-ray spectrum as a function of the scale variable can be obtained with extensive simulations of p-p interactions based on collider measurements as it was done by, e.g. Kelner et al. (2006) and Kafexhiu et al. (2014). These parameterizations show that the spectral energy distribution (SED) of gamma-rays peaks at around $0.1E_\mathrm{p}$ for mono-energetic protons. If one considers instead a cutoff power law distribution for protons of the form

$$\frac{\mathrm{d}N_\mathrm{p}}{\mathrm{d}E_\mathrm{p}} \propto \left(\frac{E_\mathrm{p}}{1\,\mathrm{TeV}}\right)^{-\Gamma_\mathrm{p}} \exp\left(-\frac{E_\mathrm{p}}{E_{c,\mathrm{p}}}\right), \tag{2.16}$$

the gamma-ray spectrum is following Kappes et al. (2007):

$$\frac{\mathrm{d}N_\gamma}{\mathrm{d}E_\gamma} \propto \left(\frac{E_\gamma}{1\,\mathrm{TeV}}\right)^{-\Gamma_\gamma} \exp\left(-\sqrt{\frac{E_\gamma}{E_{c,\gamma}}}\right) \tag{2.17}$$

This shows that an energy cutoff in the proton spectrum is transformed into a more gradual cutoff in the gamma-ray spectrum. The cutoff energy is reduced by:

$$E_{c,\gamma} \approx 0.04 \times E_{c,\mathrm{p}} \tag{2.18}$$

The gamma-ray index is similar or only slightly harder than the proton index:

$$\Gamma_\gamma \approx \Gamma_\mathrm{p} - 0.1 \tag{2.19}$$

The gamma-ray SED based on a proton distribution following a power-law with a cutoff at 100 TeV and an index of 2 is shown in Figure 2.6. Furthermore, the cutoff energy and the spectral index have been varied to emphasize the effect on the gamma-ray SED. A characteristic low energy cutoff, specifically prominent for indices ≥ 2, can be observed which is often referred to as the "pion bump". The exact energy of the turnover in the SED depends on the spectral index of the primary proton distribution as it becomes evident in Figure 2.6, but it will typically be in the few 100 MeV range. The pion bump occurs, because the gamma-rays produced by the decay of the neutral pion carry away at least the rest mass energy of the pion which results into a symmetric distribution of the gamma-rays in log energy scale around $m_{\pi^0}/2 = 67.5$ MeV in the rest frame of the pion (Stecker, 1970). The detection of a pion bump in the gamma-ray spectrum can hence lead to a clear association with hadronic emission, whereas otherwise, a clear distinction with regards to leptonic processes based on other spectral features is difficult.

Besides the rather simple assumptions of a similar spectral index of the accelerated proton and gamma-ray distribution one has to also keep in mind energy-dependent escape and diffusion. Especially if the gamma-rays are not produced close to the accelerator itself the spectral shape can be altered significantly (see e.g.

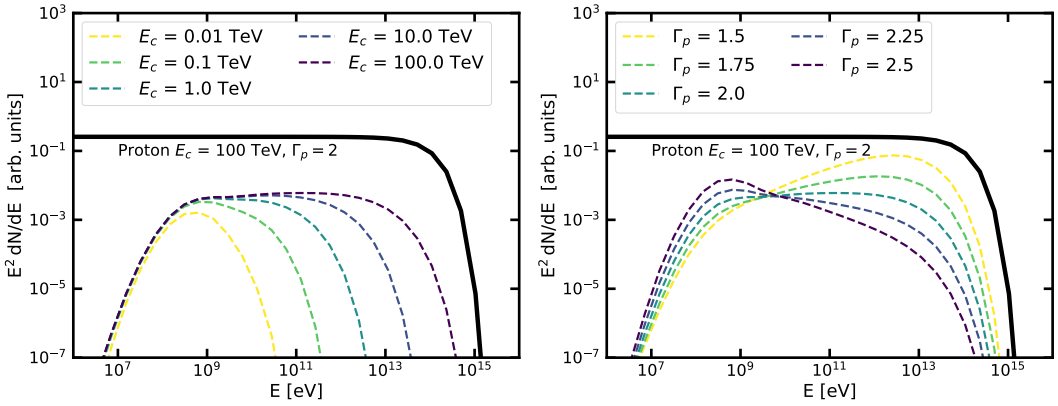

(A) Varying E_c (B) Varying Γ_p

FIGURE 2.6: **Spectral energy distribution of gamma-rays from hadronic interactions**
The spectral energy distribution of protons injected with $\Gamma_p = 2$ and $E_c = 100$ TeV is shown in black in both plots. The proton and gamma-ray energy fluxes are scaled arbitrarily. In **A** the cut off energy E_c is varied, and the resulting gamma-ray spectra are shown. In **B** the spectral indices of the injected proton distribution are altered and the resulting gamma-ray spectra are compared. The gamma-ray spectra were calculated with the modeling package Gamera[7], which uses the parametrizations from Kafexhiu et al. (2014).

Gabici et al., 2007). The overall flux normalization of the gamma-ray flux with respect to the proton flux depends mainly on the number density n of the target material, which determines the interaction rate. Assuming a source at distance d with an energy output E_{pr}, of which a fraction ϵ_{CR} is used for the acceleration of cosmic rays, the gamma-ray flux at earth can be approximated as (Funk, 2015):

$$F_\gamma(\geq 100\,\mathrm{MeV}) = 4.4 \times 10^{-7} \epsilon_{CR} \frac{E_{pr}}{10^{51}\,\mathrm{erg}} \left(\frac{d}{\mathrm{kpc}}\right)^{-2} \frac{n}{\mathrm{cm}^{-3}}\,\mathrm{cm}^{-2}\,\mathrm{s}^{-1} \tag{2.20}$$

Additionally to the described p-p interactions under certain conditions also the photomeson production ($\mathrm{p} + \gamma \rightarrow \mathrm{N} + k\pi$) can play a role. This is the case if the density of low-energy radiation exceeds by far the gas density. However, this process is not relevant for the physical environments described in this thesis and therefore will not be discussed in detail here. Further information can be found for example in Kelner and Aharonian (2008).

2.2.3 Known gamma-ray sources

Gamma-ray astronomy has evolved quickly over the last decades providing several thousand detected sources in the HE regime (Abdollahi et al., 2022b) and also an increasing catalog of VHE sources. Currently, there are ∼250 detected sources in the

[7]More info on Gamera can be found in Hahn et al. (2022) and at `http://libgamera.github.io/GAMERA/docs/main_page.html`.

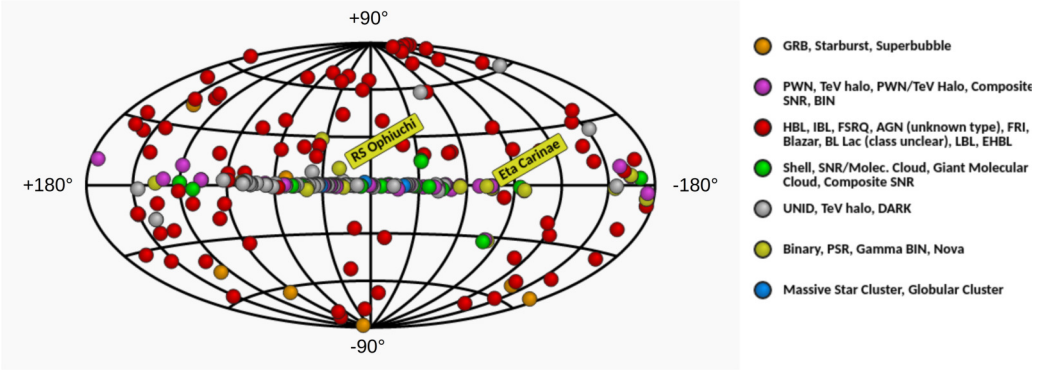

FIGURE 2.7: **Full sky map of VHE gamma-ray sources**
All significantly detected sources from ground-based observatories in the VHE regime are shown. The sky is depicted in Galactic coordinates. The colors show the different known or unknown source class associations. The two main sources for this thesis are labeled. AGN stands for active galactic nuclei, GRB for gamma-ray burst, PWN for pulsar wind nebulae, and SNR for supernova remnants. Reproduced from TeVCat[9](Wakely and Horan, 2008), where the meaning of the other source class acronyms can be found.

VHE energy regime collected by the constantly updated TeVCat[8] catalog (Wakely and Horan, 2008). An overview of all theses sources and their locations on the sky is presented in Figure 2.7. Whereas a clear source association is not possible for all of these objects, there exist a few source classes with well-known counterparts in other wavelengths.

Typical extragalactic sources are active galactic nuclei (AGN) and gamma-ray bursts, only recently detected in the VHE regime (H.E.S.S. Collaboration et al., 2019; H.E.S.S. Collaboration et al., 2021; MAGIC Collaboration et al., 2019). Known galactic VHE sources are supernova remnants, pulsar wind nebulae and gamma-ray emitting binaries. An overview of the acceleration and emission mechanisms in these systems can be found in e.g. Hinton and Hofmann (2009). The verification studies included in this thesis in Chapter 4 made use of the signal from two very bright and relatively well understood sources, the pulsar wind nebula connected to the Crab pulsar and the AGN PKS 2155-304.

2.2.4 Gamma-ray binaries

The majority of stars are believed to be in binary systems (Duchêne and Kraus, 2013), making the field of studies on such objects extremely broad. But in order to produce detectable non-thermal emission in the VHE gamma-ray regime only a few extreme candidates need to be considered. Up to now, 11 VHE gamma-ray binary systems were detected with a variety of acceleration and emission mechanisms. An overview

[8]More information on TeVCat and the catalog itself can be found at `http://tevcat2.uchicago.edu/`.
[9]see footnote 8

of these gamma-ray binaries can be found in, e.g. Chernyakova et al. (2019). In most of these systems, the binary consists of a compact object with a stellar companion. The nature of the compact object is only known for a few systems. Examples are PSR B1259-63 and PSR J2032+4127, which both are composed of a pulsar together with a massive companion (H.E.S.S. Collaboration et al., 2013; Abeysekara et al., 2018b) and build up a small-scale pulsar wind nebula. Recently, TeV emission powered by strong jets in the microquasar SS433 was confirmed (Abeysekara et al., 2018a; Olivera-Nieto, 2023), making it the first microquasar detected in VHE gamma-rays. The majority of gamma-ray binaries have no clearly identified compact object and acceleration mechanism yet but similar scenarios are considered for those (Chernyakova et al., 2019). Additionally, nova outbursts from binary systems consisting of a white dwarf (WD) and a companion star were established as a new class of VHE sources with the detection of gamma-ray emission from RS Ophiuchi (H.E.S.S. Collaboration et al., 2022; Acciari et al., 2022).

Clearly distinct in their nature are colliding wind binaries CWB, which do not contain a compact object but two massive stars with powerful winds instead. In the collision region of the two winds characterized by high mass-loss rates and high velocities two shock fronts can form, at which particles can be accelerated (e.g. Eichler and Usov, 1993). Eta Carinae is one of only two known gamma-ray emitting CWB together with γ-velorum (Martí-Devesa et al., 2020). However, η Car is the only CWB detected at energies above hundred GeV (H.E.S.S. Collaboration et al., 2020). There are a few other CWB, for which potential gamma-ray emission could be expected (Werner et al., 2013) but so far has not been observed. This makes η Car a very unique laboratory.

The properties of RS Oph as well as of η Car are introduced in the following, as the gamma-ray emission from these two systems is discussed in great depth in this thesis.

2.3 Eta Carinae - A colliding wind binary

Eta Carinae is a massive binary system, located in the Carina Nebula deep in the southern sky. The Carina Nebula, also known as NGC 3372, is a massive H II region with ongoing star formation, extending over diameters of 40 pc. The total mass of ionized hydrogen in the H II region is about $10^5\,M_\odot$. Located at a distance of $\sim$2.3 kpc (Davidson and Humphreys, 1997) the nebula hosts a collection of massive O-type stars (Smith, 2006; Berlanas et al., 2023) and open stellar clusters (Preibisch et al., 2011). Examples of these open clusters are Trumpler 16 and Trumpler 14. The majority of the most massive stars are found to exist in binary systems (Duchêne and Kraus, 2013) with a lower limit of 35 % but likely a considerably higher fraction found for the Carina Nebula (Berlanas et al., 2023). η Car situated within Trumpler 16 is the most famous example of a massive binary. The Carina Nebula itself shows

FIGURE 2.8: **Mosaic of the Homunculus Nebula and η Car situated within the Carina Nebula**
The Carina Nebula was observed with the Wide Field Imager on the MPG/ESO 2.2-metre telescope. The Homunculus Nebula in the middle was taken with the NACO near-infrared adaptive optics instrument on the VLT. The right panel shows η Car itself as seen with the Very Large Telescope Interferometer. Image Credit: ESO/G. Weigelt[10].

vast diffuse emission in the optical light with a lot of pronounced features and substructures as it can be seen in Figure 2.8.

η Car has been observed almost continuously over centuries, as it caught the attention of astronomers already in early times due to a few drastic changes in its luminosity. The observation history summarized here follows the more detailed description in Davidson and Humphreys (2012). During the 17th and 18th centuries, it was known as a bright but not extraordinarily bright star with historical records suggesting a visual brightness between 4th and 6th magnitude. In 1837 a rapid brightening occurred up to a maximum visual magnitude of -1 mag, which meant η Car was the second brightest star in the sky for a certain period of time until it faded again in 1858. Measurements taken during that time suggest that this episode, referred to as the "Great Eruption", was due to a supernova impostor event (Davidson and Humphreys, 2012). In this event, a mass of $10\,M_\odot$ or more was ejected in an explosion similar to supernovae but not destroying the primary star itself. The Homunculus Nebula surrounding η Car with a present-day size of ∼20000 au is the visible remnant of this event consisting of the gas expelled during the eruption. After fading to quiescence magnitudes of $m_v \approx 7.7$ mag, a second smaller eruption happened between 1887 and 1895 noticeable by a brightening by 1.5 magnitudes and likely creating the so-called Little Homunculus. Since then, η Car has shown no signs of further eruptions but after a quiescence period around 8th magnitude until

[10] https://www.eso.org/public/germany/images/eso1637a/

Parameter	η Car A	η Car B	Reference
M [$M_\odot$]	90	30	Hillier et al. (2001)
R [$R_\odot$]	100	20	Corcoran and Hamaguchi (2007)
L [10^6 $L_\odot$]	4	0.3	Parkin et al. (2009)
T_s [10^3 K]	25.8	30.0	Parkin et al. (2009)
$\dot{M}$ [$M_\odot$ yr^{-1}]	5.0×10^{-4}	1.4×10^{-5}	Parkin et al. (2009)
v_∞ [km s^{-1}]	500	3000	Pittard and Corcoran (2002)

TABLE 2.1: **Stellar parameters of η Car A and η Car B**
M denotes the mass, R the radius, L the luminosity and T_s the surface temperature of each of the two stars. $\dot{M}$ is the mass loss rate of the wind and v_∞ its terminal velocity.

the 1940s it has been gradually brightening again with a current-day visual magnitude of $m_v \approx 4.0$ mag[11]. The Homunculus Nebula and a close-up on η Car is shown in Figure 2.8.

2.3.1 Properties of the system

The general properties of the system are well established in some aspects but are still uncertain in others. Whereas its nature as a binary system is well known (e.g. Davidson and Humphreys, 2012), the binary system itself cannot be resolved even by modern instruments making the exact derivation of the characteristics of the two stars difficult. Furthermore, the surrounding Nebula distorts the view onto η Car for e.g. spectroscopic instruments. Hence the properties of the individual stars are not known with high precision. In the following, estimates of the properties from literature are presented. For further details on the uncertainties of these estimates the quoted sources should be consulted.

The primary star η Car A is believed to be a luminous blue variable (Davidson and Humphreys, 1997) with a mass larger than 90 $M_\odot$ (Hillier et al., 2001) making it one of the most massive known stars in our galaxy. The secondary star η Car B is a hotter O-type or Wolf-Rayet star (Iping et al., 2005) with a smaller but not well-constrained mass $\leq 30\,M_\odot$ (Hillier et al., 2001). The masses and other stellar parameters are summarized in Table 2.1. Before the Great Eruption and potential previous eruptions the combined mass of the system must have been significantly higher with estimates of 150 $M_\odot$ for the initial mass of η Car A alone (Smith, 2008). The age of the system is estimated to be $\sim 2 - 3 \times 10^6$ years (Mehner et al., 2010).

The two stars are assumed to exhibit strong stellar winds. The wind of η Car A is comparatively slow but dense with a high mass-loss rate. The secondary wind is on the other hand faster but has a lower mass-loss rate. Estimates of these quantities are also presented in Table 2.1.

[11] This is based on the light curve viewed on 20 February 2023 using the AAVSO database (`https://www.aavso.org/`).

Parameter	System	Reference
Distance [kpc]	2.3	Davidson and Humphreys (1997)
a [au]	15.4	Madura et al. (2012)
ϵ	0.9	Mehner et al. (2015)
Period [d]	2022.7	Teodoro et al. (2016)
Inclination [°]	130 - 145	Teodoro et al. (2016)
Epoch [MJD]	2456874.4	Teodoro et al. (2016)

TABLE 2.2: **Orbital parameters of η Car**
a denotes the semimajor axis and ϵ the eccentricity of the orbit. The epoch is given in Modified Julian Days (MJD) and refers to the 2014 periastron passage.

From spectroscopic and X-ray measurements spanning several orbits the binary period is by now precisely known, whereas the exact geometry of the orbit is not as certain. The general consensus is that the binary system is characterized by a highly eccentric ($\epsilon \approx 0.9$) orbit with an orbital period of 5.5 years. The orbital properties are summarized in Table 2.2. During the periastron passage the two stars are extremely close at scales of $\sim$1 au. Therefore, η Car can be used as a unique laboratory with drastically changing conditions on time scales accessible to observers.

2.3.2 Particle acceleration in η Car

In massive binaries with strong winds such as η Car, a wind collision region (WCR) is formed. In this region between the two stars the two winds collide, which is sketched in Figure 2.9a. As a consequence, a contact discontinuity is formed at the surface at which the ram pressure of the two winds is equal. Thus, one can derive the distances r_1 and r_2 of the contact discontinuity from each star following Eichler and Usov (1993) as:

$$r_1 = \frac{\sqrt{\eta}}{1+\sqrt{\eta}} D,\ r_2 = \frac{1}{1+\sqrt{\eta}} D \quad \text{with} \quad \eta = \frac{\dot{M}_1 v_{\infty,1}}{\dot{M}_2 v_{\infty,2}} \tag{2.21}$$

Here, D is the separation of the two stars. The contact discontinuity is therefore closer to the star with smaller $\dot{M} v_\infty$, which is for η Car the companion star η Car B. As illustrated as well in the sketch (Figure 2.9a) it also bends around η Car B. On each side of the contact discontinuity, a shock is formed associated with the stellar winds. In each of these two shocks particles (hadrons or leptons) can be accelerated via diffusive shock acceleration. The particles get accelerated along the contact discontinuity, until the shocks disappear at larger distances, as the winds move more parallel with respect to each other. After this point, the outflows can mix and are assumed to be almost ballistic. Because of that, this region is also referred to as the ballistic region, whereas the inner region is named shock cap (Parkin and Pittard, 2008). The geometry of the shock cap can be skewed due to the orbital motion. This and the general geometry of the system are visualized for two orbital phases close

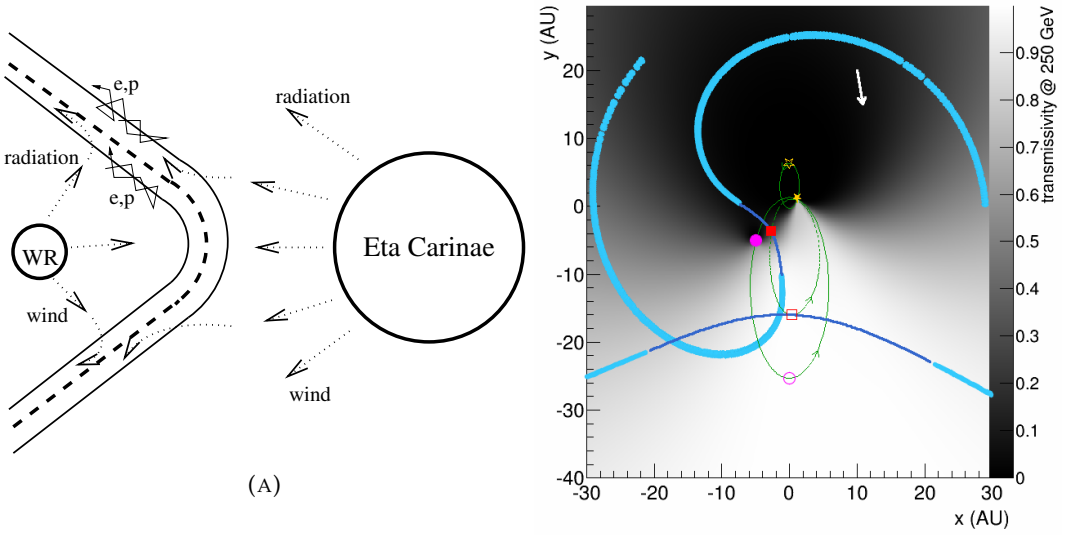

FIGURE 2.9: **Schematic explanations of particle acceleration regions in η Car**
In **A** the contact discontinuity (dashed) formed in the wind collision region is schematically drawn with the two shocks on either side. η Car A is denoted as Eta Carinae and η Car B as WR. The contact discontinuity is closer to and bent around η Car B due to the weaker wind of the companion. At the shocks, electrons and protons can be accelerated. In **B** the geometry of the binary system, the shock cap (dark blue) and the ballistic region (light blue) for phases 0.04 (solid symbols) and 0.5 (open symbols) are schematically depicted. The star and the green solid lines denote the primary, the circle and the long dashed line the companion and the rectangles and short dashed lines the stagnation point. The white arrow depicts the projected line of sight to the observer and the underlying map depicts the transmissivity at 250 GeV. Taken from Bednarek and Pabich (2011) (**A**) and Ohm et al. (2015) (**B**).

to periastron and apastron in Figure 2.9b. As can be seen, due to the highly eccentric orbit, the size of the shock cap changes significantly over the orbital period.

Particles accelerated within η Car can subsequently produce gamma-rays following the processes outlined in the previous section. Gamma-gamma absorption due to the intense photon fields plays a non-negligible role for gamma-rays above ∼30 GeV (Ohm et al., 2015; White et al., 2020) for η Car. These high energy gamma-rays can produce electron-positron pairs in interactions with the strong stellar radiation fields, leading to an energy-dependent absorption. As it is shown in Figure 2.9b the changing geometry of the system over its orbit would imply a phase dependency of this effect. However, it also depends strongly on the size and location of the assumed gamma-ray emission region.

2.3.3 Multiwavelength view

The measurements of η Car in the optical waveband spanning over centuries exposed several discrete events, such as the Great Eruption, and clear long-term variability. Typical time scales for the different brightness states are between 10 and 200 years. This long-term optical variability is connected to the evolution of the system but not inherently to its binary nature. The binary nature was discovered through spectroscopic measurements, which showed the fading or even full disappearance of high excitation emission lines for weeks to months (e.g. Teodoro et al., 2016). The repeated detection of this behavior every 5.5 years resulted in a precise measurement of the recurrence period of the spectroscopic cycle, which was associated with the orbital period of the system. The phase is defined in such a way that phase $\phi = 0$ is coincident with the periastron passage modeled from the disappearance of Helium emission lines (Teodoro et al., 2016). The variability on this time scale has subsequently been observed in many other wavebands (Damineli et al., 2008; Teodoro et al., 2016).

The most prominent example is the similar variability time scale discovered in the X-ray regime between 2 and 10 keV (e.g. Corcoran et al., 2017; Kashi et al., 2021). As it can be seen in Figure 2.10, using X-ray observations with RXTE[12] and Swift-XRT[13] presented in Corcoran et al. (2017), the X-ray flux is at its quiescent level for most of the period. Roughly a year prior to the periastron passage at phase $\phi \approx 0.8$ the X-ray flux starts to gradually increase reaching a maximum approximately a month prior to the periastron passage. The maximum flux is a factor $\sim$3 higher than the quiescent flux. After the maximum, the flux quickly drops reaching a minimum well below the quiescent flux at almost the same time as the periastron passage. The flux in this minimum is suppressed by a factor 10 or more with respect to the quiescent flux. The X-ray minimum has a variable duration ranging between 30 and 70 days in the 5 observed periastron passages with sensitive X-ray instruments (Kashi et al., 2021). Afterward, the flux quickly recovers and is after around 20 days back to the quiescent level. Whereas the X-ray emission shows qualitatively a similar behavior for each orbit, a clear orbit-to-orbit variability can be observed.. The rise towards the X-ray maximum shows strong variability on short timescales and the length of the X-ray minimum is significantly changing from orbit to orbit with the 2021 periastron passage showing the fastest recovery of the last 5 passages (Kashi et al., 2021).

The X-ray variability is likely related to the changes in the WCR, in which the thermal X-ray emission is thought to be produced. Only the fast companion wind can produce high enough temperatures in the WCR to explain the observed X-ray spectrum. The rise and X-ray maximum shortly before periastron can be explained

[12]The Rossi X-Ray Timing Explorer (RXTE; Levine et al., 1996) was an X-ray telescope operated from 1995 to 2012.

[13]The X-Ray Telescope (XRT; Gehrels et al., 2004) is operated on board of the Neil Gehrels Swift Observatory launched in 2004.

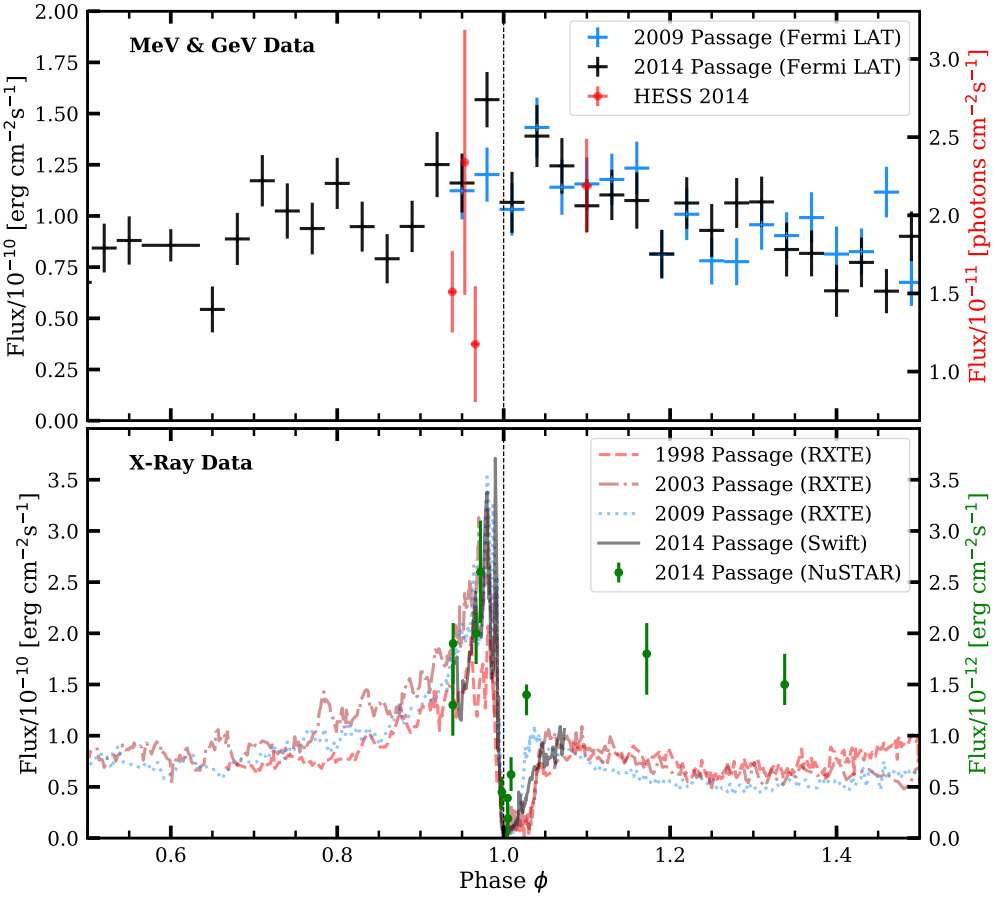

FIGURE 2.10: **Multi wavelength light curve of η Car**
All data sets are presented as a function of orbital phase ϕ using the ephemeris from Teodoro et al. (2016). In the upper panel, the H.E.S.S. flux points from H.E.S.S. Collaboration et al. (2020) taken around the 2014 periastron passage are shown together with the Fermi-LAT flux points over two orbits from White et al. (2020). In the lower panel NuSTAR observations between 30 and 50 keV from Hamaguchi et al. (2018) taken around the 2014 periastron are presented. X-ray observations between 2 and 10 keV were taken with RXTE and Swift for the 1998-2014 periastron passages (Corcoran et al., 2017). The dashed line represents the periastron passage at phase $\phi = 0$.

by the expectation that the X-ray luminosity scales with the distance d_2 between the secondary star and stagnation point as $1/d_2$ (Davidson and Humphreys, 2012). Therefore a significant rise toward periastron connected with the highly eccentric orbit is expected. However, to explain the X-ray minimum and subsequent recovery other effects need to be considered. The three most broadly accepted theories (see e.g. Parkin et al., 2009) are described briefly in the following:

- **The eclipse theory**: In this theory, the X-ray emitting region of the WCR is eclipsed by the primary star itself or by the dense wind of the primary. This would block the X-ray radiation for observers on earth but not imply an actual fading of the X-ray emission.
- **Increased mass-loss theory**: As luminous blue variables have shown significant variability on many time scales (de Groot et al., 2001), there could be phase-locked variability on the mass-loss from the primary star. This could lead to a shell-ejection event during periastron.
- **Shutdown of companion's wind**: Due to the very small stellar separation during periastron, the WCR could move into the acceleration region of the secondary wind, which could cause a collapse of the WCR onto the surface of the secondary star (Akashi et al., 2006). This would result in an actual intrinsic suppression of the X-ray luminosity.

More information on these theories can be found in e.g. Parkin et al. (2009) and references therein. The eclipse theory has difficulties to explain the observed duration and variability of the X-ray minimum. The distortion of the WCR was investigated with 3D hydrodynamical simulations by Parkin et al. (2011), but up to date no clear consensus has been reached.

The hard X-ray component between 20 keV and 50 keV as monitored by NuSTAR[14] (see Figure 2.10) during the 2014 periastron passage (Hamaguchi et al., 2018) traces the non-thermal X-ray component. Qualitatively a similar behavior as for the thermal X-ray emission is visible with some residual emission during the X-ray minimum. This might imply that the non-thermal X-rays are produced in a slightly different part of the WCR but closely connected to the source of thermal X-rays (Hamaguchi et al., 2018). However, a recent model by White et al. (2020) showed that the non-thermal residual emission during periastron could be explained by secondary electrons produced in hadronic interactions.

HE gamma-ray emission coincident with η Car was first detected shortly after the launch of the Fermi-LAT experiment (Abdo et al., 2010). Since then η Car was constantly monitored covering by now 3 periastron passages (see e.g. Reitberger et al., 2012; Reitberger et al., 2015; Balbo and Walter, 2017; White et al., 2020; Martí-Devesa and Reimer, 2021). This allows the derivation of a HE light curve. The 2009

[14]The Nuclear Spectroscopic Telescope Array (NuSTAR; Harrison et al., 2013) is a high energy X-ray telescope operated since 2012.

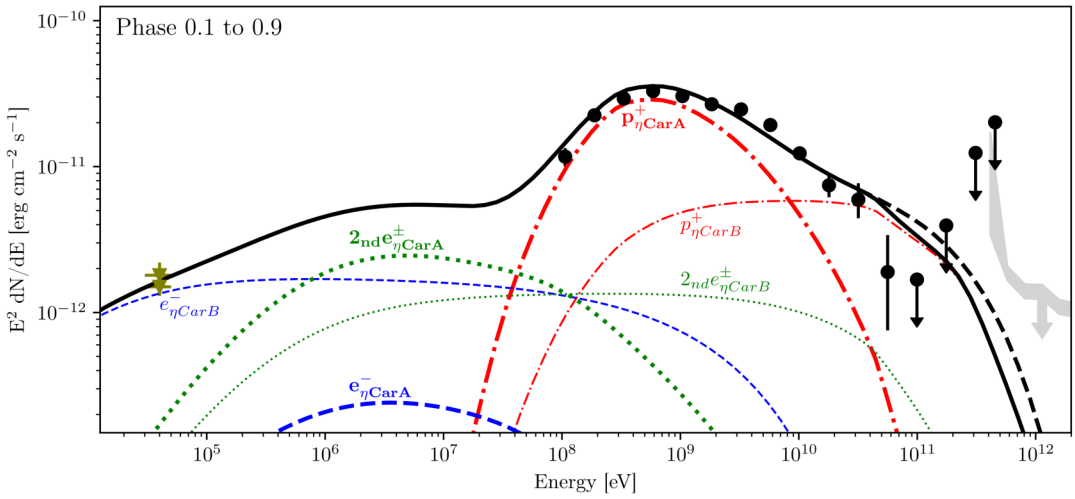

FIGURE 2.11: **Multiwavelength spectrum of the non thermal emission from η Car**
The off phase away from periastron (phase 0.1 to 0.9) is shown. Hard X-ray flux points from NuSTAR are presented in olive green and taken from Hamaguchi et al. (2018). The Fermi-LAT flux points from White et al. (2020) are shown in black. In grey, the upper limit for the off phase from H.E.S.S. Collaboration et al. (2012) is shown. The colored lines indicate the contribution to the gamma-ray flux from the different particle populations accelerated at the two shocks. The black line shows the total gamma-ray flux including absorption and the dashed line without absorption. Adapted from White et al. (2020).

and 2014 passages are shown in the upper panel of Figure 2.10. The sensitivity of Fermi-LAT however does not allow for a test of time scales shorter than months. There are hints for a time variability with an increased flux around periastron and a suppression of flux away from periastron. However, there is some orbit-to-orbit variability further confirmed by the analysis of the 2020 periastron passage (Martí-Devesa and Reimer, 2021) making clear conclusions on the HE light curve difficult.

The Fermi-LAT spectrum can provide clues about the nature of the non-thermal emission, especially whether it is stemming from hadronic or leptonic processes. White et al. (2020) claim the clear signature of a pion bump in the HE spectrum, which is further supported by the systematic study of Abdollahi et al. (2022a) that favors for η Car a broken power law representation over a simple power law on a 4σ level. The pion bump feature can be seen in Figure 2.11, where White et al. (2020) contribute the majority of the emission between 100 MeV and 10 GeV to protons accelerated at the shock on the side of the primary star. Higher energy emission above 10 GeV would then mostly be associated with protons accelerated at the shock associated with the wind from the companion star. Some small additional contribution in the HE regime could originate from secondary electrons radiating via inverse Compton scattering. The model used is in detail described in their paper and in Ohm et al. (2015), where it is originally introduced.

In the VHE regime H.E.S.S. provided upper limits (H.E.S.S. Collaboration et al., 2012) and an actual detection above 200 GeV around the 2014 periastron passage

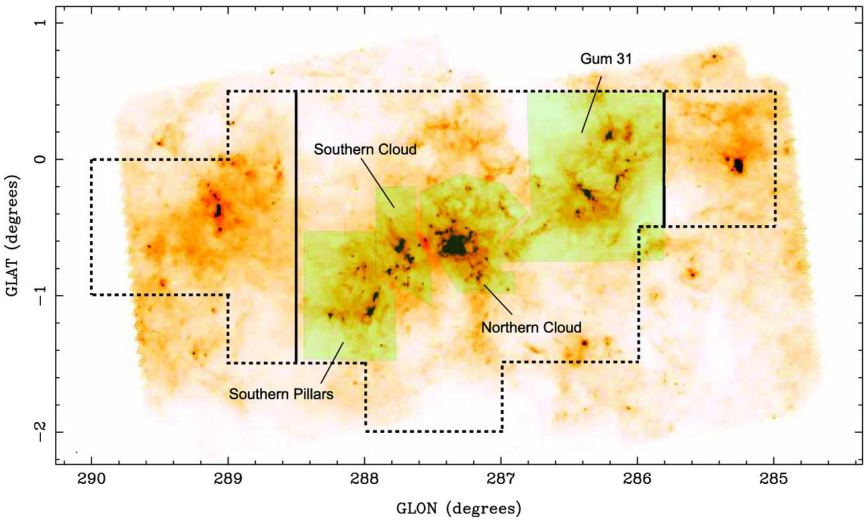

FIGURE 2.12: **Dust emission map of the CNC-Gum31 complex**
A Herschel map at 500 μm (Molinari et al., 2010) of the full CNC-Gum31 region is shown with the main molecular cloud structures highlighted. Taken from Rebolledo et al. (2015).

(H.E.S.S. Collaboration et al., 2020). The light curve points before and after the 2014 periastron are also shown in the upper panel of Figure 2.10. No observations were possible during the actual periastron passage due to visibility constraints. Therefore, the 2020 periastron was the first periastron passage monitored in depth by H.E.S.S., for which the results are presented in this thesis (Chapter 6). Furthermore, in that chapter also the caveats connected to the results from the 2014 periastron passage will be discussed in detail together with the interpretation of the VHE detection.

2.3.4 Surroundings

The environment outside the η Car system is complex and diverse up to large scales. One of the most prominent feature is the Homunculus Nebula created in the Great Eruption, which encloses η Car in an hourglass shape (see also Figure 2.8). The distances of the polar lobes from the binary itself is on the order of 20000 au and its mass is estimated to be between 11 $M_\odot$ and 35 $M_\odot$(Smith, 2008). It consists of gas and dust and heavily absorbs thermal radiation from η Car which it re-radiates in the infrared regime.

The Carina Nebula Complex (CNC) itself is a unique environment hosting a variety of molecular clouds spanning over large regions of the Nebula. Following Rebolledo et al. (2015), 3 large cloud structures can be identified, the Northern Cloud, the Southern Cloud and the Southern Pillars. Close to it, roughly 1° to the northwest is the H II region Gum 31 with the stellar cluster NGC 3324. The physical properties of Gum 31 are not yet fully explored, but the similar distance of 2.5 kpc (Barnes et al., 2010) suggests a physical connection to the CNC. The molecular clouds are shown in Figure 2.12. The combined estimated gas mass in these regions is up to a few 10^5 $M_\odot$ (Rebolledo et al., 2015). Therefore, the molecular clouds within the CNC and Gum

31 as well as the Homunculus could be potential target material to produce gamma-rays. The CRs could either originate from η Car or other potential CR factories in the CNC. A study on this is presented in this thesis (Chapter 7). Potential other sources of CRs within the region include other massive binary systems not yet detected in HE gamma-rays, some potentially unrecognized supernova remnants (Smith et al., 2000) and massive stellar clusters such as Trumpler 14 and Trumpler 16 (Vieu et al., 2022).

2.4 Novae

Novae are eruptive transient phenomena in close binary systems consisting of a white dwarf (WD) and a stellar companion. The stellar companion, either a main sequence star, a red giant (RG) or a subgiant, accretes matter onto the surface of the WD. The accretion can happen either via Roche lobe overflow in a cataclysmic variable or via the stellar wind of the companion. The material accumulates on the surface of the WD continuously increasing in temperature and density. This triggers at some point a thermonuclear explosion on the surface. This eruption nearly exclusively ejects the accumulated material keeping the WD itself mostly intact. Because of that, a nova can be a recurrent process, happening many times for the same system with strongly varying recurrence periods from a few to 10^7 years (Yaron et al., 2005; Wolf et al., 2013).

The explosion is seen in many wavelengths as a sudden brightening due to intense thermal emission as the ejecta is moving outwards from the WD. This leads to a rapid rise to a maximum in the optical light curve followed by a more gradual decline on the scale of days to months. The nature of novae has been an active field of research for many decades, for which extensive reviews can be found in, e.g. Gallagher and Starrfield (1978) and Bode and Evans (2008).

Novae itself are typically classified into several sub-classes. Following Chomiuk et al. (2021) these are:

- **Classical nova**: Nova originating from a Roche lobe filling secondary with typically small accretion rates. No recurrence has been observed.
- **Embedded nova**: Nova originating from a system with an evolved companion. The interaction with the companion wind plays an important role for the observed characteristics.
- **Symbiotic nova**: Subclass of embedded novae with slowly evolving eruptions.
- **Recurrent nova**: All novae for which more than one eruption was recorded. Obviously, this class is limited by the history of modern-day astronomy to only include novae with recurrence periods of 100 years or less.

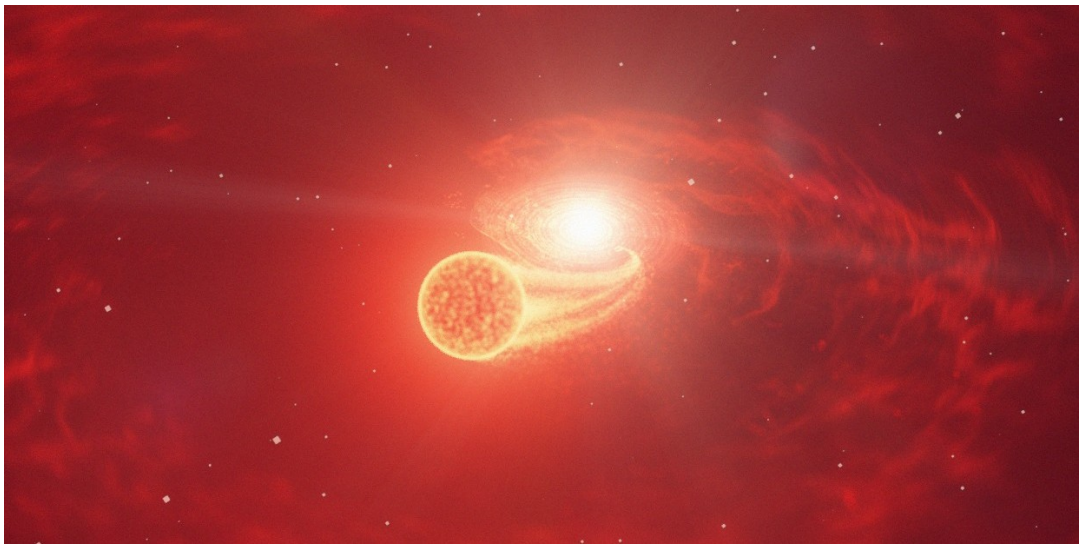

FIGURE 2.13: **Artistic impression of RS Ophiuchi**
The accretion flow from the wind of the RG towards the WD is shown, where it accumulates on the surface. This eventually triggers a thermonuclear explosion. Image Credits: DESY/H.E.S.S., Science Communication Lab

2.4.1 Recurrent novae

The recurrence rate of a nova depends on two main properties, the accretion rate and the mass of the WD. To have recurrence times lower than 100 years, a high accretion rate, $\dot{M} \sim 10^{-7} \mathrm{M}_{\odot}\ \mathrm{yr}^{-1}$, and a high mass of the WD, $M_{wd} \geq 1\mathrm{M}_{\odot}$, is needed (Chomiuk et al., 2021). Until today ten novae have been clearly identified as recurrent novae, which are described in detail in Schaefer (2010). The author shows that recurrent novae have different mean characteristics from the classical nova population but are not a homogeneous class themselves showing a huge variety of different features. Nevertheless, the outbursts of one recurrent nova are consistent in their light curves to previous outbursts. The time between two outbursts though can be variable making any firm prediction for new outbursts on smaller time intervals than 10 years almost impossible.

2.4.2 RS Ophiuchi

RS Ophiuchi (RS Oph) is a recurrent nova with by now 9 detected outbursts. The recurrence period varied between 9 and 26 years with the first recorded outburst in 1898 and the last one in 2021. This recent event will be discussed in detail in Chapter 5 and was following a previous outburst in 2006. RS Oph has a typical peak optical brightness of $m_V \approx 4.8$ mag (Schaefer, 2010). RS Oph consists of a heavy carbon-oxygen WD with $1.2 - 1.4\,\mathrm{M}_{\odot}$ (Mikołajewska and Shara, 2017) and a RG with mass $M_{rg} = 0.68 - 0.8\,\mathrm{M}_{\odot}$ (Brandi et al., 2009). The orbit has a period of 453.6 days, an inclination of 49° - 52° and an orbital separation of 1.48 au with almost no eccentricity (Brandi et al., 2009; Booth et al., 2016). The accretion rate is high,

$\dot{M} \approx 5 \times 10^{-7}\,\mathrm{M}_\odot\,\mathrm{yr}^{-1}$ (Booth et al., 2016). An illustration of RS Oph is depicted in Figure 2.13.

Its distance is debated in the field with an established estimate of 1.4 kpc based on an average over measurements with several techniques (Barry et al., 2008). However, parallax measurements with the Gaia satellite suggested a larger distance of 2.3 kpc or 2.7 kpc (Gaia Collaboration et al., 2018; Lindegren et al., 2021). The Gaia measurements might be less precise due to the effects of the binary motion, which is not accounted for in the parallax measurement. Hence for this thesis, a value of 1.4 kpc is adopted.

The last outburst in 2006 was already monitored with a variety of different instruments in different wavebands. Interestingly, infrared and X-ray measurements already suggested an acceleration of particles up to TeV energies (Tatischeff and Hernanz, 2007) but the new generation of sensitive gamma-ray instruments either didn't exist yet (Fermi-LAT) or did not have a designated nova follow-up program (H.E.S.S.).

2.4.3 Particle acceleration in novae

Even though signs suggesting non-thermal radiation from novae existed, the repeated detection of gamma-rays from mostly classical novae with Fermi-LAT triggered some surprise in the community. Up to now 16 novae were detected and published with Fermi-LAT of which the HE light curves of 12 of those are shown in Figure 2.14. The characteristics of the detected novae up to 2021 before the outburst of RS Oph (see Chapter 5) can be found summarized in Chomiuk et al. (2021) and references therein.

The spectra show typically a cut-off at 1-10 GeV. Consequently, no detection of VHE gamma-rays was achieved up to the RS Oph 2021 outburst. The light curves are characterized by varying durations with significant emission over days up to several weeks. Some of the brightest novae also exhibit correlations between the optical and gamma-ray light curves (Li et al., 2017; Aydi et al., 2020).

The question, if gamma-rays are expected from all novae or not, is inherently correlated to the sensitivity of the gamma-ray instruments making a clear conclusion difficult. Nevertheless, Franckowiak et al. (2018) showed in their study that claims of a similar gamma-ray luminosity for all novae are not valid, but that the luminosities range over at least two orders of magnitude.

In order to produce gamma-rays, novae must possess strong shocks at which diffusive shock acceleration of leptons and hadrons can occur. The shocks at which the acceleration takes place could be external shocks expanding into the wind of the companion star. Such a scenario is sketched in Figure 2.15. For novae without a strong wind from the companion, gamma-ray emission might potentially originate from internal shocks. Internal shocks can be formed within the ejecta if, e.g. outflows with different velocities collide. Their properties are described in more detail in Chomiuk et al. (2021).

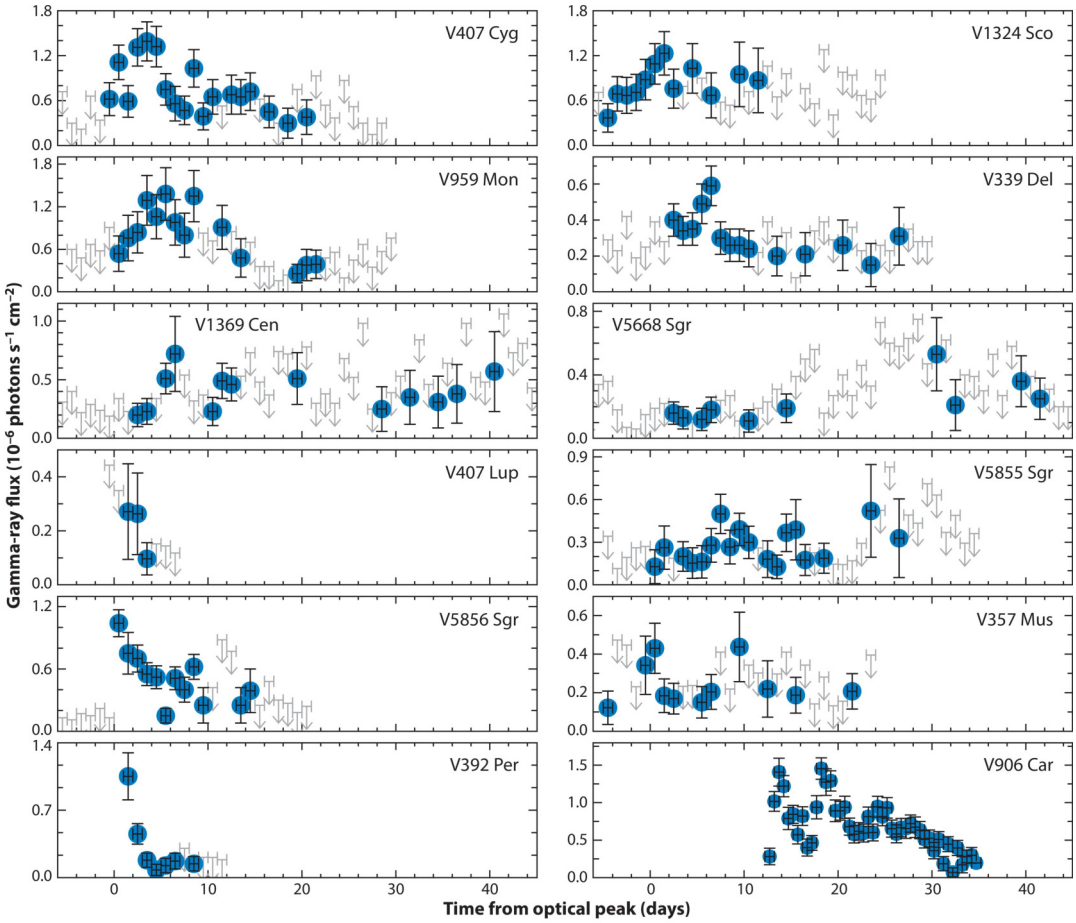

FIGURE 2.14: **Gamma-ray emitting novae discovered by Fermi-LAT** The HE light curves for 12 novae detected by Fermi-LAT for energies above 0.1 GeV are shown. The blue dots stand for flux points above 2σ significance, whereas in grey upper limits are shown for time intervals without significant emission. T = 0 always represents the time of maximum in the optical light curves, except for V959 Mon, where it is the first gamma-ray detection. Taken from Chomiuk et al. (2021).

Based on the Fermi-LAT detections both hadronic and leptonic scenarios were considered in the individual studies to be the dominant origin of the gamma-ray flux. From the observed HE spectra an overall preference for the hadronic scenario could be found. Following Chomiuk et al. (2021) this is mostly based on:

- The observation of a low energy cutoff coincident with the position of the "pion bump".
- Large synchrotron losses for electrons in the strong magnetic fields needed for acceleration.
- Spectral indices < 2 for electron distributions, which is not in line with the prediction from diffusive shock acceleration (see Section 2.1.1).
- Prediction of non-thermal X-ray emission for the leptonic scenario, which was not found yet. Some constraints on this were derived from, e.g. the bright nova V906 Car (Aydi et al., 2020).

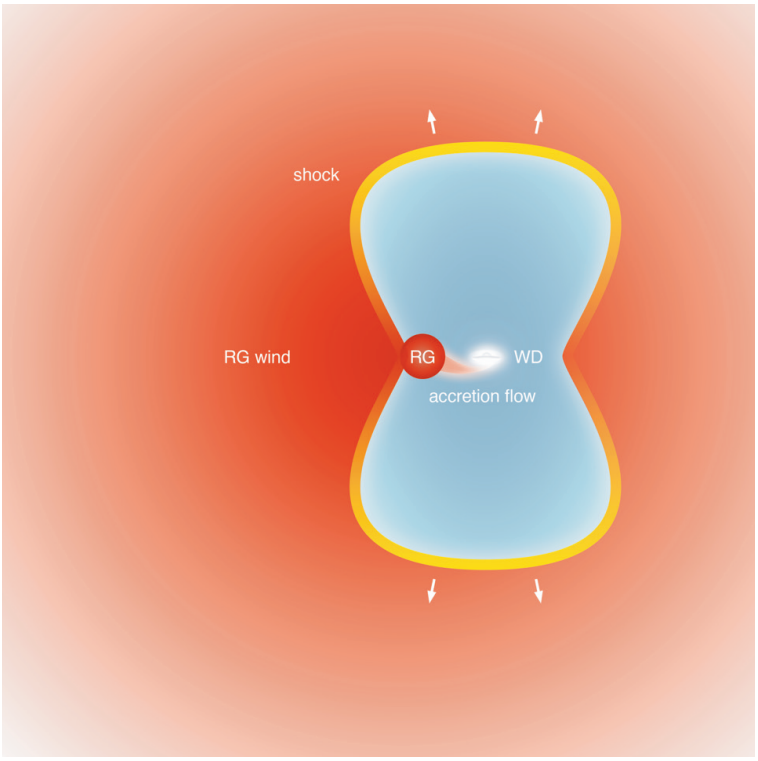

FIGURE 2.15: **Schematic of external shock model**
The thermonuclear explosion is launched near the surface of the white dwarf (WD). The shock is expanding as a bipolar blast wave moving orthogonal to the accretion disk, into the wind of a red giant (RG). The bipolar expansion is not expected for all novae but is based on RS Oph. The color gradient of the shock indicates the expansion velocity, whilst the gradient of the surrounding medium indicates the density of the RG wind. Material internal to the shock is shown in blue. Taken from H.E.S.S. Collaboration et al. (2022).

These points hint at a dominantly hadronic origin of the gamma-rays in novae, but the evidence is not strong enough to fully rule out the leptonic scenario. Additional evidence for hadronic scenarios is discussed for the 2021 outburst of RS Oph in Chapter 5.

2.5 Summary and outlook

This chapter presented an overview of the physical processes through which cosmic rays are accelerated and subsequently emit gamma-rays. Only the processes and phenomena most relevant to this thesis have been described and it should not be considered as a complete review. Furthermore, two classes of binary systems were introduced, that can accelerate particles to high energies and can be detected in gamma-rays. Firstly colliding wind binaries and especially η Car, one of the most peculiar objects in the galaxy, together with its surroundings were described. The details of its gamma-ray emission over its orbit are presented in Chapter 6, whereas

potential cosmic rays escape from it is discussed in Chapter 7. Additionally, novae and their non-thermal emission components were introduced. Special emphasis was laid on the recurrent nova RS Oph. Its most recent outburst and the subsequent detection in gamma-rays is presented in Chapter 5.

Whereas some of the general concepts described in this chapter are well established, the field of astroparticle and cosmic ray physics is rapidly evolving. With the advance in neutrino detectors, a new window to the field is opening up and the current generation gamma-ray experiments will eventually be surpassed by more sensitive observatories already in the developing phase. Nevertheless, the field of current-day gamma-ray astronomy can still provide a unique window to the high-energy universe. Therefore in the next chapter, the detection techniques and characteristics of gamma-ray instruments are discussed.

Chapter 3

Detection of gamma-ray sources

The term gamma-rays typically refers to the highest energy end of the photon spectrum, with photon energies above 0.2 MeV. As the atmosphere is opaque to radiation of such high energy, any astronomical instrument must be either placed outside the atmosphere with satellites or use an indirect detection technique.

The energy band in the MeV domain (between $\sim$0.2 MeV and $\sim$100 MeV) suffers from a lack of competitive instruments due to instrumental difficulties (De Angelis et al., 2021). Especially, the absence of the typical gamma-ray signature, creating an electron-positron pair, below a few MeV and a high instrumental background make the development of sensitive instruments difficult. In the adjacent HE gamma-ray regime, satellite instruments such as most notably Fermi LAT, have been operated with great success detecting more than 5000 sources (Abdollahi et al., 2022b). The detection and analysis principles of Fermi-LAT are described in detail in Section 3.3. Fermi-LAT is operated as a survey instrument constantly monitoring the gamma-ray sky.

As shown in Figure 3.1 at the transition to the VHE gamma-ray regime above $\sim$100 GeV the Fermi-LAT point source sensitivity is outperformed by current and future ground-based IACT telescopes like H.E.S.S. and CTA. The lower exposure times of IACT arrays due to their nature as pointing instruments with a limited field of view (FoV), is compensated by much larger effective detector areas. The IACT technique in general with special emphasis on H.E.S.S. and the data analysis pipeline are described in detail in Section 3.1 and Section 3.2.

At even higher energies, the so-called ultra-high energy (UHE) regime, particle detector arrays like the High Altitude Water Cherenkov (HAWC) observatory and the Large High Altitude Air Shower Observatory (LHAASO) offer good sensitivity up to several hundreds of TeV. Combining the different instrument types provides good coverage of the full HE to UHE energy regime. Hence any astrophysical gamma-ray source can quite often be observed in several decades of energies.

In this thesis, the synergy and combination of the Fermi-LAT and H.E.S.S. observations will be at the core of the results presented in Chapter 5, Chapter 6 and Chapter 7. Consequently, these two instruments and their underlying principles are presented in the following.

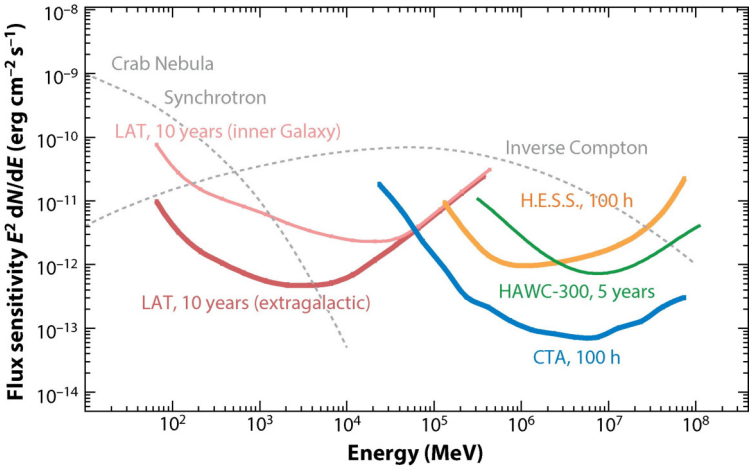

FIGURE 3.1: **Comparison of point-source sensitivity of selected (very) high-energy instruments and projects**
The sensitivity of Fermi-LAT with an exposure of 10 yrs is shown for galactic and extragalactic sources. The sensitivity of current IACT instruments with the example of H.E.S.S. is compared to the next generation CTA array assuming an exposure of 100 h. Additionally, the 5-year sensitivity of the particle detector array HAWC is drawn. For reference also the spectral components of the Crab Nebula, the standard candle in gamma-ray astrophysics, are shown. Taken from Funk (2015).

3.1 Imaging Atmospheric Cherenkov Telescopes

As most astrophysical sources in the VHE regime exhibit a rather steeply falling spectral behavior, expanding the energy range beyond 100 GeV imposes the need for large collection areas. Such large detectors are beyond the limitations, both technical and monetary, for satellite experiments. Fortunately, VHE gamma-rays penetrating the Earth's atmosphere cause a distinct signal that can be observed by ground-based stations. This offers an indirect but still precise view into the VHE sky.

3.1.1 Air showers

Gamma-rays stemming from either galactic or extragalactic accelerators, as discussed in Chapter 2, reach the Earth's atmosphere pointing directly back to their source. In much higher numbers also charged cosmic rays hit the Earth's atmosphere. Their composition is dominated by protons but also alpha particles and heavier nuclei as well as electrons are contained, as discussed in Section 2.1.

After penetrating the atmosphere and interacting with air particles, both, photons and cosmic rays, produce a cascade of relativistic secondary particles usually called an extensive air shower (EAS). The shower development and content depend heavily on the nature of the primary. The atmosphere acting in this case as the calorimeter is assumed to have a density profile $\rho(h)$ as a function of height h described as

$$\rho(h) = \rho_0 \exp\left(-h/h_0\right) \tag{3.1}$$

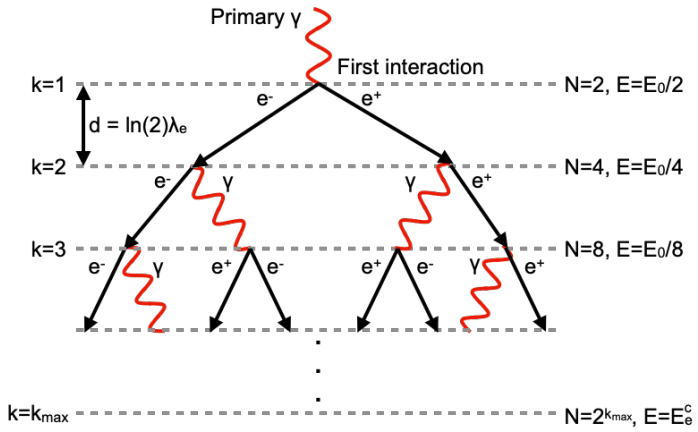

FIGURE 3.2: **Model illustrating the electromagnetic shower development**
Electromagnetic showers can be described by the simple Heitler model. A primary gamma-ray (γ) interacts with an air nucleus starting an electromagnetic cascade. After each step k, the number of particles is doubled and the energy per particle decreases accordingly. The shower development starts to stop, once the critical energy for electrons E_e^c is reached. Taken from Ruiz Velasco (2021).

with $\rho_0 \approx 1.225\,\mathrm{kg\,m^{-3}}$ and $h_o \approx 8.4$ km (NASA, 1976). The slant depth $X(h)$ from the top of the atmosphere downwards is then:

$$X(h) = \int_h^\infty \rho(z)\mathrm{d}z \tag{3.2}$$

Electromagnetic showers If the primary is a photon or lepton, an electromagnetic air shower caused by pair production and bremsstrahlung (Bethe and Heitler, 1934) develops. A photon creates an electron-positron pair in the Coulomb field of an air nucleus. The subsequent particles get deflected in the electric field of another nucleus producing a photon via bremsstrahlung that can once again create an electron-positron pair. This process and the longitudinal shower development can be described by the simple Heitler model (Heitler, 1954). With this model, approximations for the shower properties can be retrieved. Starting with one primary particle with energy E_0, after one interaction length $d = ln(2)\lambda_\mathrm{e}$ two particles with energy $E_0/2$ are produced. For air the characteristic radiation length is $\lambda_\mathrm{e} = 37\,\mathrm{g\,cm^{-2}}$. After each subsequent interaction length, the number of particles N is doubled. After a certain number k of interaction lengths, the number of particles in the shower is then $N = 2^k$ and the energy per particle $E = E_0/2^k$. This process is sketched in Figure 3.2.

As the particle energy is reduced, ionization losses start to play a role. The critical energy at which this ionization energy loss and the bremsstrahlung loss are equal is for air $E_c = 86$ MeV (Engel et al., 2011). As a consequence, the shower starts to die

out and the maximum number of particles $N_{max} = \frac{E_0}{E_c}$ is reached at a penetration depth of $X_{\max} = \lambda_e \ln \frac{E_0}{E_c}$.

The lateral spread of the shower is caused by the Coulomb scattering of electrons off air atoms described by the Moliere radius (Moliere, 1948), corresponding to roughly 80 m on sea level.

Hadronic showers For hadrons as primaries a differently evolving air shower occurs, consequently labeled hadronic shower. The cosmic ray nucleus scatters inelastically on air nuclei in strong force interactions. This produces mostly pions ($\pi^{\pm}$ and π^0) but also in lower numbers nucleons (n,p), nuclear fragments (N), kaons and hyperons. A generalization of the Heitler model for the hadronic components was derived by Matthews (2005). There, typically $\sim$10 secondary particles are created in an interaction with two-thirds charged particles like $\pi^{\pm}$ and one-third neutral particles like π^0. As the neutral π^0 quickly decays into two gammas and a subsequent electromagnetic shower is started, the electromagnetic shower component created by each interaction is roughly one-third.

The $\pi^{\pm}$ can interact again with air nuclei or if they are below a typical decay energy $E_{c,\pi} \lesssim 30$ GeV (Engel et al., 2011) decay into mostly muons ($\mu^{\pm}$) and muon neutrinos ($\overset{(-)}{\nu}_{\mu}$). Hence after k generations the energy in the hadronic component E_{had} is given by $E_{\text{had}} = \left(\frac{2}{3}\right)^k E_0$ (Engel et al., 2011) with the electromagnetic component carrying away the remaining energy. The lateral spread of the shower is governed by the transverse momentum of secondary hadrons, leading to large angles relative to the shower axis. A sketch of the shower development is drawn in Figure 3.3.

Shower properties and differences As it is of crucial importance to distinguish hadron-induced showers from photon-induced showers for IACTs, the main differences need to be exploited. As discussed above, the lateral spread of electromagnetic showers is smaller, yielding narrow showers in comparison. Furthermore, hadronic showers develop several electromagnetic sub-showers resulting in a less regular and highly variable structure. Additionally, the number of muons in hadronic showers is considerably higher by roughly two orders of magnitudes (Gaisser et al., 1991), which can be exploited for a muon-veto scheme in IACTs (Olivera-Nieto et al., 2021). Due to the larger interaction length for pions, they also penetrate deeper into the atmosphere.

In Figure 3.4 simulated showers from a 300 GeV gamma-ray and 1 TeV proton primary are compared, clearly depicting the broader more irregular nature of the proton shower.

Cherenkov light from air showers Cherenkov radiation is named after its discoverer (Cherenkov, 1934). It is emitted by charged particles traveling through a dielectric medium with a speed $v > c/n$, thus greater than the speed of light in the medium with refractive index n. With the refractive index of air at sea level,

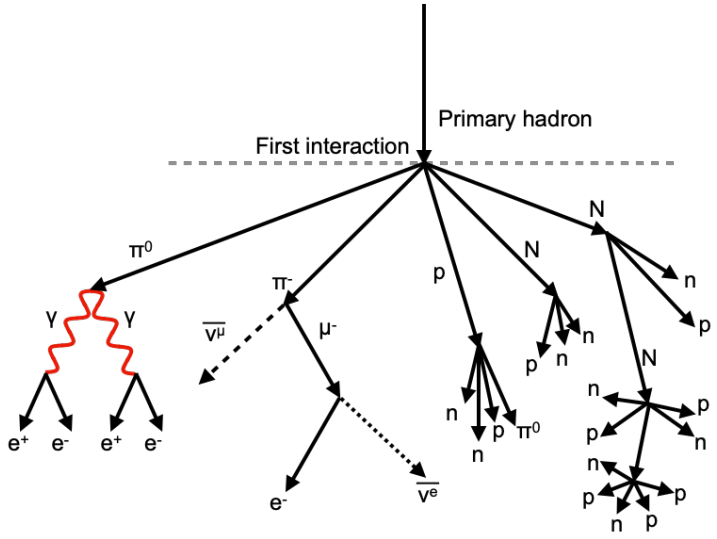

FIGURE 3.3: **Model illustrating the hadronic shower development** A primary hadron scatters inelastically on an air nucleus, creating several subshowers. Some of the subshowers evolve electromagnetically, whereas others undergo further hadronic interactions. The type of secondary particles and the shape of the subshowers can be quite varied. Taken from Ruiz Velasco (2021).

$n = 1.00029$, this results in threshold energies of ∼21 MeV, ∼4.4 GeV and ∼39 GeV for electrons, muons and protons, respectively. Therefore, EAS induced by very high energy photons and hadrons will both cause emission of such radiation dominated by the leptonic component.

A sketch of the mechanism responsible for Cherenkov radiation can be seen in Figure 3.5. A moving charged particle induces dipole states in the atoms and molecules in the medium, which afterward return to their ground state emitting electromagnetic radiation forming spherical wavefronts. If the velocity of the particle is greater than the speed of light this results in overlapping wavefronts, constructively interfering in a cone-like shape. Therefore, the Cherenkov radiation is emitted in a narrow cone with a distinct opening angle Θ_C relative to the track of the primary particle. The opening angle depends on the particle velocity $\beta = v/c$ and the refractive index as:

$$\cos \Theta_C = \frac{1}{\beta n} \tag{3.3}$$

For particles in EAS typical opening angles are about 1° to 2°, leading to a projection of the light cone on ground with a radius of ∼100 m. In the lower panel of Figure 3.4, typical Cherenkov light pools for an electromagnetic and hadronic shower are shown. The narrow and well-constrained electromagnetic shower causes a well-constrained cumulated light pool with a radius of ∼125 m, whereas the irregular and wider nature of the hadronic shower is also visible in the corresponding Cherenkov

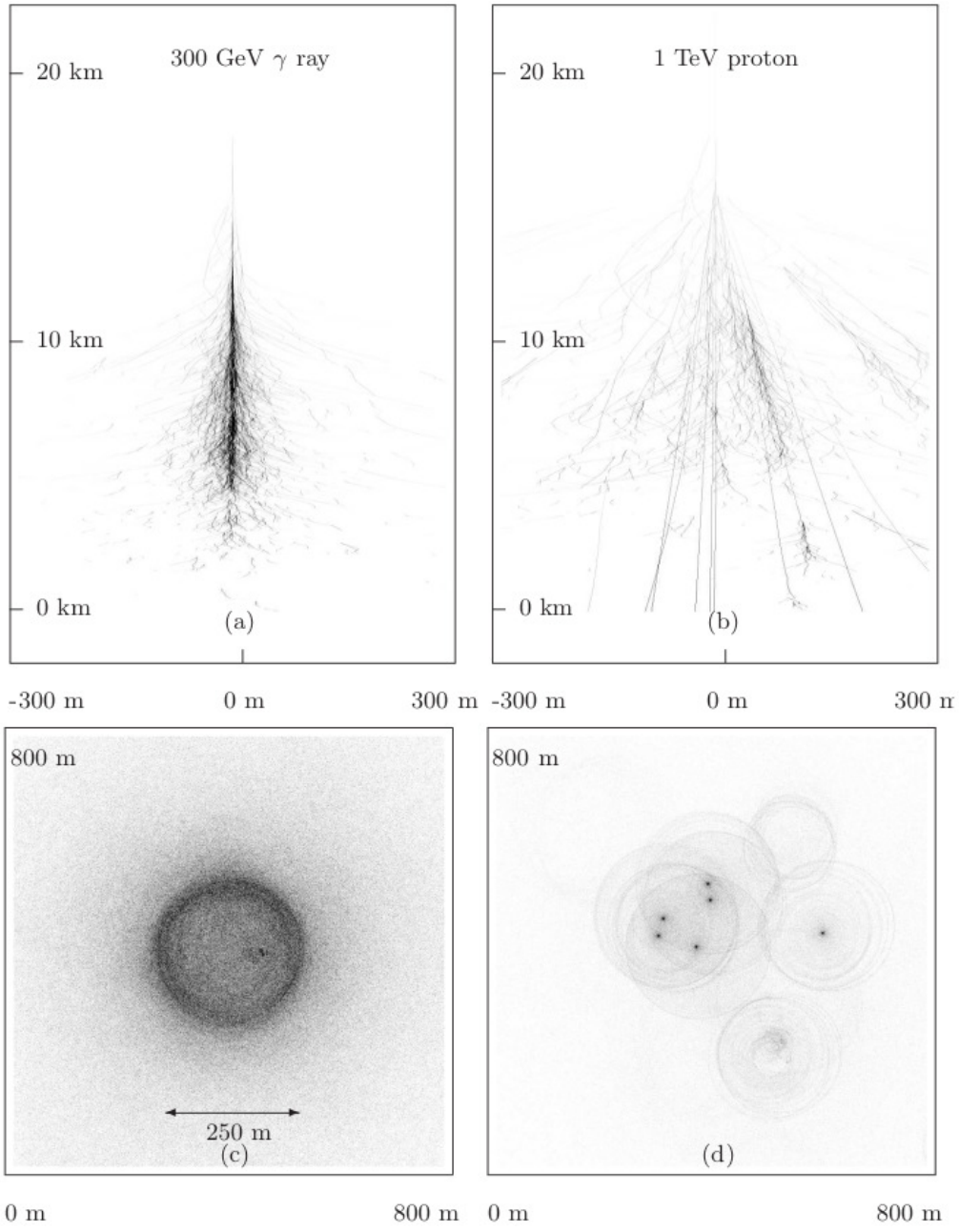

FIGURE 3.4: **Gamma-ray and hadronic air shower and the corresponding Cherenkov emission compared**
Simulated EAS induced by a gamma-ray with an energy of 300 GeV (**a,c**) and by a 1 TeV proton (**b,d**) are depicted. In the upper panel, the longitudinal development of the particle tracks is viewed from the side and in the lower panel, the corresponding Cherenkov light pool is projected onto the ground plane. Taken from Ohm (2010).

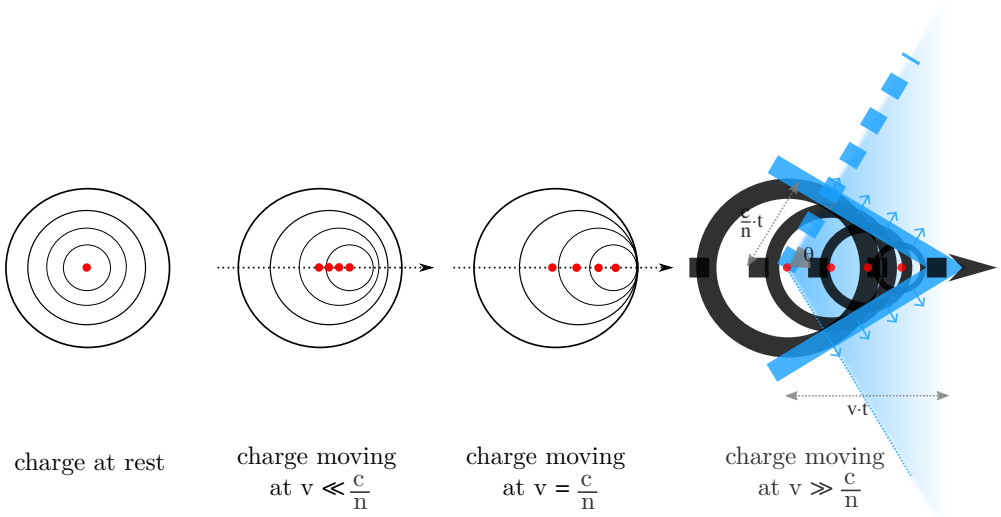

FIGURE 3.5: **Origin of Cherenkov radiation**
From left to right, a charged particle is moving with increasing velocity. For the first three cases ($v \leq c/n$), no Cherenkov signal is created. On the right the particle speed fulfills the Cherenkov criterion, causing wavefronts to interfere constructively building up a cone-like emission with a defined opening angle. Taken from Jardin-Blicq (2019).

signal. The Cherenkov signal arrives with only a small time spread on scales of a few nanoseconds, as the shower development happens in a thin shower front.

The Cherenkov spectrum for a particle with charge q can be described by the Frank-Tamm formula (Tamm and Frank, 1937) represented by the number of photons N per path length x within a wavelength interval $[\lambda_1, \lambda_2]$,

$$\frac{\mathrm{d}N}{\mathrm{d}x} = 2\pi\alpha q^2 \int_{\lambda_1}^{\lambda_2} \left(1 - \frac{c^2}{v^2 n(\lambda)^2}\right) \frac{1}{\lambda^2} \mathrm{d}\lambda, \tag{3.4}$$

where α is the fine structure constant. This in turn means that the emission is stronger for faster particles and that it is stronger for shorter wavelengths. The influence of Rayleigh and Mie scattering on photons with short wavelengths and the absorption of ultraviolet light below 300 nm through Ozon shifts the peak of the spectrum visible on the ground towards the near ultraviolet and blue wavelengths. Eventually, for an EAS caused by a 1 TeV gamma-ray only $\sim$100 photons per m^2 reach the ground, giving the need for large mirrors to collect a sufficient amount of light.

3.1.2 Basic working principles of IACTs

The fact, that incoming extraterrestrial gamma-rays produce a well-detectable optical signal via Cherenkov radiation, which can be traced back to the direction of the gamma-ray photon, is exploited via the Imaging Atmospheric Cherenkov Telescope technique. If the analogy to particle detectors is drawn, the atmosphere is hence

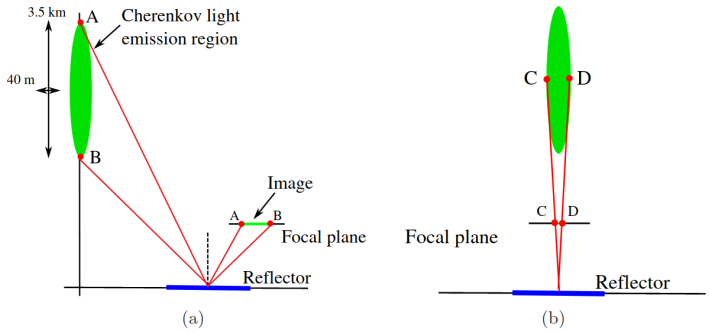

FIGURE 3.6: **Sketch of imaging principle of IACTs**
In **a** the projection of the shower axis into the focal plane of a telescope is shown. Doing this, naturally, the orientation of the image depends on the inclination of the shower with respect to the telescope's optical axis. The longitudinal shower size is represented as the length of the shower image. In **b** the shower is viewed from the telescope with the image width then showing the lateral spread of the shower. Taken from Hoppe (2008).

playing the role of a calorimeter. The large light pool on the ground causes effective detection areas of $\sim 10^5\,\mathrm{m}^2$, in which imaging telescopes can be placed. The telescopes on the ground need to be equipped with large mirrors to collect enough of the faint Cherenkov signal and cameras predominantly sensitive in the blue optical waveband. The cameras do not need to be finely pixelated as the Cherenkov signal is rather large in extent but need to be fast enough to detect the Cherenkov flashes on nanosecond scales. For this purpose photomultiplier tubes (PMTs) have proven to be a good choice for equipping the cameras.

As the Cherenkov signal of an EAS has the form of a 3D ellipsoid they are imaged in elliptical shape onto the camera. This is schematically shown in Figure 3.6. From this, it gets clear that the position of the image in the camera depends on the offset of the shower main axis from the reflector axis. Further, the major axis of the shower ellipse traces the path of the original gamma-ray and can be projected both onto the sky and the ground. With this, the direction of the shower on the sky as well as the impact point on the ground can be estimated. The length and width of the shower ellipse represent the longitudinal and lateral extent of the shower as viewed under a certain inclination.

Placing a second telescope into the light pool helps to reduce ambiguities in the direction and energy reconstruction. This is described in more detail in Section 3.2.3. Such a stereoscopic system also helps to reduce the influence of the night sky background. As the large mirrors will collect plenty of starlight, the camera detectors also record the corresponding signal as a mostly steady noise source. With a stereoscopic system statistical over-fluctuations of noise in one telescope are most likely rejected by the second telescope. The need to detect faint blue showers obviously reduces the duty cycle to dark conditions ruling out any operation during daytime or bright moon time. Furthermore, by relying on an optically transparent atmosphere,

Instrument	Lat. (°)	Long. (°)	Alt. (m)	Tels	Mirror Area (m^2)	Pixels	FoV (°)
H.E.S.S.	-23	16	1800	5	1042	960 / 1764	5 / 3.4
VERITAS	32	-111	1275	4	424	499	3.5
MAGIC	29	18	2225	2	472	1039	3.5
CTA South	-25	-70	2600	51	1528	2048 / 1764	8.8 / 7
CTA North	29	18	2225	13	2272	1855	7 / 4.3

TABLE 3.1: **Current and future IACT arrays**
The numbers were taken from Hinton and Hofmann (2009) and updated accordingly for H.E.S.S. (Bi et al., 2022) and MAGIC (Aleksić et al., 2016). The CTA layout considered is the so-called α-configuration (Zanin et al., 2022). Tels denotes the number of telescopes and the mirror area is presented for the full array. If the array is built up of different telescope and camera types the specific characteristics for pixels and FoV are given separately.

the Cherenkov signal can also be blocked by clouds or other hazy conditions. This reduces the overall observation time of IACT arrays to $\sim$2000 h or less per year depending on the location. Because IACTs are pointing instruments, the FoV for any observation is also limited, typically $\sim5^\circ$.

The first IACT instrument was built in the late 80s and operated as a single telescope with a mirror of 10 m diameter. It was located at the Whipple observatory in Arizona. With it, the first VHE source, the Crab Nebula, was detected (Weekes et al., 1989). The first multi-telescope array was the High Energy Gamma Ray Astronomy (HEGRA) system inaugurated in 1996 (Daum et al., 1997). Hence, the currently operating H.E.S.S., Very Energetic Radiation Imaging Telescope Array System (VERITAS) and Major Atmospheric Gamma-Ray Imaging Cherenkov (MAGIC) telescopes can be considered third-generation instruments. They are all operated as arrays consisting of 5, 2 and 4 telescopes, respectively. These instruments have been quite successful in increasing the catalog of known VHE sources to $\sim$250 (see Section 2.2.3). Among those, H.E.S.S. is the only current instrument located in the southern hemisphere and consisting of telescopes with different mirror areas. This concept will be expanded further for CTA, which is planned to be built in the coming years. The current design consists of two sites, one in the northern and one in the southern hemisphere, equipped with a combined 64 telescopes of 3 different sizes. The basic properties of the current and future generation IACTs are summarized in Table 3.1.

3.1.3 The High Energy Stereoscopic System

The High Energy Stereoscopic System or short H.E.S.S. is an IACT array consisting of 5 telescopes. It is located at Farm Goellschau in Namibia at the coordinates and altitude presented in Table 3.1. It started operating in 2002 and is currently scheduled to at least run until autumn 2024.

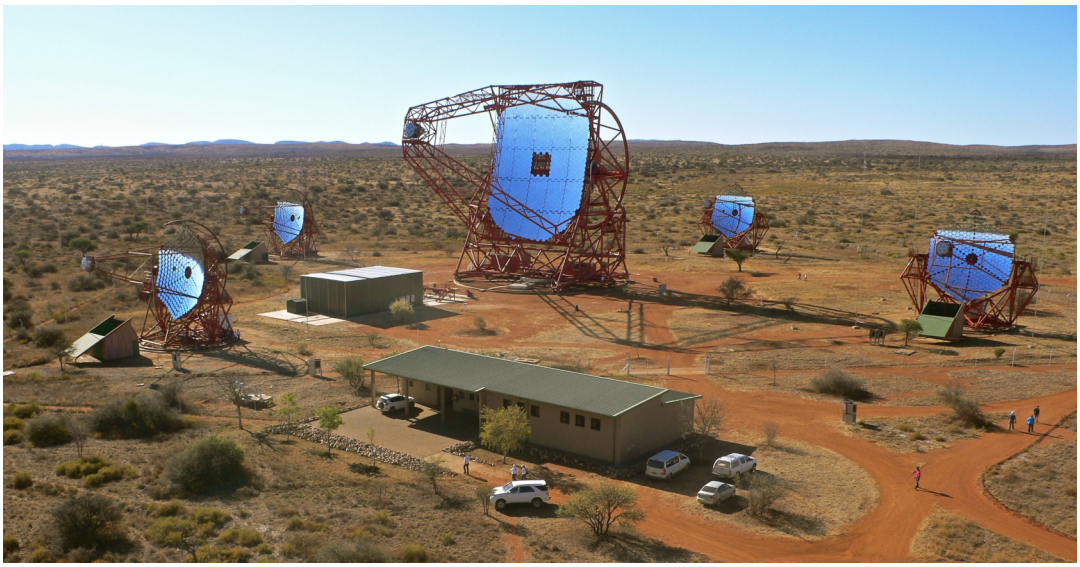

FIGURE 3.7: **The current H.E.S.S. array**
Daytime image of the H.E.S.S. array with the smaller CT1-4 telescopes arranged in a square and the large CT5 in the middle. The building in front is used for the operation of the telescopes and also hosts the data acquisition and trigger servers. Image Credit: Christian Föhr.

Array layout and instruments The first phase of array construction usually referred to as H.E.S.S. 1 was finished in 2004 and consisted of four telescopes with hexagonal mirrors with areas of 108 m^2, equivalent to a 12 m diameter. The mirrors are following the so-called Davies-Cotton (Davies and Cotton, 1957) design consisting of 382 individual facets. The camera is mounted at a focal length of 15 m. The cameras themselves were upgraded in 2016 (Giavitto et al., 2018), with the updated cameras accordingly named H.E.S.S. 1U, and consist of 960 PMTs with a pixel size of 42 mm. This is equivalent to 0.16° on the sky and the total FoV is ∼5°. The four telescopes, usually referred to as CT1-4, are arranged as a square with a 120 m side length. In 2012 an additional larger telescope was placed in the center of the array. This telescope, usually referred to as CT5 and the full 5-telescope array being labeled H.E.S.S. 2, has a mirror with dimensions of 32.6 m by 24.3 m. This is equivalent to a diameter of 28 m or a total mirror area of 614 m^2. The mirror is consisting of 875 hexagonal facets and the camera is mounted at a focal length of 36 m. The camera for the CT5 telescope was upgraded in 2019 with a FlashCam prototype (Bi et al., 2022). This consists of 1764 pixels, of which 1758 are active. The hexagonal FoV is 3.4° on average with a pixel spacing of 50 mm or 0.08°. The larger collection area of CT5 allows for the detection of fainter Cherenkov showers significantly reducing the energy threshold of H.E.S.S. A picture of the full H.E.S.S. array can be seen in Figure 3.7.

Data taking and acquisition In principle, the array can be separated into subarrays of CT1-4 and CT5 for parallel data taking on separate targets. Nevertheless, the large majority of observation runs are taken with the full five-telescope array.

The typical duration of observation runs is 28 mins, a time interval in which observation conditions should be roughly constant. The telescopes slew automatically following a given target position with a pointing accuracy of a few arcseconds (H.E.S.S. Collaboration et al., 2010b). To avoid any damage by high currents, pixels are automatically disabled if influenced by a bright light source, e.g. stars or satellites. For H.E.S.S., the pointing target of an observation is typically set with an offset of 0.5° or 0.7° from the actual scientific target, the so-called wobble-mode. This has advantages for the description of the background as discussed later in Section 3.2.5.

The trigger system is operated by the central trigger (Funk et al., 2004). Since the installation of CT5, the trigger scheme is a hybrid trigger. This means that CT5 is operated in monoscopic mode, storing all events that trigger CT5 independently of the other telescopes. CT1-4 triggers are only recorded if at least one other telescope also records an event, the so-called stereo trigger. Hence the system trigger rate consists of all CT5 mono triggers plus additional CT1-4 stereo triggers with no CT5 trigger. If the array is split the sub-arrays are operated in mono and CT1-4 stereo trigger mode accordingly. The matching of the individual telescope triggers with their time stamps using a coincidence window of 80 ns is always done in the central trigger. The trigger logic for CT1-4 follows the multiplicity trigger described in Giavitto et al. (2018), which means that a trigger is issued if at least three pixels have a signal of at least x photo-electrons (p.e.). The CT5 trigger for the FlashCam camera follows Sailer et al. (2019), meaning that a trigger is issued, whenever one of 588 overlapping 9-pixel patches records a combined intensity of more than x photoelectrons. Currently, the default trigger thresholds are set to 5.5 p.e. and 69 p.e. for CT1-4 and CT5, respectively but can be adapted to special observing conditions, as it is the case for, e.g. the η Car observations described in Chapter 6. These thresholds were set as a compromise to have as many Cherenkov triggers as possible, while not being susceptible to too many triggers by noise such as the night sky background (NSB). This keeps the overall trigger rate rather constant. The trigger rate is of course modulated by the transparency of the atmosphere and the airmass set by the target altitude through which the showers are observed. For good conditions, typical system trigger rates are 2.5 kHz to 3 kHz with the majority of triggers coming from CT5 mono.

The triggered events are then recorded by the Data Acquisition System (DAQ) described in detail in Zhu et al. (2022). Additionally to the observation runs, calibration runs, such as flat field, single photoelectron or pointing runs need to be taken regularly to allow for accurate calibration of the data as described in 3.2.1.

3.2 Data analysis of IACT data - the pipeline for H.E.S.S.

After the acquisition of the data on-site, several reduction steps (calibration and analysis) need to be performed to end up with the scientific results. For that reason, several data levels (DLs) from DL0 to DL4 are defined for IACT instruments.

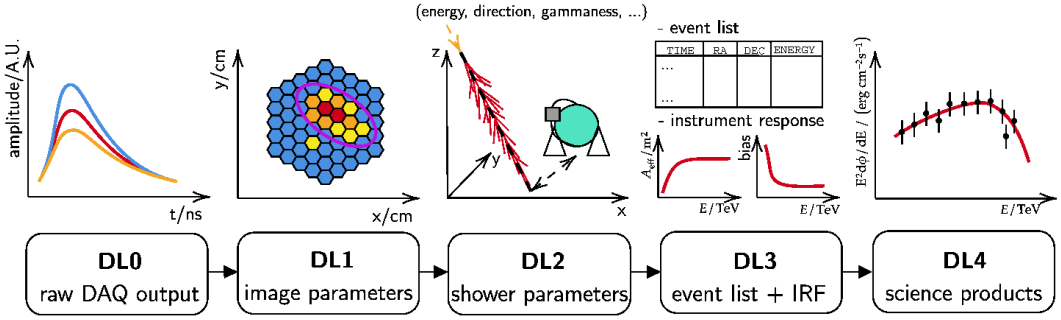

FIGURE 3.8: **Basic outline of an IACT data analysis and the different data levels involved**
The data reduction scheme for IACT analysis starts from the raw traces (DL0) and eventually leads to final scientific data products (DL4). All intermediate steps are described in detail for H.E.S.S. in the text. Taken from Nigro et al. (2021).

An in-depth description of the data levels can be found in Nigro et al. (2021) and is summarized in Figure 3.8.

The step from DL0 (raw DAQ output) to DL1 (image parameters) is for H.E.S.S. done partly already on site. The acquired pulses for each event and pixel are integrated to derive for each pixel one raw pulse intensity and time. For CT1-4 this is done with a fixed 16 ns integration window around the trigger time[1]. For CT5 the pulses are in each pixel reconstructed using a neighbor-based signal search (Bernlöhr et al., 2013; Puehlhofer et al., 2022). These steps happen already on the camera server. This raw data information is together with side products such as broken pixel lists transferred to Europe, where the rest of the conversion to DL1 and beyond is done.

For current generation IACTs such as H.E.S.S. the reduction up to DL3 (event lists & instrument response functions) is done with proprietary software. In the case of H.E.S.S., two independent chains for the reduction until DL3 exist. These are called ParisAnalysis and H.E.S.S. Analysis Package (HAP) and are typically applied both for a particular data set to have an independent crosscheck on any scientific result. As this work is solely based on HAP analysis, only this chain is described in detail. Starting from DL3, several software packages can be considered to derive scientific results (DL4). In this thesis, either the HAP internal high-level analysis or the open-source package Gammapy[2] (Deil et al., 2017) were used. Gammapy is being developed for the future CTA instrument but is compatible with any DL3 type data from H.E.S.S. and other instruments.

[1] In principle CT1-4 pulses can also be integrated using a 9 ns window based on the maxima of the neighboring pixels. This method is described in Zorn (2020) but is not routinely used by the time of writing.

[2] Currently, Gammapy is available in its release version 1.0. More information and updates can be found under `https://docs.gammapy.org/`.

3.2.1 Calibration and image cleaning

After the transfer of the raw data products as described above, these need to be calibrated to get a meaningful Cherenkov charge estimate for each pixel. For the CT1-4 cameras, the calibration is described in detail in H.E.S.S. Collaboration et al. (2004). The integrated pulses are here in analog to digital converter (ADC) counts. The resulting charge C in units of p.e. can be derived for each pixel by the following relation:

$$C = \frac{ADC - P}{G} \times FF \times B \tag{3.5}$$

Here, P is the pedestal charge, G the gain, FF the flat field coefficient and B the broken pixel flag. The CT1-4 cameras have two gain channels, a low and a high gain channel. Currently, the high gain channel is operated such that the signal from a single photoelectron is $\sim$60 ADC counts. The low gain channel is usually described by the high gain to low gain ratio, which, in this case, enters Equation 3.5 as an additional multiplicative factor, while always keeping G at the high gain value.

The gain is derived from special single-photoelectron runs and the high gain to low gain ratio from the overlap regions, where both channels are linear. The pedestal charge per pixel is estimated from the run itself averaging over events with no Cherenkov light. Thus, this includes both the effect of electronic noise as well as night sky background and allows for frequent updates of the pedestal value. The width of the pedestal distribution quantified by its root mean square (RMS)[3] value is important for e.g. the cleaning later on and further used as a measure of the NSB. The flat field coefficient per pixel is used to correct for inhomogeneities over the camera and is derived from flat field runs using light emitting diode (LED) flashers. The broken pixel flag is set to either 1 or 0 causing pixels that were switched off due to, e.g. bright stars or with known hardware issues to have no charge.

For FlashCam, the charge is derived by a simplified version of Equation 3.5. As the reconstructed charge resulting from the pulse reconstruction on the camera server C_{reco} is already in units of photoelectrons, it includes already the gain. The gain is measured from lab measurements and with only one gain channel a nonlinear regime needs to be accounted for. This is done via a calibration table also based on lab measurements. Furthermore, the baseline is measured precisely by the camera and already subtracted in C_{reco}. From the baseline also a precise conversion to the NSB rate is possible. These calibration steps are described in detail in Bi et al. (2022) and Werner et al. (2017). The resulting equation for the remaining calibration steps is:

$$C = (C_{reco} - P) \times FF \times B \tag{3.6}$$

FF and B have the same meaning as above and are derived by the same means. P here denotes the residual baseline. As the neighbor-based peak search introduces a small bias this is evaluated by averaging over events with no Cherenkov light

[3] Throughout this thesis the term RMS refers actually to the standard deviation in case of a distribution with a mean $\neq 0$.

and hence subtracted here. The width of the distribution is once again a measure of the NSB noise. The time information is corrected with the help of flat field runs measuring the trigger time in each pixel and comparing it to the median trigger time.

A calibration for the optical efficiency of the system is needed to get precise energy estimates later on. The optical system is a combination of the mirror, the funnels and in the case of FlashCam the plexiglass on top, which all suffer from degradation effects. Potentially, also a systematic degradation of the quantum efficiencies could cause dimmer images. Of course, the optical throughput can also be sometimes improved by e.g. a cleaning of the funnels or rain washing the mirrors. The calibration method deployed to correct for the changing optical throughput uses muons passing through the mirror making almost perfect rings on the camera. This is described in more detail in e.g. Mitchell et al. (2016). The expected Cherenkov emission from these muons can be derived analytically and hence the measured brightness of the ring will give an overall optical efficiency of the whole optical system. For each observation run a few hundred muons pass specific selection cuts and are used for this analysis. Hence, for each telescope and for each run an estimate of the muon efficiency is obtained and will be later applied to correct the event energies.

After these calibration steps, the images are cleaned to avoid reconstruction problems caused by statistical overfluctuations in noise. The default cleaning for H.E.S.S. is the tail cut cleaning method which is a two-step process. In the first step, all pixels with intensities smaller than 3 times the pedestal width in a given pixel are excluded. Typical pedestal width values for normal dark pixels are of the order $1 - 1.5$ p.e. and hence this will only be decisive for pixels with, e.g. bright stars. In a second step only pixels above a certain threshold, e.g. 5 p.e. and a neighbor above a second threshold, e.g., 10 p.e. are kept and vice versa. There exists also the possibility to require at least 2 or more neighbors. Currently, for CT1-4 the two thresholds are 5 p.e. and 10 p.e. and for CT5 with FlashCam 9 p.e. and 16 p.e. with an additional 2 neighbor requirement for CT5. In order to use the ImPACT reconstruction (see Section 3.2.3), a looser (4,7) cleaning with an extension of adjacent rows is also stored. A new cleaning approach mostly independent of the image intensities is introduced in this thesis in Section 4.3.

From the cleaned images typically representing elongated 2D Gaussians, basic image parameters called Hillas parameters (Hillas, 1985) based on the second moments of the image are computed and stored. These Hillas parameters are: position of centroid (x,y), length, width, orientation angle and total intensity. This parameterization is also sketched in Figure 3.9. Further, also higher-order moments such as the skewness and the kurtosis are computed. This then represents DL1 type data.

3.2.2 Monte Carlo simulations

To accurately determine the shower characteristics like energy and direction, separate gammas from hadrons and describe the instrument response, accurate descriptions of gamma and hadron showers are needed. This can be provided by building

dedicated Monte Carlo (MC) simulation sets. The simulations are a two-step process. The simple shower models described in Section 3.1.1 have been superseded by sophisticated simulation packages developed originally for the study of cosmic rays. The simulation package used for the HAP chain is CORSIKA (COsmic Ray SImulations for KAscade; Heck et al., 1998) which can create simulated EAS from different primaries like gammas, protons, heavier nuclei, muons and electrons with a given energy from a certain direction on the sky. CORSIKA makes use of hadronic interaction models like QGSJET-II (Ostapchenko, 2006) refined with measurements from particle accelerators to have a proper description of the shower development. It can also simulate the creation of Cherenkov light, which is of course crucial for IACT simulations. Some examples of simulated EAS are shown in Figure 3.4.

After the CORSIKA simulation, the resulting Cherenkov light is then piped into a simulation of the instrument layout and response. This is called sim_telarray (Bernlöhr, 2008). With this, the shower images of the simulated EAS as seen by H.E.S.S. can be retrieved. Within sim_telarray the observing conditions like the pointing of the telescopes and also telescope-dependent parameters like, e.g. the mirror reflectivity can all be adapted. In sim_telarray also the NSB can be included, either with one homogeneous value or based on an actual sky map. The validation of the telescope description is described in detail in Section 4.1.

For H.E.S.S. several primaries are usually simulated with sufficient statistics and varying energies following a power law with index -2. They can be either simulated as originating from a diffuse source with a certain size or as originating from a distinct point source. The shower origin and telescope pointing are usually varied in both altitude and azimuth. For the point source simulations, also the pointing of the telescopes is varied to emulate different wobble offsets. With this, huge libraries of both gamma-ray and proton showers can be built up. After the simulation step, the resulting simulation data is in the form of pulse shapes, which can then be treated similarly to the raw observational data to also derive DL1 equivalent simulated data sets. There, additionally, the true shower information, such as energy and direction is known and stored. The use of these simulation sets is discussed in the next section.

3.2.3 Reconstruction techniques

The two basic quantities needed to derive maps and fluxes of gamma-ray sources are the direction on the sky and the energy of gamma-ray events. For the derivation of those quantities, several means exist, of which three will be described in more detail in the following. Additionally, a step to separate EAS induced by gamma-rays from those induced by hadrons is needed, as the large majority of triggered events are caused by the latter.

Before air shower events are reconstructed, they undergo a preselection process. This includes typically cuts on minimum shower size, both in intensity and number of pixels and a local distance cut. The local distance is defined as the distance of the image centroid from the camera center. With this, severely cropped images, that

would extend over the edge of the camera can be avoided, as they would be badly reconstructed in both energy and direction.

Monoscopic reconstruction In the case of a monoscopic analysis, the images of only one telescope are considered. This is useful for CT5, which is operated in mono mode in the trigger and for which especially the low energy images are recorded by CT5 only. The mono reconstruction is described in detail in Murach et al. (2015) and Murach (2017). The inputs for it are the Hillas parameters derived from cleaned images.

For the direction reconstruction, the true shower direction should be located somewhere along the main shower axis with a certain displacement δ_{RECO} from the centroid of the shower ellipse. A sketch of this is shown in Figure 3.9a. This displacement variable is derived by setting up a neural network in regression mode with the following input parameters: Hillas width, Hillas length, the logarithm of the total image amplitude, the logarithm of the image amplitude in p.e. divided by the area of the Hillas ellipse in rad^2 (sometimes also called Hillas density), the skewness and the kurtosis.

The neural networks include an input and output layer with linear activation function and two hidden layers with a larger size of neurons. The activation function for that should be a sigmoid function[4]. The optimization is typically done using a loss function based on the mean squared error between reconstructed and true value of the trained quantity. To train the neural network point source gamma-ray simulations with known directions are used. Before the training step, selection cuts on image amplitude, number of pixels and offset of the shower centroid from the camera center are used similar to the cuts that will be applied in the analysis. This makes sure the neural network is not trained on, e.g. cropped images. At the end for each point in a phase space grid of observing conditions, namely the zenith angle, azimuth angle and wobble offset, one neural network is trained using the respective gamma simulations from the library. When it is eventually applied to data, interpolation between the resulting neural networks with adjacent observing conditions will be used to derive the reconstructed displacement value. To get the actual shower position the sign of the skewness as a measure of the head-tail difference in a shower is utilized to decide in which direction along the major axis the displacement is applied. Unfortunately, this gets increasingly ambiguous for smaller showers with only a few pixels. Similarly, also the impact point on the ground is determined with an additional neural network.

For the energy reconstruction, a third neural network with the same input parameters is set up. This time, the network is trained on the true energy of the gamma simulations as the true value. Afterward, the reconstructed energy is scaled by the ratio of the measured muon efficiency for the run and the muon efficiency derived

[4]Typical examples of sigmoid functions are the logistic function $f(x) = \frac{1}{1+\exp(-x)}$ and the hyperbolic tangent $f(x) = \frac{\exp(x)-\exp(-x)}{\exp(x)+\exp(-x)}$.

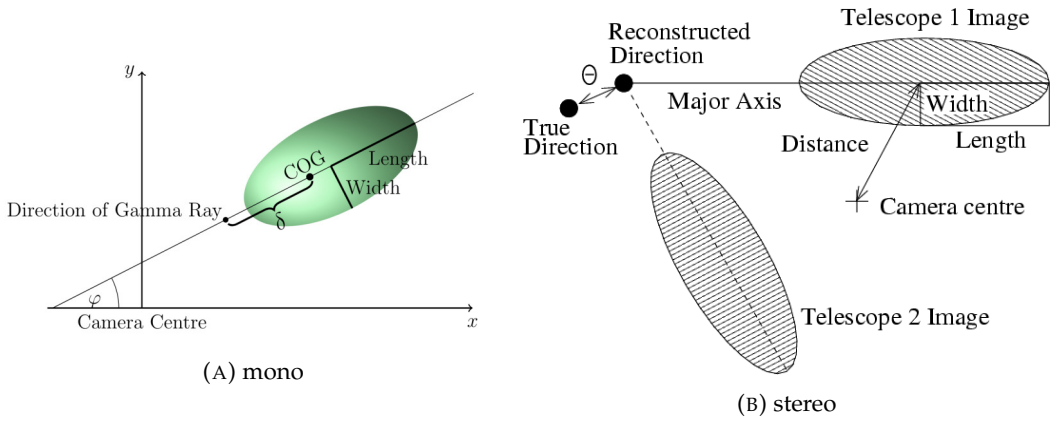

(A) mono

(B) stereo

FIGURE 3.9: **Hillas based direction reconstruction for the mono and stereo chain**
The monoscopic direction reconstruction (**A**) utilizes neural networks to find the displacement parameter δ along the major axis of the shower. The direction in which it is applied is chosen based on the shower asymmetry. In the stereoscopic analysis (**B**), the shower images from all telescopes with a detected shower are transformed into a common coordinate frame. The direction is then reconstructed as the intersection point of the major axes. Also, the definition of the Hillas parameters is sketched. Taken from Murach (2017) (**A**) and from H.E.S.S. Collaboration et al. (2006b) (**B**).

for the simulation set at hand. With this, the resulting energy is corrected for potential deviations in the optical throughput of the observation run with regard to the simulation set. As usual for the training of the neural networks, the training set is split up into a training and testing data set to check convergence and stop the training before over-fitting occurs.

Stereoscopic reconstruction If at least two cameras have recorded shower images that pass the preselection criteria, the distance can be reconstructed with the method sketched in Figure 3.9b. The different image ellipses are converted into a common coordinate frame called the nominal system. In this the intersection point of the two major axes is determined. This is then the reconstructed direction. In the case of more than two shower images, several intersection points exist, which are then combined via weighting methods making use of the image parameters. More details on this can be found in Hofmann et al. (1999). Using a similar approach but transforming the coordinates to the ground frame with the telescope positions as a reference also the impact point on the ground can be determined. The length and centroid parameters further provide information about the shower maximum X_{max}, which can be also reconstructed (Hofmann et al., 1999).

The energy reconstruction depends on lookups derived from MC simulations. For a fixed zenith angle, a given distance between the reconstructed shower direction and the camera center and for a given shower impact distance to the telescope, the energy of a shower is in good approximation a linear function of the shower size. To exploit this the gamma-ray simulation library is used to create lookups in

reconstructed impact distance, offset, zenith angle and size to predict the mean MC energy and RMS of such an event. This, of course, includes the assumption that the incident particle was a gamma-ray. For each telescope, an energy estimate is inferred and again corrected by the ratio of measured and simulated muon efficiency. The energies derived for each telescope are then combined and the resulting shower energy is the weighted mean of those.

Template based reconstruction As the reconstruction methods described above rely on a few image parameters only, it seems logical that more precise results can be achieved by taking the full image information into account and using an actual fitting routine. One such technique is the Image Pixel-wise fit for Atmospheric Cherenkov Telescopes (ImPACT) algorithm developed by Parsons and Hinton (2014).

It builds a library of image templates based on MC gamma-ray simulations. The cleaned images are extended by 2 rows to incorporate almost all shower information and then a maximum likelihood method is executed to find the best-fitting image template. Here, the result of the Hillas-based reconstruction described above is used as a seed. The fit is run jointly for all telescopes, which have recorded a shower passing the selection cuts, and the respective direction and energy of the shower are derived. The muon correction is incorporated by scaling the templates accordingly. This more sophisticated method yields an improvement in both direction and energy reconstruction. As it can be seen in Figure 3.10 for the stereo reconstruction the resulting angular resolution is $\sim$0.05° and the energy resolution $\sim$8 % for 1 TeV gamma-rays.

Other fitting approaches are also possible and have been used, e.g. the Model++ method by de Naurois and Rolland (2009) within the ParisAnalysis framework. This is based on semi-analytic models describing the main shower physics to reconstruct the images.

Gamma-hadron separation The final step towards DL2 is the derivation of the gammaness parameter ζ_{BDT}. This represents roughly the probability of an observed shower being induced by a gamma-ray. In a very simple approach cuts on the image parameters can be used to distinguish between gamma and hadrons. These so-called box-cuts are described in more detail in H.E.S.S. Collaboration et al. (2006b). As the gamma-hadron separation represents a simple classification problem with two classes, Machine Learning algorithms can be employed for a more robust and sophisticated approach. The choice of algorithm can be either a neural network as in Murach et al. (2015) or a Boosted Decision Tree (BDT) as in Ohm et al. (2009), but both show similar performance.

For the monoscopic reconstruction, the input parameters are the same as for the direction and energy reconstruction with the exception of the logarithm of the amplitude. This is replaced to not bias the network solely based on image size. The replacement variable is the length over the logarithm of the amplitude in p.e. (LoS),

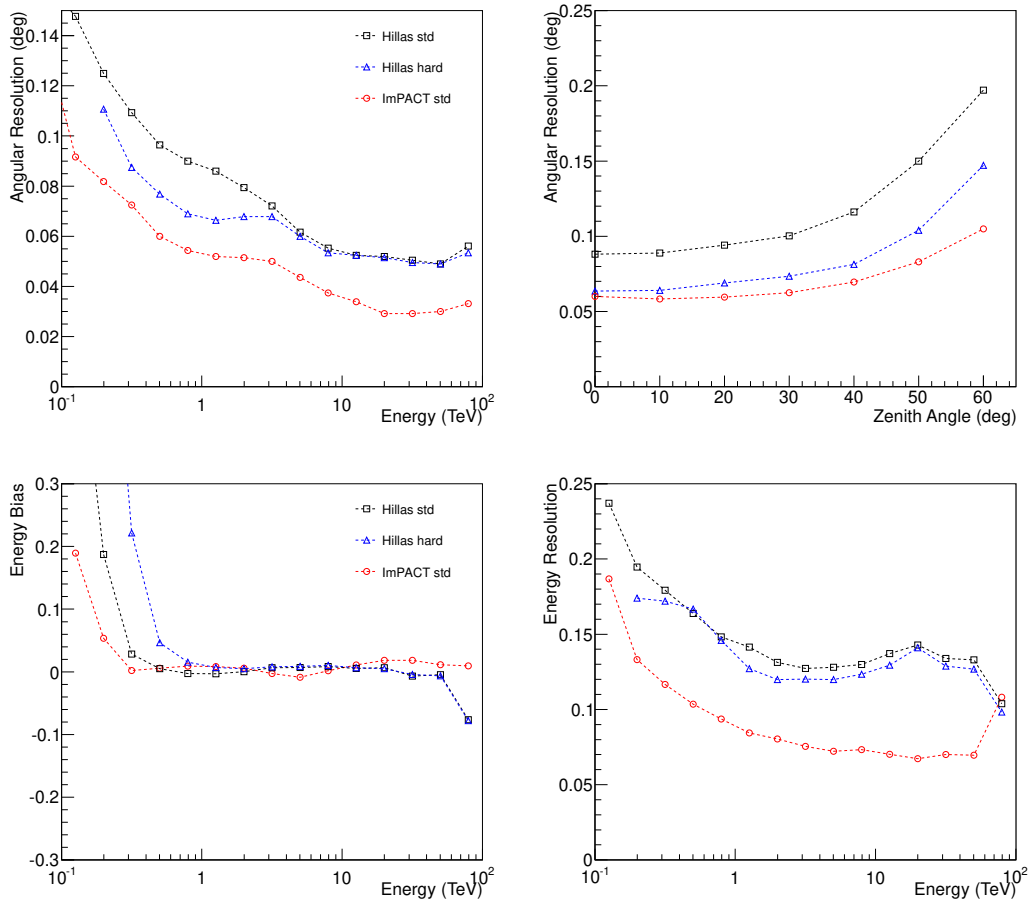

FIGURE 3.10: **Performance of the ImPACT reconstruction** In the upper panel, the improved direction reconstruction with ImPACT compared with the Hillas-based approach is shown. It is parametrized by the angular resolution referring to the 68 % containment radius based on gamma-ray simulations. In the lower panel, the improvement in the energy reconstruction parametrized by the energy bias and resolution is depicted. Adapted from Parsons and Hinton (2014).

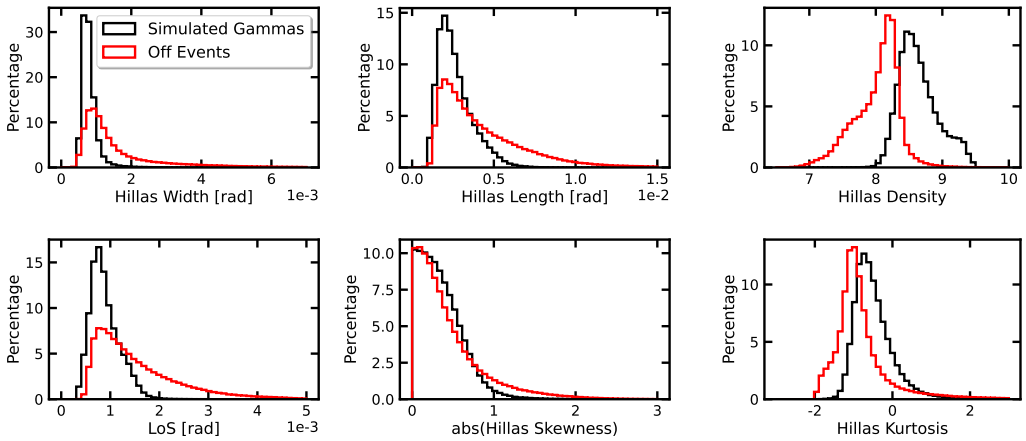

FIGURE 3.11: **Input parameters for the gamma-hadrons separation in the mono chain**
The 6 input parameters for the neural network used for the gamma-hadron separation in the mono chain are compared between simulated gamma-rays and off events. The definition of the parameters can be found in the text. Gamma-ray simulations at 45° zenith and observed off events at a similar zenith are shown. Both include already the FlashCam camera on CT5. Also already a preselection step, later introduced as safe cuts in Table 4.2, was applied.

which is a good indicator for muons originating in the upper atmosphere caused by hadronic showers. The training sample is gamma-ray simulations and so-called off events. These are events taken from observations with no strong gamma-ray source and any potential gamma-ray source and the influence of, e.g. bright stars are excluded. The distributions of the input parameter for both gamma-ray and off events are shown in Figure 3.11. These are already derived for the FlashCam camera with the mono analysis configuration described in Section 4.2.1. Again, for each point in the zenith, azimuth and offset phase space one training is run. The number of input events is restricted to never have more than a factor 2 more off events than gamma-events and vice versa to not bias the training. The resulting gammaness for an observed event is retrieved via interpolation. An example of the resulting ζ_{BDT} for the same gamma and off events that are shown in the distributions can be seen in Figure 3.12, showing clear separation power.

For the stereo discriminator, the mean reduced scaled width and length as defined in H.E.S.S. Collaboration et al. (2006b) under the gamma-ray hypothesis is used. Similarly, under the hypothesis of an off event the corresponding mean reduced scaled parameters are used. Additionally, the derived depth of shower maximum X_{max} and the average energy spread $\Delta E/E$ are input parameters. The training is done in contrast to the mono training in energy bands using the reconstructed energy. The six energy bands are constructed to have similar and sufficient statistics in each band. A more detailed description and distributions of the input parameters and the discrimination variable can be found in Ohm et al. (2009). With this then the DL2 (shower parameters) level information is complete.

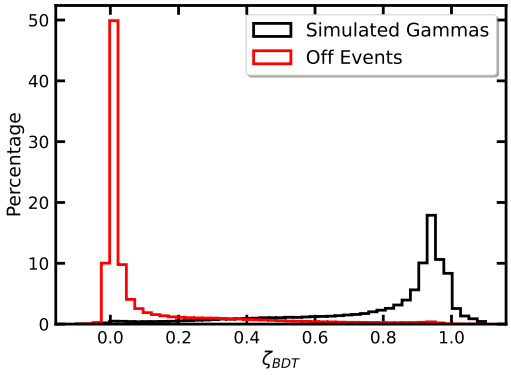

FIGURE 3.12: **Gamma hadron separation value ζ_{BDT} as trained for the mono reconstruction**
A neural network was used for the training with true values of 0 and 1 for the off events and gammas respectively. In this example, the neural network was set up in regression mode allowing values < 0 and > 1. This does not affect an eventual separation cut, but the output should not be interpreted as a probability. It was applied to simulated gamma-rays at 45° and off events with a similar zenith angle.

To have a selection of gamma candidate events, sometimes also called postselection, a cut on the gammaness can be applied. This is done for the mono reconstruction by using a hard cut, keeping all events above a certain ζ_{BDT} value. For the stereo reconstruction, the ζ_{BDT} value is transformed to represent an actual energy-independent gamma-ray efficiency. For this, energy-dependent thresholds are computed on MC simulations and stored as a lookup. Confusingly, the cut on gamma-ray efficiency is sometimes still called ζ_{BDT} within the H.E.S.S. nomenclature. This different meaning of ζ_{BDT} for monoscopic and stereoscopic analysis has to be kept in mind for further reference.

The optimization of the ζ_{BDT} cut is usually done for selected source flux levels and spectral shapes together with the size of the integration region Θ discussed in Section 3.2.5. Hence for the stereo configuration with ImPACT, two typically used cut sets are the standard and hard cuts. The standard cuts were derived assuming a source with a spectral index of 2.6 and a flux at 1 TeV of 10 % of the Crab Nebula, the hard cuts for a source with index 2 and a flux of only 1 % of the Crab Nebula. They are summarized in Table 3.2. The monoscopic cut values are derived as part of this work and summarized in Table 4.2.

Instrument Response Functions The Instrument Response Functions (IRFs) are based on gamma-ray MC simulations to quantify the response of H.E.S.S. on gamma-rays. Only with this, the measured counts can be later transformed into meaningful physical quantities, such as a flux. This step will be later discussed in Section 3.2.5. The instrument response can be written as:

$$R(p, E \mid p_{true}, E_{true}) = A_{eff}(p_{true}, E_{true}) \times PSF(p \mid p_{true}, E_{true}) \times E_{disp}(E \mid p_{true}, E_{true}) \quad (3.7)$$

Configuration	Image Intensity (p.e.)	Local Distance (m)	ζ_{BDT}	Θ ($^\circ$)
standard	60	0.525	0.83	0.07
hard	200	0.525	0.8	0.07

TABLE 3.2: **Cuts of stereo ImPACT analysis configuration**
Both preselection and postselection cuts are shown. Preselection cuts are based on the properties of the cleaned images and postselection cuts on the neural-network based reconstruction and separation. The integration radius Θ is derived under the assumption of a point source and only applied for certain analysis methods. This is discussed in more detail in Section 3.2.5.

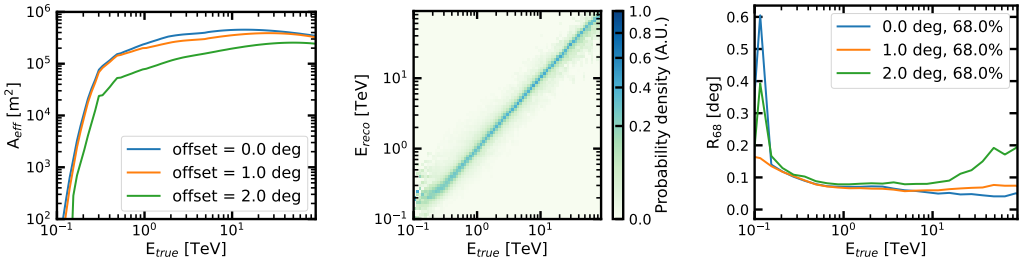

FIGURE 3.13: **Typical IRFs for a stereo analysis configuration**
The effective area A_{eff} is shown for a specific pointing position of an example observation run as a function of true energy. The offset denotes the source offset from the camera center. The energy dispersion matrix in the middle is shown for a fixed offset E_{disp}. In the right panel, the *PSF* is parametrized by its 68 % containment radius R_{68} for several offsets.

p_{true} denotes the true position of a gamma-ray and E_{true} its true energy. p and E are the respective reconstructed quantities. The IRFs needed are the effective area A_{eff} of the instrument, the energy dispersion E_{disp} and the point spread function (*PSF*).

The effective area A_{eff} is typically given in units of m^2 and describes the area on the ground the telescopes are effectively sensitive to. To derive it from simulations, the ratio of gamma events after all cuts and the number of simulated events is derived in bins of true energy and at the true position. This is then multiplied by the area the events were simulated over. Its product with the observation time is called the exposure.

The energy dispersion E_{disp} gives the probability that an event is reconstructed at an energy E assuming a true energy E_{true} and a true position p_{true}. For IACTs it is typically given as a probability density.

The *PSF* describes the probability of reconstructing an event at a certain position p, if the true position is p_{true} and the event has a true energy E_{true}. Here, radial symmetry is assumed such that the angular separation of true and reconstructed position is actually considered.

Examples depicting the IRFs for a stereoscopic analysis configuration are shown in Figure 3.13. As the IRFs are multidimensional some parametrizations like, e.g. the

68 % containment radius R_{68} are considered to allow a simple visualization. Within the H.E.S.S. analysis the gamma-ray simulation library is used to build up lookups of IRFs. To get the IRFs for one specific run with a certain target position again an interpolation scheme is used. Together with the event lists after gamma-hadron separation cuts the IRFs build up the DL3 data which can either be further analyzed within the HAP framework or exported. For the export, a common gamma-ray astro data format (Nigro et al., 2021) based on the Flexible Image Transport System (FITS) format can be used. This allows higher-level analysis of DL3 data with tools such as Gammapy.

3.2.4 Basic statistical assumptions

Before turning to the discussion on the extraction of maps and spectra some statistical methods need to be introduced. The goal of any IACT analysis is to detect a significant signal from a certain sky position. Two approaches are feasible, an estimate based on the measured excess counts or an estimate based on a model for the source ($\mathcal{H}_1$). For both approaches a hypothesis test is done in which either is tested against the null hypothesis ($\mathcal{H}_0$) of no source being present. The likelihood of a given hypothesis is $\mathcal{L}$. This results then in the test statistic TS (Mattox et al., 1996):

$$TS = -2(\log \mathcal{L}(\mathcal{H}_0) - \log \mathcal{L}(\mathcal{H}_1)) \tag{3.8}$$

The test statistic is in simple terms a measure of how much the source hypothesis is preferred over statistical background fluctuations for a measured excess signal. Following Mattox et al. (1996), in the case of one degree of freedom between the two hypotheses it can be transformed into a significance σ by taking the square root, so $\sigma = \sqrt{TS}$. As the test statistic is always positive, negative excess counts are converted to negative significances, $\sigma = -\sqrt{TS}$. The typical detection threshold in gamma-ray astronomy follows the 5σ convention applied in almost all fields of physics.

Excess based significance To detect the presence of a signal from the Poissonian counts of a counting detector, the following approach is taken. It is assumed that the detector looks at a certain on region with size A_{on} on the sky for a time t_{on}. Thus, N_{on} events will be detected. If also a background region without any suspected signal and size A_{off} is observed for a time t_{off}, N_{off} events are collected. To estimate the number of background events N_B in the on region the number of measured off-events needs to be scaled by a factor α describing the exposure ratio:

$$\alpha = \frac{A_{on} \times t_{on}}{A_{off} \times t_{off}} \tag{3.9}$$

As the on and off regions might be situated at different offsets from the camera center and at different zenith angles, the ratio of offset and zenith-dependent acceptance

for events also needs to be potentially taken into account, which is discussed for the different background estimation methods individually. Then the number of actual excess signal counts is:

$$N_S = N_{on} - N_B = N_{on} - \alpha N_{off} \tag{3.10}$$

Both N_{on} and N_{off} are described by Poisson distributions with the following probabilities:

$$P(N_{on}; N_S + N_B) = \frac{(N_S + N_B)^{N_{on}} \exp\left(-(N_S + N_B)\right)}{N_{on}!} \tag{3.11}$$

$$P(N_{off}; N_B/\alpha) = \frac{(N_B/\alpha)^{N_{off}} \exp\left(-(N_B/\alpha)\right)}{N_{off}!} \tag{3.12}$$

The combined likelihood can then be derived as:

$$\mathcal{L}(N_{on}, N_{off}; N_S, N_B, \alpha) = P(N_{on}; N_S + N_B) P(N_{off}; N_B/\alpha) \tag{3.13}$$

Following Equation (17) from Li and Ma (1983) the resulting signal significance σ based on a likelihood ratio test is:

$$\sigma = \sqrt{2} \left\{ N_{on} \ln \left[\frac{1+\alpha}{\alpha} \left(\frac{N_{on}}{N_{on} + N_{off}} \right) \right] + N_{off} \ln \left[(1+\alpha) \left(\frac{N_{on}}{N_{on} + N_{off}} \right) \right] \right\}^{1/2} \tag{3.14}$$

Model based significance In this approach, the measured excess counts are compared with the predicted counts of a model consisting of a background model plus some assumption on the spectro-morphological behavior of the source. With Equation 3.8 then a TS value and subsequent significance is retrieved. For this approach, the signal and the background are approximated via a model and not from the data, which in turn means that a precise background model needs to exist. For any model-based approach to work, the models need to be fitted to the data. The predicted signal counts $N_S(p, E)$ for source position p and energy E and a source flux model $\phi(p_{true}, E_{true})$ together with the instrument response $R(p, E \mid p_{true}, E_{true})$ from Equation 3.7 are:

$$N_S(p, E) \mathrm{d}p \mathrm{d}E = t_{on} \int_{E_{true}} \mathrm{d}E_{true} \int_{p_{true}} \mathrm{d}p_{true}\, R(p, E \mid p_{true}, E_{true}) \times \phi(p_{true}, E_{true}) \tag{3.15}$$

If both a background model and a source model exist, accordingly the combined model of source and background is fit to the observed data via a maximum-likelihood approach. The likelihood $\mathcal{L}$ is then given by the Poison probability described in Equation 3.11.

$$\mathcal{L}(N_{on}; N_S, N_B) = P(N_{on}; N_S + N_B) \tag{3.16}$$

3.2.5 High level analysis

The statistical concepts described in the previous section can now be applied to the DL3 type data.

On region The size of the on region is typically given by a circle with radius Θ, which is for a point source assumption optimized together with the ζ_{BDT}-cut. In most cases, it is roughly the size of the 68 % containment radius of the PSF and is summarized for the stereo and mono configurations in Table 3.2 and Table 4.2, respectively. For extended source analysis or analysis methods based on a spectro-morphological fit, the optimized Θ value does not play a role as either the on region size is larger or part of the fit.

Safe ranges As the reconstruction precision, data-MC consistency and the statistics for the derivation of IRFs drops quite drastically for positions in the FoV far away from the camera center, a maximum offset for gamma-ray events is considered. Hence only events within typically 2° are considered for the stereo analysis. For the mono analysis, this safe offset can be further reduced. Of course, if the source region itself is situated at larger offsets, the safe offset cut can not be applied. For the spectral derivation also safe cuts on the considered energies are taken into account. As the effective area rises steeply for low energies and energy confusion is much more likely (both see, e.g. Figure 3.13), this usually translates to a lower threshold of the energy. This can be either defined as the energy, at which the effective area reaches 10 % of its maximum value or the energy at which the energy bias is less than 10 %.

Background methods To derive maps and spectra it is of crucial importance to derive the background properties of the observation on hand. For any background method, exclusion regions, where no reliable background estimate is possible, are masked. As the H.E.S.S. background consists to large parts of misclassified hadronic showers, exclusion regions can be either known or suspected gamma-ray sources to avoid an overestimation of the background. Furthermore, regions around bright stars (typically with visual magnitudes $m_V \leq 5$) are excluded to avoid reconstruction problems due to high NSB or broken pixels. For H.E.S.S. several methods exist to derive the background, which will be summarized in the following. More detailed descriptions and comparisons of these can be found in Berge et al. (2007).

- The **ring background** method draws for each on region a ring with a certain inner and outer radius. These can be either fixed or with the adaptive ring method varied to find a ring radius covering enough area outside of exclusion regions to have good statistics. The counts in this ring are summed up to derive N_{off}. The exposure ratio α needs to be derived as a function of the size and

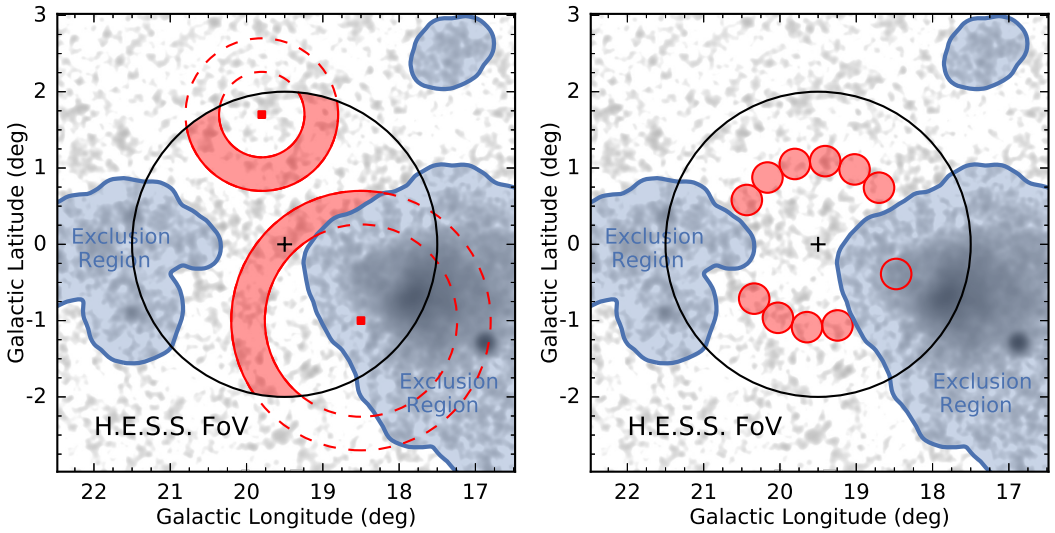

(A) Ring background

(B) Reflected regions background

FIGURE 3.14: **Ring and reflected regions background methods** **A** depicts schematically the ring background method for two positions in the FoV. The ring radii are adaptive and only the parts of the ring are considered as the background region that are outside of exclusion regions and within the safe offset from the pointing position shown by the black circle. In **B** for the same FoV the reflected regions method is illustrated. Here, as many as possible regions with the same size as the on region (empty red circle) and the same offset from the pointing position (black "+") are found. These are depicted by the filled red circles. Adapted from H.E.S.S. Collaboration et al. (2018).

the hadron acceptance of the ring. The acceptance describes the relative number of hadrons after the gamma-hadron separation cut as a function of zenith angle and offset from the camera center. Thus, it is assumed to be radially symmetric. The acceptance can be either retrieved via lookups that have been precomputed on a large set of observation runs or computed on the data set itself. The latter is only giving trustworthy results in the case of good statistics. This is usually only the case for the mono analysis. Typically, this background method is used for maps, as it is fast to compute for each pixel and potential energy dependence of the acceptance plays no role there. A visualization of this background technique is shown in Figure 3.14a.

- The **reflected regions background** requires, that observations are taken in wobble mode, meaning that the target position and pointing position are offset from each other. The default wobble offset for H.E.S.S. is 0.7°. For each on region, the reflected off regions are defined in a ring with the same offset from the pointing position and the same size as the on region. As many as possible of such regions outside of the exclusion masks are defined, resulting in a certain number of off regions n_{off}. With that, α can then simply be derived as $1/n_{off}$, as the acceptance in each of these regions can be assumed to be similar

to the on regions acceptance. This method is mostly used for spectral analysis and is visualized in Figure 3.14b.

- The **FoV background** method derives a background model from a large number of off observation runs. The gamma-ray candidate events outside exclusions are transformed into the FoV coordinate system to describe the instrument acceptance independent of the actually observed field. This background model is then fit for an observation run to the events outside of exclusion regions with its normalization and tilt[5] as free parameters. Beforehand, it is corrected for the atmospheric conditions and changes in the optical throughput of the instrument. This background model can also be set up in different energy bands allowing for combined spectro-morphological analysis. This is described in more detail in Mohrmann et al. (2019).

- The **On/Off background** method uses off measurements on a similar field to derive the background characteristics. The off observations should be taken at a similar zenith angle and with similar atmospheric conditions. The normalization α is then computed from the ratio of event numbers between on and off measurements outside of the exclusion regions. This has the advantage that no assumption on the acceptance, e.g. a smooth radially symmetric behavior as for the ring background is made. This background method is especially useful for the analysis of special FoVs, where the other background methods reach their limits.

Significance maps and values A crucial scientific result of any analysis is a map of the gamma-ray sky to detect potential sources. Pure excess maps are hard to interpret, as it is not clear if a detected excess is really significant or not. Therefore, significance maps are the typical choice. In those, for every pixel a significance value with the methods discussed above is calculated. Typically, the excess is beforehand correlated with a top-hat smoothing of a certain radius. The smoothing radius should be chosen with respect to the expected signal size, e.g. for a point-like hypothesis be roughly equal to the PSF or on region size. The background counts can be either derived from the value of the fitted FoV background or On/Off background in each pixel or by doing a ring background estimation for each individual sky region.

The significance map with the exclusion regions masked is a good metric for the quality of the background normalization. The pixel-wise values should represent a Gaussian distribution with a width of 1 and a mean of 0. Any deviation from this ideally normalized background estimate can be used to, e.g. assess the systematics arising from improper background modeling. All the individual steps as well as resulting significance maps are shown in Figure 3.15 as an example of a mono analysis with the ring background method of a small Crab Nebula data set.

[5]The tilt changes the spectral index of the power-law model describing the spectral shape of the background.

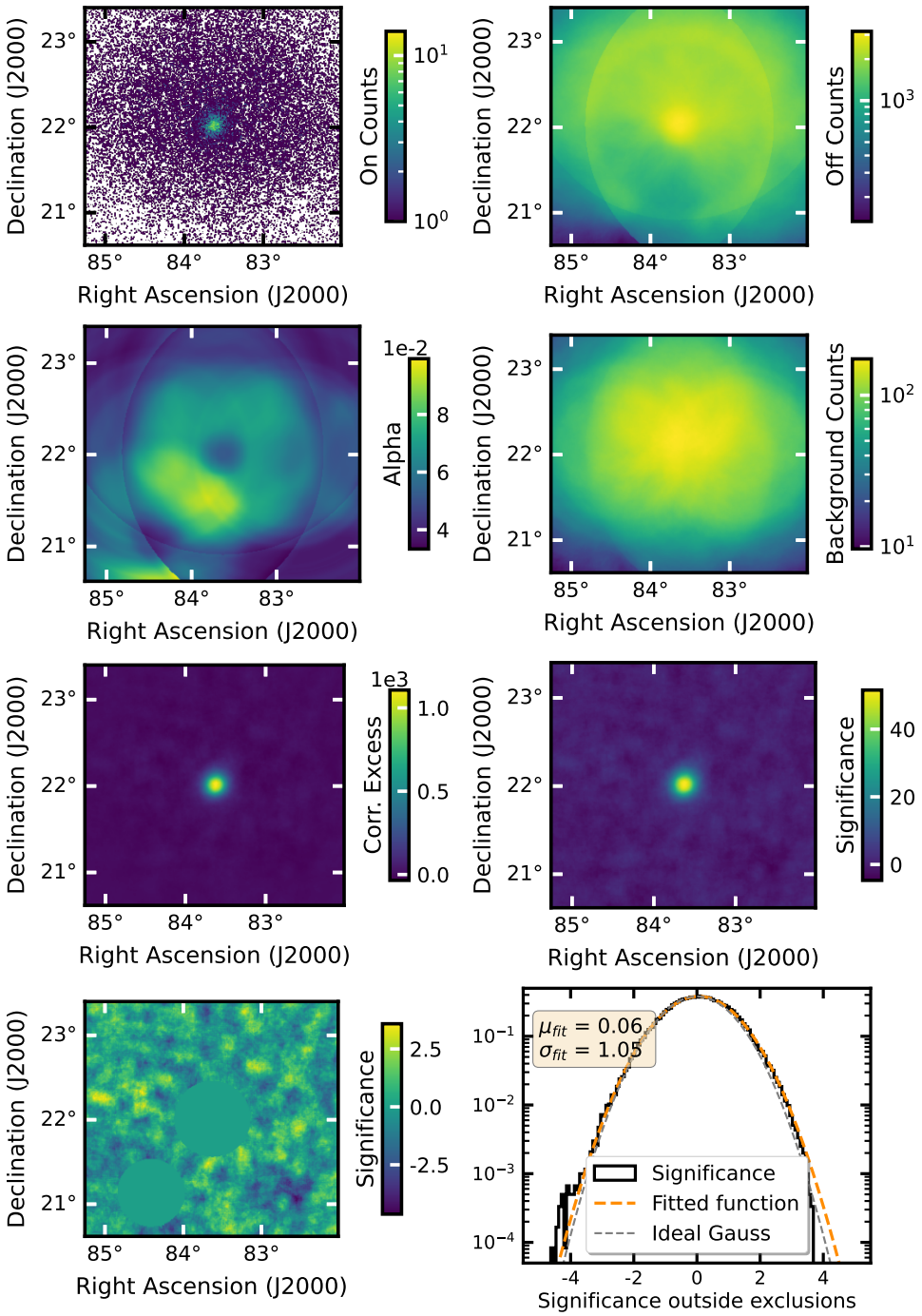

FIGURE 3.15: **Derivation of maps in gamma-ray astronomy**
All maps are derived from the same mono analysis on a small Crab Nebula data set. In the top row, the raw on counts as well as the off counts derived with the ring background method are shown. Hence, the off counts are already ring-correlated. In the second row, the background normalization α correlated with a top-hat kernel of size $\Theta = 0.1°$ and the resulting background counts are derived. The ring structures from the ring background method are still clearly visible. In the third row, the correlated excess counts with the correlation radius Θ and the derived significance are calculated. The bottom row shows the significance outside of the exclusion regions both as a map and as a distribution with a Gaussian fit. The background normalization deviates only slightly from the ideal case. As it is the case here, the significance distribution counts are normalized to an area of 1. This will be the case for all significance distribution throughout this thesis and will not be mentioned specifically.

Spectral modeling To derive the spectral behavior of a source depicted by the spectral energy distribution (SED), a model is fit to the excess data. This can either be a combined spectral and morphological model (3D) or a simple spectral model (1D). In either case, many spectral models describing the differential flux $\phi(E) = \frac{\mathrm{d}N}{\mathrm{d}E}$ as a function of energy E are implemented in either Gammapy or HAP. For this thesis only the typical ones will be explicitly stated:

- The power law with spectral index Γ and flux normalization ϕ_0 at a reference energy E_0:
$$\phi(E) = \phi_0 \left(\frac{E}{E_0}\right)^{-\Gamma} \tag{3.17}$$
- The power law with an additional exponential cutoff $\lambda = 1/E_{cut}$ and cutoff index α:
$$\phi(E) = \phi_0 \left(\frac{E}{E_0}\right)^{-\Gamma} \exp\left(-(\lambda E)^{\alpha}\right) \tag{3.18}$$
- The log-parabola with index α, curvature β, flux normalization ϕ_0 and reference energy E_0
$$\phi(E) = \phi(E) = \phi_0 \left(\frac{E}{E_0}\right)^{-\alpha-\beta\log(E/E_0)} \tag{3.19}$$

The reference energy E_0 can be either set at a fixed value or be derived from the decorrelation energy[6], at which the correlation of the flux amplitude with the other free parameters is assumed to be minimal.

The predicted signal counts assuming a source model follow Equation 3.15. If no background model is available but a number of background counts per energy bin is derived, the likelihood following Equation 3.13 can not be directly evaluated. The likelihood $\mathcal{L}$ is then maximized in a two-step process, typically referred to as the profile likelihood method. First the background counts N_B that maximize the likelihood are derived from $\frac{\delta \log(\mathcal{L})}{\delta N_B} = 0$. Then, this value is injected into Equation 3.13 to maximize the likelihood with regards to N_S. That this approach works is shown in, e.g. Deil (2011). This is the case for the reflected regions background and the On/Off background method.

For the on and off counts a certain on region size and corresponding background regions are assumed. This is hence also called "1D" analysis or aperture photometry. Then the excess is derived in predefined energy bins and the model is fit to this data. The energy bins are defined with a binning of 24 bins per decade within HAP but can be chosen freely in Gammapy. The fitting routines employed are based on the well-established MINUIT framework (James and Roos, 1975) and described in more detail in, e.g. Deil (2011). An example of a fit[7] of a power-law spectral model to

[6]The decorrelation energy E_0 is for the power law model $E_0 = \exp\left(\frac{\mathrm{cov}(\phi_0,\alpha)}{\phi_0 \Delta\alpha^2}\right)$ GeV with the covariance error matrix *cov*, see Abdo et al. (2009).

[7]For this example the tutorial on `https://docs.gammapy.org/1.0/tutorials/analysis-1d/spectral_analysis.html` was followed.

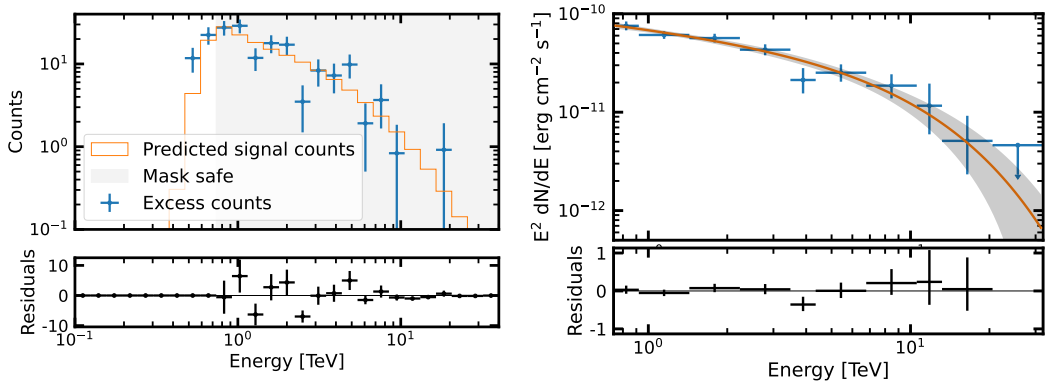

(A) Resulting model counts

(B) SED with flux points

FIGURE 3.16: **Spectral aperture analysis**
The excess counts are derived in an aperture of 0.11° from four Crab runs. A power-law model is fit to the data with the resulting predicted counts in each energy bin compared to the excess in **A**. The residuals depicted are the excess counts - model counts. The safe mask considered is 10 % of the effective area. In **B**, the resulting spectral model with uncertainties is shown together with the derived flux points. The residuals depicted here are relative to the model flux.

the 4 Crab runs from the H.E.S.S. public data release[8] using the reflected regions background method is presented in Figure 3.16.

Flux points derivation and upper limits Flux points in Gammapy are derived by refitting the best-fit spectral model to the excess points in a certain energy bin but keeping the index fixed. In the HAP framework a simpler approach is done, as the predicted model flux in an energy bin is scaled by the ratio of excess and predicted model counts. This will give rather similar results nevertheless (Mohrmann et al., 2019). Whereas the energy binning for the flux points in Gammapy is chosen by the user, within HAP the energy bins are regrouped together to reach significances of at least 2 σ in each bin.

If the 2 σ threshold is not met, upper limits are derived. The method for upper limits derivation follows the profile likelihood estimation described in Rolke et al. (2005). The confidence interval used for upper limits is 95 % if not stated otherwise.

Light curves and upper limits Light curves are derived by integrating the differential (energy) flux between two energies, e.g.

$$\Phi = \int_{E_{min}}^{E_{max}} E \frac{\mathrm{d}N}{\mathrm{d}E} \mathrm{d}E \tag{3.20}$$

for a certain time period. To derive light curve points for each time interval the spectral model is refitted and the corresponding flux value is derived. Typically it is

[8] More info on the data set can be found on `https://www.mpi-hd.mpg.de/hfm/HESS/pages/dl3-dr1/`.

assumed that the spectral behavior is stable. Hence, the spectral shape parameters (like, e.g. the index) are usually fixed and only the flux normalization is freed for the fit. For the upper limit derivation again the profile likelihood method by Rolke et al. (2005) is used assuming a certain spectral index. The confidence interval used for upper limits is again 95 % if not stated otherwise and the threshold for a light curve point is 2 σ.

3.3 Fermi Large Area Telescope

The Fermi Gamma-ray Space Telescope, formerly known as GLAST, was launched on June 11, 2008. It is operated by the National Aeronautics and Space Administration (NASA) in cooperation with several other institutions worldwide. It is the successor to the Compton Gamma Ray Observatory (CGRO) carrying the Energetic Gamma Ray Experiment Telescope (EGRET). EGRET was quite successful in providing the first complete sky survey in the gamma-ray regime consisting of 271 sources between 30 MeV and 10 GeV (Hartman et al., 1999). Fermi hosts two instruments the Large Area Telescope (LAT) and the Gamma-ray Burst Monitor (GBM). Whereas the GBM is specifically equipped to detect gamma-ray bursts down to 10 keV energies, the LAT offers a more sensitive view on the HE gamma-ray sky at 20 MeV to 300 GeV energies. The sensitivity curve based on 10 years of operation can also be found in Figure 3.1.

3.3.1 Technical description

Fermi Satellite The Fermi satellite orbits the Earth on a circular orbit at an altitude of 565 km and with an inclination of 28.5°. Its orientation is always such that the instruments look away from earth alternating the pointing between 50° north and south on subsequent orbits. This is called rocking and results in almost uniform exposure after two orbits. The instruments will sweep across the sky ∼16 times per day. The satellite's core dimensions are 2.9 m in height and 1.8 m in width and depth. The solar panels, that generate the power, have a maximum span of 15 m. Its basic design and the location of the instruments can be seen in Figure 3.17a. It can transfer data back to earth with a fast 40 Mbits/s downlink rate. The Fermi project has been extended to 2025, with further extension possible still.

Large Area Telescope Photons in the energy range of the LAT (20 MeV to 300 GeV) primarily interact with matter via pair conversion. The principle is similar to the air showers described in Section 3.1.1, but with a different detector material. Nevertheless, gamma-ray and hadronic primaries will show distinctively different characteristics that can be exploited for background rejection. The basic LAT detector layout is described in Atwood et al. (2009), presented schematically in Figure 3.17b and will be summarized briefly. The instrument consists of:

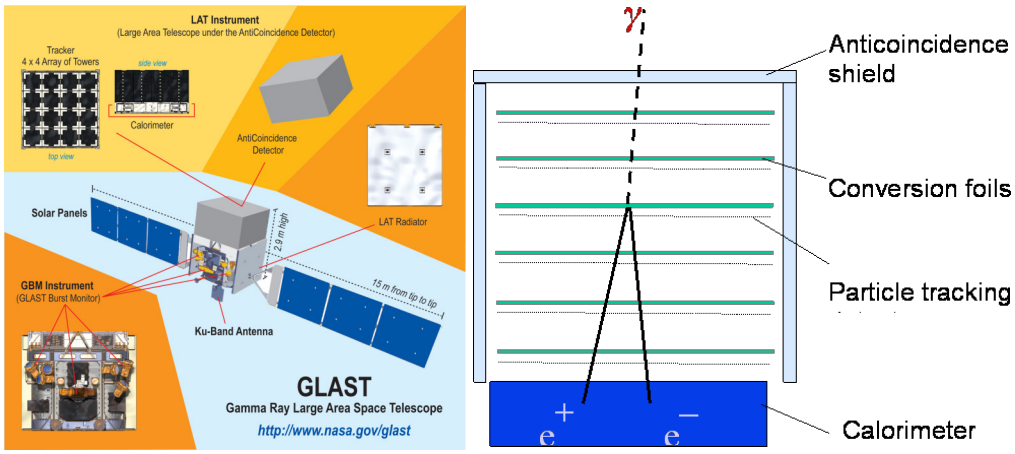

(A) Satellite schematic (B) LAT design

FIGURE 3.17: **Schematic of the Fermi satellite and its Large Area Telescope**
The schematic in **A** depicts the position of the instruments on the satellite as well as its main characteristics. The LAT consists of an anti-coincidence detector, conversion foils, trackers and calorimeters, schematically drawn in **B**. Picture Credits: NASA

- An anti-coincidence shield sensitive to charged particles. It encompasses the full detector.
- Conversion foils consisting of thin layers of high-Z (Tungsten) material. Here, an incoming photon can undergo pair conversion under the influence of charged nuclei.
- Particle tracking detectors made of silicon between the conversion foils, which measure the tracks of the resulting electrons and positrons.
- Calorimeters made of CsI, with a thickness of ∼10 radiation lengths and equipped with photo diodes. With this, the shower profile can be measured in 3D. This allows for a good energy measurement even in the case of energy leakage and some further hadron rejection power.
- Data acquisition modules.

The layers except the anti-coincidence shield are grouped in 4x4 arrays of identical towers, as it can be seen in Figure 3.17a. A gamma-ray signal has thus the following signature:

- No anti-coincidence signal is detected.
- At least two tracks start from a common origin in the tracker volume. This is the location at which the pair production happens.
- An electromagnetic shower is seen in the calorimeter.
- Additional discrimination parameters building up a classification tree have been derived from simulations. More details on the derived classification tree

can be found in Atwood et al. (2009). Partly the discrimination is already applied on the satellite.

The trigger is set up such that events causing detector hits in at least three planes automatically result in a readout of all instrument parts. Whereas the number of gamma-ray triggers is only ∼2 per second, the hadronic background has rates of a few kHz. It is reduced on-site via the anti-coincidence measurement and the other characteristics stated above to ∼30 Hz to allow efficient data transfer to earth. The FoV for LAT is 2.4 sr and its exposure is such that every sky position is viewed for ∼30 min every two orbits or 3 hours.

3.3.2 Data reduction and analysis pipeline

The data reduction is automatically run on the incoming data producing high-level analysis ready DL3 type data. This DL3 level data is then accessible to the community. The state-of-the-art data is processed with the P8R3_V3 version of the Pass 8 reconstruction.

Event reconstruction The concepts for calibration, reconstruction and background rejection will only be discussed in a very short overview. For a more in-depth description, the relevant literature should be visited (see e.g. Atwood et al., 2009; Ackermann et al., 2012; Rochester et al., 2010; Atwood et al., 2013). The outline of the different steps is also shown schematically in Figure 3.18. As for IACTs, the Fermi reconstruction relies heavily on accurate MC simulations of gamma-rays and background particles hitting the detector and the eventual detector response. The background model is derived from existing space and balloon missions measuring the cosmic-ray flux, such as AMS[9] (AMS Collaboration et al., 2002) or BESS[10] (Haino et al., 2004).

In general, the data from the 3 LAT subsystems (tracker, calorimeter and Anti-Coincidence Detector) needs to be reconstructed and afterward combined to derive event-level parameters such as energy, direction and probability to be a gamma-ray. The tracker data is reconstructed using a tree-based tracking description, which builds up tree-like structures describing the shower. These can be used to derive the main tree axis, which allows for a connection with the calorimeter information and is also the most important parameter for the direction reconstruction. For the calorimeter information a clustering step is run, to identify and reject so-called ghost events away from the gamma-ray shower. The Anti-Coincidence Detector data is connected with the data from the tracker and the calorimeter to better reject background events.

For the final reconstruction of the events, Classification Trees trained with input from all subsystems are used to derive energy, direction and particle type.

[9]The Alpha Magnetic Spectrometer (AMS) is a particle detector on the International Space Station.
[10]The Balloon-borne Experiment with a Superconducting Spectrometer (BESS) is a series of balloon experiments launched in Antarctica.

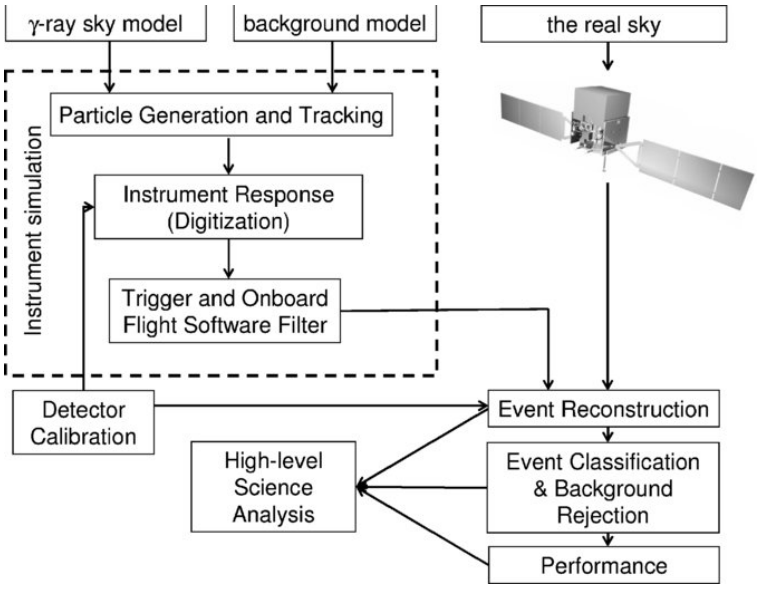

FIGURE 3.18: **Schematic of the data simulation, calibration and reconstruction for Fermi LAT**
The different steps and dependencies of the intermediate data processing towards high level DL3 type data are shown. Taken from Atwood et al. (2009).

Event selection Finally, several quality levels for the photon event lists are defined. These so-called event classes allow for choosing the best compromise on the desired accuracy and statistics and effective area depending on the science goal. Examples[11] are here the "TRANSIENT" class with very loose cuts, the "SOURCE" class with more restrictive cuts and the "ULTRACLEANVETO" class for the lowest cosmic ray contamination. Events within a class are subdivided into event types by three possible ways. Firstly they can be divided into "FRONT" and "BACK" type events based on where they converted. Secondly, they are grouped into 4 quartiles with respect to the quality of their reconstructed direction (PSF0-3). Lastly, they are grouped into 4 quartiles with respect to the quality of their reconstructed energy (EDISP0-3). For a specific analysis, one event class needs to be selected (e.g. SOURCE) and only one event type can be used for further selection (e.g. it is not possible to select for both PSF3 and EDISP3).

IRFs and typical performance For the selected event class and type the relevant IRFs are then considered in the analysis. The definition of the IRFs is similar to the IACT case (see Equation 3.7).

Figure 3.19 compares the IRFs for different event classes and types. The influence of the selected event class on the effective area can be clearly seen with the effective area at 10 GeV ranging from $\sim$0.78 m^2 for the ULTRACLEANVETO class to $\sim$0.94 m^2 for the TRANSIENT class. As the SOURCE class (evclass = 128) is the recommended class for most point source analysis with longer integration times, the performance

[11] An overview of all classes and types and their description can be found on `https://fermi.gsfc.nasa.gov/ssc/data/analysis/documentation/Cicerone/Cicerone_Data/LAT_DP.html`

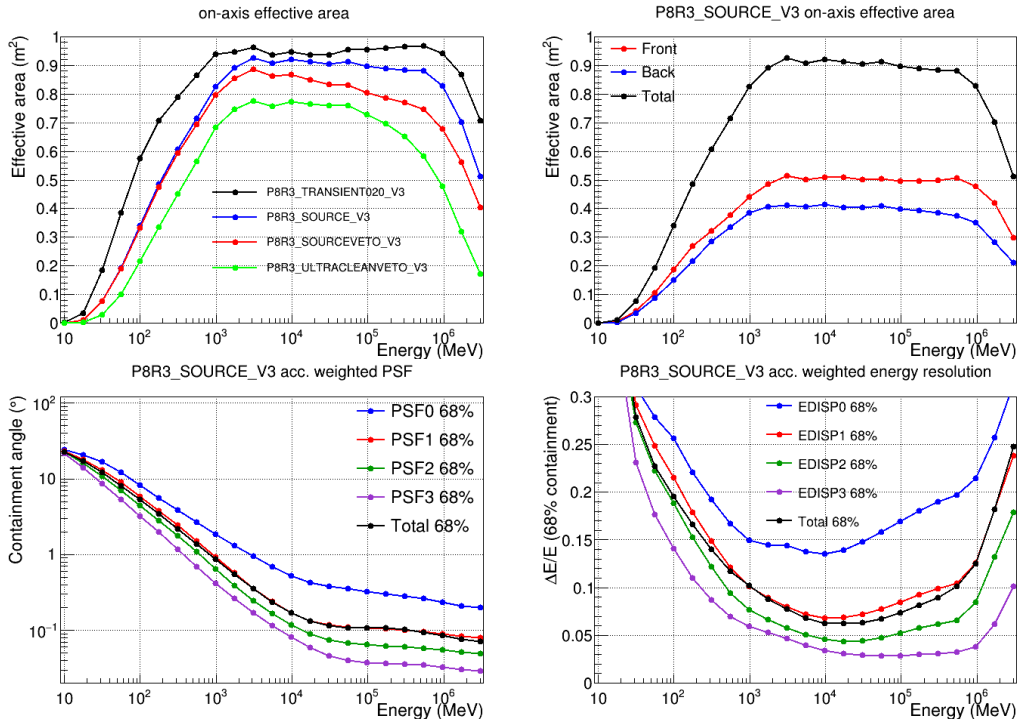

FIGURE 3.19: **Performance of Fermi LAT**
The upper row describes the effective area for the different event classes on the left and the FRONT and BACK type selection for the SOURCE class on the right. In the lower row, the 68 % containment radius of the PSF and energy resolution are shown for the SOURCE class. Here the total event class data set as well as the different event types based on the quartile selection are compared. The plots were taken from the public Fermi LAT performance web page[12]for Pass 8 version P8R3_V3.

is further described using this class and both BACK and FRONT type (evtype =3) events with no restriction on the PSF or energy dispersion. At 10 GeV the total effective area is $\sim$0.9 m^2 with a slightly higher contribution from FRONT events. The total PSF has a size of $\sim$0.2° at 10 GeV, but is in general hugely energy dependent, with the low energy PSF on the size of a few degrees and dropping to $\sim$0.1° for energies above 30 GeV. Selecting PSF3 events can bring an improvement of factor 2 to 3. The total energy resolution is for 10 GeV gamma-rays $\sim$0.06. It is actually best for energies of 10 GeV to 30 GeV and increases both towards lower and higher energies. Selecting EDISP3 events can yield an up to factor 2 improvement again.

High level analysis framework The high-level photon list data can be analyzed using Fermitools[13], which is the official Fermi Science tools analysis package. The current release version is 2.2.0. Fermitools can also be accessed via FermiPy[14] (Wood

[12] `https://www.slac.stanford.edu/exp/glast/groups/canda/lat_Performance.htm` , visited on Jan 10, 2023
[13] `https://github.com/fermi-lat/Fermitools-conda/wiki`
[14] `https://fermipy.readthedocs.io/en/latest/index.html`

et al., 2017), currently released in version 1.2, which is a python based open source framework.

Event data within a certain sky region can be downloaded together with the spacecraft file, which provides the position and orientation info for the spacecraft. Furthermore, a cut on the maximum zenith angle, for point source analysis typically 90°, should be included following the LAT recommendations[15]. Additionally, event and time intervals for the analysis need to be specified. Lastly, the event class and type is selected together with the matching IRFs. To build up the model in the next step a Galactic interstellar emission model describing the diffuse gamma-ray flux and an isotropic spectral template describing the remaining background contamination for the selected event class and type is needed. To retrieve the models for the individual sources a source catalog from which the model is built needs to be specified. The latest source catalog for Fermi is the fourth Fermi Large Area Telescope catalog (4FGL) (Abdollahi et al., 2020), which is available in the third data release version (Abdollahi et al., 2022b), spanning 12 years of data.

Spectro-morphological fit To fit a target region, a model is built up from the diffuse and isotropic components, all known sources from the catalog and potentially additional user-defined sources. Of course, it is also possible to exclude some sources from the model. For each source, the spectral model and spatial model from the catalog are taken and the spectral parameters are freed. The same is done for the diffuse component and the additional and target sources for which a specific spectral and spatial model is set. The spectral models are typically the same as already described in Section 3.2.5. The spatial models can have different forms, e.g. a point-like source, a Gaussian extended source or an arbitrary shape derived from a spatial map. The combined model consisting of the background and target source models is then in potentially several iterations fit to the data following a maximum likelihood approach. This follows the concepts discussed in Section 3.2.4 and Section 3.2.5. At the end, a (residual) TS or significance map is retrieved and the TS values for the sources and the best-fit spectral parameters and morphology can be accessed.

Derivation of flux points Flux points are derived with a user defined binning in a similar approach as for the H.E.S.S. flux points. This means, in each bin the normalization is refitted either by fixing the source spectral index or assuming a spectral index of 2 in each bin. Upper limits are again calculated for energy bins with significance values $< 2\,\sigma$.

[15]More information can be found on `https://fermi.gsfc.nasa.gov/ssc/data/analysis/documentation/Cicerone/Cicerone_Data_Exploration/Data_preparation.html`.

3.4 Outlook and conclusion

In this chapter, two state-of-the-art operating facilities have been introduced. Together Fermi-LAT and H.E.S.S. cover the gamma-ray regime in the energy range between 30 MeV and 100 TeV. Since H.E.S.S. is the only IACT located in the southern hemisphere, it still possesses unrivaled sensitivity for the southern gamma-ray sky. Because the two instruments operate quite differently with Fermi constantly surveying the sky and H.E.S.S. operating as a pointing instrument, a lot of synergies exist between these two. As it will be discussed in more detail in the following sections not only combined analysis of the two instruments are possible, but also H.E.S.S. triggers on transient phenomena often rely on the detection of gamma-rays by Fermi LAT.

In the near future, the currently planned CTA observatory will improve the VHE sensitivity even more. Unfortunately, for Fermi LAT no succeeding instrument is in sight. Even though the current operation cycle until 2025 might well be extended further, its lifetime is finite. Currently, only studies showing the potential of an improved Fermi LAT like instrument exist (e.g. Peron and Aharonian, 2022), but no actual project is underway to achieve a rather smooth succession. Hence, it is likely that the HE sky below the CTA energy range and the nice synergy with the VHE observations might be inaccessible in the future.

Chapter 4

Validation and improvements of the H.E.S.S. analysis

As outlined in Section 3.2 the data analysis for IACTs such as H.E.S.S. is an interplay of many distinct steps and various techniques. Hence a good understanding and end-to-end validation of these steps are of crucial importance in order to retrieve reliable scientific results. Therefore, in this chapter, the validation of the array simulations for the latest H.E.S.S. hardware configuration in the HAP chain is presented. The results are then used to define an analysis configuration for monoscopic reconstruction valid for the full FlashCam era. This analysis configuration is tested on known scientific targets to have a proper high-level validation of the full chain. With this chain, the H.E.S.S. mono results discussed in Chapter 5 are obtained. Additionally, a novel image-cleaning approach for the H.E.S.S. instruments on the example of FlashCam is discussed. This makes use of not only the intensity but also the time information of the signal with the goal to keep as much shower information as possible while not being susceptible to noise influence. This shows particularly promising results to improve the low-energy mono reconstruction.

The simulation validation was a collaborative effort with Johannes Schäfer, Tim Holch and Fabian Leuschner. In this joint project, I carried out the first analysis of the Crab Nebula with FlashCam data, which motivated the effort due to the apparent discrepancies. Furthermore, I was responsible for the checks on basic pulse properties (Section 4.1.1), photoelectron definition and conversion (Section 4.1.3), flat field amplitude and time (Section 4.1.4), trigger threshold (Section 4.1.5), the influence of pedestal bias on muon calibration in Section 4.1.6 and the image cleaning and background validation (Section 4.1.7). These checks are described in more detail in the following section and the other key results are outlined. A short summary of the results can also be found in Leuschner et al. (2023), but more elaborate descriptions are given in this thesis as well as being prepared in Schäfer (2023) and Leuschner (2023).

For the science verification, I ran the simulations, defined and trained the analysis chain and computed the IRFs. I also developed an advanced science verification plan based on previous verifications of the H.E.S.S. system. I was responsible for the scheduling of the desired targets as well as for monitoring the data quality to have a

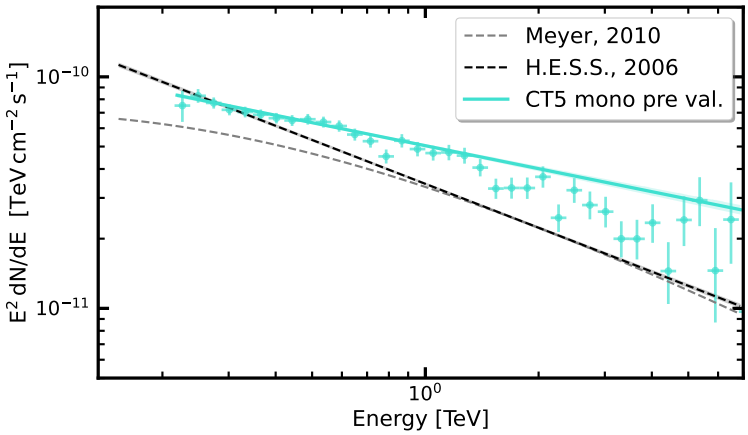

FIGURE 4.1: **Crab Nebula mono spectrum before validation**
The power law spectral fit for the mono stereo analysis with the mono flux points before the validation effort is shown. The SED is based on ∼10 h of Crab observation taken during the first months after FlashCam was installed at CT5. The power-law spectrum from H.E.S.S. Collaboration et al. (2006b) and the model spectrum from Meyer et al. (2010) are added for comparison.

suitable data set. Moreover, I carried out the analysis of the PKS 2155-304 and Crab Nebula data sets and the described connected tests.

For the time-based image cleaning, I implemented the concept into the HAP framework, optimized the parameters, derived the test analysis configurations and computed the performance checks discussed in the chapter.

4.1 Data - Monte Carlo consistency

MC simulations and their consistency with data are crucial for the analysis of data taken by H.E.S.S. as they are the basis for both the reconstruction techniques as well as the creation of IRFs as summarized in Section 3.2. After the installation and commissioning of the FlashCam camera at CT5 in the autumn of 2019, the first high-level verifications yielded unsatisfying results. Especially the flux of the Crab Nebula, typically used as a standard candle in VHE astronomy, was reconstructed too high. The Crab spectrum was derived using a power law spectral model (Equation 3.17). As it is evident in Figure 4.1, this resulted in a harder spectral index ($\Gamma = 2.33 \pm 0.02$) and a 46 % higher flux normalization at 1 TeV of $\phi_0 = (5.04 \pm 0.08) \times 10^{-11}\,\mathrm{TeV}^{-1}\,\mathrm{cm}^{-2}\,\mathrm{s}^{-1}$ compared with H.E.S.S. reference spectrum from H.E.S.S. Collaboration et al. (2006b). Both these deviations could not be explained within the typical systematic uncertainties of the H.E.S.S. reconstruction of 20 % on the flux and $0.1 - 0.2$ on the spectral index (H.E.S.S. Collaboration et al., 2006b; H.E.S.S. Collaboration et al., 2017). However, no inconsistency was found in the high-level analysis itself. As also the image parameter distributions for the CT1-4 stereo analysis showed a mismatch between data and MC, a bottom-up approach was initiated to validate the MC simulations and their consistency with data for the full array.

This end-to-end validation of the HAP chain for the full 5 telescope array focussing on the FlashCam and H.E.S.S. 1U cameras is presented in the following. For reference purposes, a designated hardware phase was chosen, that starts with the gain adaption in the H.E.S.S. 1U cameras to 60 ADC/p.e. in June 2020 and lasts until the change of the trigger boards in these cameras in March 2022. For CT5 the validation period lasts from the FlashCam installation in November 2019 to at least March 2023[1], as no hardware changes had to be done on this telescope. The approach taken is to validate the chain starting in a bottom-up approach from low level to higher levels to have fully validated DL3 type data products (see Section 3.2) at the end. Furthermore, the general concepts should be repeatable also for previous H.E.S.S. hardware phases. For simplicity, in the next chapters most results will be shown for CT5 and for CT1 as the representative for CT1-4. All simulations were run with CORSIKA version 77402 and sim_telarray release 2021-03-03.

4.1.1 Basic pulse properties

In the first step, the basic simulation properties and configurations were checked with calibration simulations. The goal is to verify the proper handling of the pulse shapes and positions from both calibration and shower simulations depending on the input parameters. This is done independently of a comparison with actual data. Calibration simulations make use of so-called laser events, which are simulated nanosecond pulses similar to Cherenkov light with a wavelength of 400 nm illuminating the camera. Within the simulation setup, the laser parameters such as intensity and time offset were varied. Afterward, the raw traces were plotted to identify any possible problems. Due to the different internal naming schemes, for CT1-4 the intensity is given in ADC counts, whereas for CT5 in units of the least significant bit (LSB). Simple sanity checks on the variations of time offsets and different laser intensities are shown in Figure 4.2. The variation of these parameters affects the simulated pulses as expected. For one specific setting also event-to-event and pixel-to-pixel variations were evaluated. For the peak amplitude, this resulted in a relative standard deviation of $\sim$2 % for the pixel-to-pixel variation and $\sim$4 % for the event-to-event variation. The time of the peak is shifted by a maximum of 1 ns. This can also be seen in Figure 4.2 for the event-to-event variation.

The basic pulse shape was also investigated on simulated gamma showers. As it can be seen in Figure 4.3, the dependence of pulse amplitude on true shower intensity can be reproduced. Furthermore, the time of the pulse peak is well situated in the integration window, which is variable for CT5 but a fixed 16 ns window for CT1-4. The fixed integration window also explains the varying peak time of the pulses for CT1-4. Hence with these simple sanity checks, it can be shown, that the basic properties of the simulated pulses reproduce the simulation parameters as expected and are stable against any obvious deviations.

[1] The end of the validation phase for CT5 is set by the time this thesis is written. It might well extend further into the future.

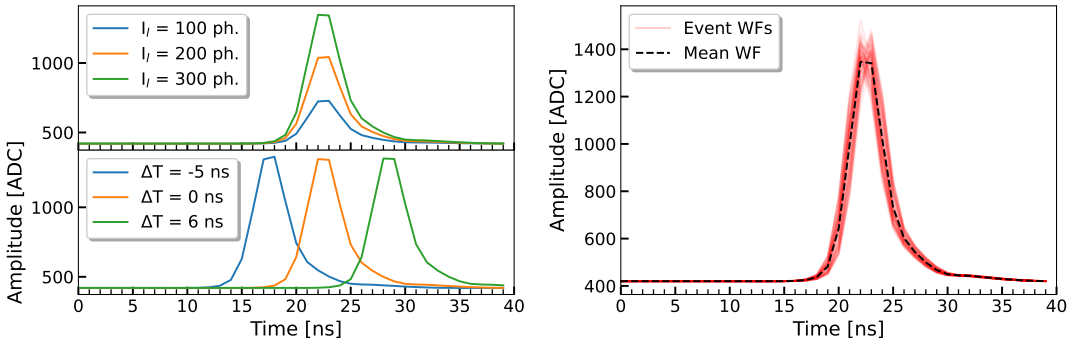

(A) CT1

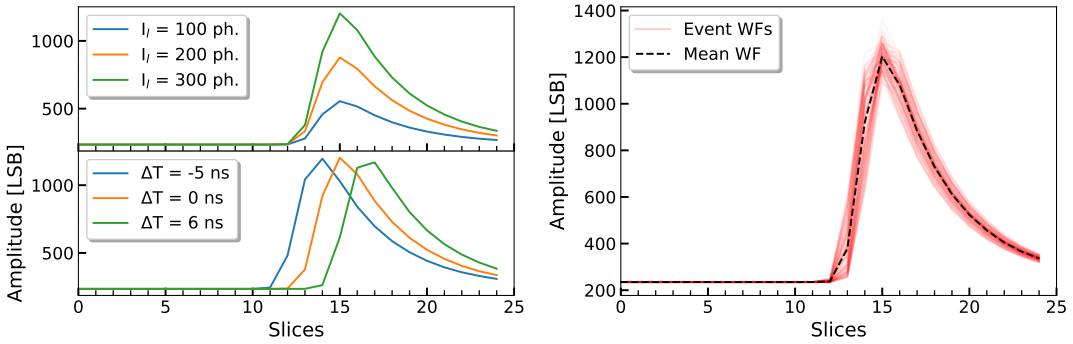

(B) CT5

FIGURE 4.2: **Pulse shape variations of laser simulations**
On the left, the laser intensity I_l and the laser time offset ΔT are varied and the effect on the pulses is shown. The right panel displays the individual event-wise waveforms (WFs) of 100 events together with the mean waveform.

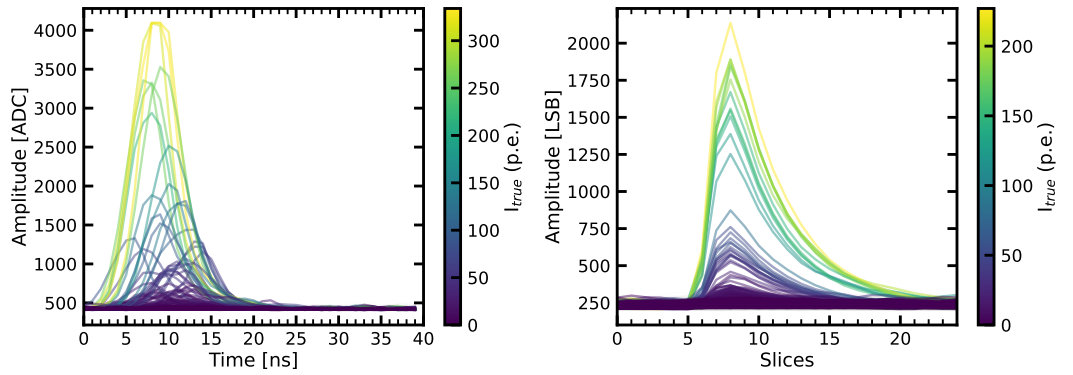

(A) CT1

(B) CT5

FIGURE 4.3: **Pulse shapes of shower simulations**
For each telescope one example event with the individual pixel waveforms is shown. The true intensity originating from the shower I_{true} varies between 0 and a few hundred p.e. for the pixels, depicting the influence of the shower intensity on pulse amplitude and time of maximum.

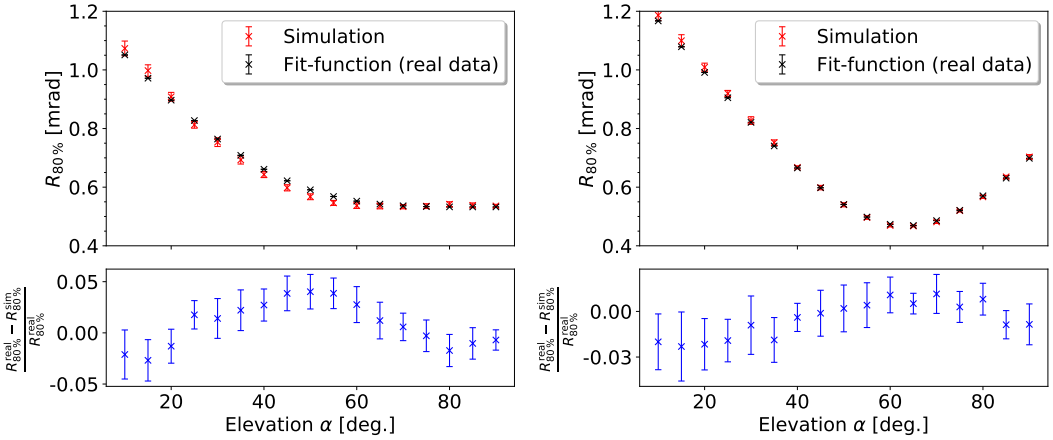

(A) CT1 (B) CT5

FIGURE 4.4: **Validation of optical PSF**
The optical PSF described by its 80 % containment radius R_{80} for CT1 (**A**) and CT5 (**B**) is shown as a function of elevation α and compared to real data. The real measurements were evaluated at different elevations using a fitting method, which is described in Cornils et al. (2003). The simulations were assessed directly at the simulated elevations. Only the simulated PSF after the adjustments is shown and was provided by Johannes Schäfer (see also Schäfer, 2023).

4.1.2 Optical components

The optical PSF of the individual telescopes can be validated using the ray-tracing feature of sim_telarray. The system response is assessed utilizing parallel light as an input. A reference star is simulated at a large, practically infinite distance. The telescopes are pointed at that reference star with a potential pointing offset to probe the off-axis response. As a description of the optical PSF, a circle is chosen such that it contains 80 % of the total signal. This 80 % containment radius R_{80} is evaluated for simulations of different telescope elevations α and compared to measurements obtained with the same hardware configuration. The simulated R_{80} in sim_telarray is assessed with the following equation:

$$R_{80}(\alpha) = \sqrt{R^2_{min} + d_1^2 \cdot (\sin(\alpha) - \sin(\alpha_0))^2 + d_2^2 \cdot (\cos(\alpha) - \cos(\alpha_0))^2} \tag{4.1}$$

The free parameters R_{min}, d_1, d_2 and α_0 need to be specified in the simulation configuration. To minimize the deviation between simulated and measured R_{80}, they were altered iteratively until a good match was found. With this approach, new telescope-dependent parameters were derived, which reduce the R_{80} deviation from up to 20 % to $< 5\,\% \approx 0.4$ mm in the focal plane. This is considered acceptable. The adjusted optical PSF and its comparison to measurements are shown in Figure 4.4. The optical PSF before the adjustments and more details on the method and results can be found in Schäfer (2023).

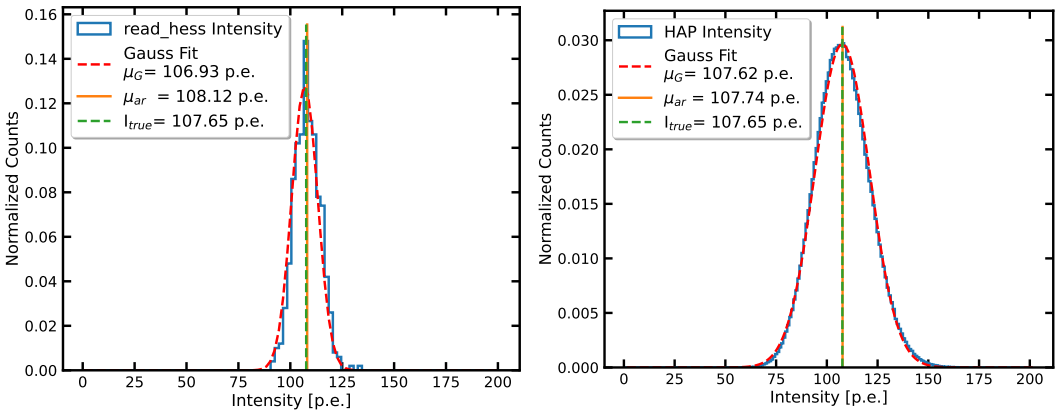

(A) read_hess (B) HAP

FIGURE 4.5: **Check of photoelectron conversion with and without HAP**

A shows the pixel-wise intensity averaged over one event as derived with read_hess outside of the HAP framework assuming a fixed integration window. In **B** the pulse reconstruction is done within the HAP MC framework making use of the same pulse reconstruction as applied to data. For both cases also the true flat field intensity per pixel from sim_telarray is shown as I_{true} compared to μ_G derived from fitting a Gaussian to the distribution as well as the arithmetic mean μ_{ar}.

4.1.3 Photoelectron consistency

For FlashCam, flat field simulations with a known laser intensity of 300.0 photons/pixel resulting in an average true intensity of 107.7 p.e./pixel were computed. These were analyzed by two means. Firstly, independently from the HAP framework the read_hess tool[2] was utilized. This gives the average pixel intensity for each event assuming a fixed integration window. Secondly, the simulation were converted to the Sash[3] format using the HAP MC conversion pipeline and FlashCam reconstruction as implemented for observational data returning one intensity value per pixel. Both tests yielded matching distributions with mean values agreeing within $< 1\,\%$ with the true simulated intensity, as it is shown in Figure 4.5.

For H.E.S.S. 1U, the p.e. definition had been already validated by Zorn (2020). He derived a necessary conversion factor of 0.92 as a consequence of the different gain calibration procedures in simulations and observations.

4.1.4 Flat field amplitude and time

Flat field runs are an important asset for the overall calibration of the cameras (see Section 3.2.1 for more details). Similarly, the camera response in simulations can be compared using flat field simulations with a laser at 400 nm wavelength. The laser settings can be adopted in brightness, delay and variance. As the actually used flat

[2]The tool read_hess is part of the hessioxxx package. Further details can be found on `https://www.mpi-hd.mpg.de/hfm/~bernlohr/sim_telarray/`

[3]Sash is the internal data structure used within the H.E.S.S. software.

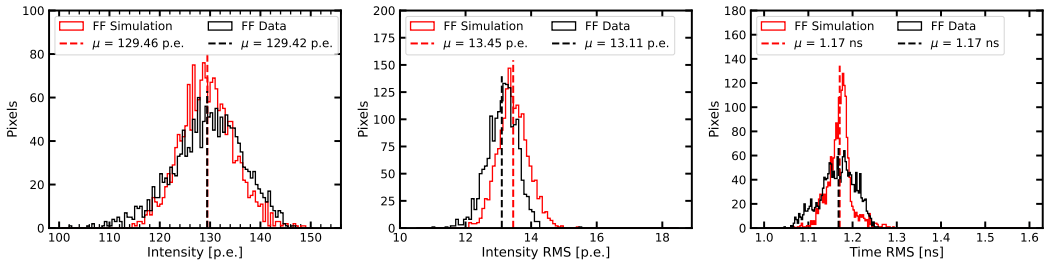

(A) Intensity (B) Intensity RMS (C) Time RMS

FIGURE 4.6: **Flat field distributions compared between simulations and data**
All plots show the distribution from flat field runs over the camera. The RMS hence shows the event-to-event variability. The laser intensity and variability have been set to match the mean in data for the intensity (**A**) and intensity RMS (**B**) within reasonable accuracy. The mean values are highlighted with dashed vertical lines. The distribution in time RMS (**C**) also shows good agreement in its mean between simulation and data.

field devices are not precisely known in their characteristics, the laser simulation settings need to be matched to the data. The flat field simulations need to be converted to the Sash format readable by HAP without the default intrinsic flat field correction by sim_telarray.

Such simulations were compared to one example flat field run of the validation phase. The laser brightness was set to match the measured flat field brightness and the laser variance to match the measured intensity variability expressed as the RMS. This is shown in Figure 4.6 together with the time RMS for FlashCam. The spread in time also shows good agreement in its mean value with the flat field data. Intensity is here the mean intensity averaged over all events in a pixel and the distribution has one entry for each of the 1758 active pixels of the camera. Hence the RMS is a description of the event-to-event variability and the spread of the distributions itself of the homogeneity of the camera response. Whereas the event-to-event variability can be well reproduced by the simulations, the camera response is a bit less homogeneous for actual observation data, especially in the time domain. A potential reason for that could be the mix of 7 and 8 dynode PMTs in the installed FlashCam camera, whereas simulations are only run with the 7 dynode PMTs. A similar procedure can be also applied to the H.E.S.S. 1U cameras but is not described in detail here.

4.1.5 Check of trigger threshold

The FlashCam trigger setting for its use on CT5 is a sum trigger based on 588 overlapping sectors containing 9 pixels each (Sailer et al., 2019; Bi et al., 2022). Therefore, the brightest sector in an event is characteristic of the trigger decision and its intensity in units of p.e. is the relevant quantity to compare the trigger behavior between simulation and data. The trigger threshold for observation runs is currently set at a value corresponding to 69 p.e. For observations of particularly bright regions of

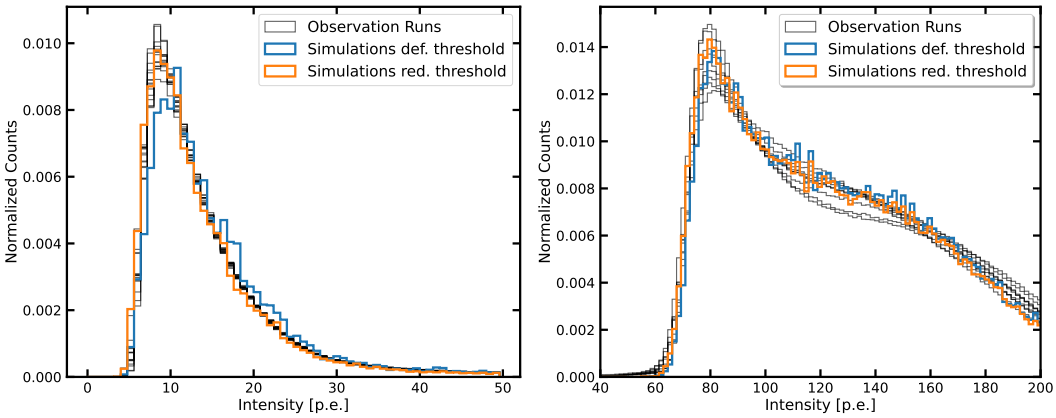

(A) CT1- 3rd brightest pixel (B) CT5 - brightest sector

FIGURE 4.7: **Trigger threshold evaluation**
For CT1 the intensity of the 3rd brightest pixel from simulations before and after reducing the trigger threshold is shown (**A**) and compared to observation runs. For CT5 (**B**) the distribution of the brightest 9-pixel sector is drawn. Here also simulations before and after a small reduction in trigger threshold compared to several observation runs are shown.

the sky and moonlight conditions the trigger threshold is adjusted. Nevertheless, the validation was carried out for the default trigger settings and the other trigger settings are eventually scaled accordingly. As they comprise the large majority of triggered events, proton simulations were used and weighted to represent a spectral index of 2.7 similar to the measured proton spectrum (see Section 2.1). The observation runs were chosen such that they were taken under typical NSB and good atmospheric conditions. Furthermore, no known strong gamma-ray source should be in their field of view. As it is evident from Figure 4.7b, a slight decrease in the simulated trigger threshold would match the observed threshold better. To quantify that the 50 % point of the rising edge was determined and compared. In conclusion, this yielded a re-adjustment of the CT5 trigger threshold by 3.7 % in simulations. This led to a match within the applied binning, with a remaining uncertainty of 1 % due to the finite bin width.

The H.E.S.S. 1U cameras are operated with a majority trigger (Giavitto et al., 2018) currently set to require at least 3 pixels above 5.5 p.e. Therefore, the distributions of the 3rd brightest pixel of triggered events is a good metric to describe the trigger behavior. The trigger threshold is not directly set at a certain p.e. level in sim_telarray for the H.E.S.S. 1U cameras, but a combination of several parameters that then describe an effective trigger threshold. Comparing the distributions of the 3rd brightest pixel in proton simulations with the measured distribution from observation runs, a mismatch in the trigger threshold was found (see Figure 4.7a). Together with the effort to match the trigger rates as described in the next section, this motivated a reduction of the simulated effective threshold by 27 %, which gave an acceptable match to the observed threshold.

4.1.6 Trigger rate consistency

To combine the influence of the trigger threshold, the night sky background, the atmosphere, the optical description and the optical throughput, the trigger rates before any cuts are a good quantity for comparison. As the measured trigger rates are dominated by hadronic showers, the investigation of the trigger rates in simulations is achieved with proton simulations. To account for heavier nuclei it is necessary to apply a correction factor. This was validated beforehand with dedicated simulations of different primaries (He, N, Si, Fe) to be consistent with the adopted ≈ 1.34 for the trigger rates of the H.E.S.S. array. More details are provided in Schäfer (2023). To calculate the raw trigger rates of the simulations, the effective area derived from the simulations is folded with a CR proton spectrum. The effective area is computed considering the amount of simulated and triggered showers, simulated area and solid angle. The Global Spline Fit model by Dembinski et al. (2017) was used to describe the proton spectrum, as it also takes spectral features deviating from a simple power law into account (see also Section 2.1). As described in Section 3.1.3, H.E.S.S. is operated in a hybrid fashion. Therefore, the system trigger rate consists of CT1-5 stereo triggers and additionally CT5 mono triggers. Hence, on a telescope level, the important trigger rates to compare are for CT1-4 the stereo participation rate and for CT5 the mono rate (Giavitto et al., 2018; Puehlhofer et al., 2022).

The instrument-specific settings being adapted were trigger threshold (see Section 4.1.5), optical PSF (see Section 4.1.2), NSB values, and mirror reflectivity. The NSB was set to a value consistent with the median of observations excluding observations on exceptionally bright fields. This led to an increase of the NSB of more than 50 % in simulations, as the previously used NSB estimate was derived from a dark extragalactic field only. More details on the NSB estimate are described in Leuschner (2023).

The reflectivity was derived from muon efficiencies following Mitchell et al. (2016) by matching muon simulations to the combined distribution of a subset of runs. Additionally, the proper use of the pedestal bias and width for simulations and accordingly in the muon chain led to a $\sim$8 % reduction in derived muon efficiencies for CT5 (see Figure 4.8). This had to be accounted for by increasing the reflectivity in simulations accordingly to obtain a good match with the measured efficiencies again. For CT1-4, the effect was only marginal, as there is no pedestal bias introduced after the pulse integration (see Section 3.2.1). The CT1-4 reflectivities had to be actually reduced to better match the measured muon efficiencies during the reference time period.

Furthermore, measurements of the atmospheric optical depth by the Aerosol Robotic Network (AERONET) (Holben et al., 1998), which operates a station on the H.E.S.S. site, motivated a revisiting of the atmospheric transmission profile. Adapting the aerosol content to match the mean observed optical depth outside of the biomass burning season, resulted in a reduction of the aerosol level by 50 %. This increases the observed Cherenkov photon flux by a few percent, as it can be seen in

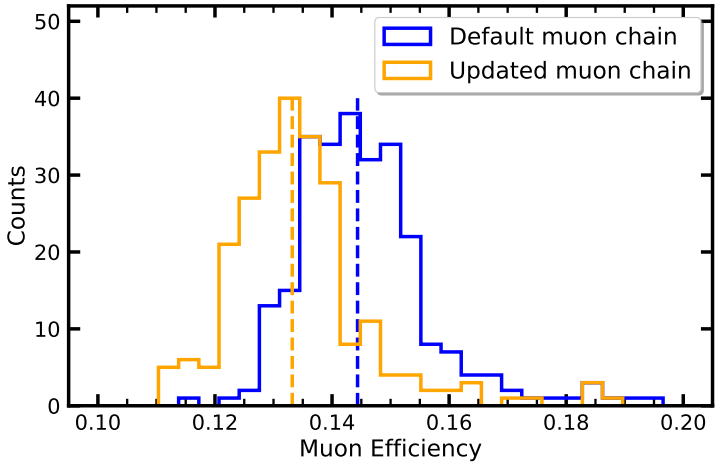

FIGURE 4.8: **Influence of proper pedestal treatment on muon chain**
The effects of including the measured pedestal bias and width for simulations in the muon reconstruction chain are shown with its effect on the derived muon efficiency for CT5. The muon chain without these adaptions is labeled as default, whereas the improvements are part of the updated chain.

Parameter	Change CT1-4	Effect CT1-4	Change CT5	Effect CT5
Aerosol level	$-50\,\%$	$+10\,\%$	$-50\,\%$	$+12\,\%$
Trigger threshold	$-27\,\%$	$+41\,\%$	$-4\,\%$	$+6\,\%$
Mirror reflectivity	$-2.4\,\%$	$-15\,\%$	$+8\,\%$	$+23\,\%$
NSB	$+67\,\%$	$+3-6\,\%$	$+55\,\%$	$+6\,\%$
Optical PSF R_{80}	$20\,\%$	$+1\,\%$	$9\,\%$	$< +1\,\%$

TABLE 4.1: **Change of simulation parameters and their effects on the trigger rates**
For CT1-4 the stereo participation and for CT5 the mono trigger rates are compared. For the telescope-specific parameters, the changes and effects differ between CT1-4 and the average value is quoted.

Figure 4.9. Consequently, a larger fraction of the simulated showers will trigger the telescopes. A detailed study on the effect of varying atmospheric conditions measured by AERONET on the Cherenkov light yield is available in Holch et al. (2022).

Additionally, some general simulation settings, such as the simulated energy range and the view cone were chosen carefully to include as many triggered events as possible (see Schäfer, 2023).

The individual adjustments are summarized in Table 4.1 together with their effects on the telescope trigger rates. The largest effects for CT5 were due to the increased mirror reflectivity and decreased aerosol level both increasing the simulated trigger rates. For CT1-4, the dominant positive effects were caused by the readjusted trigger threshold together with the aerosol level, substantially increasing the trigger rates, even though the reduced mirror reflectivities had the opposite effect. The resulting trigger rates before and after the adjustments can be seen in Figure 4.10 as a

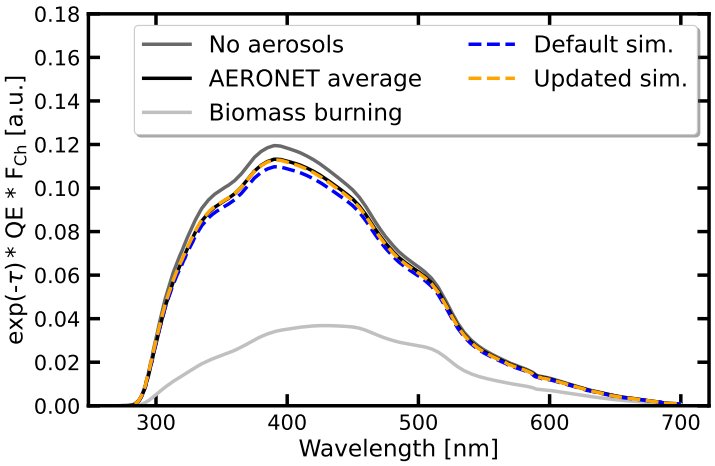

FIGURE 4.9: **Reassessment of atmospheric transmission profiles for H.E.S.S.**
Several atmospheric transmission profiles corresponding to different observing conditions and aerosol optical depths τ are compared in their effect on the Cherenkov light yield detected by CT5 on the ground. The Cherenkov flux F_{ch} is originating from a height of 15 km. The AERONET average profile is derived assuming the mean aerosol content during good observing conditions, whereas an example for the atmospheric conditions during the biomass burning seasons is also shown. The aerosol content used in the H.E.S.S. simulations was updated from its previous default value to better match the average good observing conditions. The profiles and the Cherenkov yield were derived by Tim Lukas Holch using Py6S and Modtran following Holch et al. (2022).

function of the zenith angle. For CT1 and CT5, both the simulated and real trigger rates are shown. The runs for the calculation of the real trigger rates were selected based on non-extreme NSB and good atmospheric conditions. The uncertainty intervals indicate the investigated systematic uncertainties assuming an uncertainty of 5 % for the muon efficiency, different hadronic interaction models and the general implementation of H.E.S.S. in the sim_telarray package. The resulting trigger rates after the combined adaptions show a drastic improvement in their consistency with the measured trigger rates and deviate on average < 10 % from the measured rates. Hence within the assumed systematic uncertainties, the trigger rates reveal good MC - data consistency. More details on the methods and results summarized in this subsection can be found in Schäfer (2023).

4.1.7 Cleaning and background validation

Recorded shower images are calibrated as described in more detail in Section 3.2.1 and afterward cleaned to avoid any major influence of noise on the image reconstruction. The classical cleaning algorithm is based on the tail cut method (see also Section 3.2.1). For CT1-4 this is done using cuts of (5,10) p.e., whereas for CT5 the cuts are (9,16) p.e. with an additional two neighbor requirement. Using the cleaned

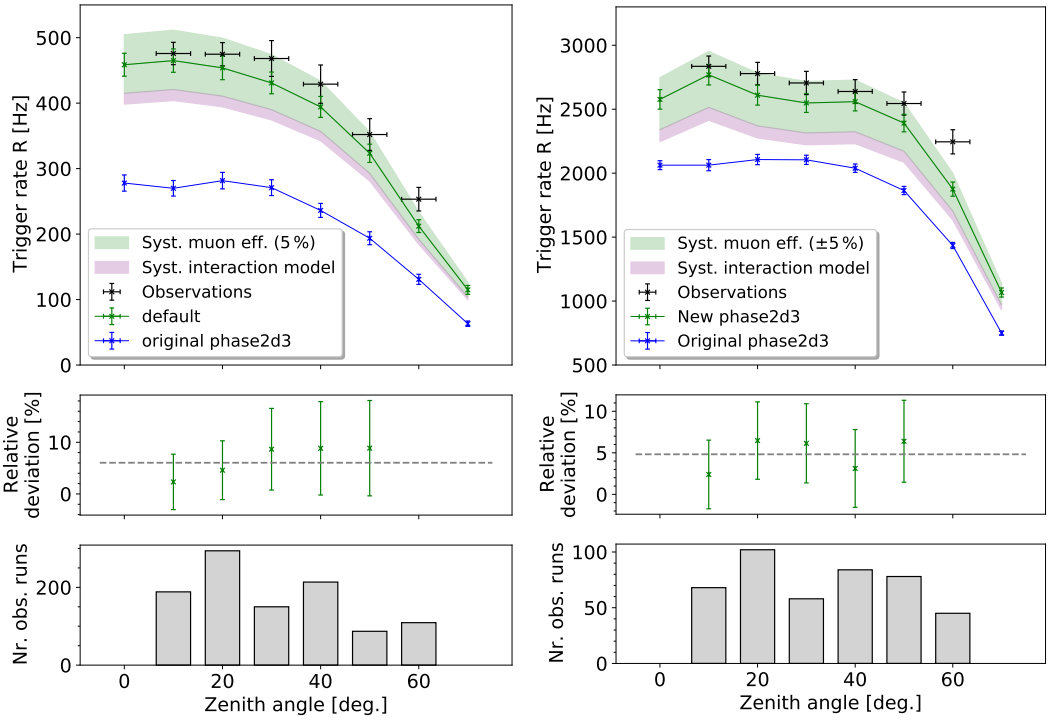

(A) CT1 stereo participation trigger rate

(B) CT5 mono trigger rate

FIGURE 4.10: **Simulated and real zenith-dependent trigger rates for CT1 and CT5**
For CT1 the stereo participation rate and for CT5 the mono rate is compared. The trigger rates before and after the adaptations summarized in Table 4.1 are shown. The uncertainty bands include the different investigated systematic uncertainties as discussed in the main text. The middle panel shows the relative deviation after the adaptation and the lower panel the number of runs in each zenith angle bin, from which the mean observed trigger rates were derived. Figure provided by Johannes Schäfer (see also Schäfer, 2023).

images, the image properties can be described in a parametrized form by deriving the Hillas parameters (see Section 3.2.1; Hillas, 1985). The image properties of proton simulations were compared to those of observation runs. A good match of the resulting distributions is evidence for a correct description of the hadronic background. The observation runs were selected with a similar approach as in the previous validation step and a subset with zenith angles between 15° and 25° was picked. The proton simulations were simulated accordingly at 20° and include all changes as summarized in Table 4.1. Again they were weighted by energy to represent the measured CR proton spectrum (Dembinski et al., 2017).

Typically preselection cuts on image size and number of pixels are applied as the first selection stage of any analysis method. These were set at 5 pixels and 80 p.e. per image for this study.

The distribution of image intensities and Hillas length/intensity are shown in Figure 4.11. The length/intensity distributions trace the images of muon arcs originating higher in the atmosphere. Hence they are a good indicator for a good match

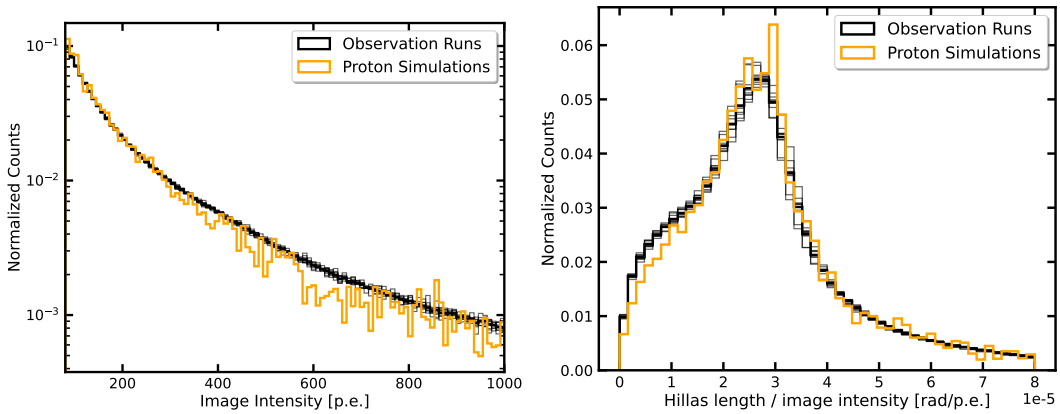

(A) CT1

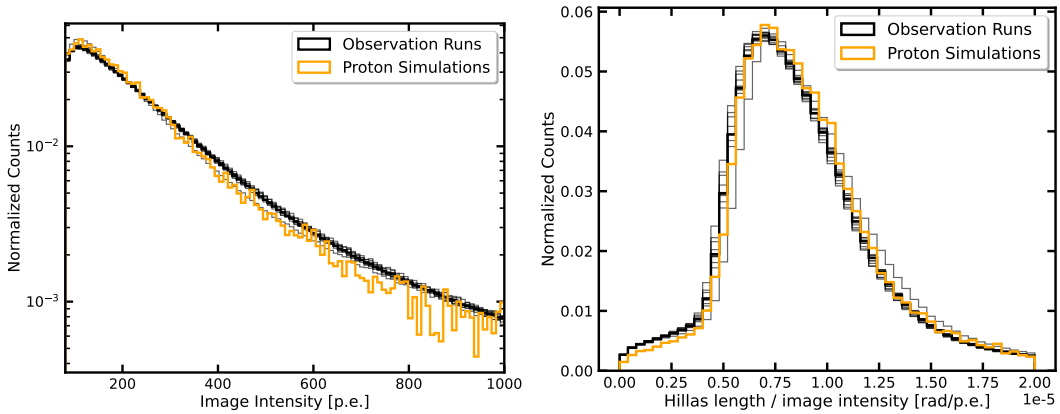

(B) CT5

FIGURE 4.11: **Hillas parameter comparison after cleaning**
On the left, the distribution of image intensities in the cleaned images is shown, whereas on the right the distributions of the Hillas length divided by the image intensity are presented. Applied cleaning levels and selection cuts are described in the text. The proton simulations were computed at 20 ° zenith. Several observation runs with no strong gamma-ray source at similar zeniths are shown in light black with the combined distribution marked by the thick black line.

of atmospheric conditions between simulations and data. The image amplitude distributions show a reasonable agreement of the overall optical response with reality. Therefore, it can be concluded that lower-level adaptations still provide a good match after the cleaning level and that the cleaning has the same effect on both simulations and data.

4.1.8 Summary and outlook

The simulation validation efforts within the HAP chain were set up as a proper end-to-end verification starting from low-level basic MC checks. Subsequently, MC-data consistency was checked with calibration runs, at the trigger level and eventually after the image cleaning and the derivation of image parameters. During this process for both, CT1-4 and CT5, several significant mismatches were found, which required a necessary adaptation of simulation parameters. The adapted parameters

were, most notably, the optical PSF, the trigger threshold and the mirror reflectivity for each telescope. Furthermore, the general observation conditions concerning the mean aerosol level in the atmosphere and the NSB had to be adapted. With these changes, a good match in the trigger behavior and rates between simulations and observation runs could be obtained. The achieved consistency is further evident in the image properties after cleaning. This will greatly increase the robustness of current and future scientific results by H.E.S.S.

The higher level validation of the reconstruction chains, gamma-hadron separation efficiency and IRFs involve several training steps and the setup of a full analysis configuration. Hence this will be discussed for the CT5 mono analysis in the next chapter as part of the science verification. The high-level validation of the CT1-4 stereo analysis and other analysis chains like the hybrid or event class-based analysis is an ongoing effort within the H.E.S.S. collaboration but is not within the scope of this thesis. Furthermore, schemes for the correction of differing telescope throughputs and atmospheric conditions are currently investigated both within the HAP pipeline and outside of it based on the AERONET data (Holch et al., 2022). This will make it possible to have simulation settings valid for a wider range of observing conditions and correct for any deviations afterward. The concepts applied in this section will also prove valuable for any similar efforts within CTA, for which the simulations also rely on the combination of CORSIKA and sim_telarray. Especially, the simulations for the FlashCam cameras, which will be mounted on the middle-sized telescopes, are important for CTA.

4.2 Science verification of FlashCam installed at CT5

After the installation and commissioning of the FlashCam type camera at the CT5 telescope in October 2019 (Bi et al., 2022), the technical verification included several checks and iterations of, e.g. the optical setup and trigger settings. Further low-level and calibration tests like the pixel participation fraction and center of gravity of image showers were monitored. Starting from December 2019 the hardware and trigger settings were fully checked and kept stable. Hence a scientific verification campaign started including the following targets:

- **The Crab Nebula** - as a bright and compact steady source, that allows a verification of MC gamma simulations vs. excess events, the gamma-ray acceptance as a function of offset, effective areas and resulting reconstructed spectra.
- **PKS 2155-304** - as a bright point-like source allowing verification of the gamma-ray point-spread-function.
- **Eta Carinae and surrounding field** - as a region with high and inhomogeneous night sky background to check trigger stability in extreme conditions. The Eta Carinae observations are discussed in Chapter 6.

Image Intensity	Image Pixels	Local Distance	ζ_{BDT}	Θ
250 p.e.	10	0.8 m	0.85	0.126°

TABLE 4.2: **Cuts of safe mono analysis configuration**
Both preselection and postselection cuts are shown. Preselection cuts are based on the properties of the cleaned images, postselection cuts on the neural-network-based reconstruction and separation.

- **The Vela Pulsar** - as a target for testing the time stamps of the full array. The data set was analyzed by Heiko Salzmann and results can be found in Puehlhofer et al. (2022).

Preliminary results of these studies were shown as part of Puehlhofer et al. (2022). However, the analysis configuration used there was not yet based on the improvements discussed in Section 4.1 and updated results are shown in the following subsections.

4.2.1 Monoscopic analysis configuration

The monoscopic analysis configuration follows the approach outlined in Section 3.2.3 and described in more detail in Murach et al. (2015). The main constituent of it are simulations[4] based on the improved simulation configuration discussed in Section 4.1. The full simulation set consists of gamma point source simulations at zenith angles between 0° and 60°, wobble offsets between 0° and 3° and north and south azimuth angles. A zenith-dependent energy and simulated area range have been adopted from previous simulation sets to have good computing efficiency and accuracy for all zenith angles. Furthermore, also muon simulations with this configuration were utilized to estimate the optical throughput of the simulations. As described in Section 3.2.3, this is used in the analysis to correct event energies accordingly.

The gamma simulations are reduced to a DL1 equivalent level. The selected tail cut cleaning for the mono analysis is a dual threshold cleaning as described in Section 3.2.1 set at 9 p.e. and 16 p.e. Additionally, a two neighbor requirement is set in the cleaning. The cleaning level is scaled from the (5,10) p.e. cleaning used for the old CT5 camera based on the increased quantum efficiency and hence larger NSB noise of FlashCam. The mono configuration includes preselection cuts on image intensity, number of pixels in the cleaned image and a cut on the local distance of the shower center from the camera center to avoid cropped images. The cuts are summarized in Table 4.2. Due to its high image intensity cut of 250 p.e. the configuration will be further referred to as "safe" cuts.

The direction and energy reconstruction are based on multilayer-perceptrons in regression mode and in classification mode for the gamma-hadron separation. In

[4]The simulations were run with CORSIKA version 77402 and sim_telarray release 2021-03-03.

contrast to previous implementations (Murach et al., 2015), the Keras[5] framework was used for training with only the resulting weights afterward being exported to a format readable by HAP. The setup of the neural networks included two dense hidden layers with 20 nodes and a sigmoid activation function[6]. The parameters included in the training are based on Hillas parameters and listed in Section 3.2.3. In contrast to previous reconstruction configurations, the skewness of the Hillas ellipse was inserted into the training with its absolute value. With this one can avoid inhomogeneities of the reconstruction and separation response over the camera. The sign of the skewness still enters the direction reconstruction at the end, as it decides in which direction the displacement factor δ_{RECO} is applied. The optimization was done utilizing a loss function computing the mean squared error.

For the gamma-hadron separation training event lists from observation runs with no strong gamma-ray source and grouped in zenith and azimuth bins were used. Beforehand, also a basic run selection was applied to reject potentially problematic runs with technical issues or bad observation conditions. Furthermore, exclusion regions of known gamma-ray sources and bright patches of the sky were used to mask the image. The exclusion mask was applied following a special background technique developed and described in detail in Marandon (2010). This enlarges exclusion regions to the form of circular sectors to also keep the same radial acceptance as the full data set.

Examples of the input parameters as well as the gamma-hadron separation discriminator value derived for this configuration can be found in Figure 3.11 and Figure 3.12 in the previous chapter.

After the training step, the postselection cuts were chosen as summarized in Table 4.2. These values were based for the Θ-cut on the mean angular resolution and for the ζ_{BDT}-cut on returning a good separation power while keeping a reasonable high gamma efficiency. Both cuts have not been optimized on a particular source spectrum or flux level, as the configuration, with its comparably high image intensity cut, is intended to work robustly for all potential sources. The resulting angular resolution, energy bias and effective area are shown in Figure 4.12 and compared to the last analysis configuration of the old CT5 camera. One can see improvement in performance in the core energy range of mono below 1 TeV even with the safe and non-optimized cuts. The drop in performance for very low energies is due to the high preselection cut but this region is typically excluded by safe energy thresholds anyways (see Section 3.2.5 for more details). There are some apparent issues above $\sim$1 TeV due to the non-realistic handling of saturation effects in the simulation set on hand. This problem has been solved and will not influence future analysis configurations. For these energetic events, the mono reconstruction is anyways not as well

[5]Keras (`https://keras.io/`) is a python-based interface to run the machine learning open source platform TensorFlow

[6]In this case the logistic function $f(x) = \frac{1}{1+\exp(-x)}$ is used

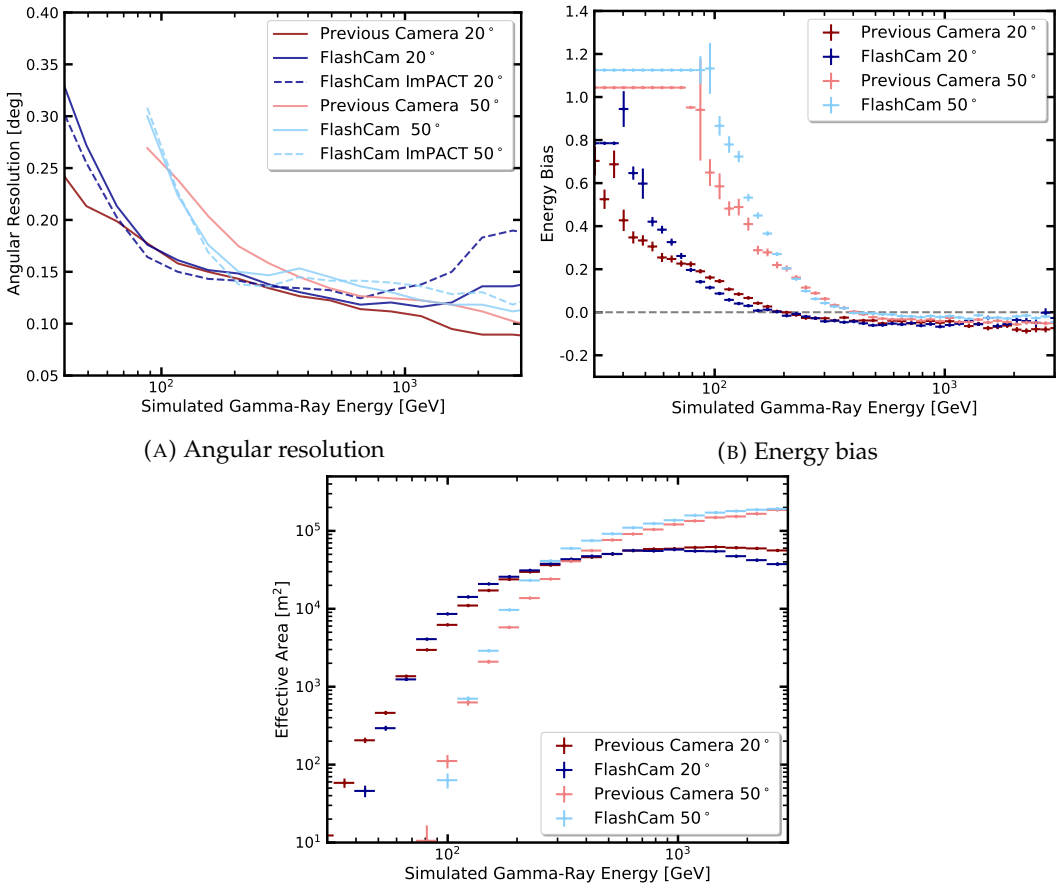

(A) Angular resolution

(B) Energy bias

(C) Effective Area

FIGURE 4.12: **Performance of mono reconstruction with safe configuration**
A and **B** show angular resolution and energy bias for the safe configuration for the mono analysis of FlashCam compared with the standard mono configuration for the previous CT5 camera. For the angular resolution also the ImPACT version of the safe configuration is added. **C** depicts the corresponding effective areas. For all plots the IRFs are compared at 20° and 50° zenith with an offset of 0.5° .

suited as stereo configurations. Evaluating the performance at 20° zenith, the angular resolution is $\leq 0.15°$ for showers above 100 GeV, which is also the point at which $\sim$10 % of the maximum effective area is reached. The energy bias is $\leq$ 0.1 above $\sim$100 GeV. The systematic shift to slightly negative energy biases above $\sim$200 GeV is likely due to the setup of the neural network for the energy reconstruction. Low-energy showers only pass the preselection cuts if they are brighter than the average shower at this energy. Therefore, they will be reconstructed at a larger energy leading to large positive biases at low energies. As the neural network is optimized by minimizing the overall loss function, it hence slightly underpredicts the energies for showers at larger true energies.

The safe configuration was expanded to be used with ImPACT reconstruction. In the ImPACT mono reconstruction, the neural network-based reconstructed direction will be used as a seed for the ImPACT fit. The energy reconstruction of ImPACT is

disabled for mono to decrease the number of free parameters for the fit based on only one shower image. The neural network-based reconstructed energy is thus passed on through the ImPACT reconstruction. The gamma-hadron separation for ImPACT is also the same. Hence, any positive effects of the ImPACT reconstruction are only visible for the direction reconstruction. This is quantified by the slight improvement visible in the angular resolution for the core mono energy range, especially below 500 GeV (see Figure 4.12a).

4.2.2 Crab Nebula - The standard candle in VHE astronomy

The Crab Nebula is conventionally used as the standard candle in VHE astronomy due to its high and stable flux. It was already used in previous studies of the H.E.S.S. performance and sensitivity (H.E.S.S. Collaboration et al., 2006b). Combining data from the verification campaign in winter 2019/2020 and the following year a large data set with default wobble offsets at 0.5°and 0.7° is available. The data set consists of 46 runs or 20.9h at a mean zenith of 46.4°, close to the culmination point of Crab. Additional data was taken at wobble offsets of 1.0°, 1.5°and 2.0° with at least 5 runs per offset.

Crab Nebula excess events The Crab Nebula low offset data set analyzed with the safe mono configuration has ∼20000 events after all cuts in the on region with size Θ. Using the reflected background method ∼40000 off events in on average 11.5 off regions with the same size as the on region are found. This yields more than 16500 excess events in the on region. For those, the distribution of a particular parameter can be obtained by subtracting the distribution of it in off events divided by the number of off regions from the distribution of it in on events. This is further called the excess distribution, which should, to first order, resemble pure gamma-rays.

Hence, the excess events can be compared to simulated gamma events at similar zenith and offset. For that gamma-simulations at correspondingly small wobble offset of 0.5° and at zenith angles of 45° and 50° were analyzed with the same configuration and combined. To be comparable to the Crab events, the MC event distributions have been weighted to represent a spectrum with a power law index of 2.5. The resulting distributions in Figure 4.13 demonstrate good agreement for the basic image properties that enter the reconstruction and separation neural networks directly and indirectly. Moreover, the regression output for the direction reconstruction, the displacement value δ_{RECO}, matches between observed and simulated gamma-rays along with the derived energies. The gamma-hadron separation parameterized by ζ_{BDT} also behaves quite similar in both cases. Thus, the reconstruction and gamma-hadron separation steps can be deemed validated.

Gamma-ray acceptance The data set with varying large offset angles can be utilized to derive the Crab excess rate as a function of wobble offset. Assuming radial symmetry, this can be interpreted as a measure of the gamma-ray acceptance over

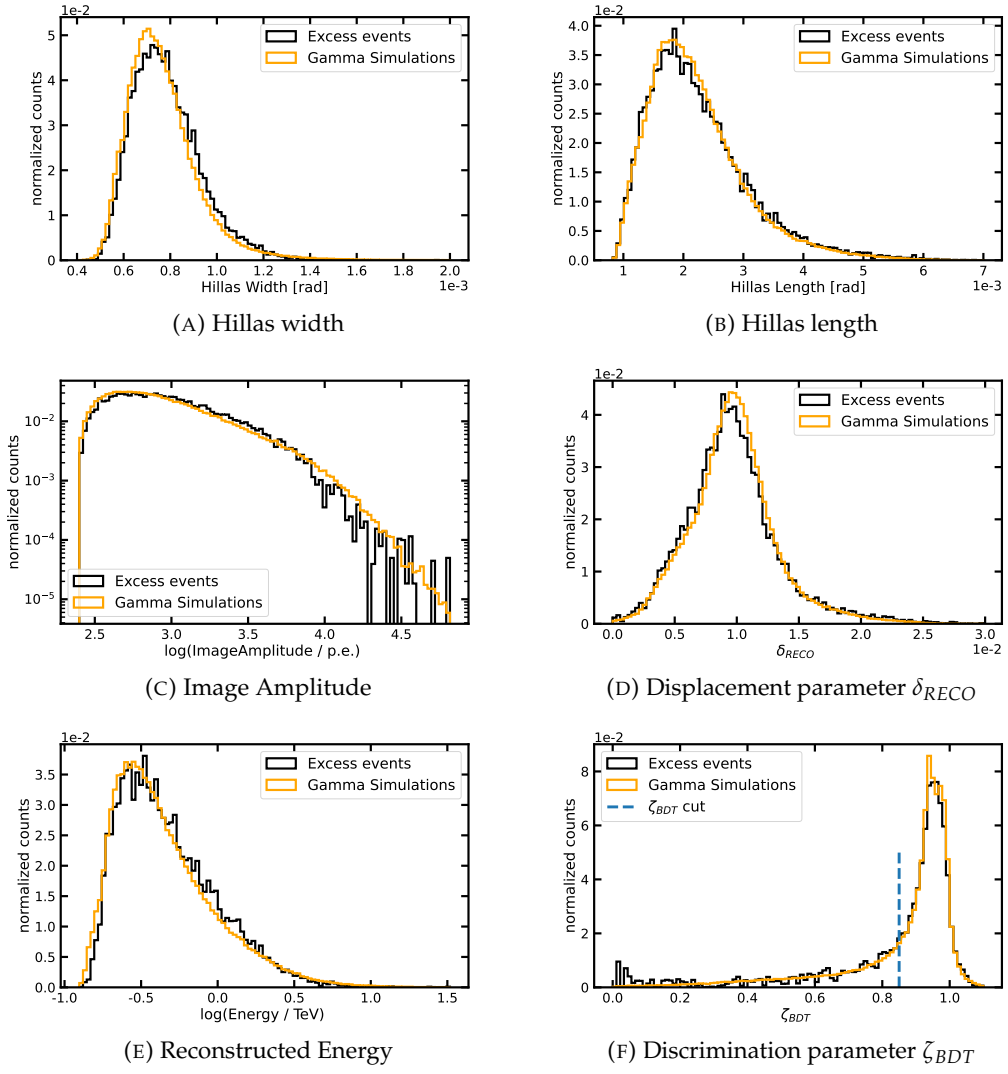

(A) Hillas width

(B) Hillas length

(C) Image Amplitude

(D) Displacement parameter δ_{RECO}

(E) Reconstructed Energy

(F) Discrimination parameter ζ_{BDT}

FIGURE 4.13: **Crab gamma-ray events compared with simulations** The distributions of Crab gamma-ray events are derived from the excess events after all selection steps as described in the text. The simulations have matching observation conditions. **A, B, C** show the Hillas width and length as well as the image amplitude, that enter either directly and/or as combinations the neural networks for all reconstruction steps. In **D, E, F** the output of the reconstruction steps is compared. For **F** a very loose gamma-hadron separation cut has been applied to show the full distribution. Furthermore, the actual cut value for ζ_{BDT} is highlighted. All distributions have been normalized to an area under the curve of 1.

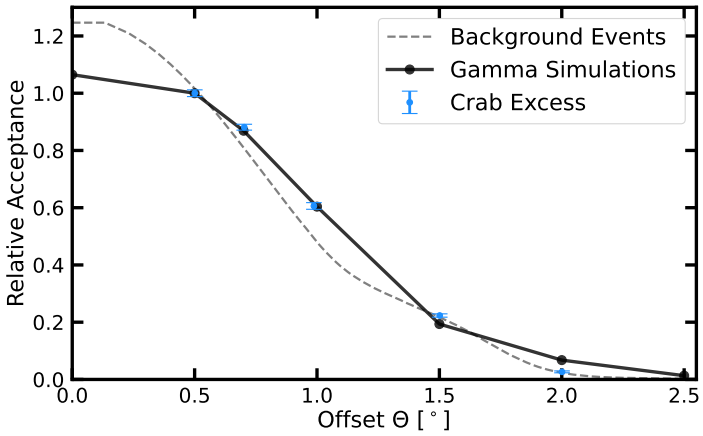

FIGURE 4.14: **Relative acceptance of gamma-ray events**
Predicted relative gamma-ray rates (from MC simulations) and those measured from data using the safe mono configuration are compared. Additionally, the relative acceptance from background events passing the gamma-hadron separation cuts is shown. All acceptance curves have been normalized to 1 at 0.5° offset.

the camera. At least one run existed for each of the four wobble directions for each offset value. The resulting acceptance is normalized relative to the rate at 0.5°. The same is done for gamma-ray simulations at 50° with varying offsets and for the background acceptance derived from observations with no strong gamma-ray source at similar zeniths. The resulting acceptance in Figure 4.14 shows a good match between observed and simulated gamma-rays. The observed background acceptance has a narrower shape.

High level analysis and spectrum The subsequent analysis of the data set with small offsets yielded a clear detection of the Crab nebula at significances of 38.1 $\sigma/\sqrt{\mathrm{h}}$ and 38.9 $\sigma/\sqrt{\mathrm{h}}$ for the reflected and ring background method (see Section 3.2.5), respectively. The corresponding map for the ring background analysis is presented in Figure 4.15 including as well the significance map and distribution outside of the exclusion regions. The map is besides the strong signal from the Crab Nebula without any strong features and the significance distribution can be described by a slightly wider than optimal Gaussian with a width of 1.19 σ. This is in line with previously published results using mono reconstruction (see e.g. H.E.S.S. Collaboration et al., 2017) and can be accounted for by a correction of the detection significances. The nonoptimal background description needs to be also included in the evaluation of potential systematics, as it is done in, e.g. H.E.S.S. Collaboration et al. (2017).

The derivation of the Crab Nebula spectrum is the high-level test to confirm and validate all previously mentioned steps in data processing, simulation consistency and analysis methods. The extraction of the spectral result is based on the reflected regions analysis and follows the forward-folding method as described in Section 3.2.5.

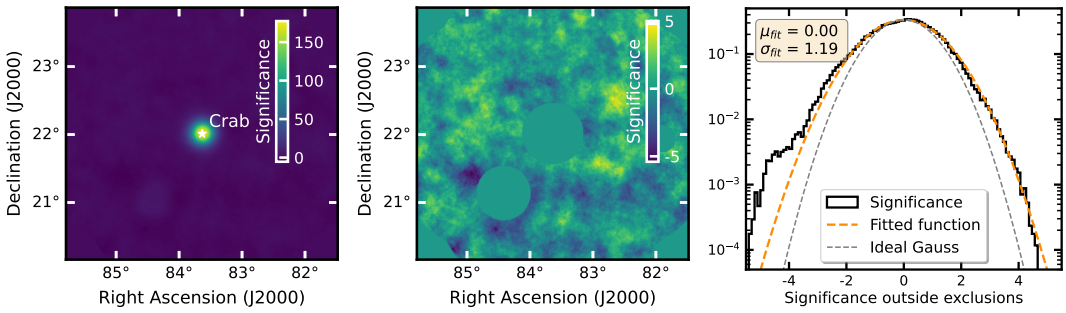

(A) Significance map (B) Masked significance (C) Sign. distribution

FIGURE 4.15: **Crab analysis results with the safe mono configuration**
The Crab Nebula is highlighted by the white star in the significance map (**A**). Additionally also the significance outside the exclusion mask around the Crab Nebula and bright stars is shown as a map and with its significance distribution. The result of a Gaussian Fit to the distribution is compared to an ideal Gauss with a width of 1.

Model	**Index** α	β	**norm** ϕ_0 $[10^{-10}\,\mathrm{TeV}^{-1}\,\mathrm{cm}^{-2}\,\mathrm{s}^{-1}]$	$\mathbf{E}_0$ [TeV]
Power Law	2.472 ± 0.012	/	(1.803 ± 0.016)	0.54
Log Parabola	2.471 ± 0.013	0.158 ± 0.014	(0.781 ± 0.010)	0.79

TABLE 4.3: **Crab Nebula spectral results**
The log parabola and power law are defined in Equation 3.19 and Equation 3.17, respectively. The reference energy E_0 is the decorrelation energy. The quoted uncertainties are statistical.

The result is summarized in Table 4.3 for two different spectral models, a log parabola and a power law model. The log parabola is defined as introduced in Equation 3.19 and the power law following Equation 3.17 with spectral index α. The log parabola model is considered because it describes the spectral properties of the Crab Nebula, showing an evident curvature over a larger energy range, better. This is suggested by measurements from a variety of gamma-ray instruments (see e.g. Aleksić et al., 2015; Nigro et al., 2019). However, the power law model can still result in a robust description of the spectrum over a limited energy range and has been used for the H.E.S.S. studies on the Crab Nebula previously (H.E.S.S. Collaboration et al., 2006b). Therefore, the power law model from H.E.S.S. Collaboration et al. (2006b) was chosen as the reference spectrum. Additionally, the results are compared to the theoretical model SED from Meyer et al. (2010) matched to data from several instruments. The energy threshold of the mono analysis is 196 GeV, set by the safe energy range defined as the range, where the effective area is at least 10 % of its maximum. Furthermore, the same data set was independently analyzed with mono and stereo reconstruction to crosscheck internal consistency. This is summarized in Figure 4.16.

Compared to the H.E.S.S reference spectrum given by a power law, the index is slightly smaller as expected by the observed hardening of the spectrum towards smaller energies better described by the log parabola. Evaluating the model at 1 TeV

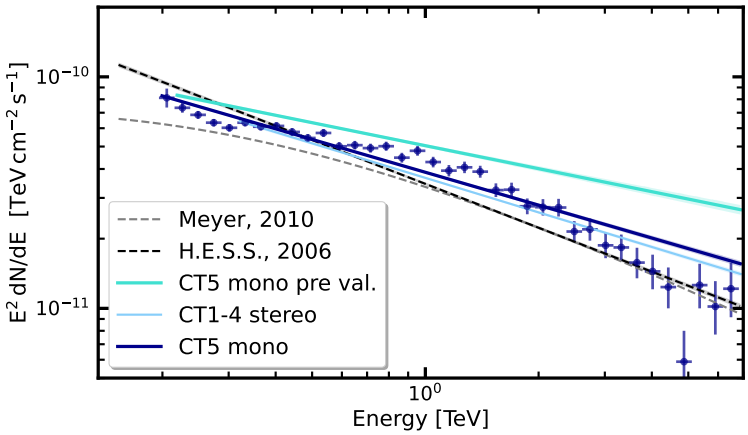

FIGURE 4.16: **Crab Nebula mono spectrum**
The power law spectral fits for the mono and stereo analysis together with the mono flux points are shown. For reference also the derived mono spectral fit obtained before the MC validation effort is plotted. The power-law spectrum from H.E.S.S. Collaboration et al. (2006b) and the derived model spectrum from Meyer et al. (2010) are added for comparison.

gives a norm of $\phi_0 = (3.87 \pm 0.05) \times 10^{-11}\,\mathrm{TeV}^{-1}\,\mathrm{cm}^{-2}\,\mathrm{s}^{-1}$, which is ∼12 % higher comparing it to the norm from H.E.S.S. Collaboration et al. (2006b). Therefore, the values agree within the there derived systematic uncertainties assumed to be 20 % of the flux. The crosscheck with the stereo analysis on the same data set results in an excellent agreement within a few percent, as the derived power law has a norm of $\phi_0 = (3.66 \pm 0.04) \times 10^{-11}\,\mathrm{TeV}^{-1}\,\mathrm{cm}^{-2}\,\mathrm{s}^{-1}$ at 1 TeV and an index of 2.496 ± 0.012. The energy threshold of the stereo analysis is comparably higher at 383 GeV. The drastic improvement due to the validated simulation chain is also evident both visually in Figure 4.16 and in the derived spectral properties.

With this, the full spectral reconstruction for the mono analysis of FlashCam data is verified within the systematics.

4.2.3 PKS 2155 - A bright extragalactic point source

The active galactic nucleus PKS 2155-304 is even in its quiescent state a bright gamma-ray source (H.E.S.S. Collaboration et al., 2010a). It is visible as a point source for H.E.S.S. and can therefore be used as a test of the PSF description in reality, comparing it to the PSF derived from simulations. During the science verification campaign, the system was observed for ∼5 h under varying zenith angles between 25° and 55° resulting in a mean zenith angle of 38°. PKS 2155-304 was detected with significances of 27.5 σ and 28.2 σ with the reflected and ring background methods using the mono reconstruction (see Figure 4.17a). The spectrum above 133 GeV can be described as a power-law with index 3.36 ± 0.09 and a norm of $\phi_0 = (2.76 \pm 0.14) \times 10^{-10}\,\mathrm{TeV}^{-1}\,\mathrm{cm}^{-2}\,\mathrm{s}^{-1}$ at a reference energy of 274 GeV. The index is within errors compatible with the index derived by H.E.S.S. Collaboration et al. (2010a) for the quiescent state, whereas the flux at 1 TeV is comparably higher.

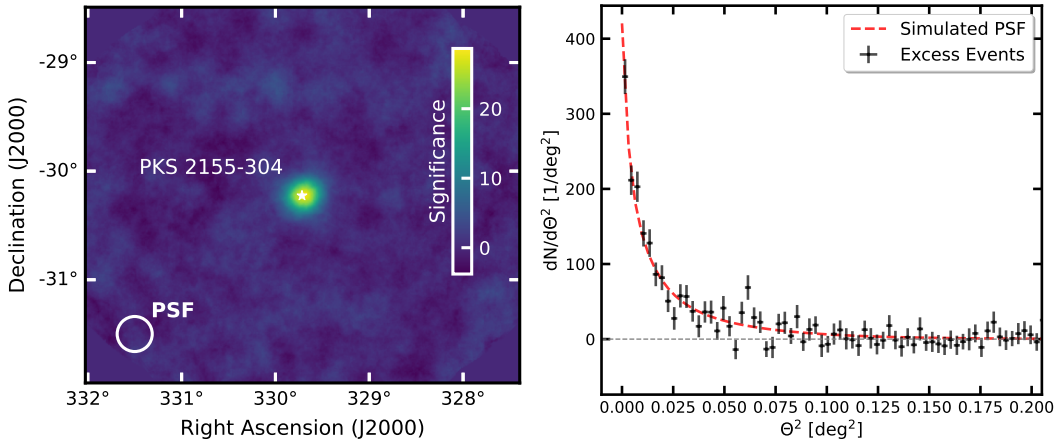

(A) Significance map

(B) PSF of Excess events

FIGURE 4.17: **Point Spread Function derived from PKS 2155-304 observations compared to simulations**
In **A** the significance map of the PKS 2155-304 observations analyzed with the mono configuration is shown. For comparison the 68 % containment radius of the corresponding MC PSF is added as a circle. The radial distribution of excess events is compared to the fitted shape of the simulated PSF in **B**.

However, due to the variable nature of PKS 2155-304 no clear conclusion can be drawn from this. To compare the observed to the simulated PSF, the PSF lookups are combined to have a matching zenith angle and wobble offset distribution and the simulated events are weighted by their energy to represent a spectrum with the measured spectral index. The derived PSF as a function of radial offset from the source position Θ is described as a 3-component Gaussian of the form (Deil, 2011)

$$PSF(\Theta) = S\left[\exp\left(-\frac{\Theta^2}{2\sigma_1^2}\right) + A_2\exp\left(-\frac{\Theta^2}{2\sigma_2^2}\right) + A_3\exp\left(-\frac{\Theta^2}{2\sigma_3^2}\right)\right]. \tag{4.2}$$

S,A_2 and A_3 are the relative normalizations of the three components, whereas σ_{1-3} denotes the width of the respective component. With this description, one can account for contributions from well and poorly reconstructed events. The 68 % containment radius from simulations matched to the PKS 2155-304 data set is $R_{68} = 0.161°$. This is overlayed as a circle of appropriate size in Figure 4.17a. The resulting curve from the simulated PSF is scaled to match the number of excess events in the first bin and then compared to the radial distribution of excess events from PKS 2155 in Figure 4.17b. This displays an overall good agreement of simulated and measured PSF.

4.2.4 Summary and outlook

The derivation and scientific verification of the mono analysis of FlashCam data was presented. Despite not being optimized yet, the derived safe mono configuration gives slightly better performance than the mono analysis of the old CT5 camera.

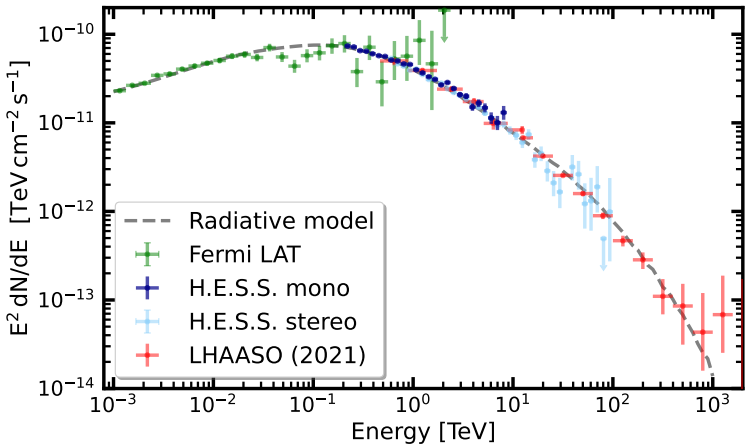

FIGURE 4.18: **Multiwavelength SED of the Crab Nebula including H.E.S.S. mono flux points**
The Fermi-LAT and H.E.S.S. flux points were provided by Tim Unbehaun. The mono analysis made use of the safe mono configuration derived in this thesis. The LHAASO points are taken from Lhaaso Collaboration et al. (2021). The radiative model was provided by Tim Unbehaun and is an adapted version of the model presented in Dirson and Horns (2022).

Tests on designated Crab Nebula and PKS 2155-304 data sets confirmed the validity of the reconstruction and gamma-hadron separation methods. Furthermore, the PSF and gamma-ray acceptance are well described in simulations. Finally, together with the simulations verification efforts described in the previous section the analysis of the Crab Nebula data set resulted in a detailed end-to-end verification of the full reconstruction chain up to spectral results, as the derived SED of the Crab Nebula is within systematics compatible with its reference spectrum. This verification of the mono reconstruction of FlashCam data essentially makes the publication of FlashCam-based scientific results feasible.

The modeling of the Crab Nebula multiwavelength SED is an ongoing effort within the H.E.S.S. collaboration. Combining the mono flux points derived with the configuration presented in this chapter with stereo flux points from several years of H.E.S.S. observations and data from the Fermi-LAT and LHAASO observatory (Lhaaso Collaboration et al., 2021) shows a good match (see Figure 4.18). This further strengthens the point of the successful verification and also shows the scientific value of the data set, making precise modeling of the gamma-ray component together with the full multiwavelength spectrum feasible. The results are currently prepared in a H.E.S.S. collaboration paper (H.E.S.S. Collaboration, 2023) led by Tim Unbehaun.

Nevertheless, the mono reconstruction can be further optimized especially by lowering the energy threshold. This will be of importance for the observation of sources with steep spectral shapes due to the absorption with extragalactic background light. Typical examples of this are AGN at high redshifts or gamma-ray bursts. The direction and energy reconstruction as well as the gamma-hadron separation is limited in its performance at low energies due to very small and dim images

providing only little reconstruction and discrimination information. Therefore, the first step toward achieving better low-energy performance is to improve on the hard (9,16) tail cut cleaning. A promising approach to this is the time-based cleaning described in the next section.

4.3 Introduction of time-based cleaning in H.E.S.S.

Traditionally image cleaning in H.E.S.S. was solely based on the intensities in each pixel. The so-called tail cut cleaning method is described in Section 3.2.1 in more detail. While the pixel intensities are a good first-order indicator if a pixel is part of the shower or not, one needs a rather hard cut to avoid that noise-only pixels become part of the cleaned shower images. This in turn can lead to cropped images with only a few pixels surviving the cleaning, especially for faint showers. The loss of image information can be a problem for the reconstruction and gamma-hadron separation techniques that are based on the cleaned images.

As both gamma and hadron-induced showers show a similar arrival time of shower photons with a gradient along the shower development axis, the timing information can be also exploited for image cleaning techniques. Some examples of reconstructed pixel intensities and times as seen by FlashCam installed at CT5 in real observations are depicted in Figure 4.19 and show the clear clustering in time for showers. As the reconstructed times of neighboring pixels that contain shower photons are closely connected, advanced clustering algorithms provide a good tool to provide a more sensitive image cleaning than the standard tail cut method. This has already been shown in studies based on MC simulation for the next generation CTA (Shayduk and CTA Consortium, 2013) and has been used by MAGIC in their reconstruction pipeline (Aliu et al., 2009)

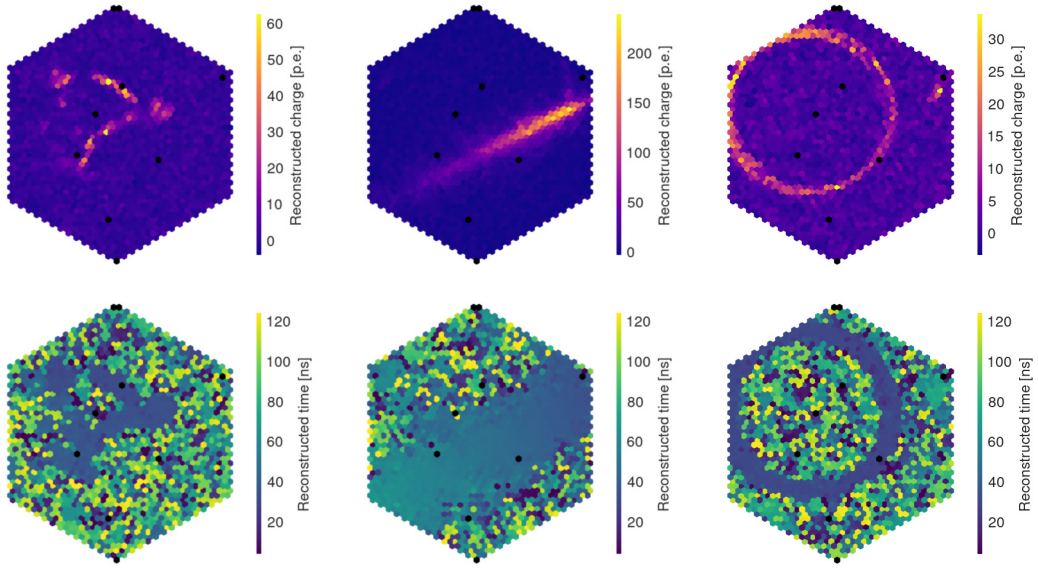

FIGURE 4.19: **Reconstructed intensity and time for several showers** Data taken from H.E.S.S. observation runs with FlashCam. The upper panel shows the reconstructed intensities per pixel for several events, and the lower panel the reconstructed time for the same events. On the left a hadronic event, in the middle a likely gamma-ray event and on the right a muon ring is shown. Images provided by Felix Werner.

4.3.1 DBSCAN - Density based clustering

DBSCAN, short for Density-Based Spatial Clustering of Applications with Noise, is a well-proven clustering algorithm developed by Ester et al. (1996). In general, it allows for the identification of clusters in an N-dimensional space. It is well suited to the cleaning of IACT shower images, as the number of clusters in the algorithm is not predefined and points that can not be assigned to a certain cluster are labeled as noise. The flexible number of clusters is a good fit for typical camera images, as hadron induced showers might contain several clusters, whereas gamma induced showers create in the large majority of cases only one cluster. The remaining pixels outside of the shower contain only noise and hence the possibility of a noise label is important for those.

The working principle of DBSCAN, independent of its actual implementation, is sketched in the following. Assuming arbitrarily spaced points in an N-dimensional space, the algorithm has the goal to find groups of points that are close together. Thereby two parameters are taken into account to define a cluster: a distance ϵ and the minimum number of points $minPts$. The distance ϵ can in principle be defined by any metric, but for simplicity, only the Euclidean metric is considered in the following. Using these parameters, points are then classified as:

- Core points, if there are at least $minPts$ within a distance ϵ of it. The point itself is included in the count.
- Density reachable points, that are not core points but are within distance ϵ of a core point.
- Noise points, that are neither core points nor density reachable from a core point.

Core points and density reachable points are then assigned to one or more clusters. All core points, that are density reachable with regards to each other plus their connected density reachable points will get the same cluster label. A typical example of the algorithm can be seen in Figure 4.20 for a two-dimensional space using specific values of ϵ and $minPts$. In the sketch, cluster, reachable and noise points are marked accordingly.

4.3.2 Implementation and adaptation for H.E.S.S.

The H.E.S.S. pulse reconstruction depends on the camera type used. As this work focuses on the implementation for the FlashCam camera, the descriptions will detail the FlashCam specific characteristics. Nevertheless, it is easily adaptable for the H.E.S.S. 1U cameras as well as the previous CT5 camera, as the information provided at the cleaning stage is similar.

FlashCam pulses are reconstructed in each pixel using a neighbor-based signal search (Bernlöhr et al. (2013) and Puehlhofer et al. (2022)). After the calibration steps,

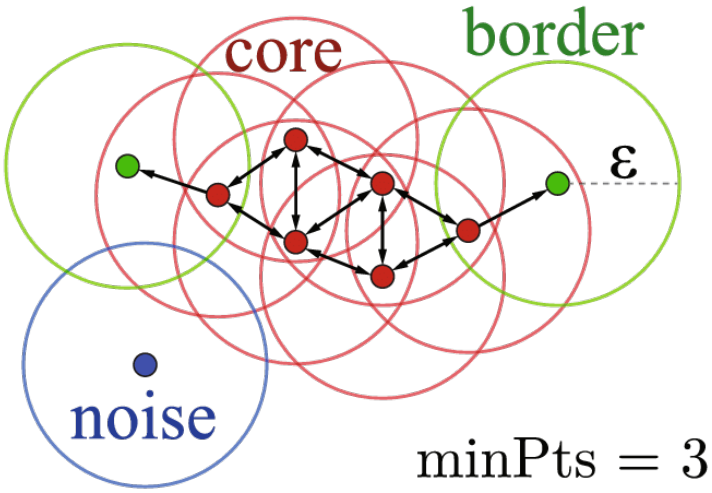

FIGURE 4.20: **Illustration of DBSCAN in 2D**
The minimum number of points *minPts* is 3, whereas the distance ϵ is the radius of the shown circles. All subsequent core points are marked with red, whereas in green are density reachable or border points connected to the same cluster. The noise point is marked in blue. All red and green points build up the cluster found by the algorithm. Image taken from Mehle et al. (2017).

one intensity and time value per pixel is returned. As the neighbor-based search implies some bias on the reconstructed times for noise pixels next to shower pixels, in the first step a pre-cut on intensity is implemented before the actual DBSCAN step. After calibration, the noise level in a pixel can be approximated as a Gaussian distribution with a mean of 0 p.e. and a standard deviation σ_{noise}. The pre-cut can be either a hard cut on a specific intensity, labeled later on as n_{hard}, or be related to the noise in a given pixel by a factor of $n_{\text{noise}} \times \sigma_{\text{noise}}$. The latter approach has the advantage that the actual noise level averaged over several previous events is taken into account. This can take care of the effect of, e.g. bright stars, whereas the hard cut can be added to have a more uniform response over the whole camera. For this study and the optimization only the n_{noise} cut is considered and the effect of the additional hard cut is discussed later on.

After applying such a first pre-cleaning step all remaining pixels enter the DBSCAN algorithm. DBSCAN is subsequently run in the 3D space consisting of the spatial position of pixels and the corresponding reconstructed pulse times. As the ϵ parameter in DBSCAN has the same value in all dimensions, it is of crucial importance to first normalize the time and geometry values of the points. For that, two parameters are introduced, a time scale (t_scale) in units of ns and a length scale (l_scale) in m. Pixel times are then divided by t_scale and pixel coordinates by l_scale. In the resulting normalized 3D space the ϵ parameter is then set to 1, whereas t_scale and l_scale will be derived as part of the optimization. The other remaining free parameter of DBSCAN is minPts.

A DBSCAN implementation[7] was integrated into the HAP framework. The specific implementation made also use of a k-d tree to precompute distances before each call of DBSCAN with the goal to save substantial computing time. After setting values for the 3 free parameters the clustering is run on the pixels that survived the pre-cleaning step. Afterward, each pixel gets assigned a specific cluster identification label (ID) or noise label and the cleaned image consists of all pixels that are members of a cluster. Even though the cleaned image includes all clusters, the cluster ID is also saved as it can be important for other algorithms, like, e.g. a cluster-based muon veto as described in Olivera-Nieto et al. (2022).

4.3.3 Parameter optimization

To check the influence of varying the four parameters (n_{noise}, t_scale, l_scale, minPts) on the cleaning, MC gamma simulations of a point source at a zenith angle of 20° and an offset of 0.5° were used. The typical noise level in these simulations is ∼1.35 p.e. For the simulations the true intensity information of simulated events I_{true} (Bernlöhr, 2008) was exploited. For each simulated shower this contains for each pixel the number of p.e., that are actually generated by the shower and not by electronic or NSB noise. This can be used to separate pixels with shower information from noise-only pixels. Also, the amount of shower light before and after cleaning can be compared. The goal of the cleaning step in general is to keep as many shower pixels and intensity as possible while not being too sensitive to noise-only pixels.

For the first iteration, the parameters have been set to a reasonable value, and only one parameter was allowed to vary. The goal was to define ranges and intervals for each parameter that could be explored in a grid search of a larger phase space. The pre-set values were $n_{noise} = 2$, t_scale = 2 ns, l_scale = 0.1 m and minPts = 5. The value for t_scale reflects the typical time gradient for a shower and the value for l_scale the pixel spacing of FlashCam of 0.05 m (Pühlhofer et al., 2019). Due to the addition of the density reachable points, minPts can also be interpreted as the minimum cluster size. An example of the true intensity images and the cleaned images with several potential subclusters can be seen in Figure 4.21 for a simulated gamma event as well as for one hadronic event.

For the parameter study as described above, the first quantity to be compared was the survival probability of pixels, that contain shower light, as a function of true pixel intensity. For a given bin $[I_{true,min}, I_{true,max}]$ in true intensity this is then the ratio of pixels in the cleaned image with $I_{true,min} \leq I_{true} < I_{true,max}$, divided by this number in the uncleaned image. Secondly, to judge the number of false positives, one can count the pixels in the cleaned image with $I_{true} = 0$ in bins of reconstructed intensity. The parameters are varied individually for one simulation run with ∼9000 triggered events and these two quantities are derived. This is presented in Figure 4.22.

[7] The implementation from `https://github.com/CallmeNezha/SimpleDBSCAN` was used and modified for use within the HAP code.

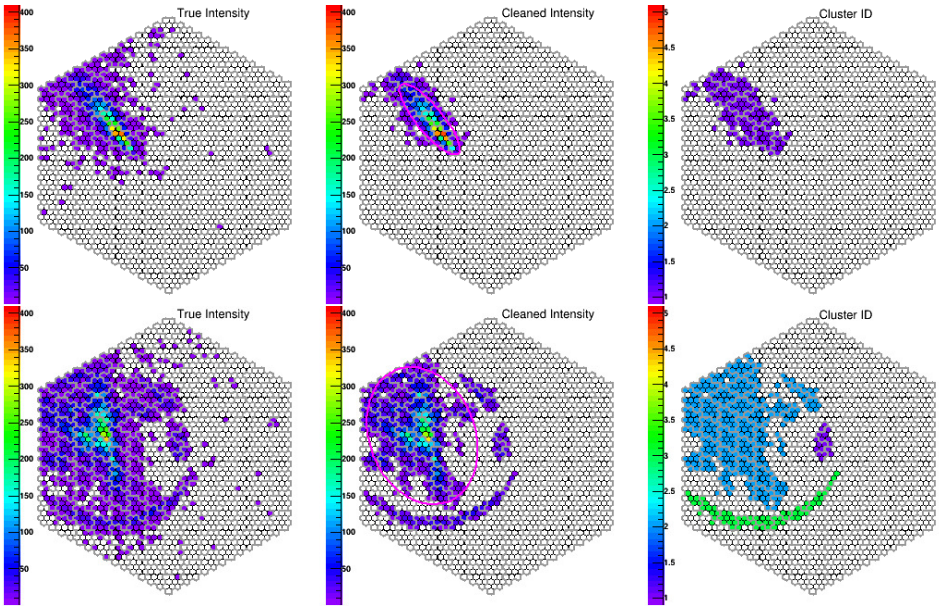

FIGURE 4.21: **True intensity, cleaned intensity and cluster ID for simulated events**
The upper row shows a simulated gamma shower and the lower row a simulated proton shower. The intensities are shown in units of p.e., with the left panel corresponding to the I_{true} induced by the shower only. The cleaned intensities in the middle are shown after running the DBSCAN implementation on these events. The right panel gives the derived cluster IDs, where the gamma shower has only one connected cluster and the proton image shows three distinct clusters.

This parameter study clearly shows that changing the two scale parameters or minPts has similar effects on the pixel survival probability. This is due to the interplay of ϵ and minPts in the DBSCAN algorithm. On the other hand n_{noise} is mostly affecting the number of false positives. If compared to the default (9,16) tail cut cleaning used for FlashCam, one can see a much larger survival probability for pixels with small true intensity for most parameter combinations, while being more susceptible to containing false positive pixels in the cleaned image.

To investigate the full parameter space a grid search with the values described in Table 4.4 was performed, resulting in a total of 360 combinations to be evaluated.

As individual noise-only pixels adjacent to a bright shower entering the cleaned

Parameter	Values	Set 1 (TimingN5)	Set 2 (TimingN3)
n_{noise}	1.5, 2.0, 2.5, 3.0, 3.5	3	3.5
t_scale (ns)	1.5, 2.0, 2.5, 3.0, 3.5, 4.0	3.5	3
l_scale (m)	0.07, 0.12, 0.17	0.17	0.12
minPts	3, 5, 7, 9	5	3

TABLE 4.4: **Defined parameter space for grid search and chosen settings**
All 360 combinations of the grid were investigated. The decision to choose the two sets is motivated in the text.

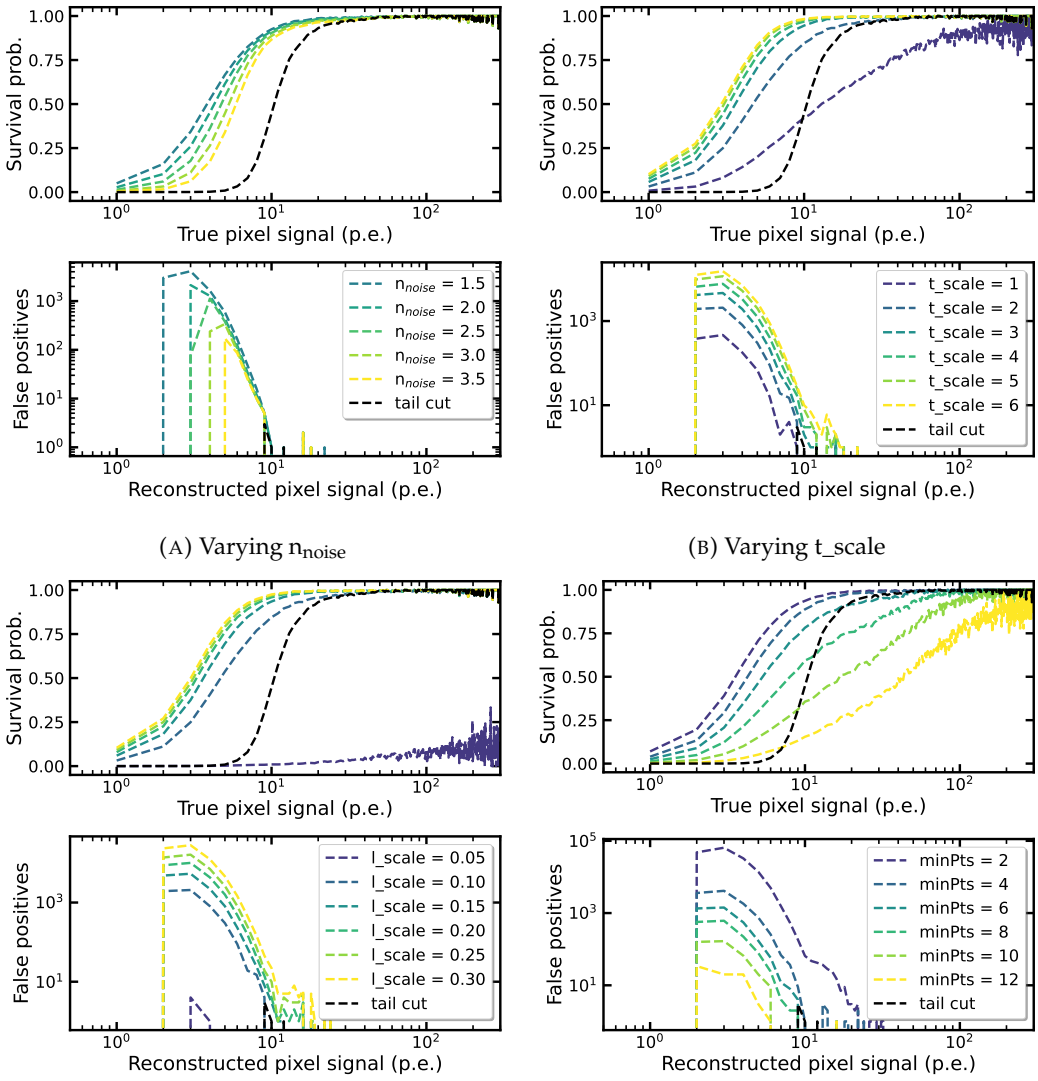

(A) Varying n_{noise}

(B) Varying t_scale

(C) Varying l_scale

(D) Varying minPts

FIGURE 4.22: **Effects of varying the individual parameters on the cleaning**

The parameters have been varied individually keeping the other 3 parameters at the default value as described in the text. The study is done on a gamma simulation with ∼9000 triggered events. The survival probability and false positive counts have been computed in linear bins with a size of 1 p.e. For comparison also the performance of the default tail cut cleaning is shown.

images might be rather negligible for deriving the shower parameters afterward, it is more important to look at the probability of noise-only clusters instead. Furthermore, also the pixel survival probability can be investigated on a shower level, as this is the crucial information entering the derivation of shower parameters, such as the Hillas parameters.

To derive the probability of clustering on noise-only pixels, an externally triggered simulation without any showers was run. This included 20000 events, for which then the number of events with successfully found clusters could be derived. This gives a probability of shower false positives. To derive a typical minimum surviving shower size $S_{min,50}$ at which most shower intensity is kept after cleaning the following approach was taken: First, the pixel-wise $I_{true,pixel}$ was summed for each event and the cumulative distribution of true shower sizes $I_{true,shower}$ of simulated gamma events was derived. The same cumulative true shower intensity was derived post-cleaning but weighting the showers with the ratio of $I_{true,cleaned} / I_{true,shower}$. $I_{true,cleaned}$ is the sum of $I_{true,pixel}$ for all pixels in the cleaned image. Deriving the ratio of these cumulative histograms one can derive the integral shower survival fraction as a function of $I_{true,shower}$. After smoothing the resulting curve with an averaging filter, $S_{min,50}$ was derived as the minimal shower size at which the shower survival fraction is at least 50 %. This means that 50 % of the true shower intensity for a typical shower of that brightness is kept after cleaning. This approach is also highlighted in Figure 4.23a for one example configuration.

The goal for finding the best parameter configurations is to have a low noise cluster probability as well as a small $S_{min,50}$. The result for all combinations can be seen in Figure 4.23b. The showers with zero detected noise clusters on the 20000 events are plotted at a probability of 10^{-5} for visualization reasons. The region of interest in the lower left corner shows two subgroups: One with $S_{min,50} \approx 90$ p.e. and no noise clusters found and one with up to a few detected noise clusters but smaller $S_{min,50} \approx 70$ p.e. From the first subgroup the combination described as set 1 in Table 4.4 is chosen, and from the second subgroup the combination labeled set 2. Both are also highlighted in red, respectively in orange in Figure 4.23b. The selection of the two sets was done in a way to have two sets different in each parameter for further testing. For simplicity, the two sets will be further referred to as TimingN5 and TimingN3 based on their minPts setting.

4.3.4 Performance in mono analysis

For the two chosen parameter sets the image properties were derived and compared with respect to the tail cut cleaning approach. Especially the number of pixels after cleaning and the corresponding image intensities are important quantities to compare, as they can be seen as a measure of image details available for further reconstruction and separation steps. As it can be seen in Figure 4.24, both these quantities show a ratio larger than 1 when dividing the intensity or number of pixels from

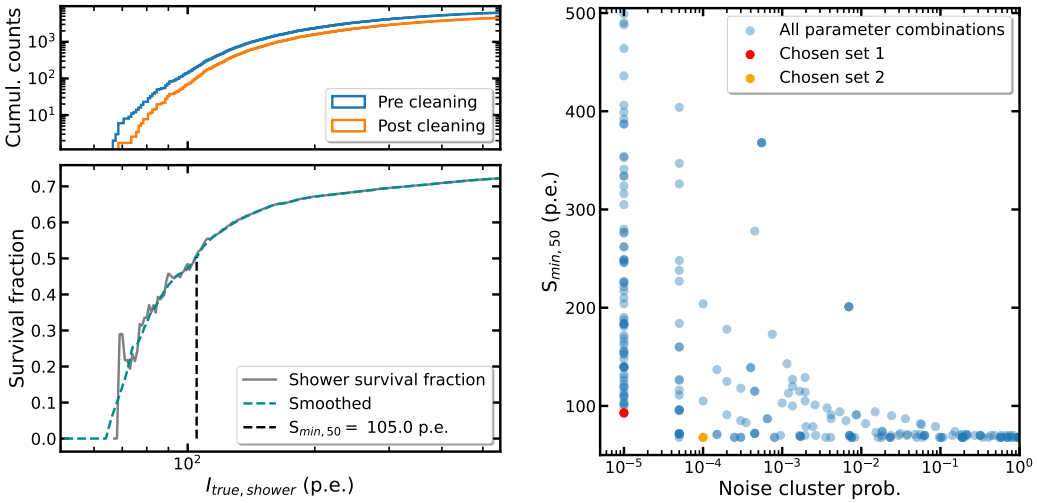

(A) Derivation of $S_{min,50}$

(B) Selection of parameter sets

FIGURE 4.23: **Shower level based selection of parameter sets** **A** shows the computation of the minimum surviving shower size $S_{min,50}$ as discussed in more detail in the text for a specific setting for the time cleaning as an example. **B** shows the minimum surviving shower size $S_{min,50}$ and the noise cluster probability derived from a noise-only simulation for each parameter combination. The noise-only simulation consisted of 20000 events, hence settings with zero noise clusters were set to an arbitrary value of 10^{-5}. The parameter sets picked for further investigation are highlighted.

time-based cleaning by the same quantity derived from the standard cleaning. Especially for small showers, with 100 p.e. in the tail cut cleaned image, the intensity after time-based cleaning is increased by 50 % or more for both investigated settings. The effect becomes less pronounced for brighter tail cut images, but the time-based cleaning is always adding additional intensity information. The same behavior can be seen in the ratio of the total pixel numbers of the cleaned images, which is also increased by 50 % or more for small showers. In general, the TimingN5 setting seems to outperform TimingN3 in these comparisons mostly due to its looser pre-cut n_{noise}. Additional tests performed on off observation runs give similar effects for hadronic showers.

To derive IRFs using the time-based cleaning, direction and energy reconstruction as well as the gamma-hadron separation had to be trained. This was done using the same neural network scheme as described in Section 3.2.3 for the mono analysis using gamma simulations at 20° and off observation runs, to which time-based cleaning had been applied. After the same preselection cuts as defined in the safe cuts (see Table 4.2), the resulting angular resolution and energy dispersion are shown in Figure 4.25a and Figure 4.25b, respectively. One can see a clear improvement with respect to tail cut cleaning for both reconstruction steps for energies below 1 TeV. The effective area was computed on preselection as well as on postselection level, which is shown in Figure 4.25c. Whereas on the preselection level, the effective area shows improvement for reconstructed energies up to ∼100 GeV, after postselection

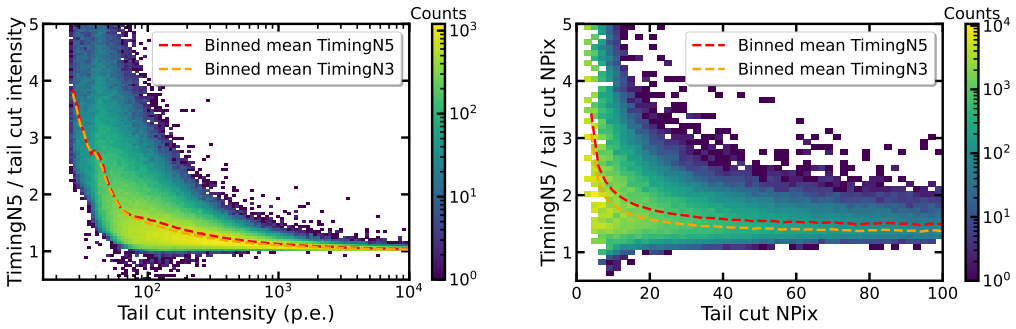

(A) Ratio of image amplitudes (B) Ratio of image pixels

FIGURE 4.24: **Image amplitude and pixel number for time-based in comparison with tail cut cleaning**
The ratios were derived from a set of 50 gamma simulation runs with ∼9000 events each. Tail cut cleaning corresponds to the default (9,16) cleaning used for FlashCam at CT5. Both plots show the respective quantities for the TimingN5 cleaning as a 2D histogram, as well as the mean value for each bin along the x-axis. For comparison also the binwise mean value for TimingN3 is shown.

the effective areas are similar to the tail cut case.

One has to take into account that the optimization of the postselection cuts, ζ_{BDT} and the size of the on region Θ, is still needed. Furthermore, also the gamma-hadron separation training has not been optimized to account for the additional information provided by the time cleaning, which is an ongoing effort, but beyond the scope of this thesis. The two time-based cleaning settings perform generally rather equally.

To test the derived analysis configurations on observational data, a subset of the Crab data set as described in Section 4.2.2 was used. The results are shown in Figure 4.26. With the ring background method, the Crab was reconstructed with high significances of 118 σ and 129 σ respectively for the two configurations similar to the result with safe tail cuts based cuts on the same data set. The background description quantified by the significance distribution outside of exclusion regions is also well normalized with a width of the distribution of 1.1 for both configurations, only deviating slightly from the optimal width of 1. This deviation is similar or smaller to the standard analysis as described in Section 4.2.2 and can be later accounted for as systematics.

4.3.5 Further studies

For the use with the ImPACT reconstruction (see Section 3.2.3 and Parsons and Hinton, 2014), extended cleaned images are needed. Similar to the tail cut approach the cleaned images are extended by two rows. As discussed in Section 4.2.1, for the mono reconstruction ImPACT is only used for direction reconstruction. In Figure 4.27a the angular resolution for the ImPACT based reconstruction using the extended time cleaned images is compared to the neural network based reconstruction. This is shown at postselection level and one can see only a small improvement

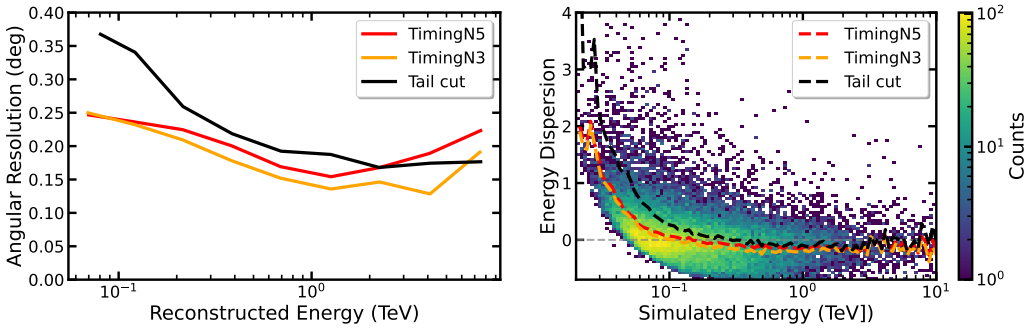

(A) Angular resolution (B) Energy dispersion

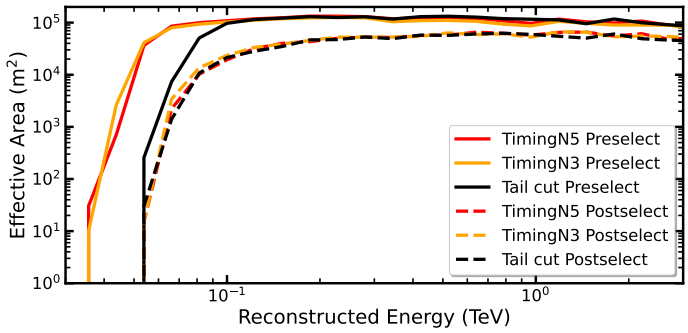

(C) Effective Area

FIGURE 4.25: **Performance of mono reconstruction with time-based cleaning**
A and **B** show the angular resolution and the energy dispersion for the two time cleaning configurations compared with the standard tail cut based reconstruction. Both are shown at the preselection level before any gamma-hadron separation cuts. **B** shows the event-by-event energy dispersion for the TimingN5 configuration as a 2D histogram. Additionally the mean per energy bin, often also referred to as energy bias, is shown for all 3 cases. **C** shows the effective area for the 3 configurations both after preselection and after postselection. For the postselection, the same cuts in ζ_{BDT} and Θ^2 have been applied to all 3 configurations.

with ImPACT. The ImPACT performance itself is rather similar to the tail cut based ImPACT reconstruction, as the extended images look very similar for loose tail cut and time-based cleaning. Hence for the mono analysis, the neural network based approach can almost reproduce the ImPACT performance with considerably less computing time, if time-based cleaning is used.

In order to have good MC - data consistency after the time cleaning step for differing NSB values, an additional intensity cut n_{hard} was implemented as already discussed in Section 4.3.2. This uniformizes the cleaning behavior for inhomogeneous NSB over the camera as well as for all observations and simulations up to a certain NSB level. As the NSB level corresponds to a certain noise level σ_{noise}, the limiting noise level is set by $n_{hard} = n_{noise} \times \sigma_{noise}$, for a time cleaning with set n_{hard} and n_{noise}. Considering that the large majority of observation targets have noise levels $\sigma_{noise} \leq 2$ p.e., $n_{hard} = 6$ p.e. was set for the TimingN5 cleaning additionally. This

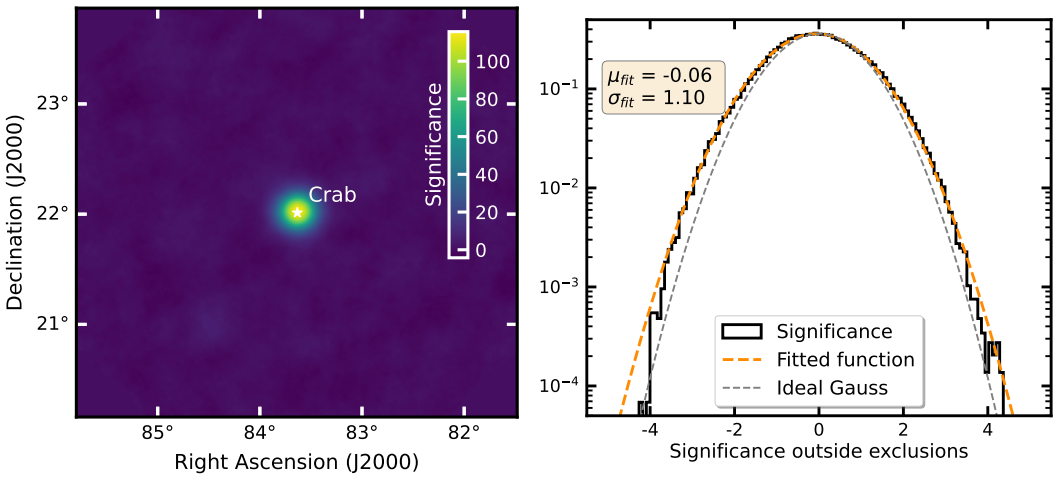

(A) Crab significance map

(B) Crab significance distribution

FIGURE 4.26: **Mono analysis of the Crab Nebula with a time-based cleaning configuration**
The resulting significance based on the ring background method and a correlation radius of 0.13° is presented in **A**. A very significant excess from the direction of the Crab nebula is clearly visible. In **B** the resulting significance distribution outside of the masked exclusion regions is shown. The result of a fit with a Gaussian distribution is compared to a Gaussian with $\sigma = 1$ and $\mu = 0$.

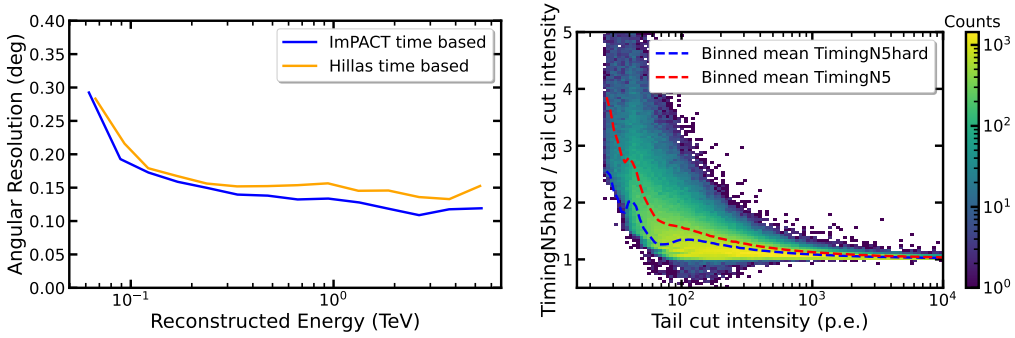

(A) Extension to ImPACT reconstruction

(B) Influence of an additional pre-cut n_{hard}

FIGURE 4.27: **ImPACT extension and influence of an additional pre-cut on time cleaning based reconstruction**
A depicts the angular resolution for an ImPACT reconstruction based on time-cleaned images compared to the neural network based reconstruction. **B** shows the intensity ratio with regards to the tail cut cleaning for a time cleaning configuration with an additional pre-cut of $n_{hard} = 6$ as a 2D histogram. Additionally, the binned mean is compared to the respective time cleaning without the additional cut.

is shown as TimingN5hard in Figure 4.27b, compared to the default TimingN5 case as described in the previous section. As expected one can see smaller image intensities after cleaning using this additional pre-cut. Nevertheless, one can still see an improvement with regard to the tail cut cleaning method. The gain is still $\sim$30 % in image intensity for small 100 p.e. showers. With such a cleaning, the reconstruction and gamma-hadron separation lookups as well as IRFs based on it would be valid for most observation runs. For the analysis of data with exceptionally high NSB, one could either derive new configurations and tables with increased n_{hard} or run designated simulations to derive these.

4.3.6 Summary and outlook

A novel cleaning technique based on shower arrival times for H.E.S.S. analysis was introduced for FlashCam images using DBSCAN, a well-known density-based clustering algorithm. The cleaning parameters were optimized using two main criteria: Keeping as much true shower intensity of the images as possible and being as little as possible susceptible to noise. From the optimization two well-performing cleaning settings were identified, for which a full mono reconstruction chain was successfully tested. The time-based cleaning configurations show a significant increase in the available shower information after the cleaning, in both number of pixels and image intensity. This yields a lot of potential for better reconstruction and separation of low energetic showers, which suffer from cropped images in the standard cleaning approach. Already the non-optimized analysis chain is equally sensitive to the default mono configuration as shown on tests using a Crab Nebula data set. Furthermore, no signs of being more susceptible to noise effects could be found. To make use of the time-based cleaning for varying observation conditions an additional fixed intensity cut per pixel can be applied, with which the time-based cleaning still outperforms the standard tail cut cleaning.
Therefore the full exploitation of the additionally provided information via time-based cleaning is a promising way to increase the low-energy performance of H.E.S.S.. This is an ongoing effort within the H.E.S.S. collaboration and, e.g. additional image parameters to be used in the reconstruction and gamma-hadron separation are being tested. Currently, already slightly improved mono and strict mono configurations with the Hillas parameter based reconstruction can be retrieved. Additionally, the DBSCAN based approach also acts as a cluster identifier, which can be used by other algorithms to identify extra components away from the main shower, which could be a hint for a hadronic origin. With this, the hadron rejection power at higher energies can be significantly improved (Olivera-Nieto et al., 2022).

Chapter 5

RS Ophiuchi - first nova detected in very-high energy gamma-rays

Novae caused by thermonuclear explosions on the surface of white dwarfs have been an active field of research for more than a century. Whereas their main characteristics are well understood in optical light (Section 2.4), the repeated detection by the Fermi-LAT satellite confirmed also their status as important high-energy astrophysical sources (Chomiuk et al., 2021). As the Fermi-LAT discoveries provided proof for powerful acceleration processes within novae (see Section 2.4.3), a follow-up campaign was put in place for H.E.S.S. to detect potential VHE emission. In order to trigger a H.E.S.S. observation, a candidate nova must be optically bright with optical magnitudes $m_v \leq 9$, significantly detected with Fermi-LAT and have high ejecta velocities ($\geq 1500\,\mathrm{km/s}$). Over the last years H.E.S.S. typically followed up on about two novae per year but most of those only satisfied parts of the conditions. Therefore up to August 2021, no nova was detected in VHE gamma-rays neither by H.E.S.S. nor by other instruments like MAGIC. The outburst of the recurrent nova RS Ophiuchi, introduced in Section 2.4.2, on August 8, 2021 fulfilled all three criteria. Therefore, H.E.S.S. observations, which are discussed in detail in the following section, were triggered in the following nights. It led to the eventual detection of VHE gamma-rays, making RS Oph the first nova detected in that regime. The characteristics and interpretation of this outburst based on the H.E.S.S. and Fermi-LAT data were published in the article "Time-resolved hadronic particle acceleration in the recurrent nova RS Ophiuchi" (H.E.S.S. Collaboration et al., 2022).

To this result I contributed by setting up, carrying out and comparing the CT5 mono analysis (see Section 5.1.2). Furthermore, I selected the validation test sets and carried out the validation and the derivation of the systematics for the CT5 mono analysis (see Section 5.1.3). Therefore, these two sections will be described in detail. The Fermi-LAT and CT1-4 stereo analysis as well as the theoretical modeling and interpretation were done by other members of the task group and will be summarized in Section 5.1.4 and Section 5.2.

Night	T_{obs} (UTC)	Livetime (hours)	ATC	NSB level	Telescopes
Aug. 09, 2021	18:17	3.2	0.90	1.0	CT1-5
Aug. 10, 2021	17:53	3.7 (2.8)	0.80	1.0	CT1-5
Aug. 11, 2021	17:44	3.7	0.65	1.0	CT1-5
Aug. 12, 2021	18:17	2.3	1.00	1.5	CT1-4
Aug. 13, 2021	17:44	2.8	1.10	2.5	CT1-5
Aug. 25 – Sep. 07, 2021	17:48; 19:47	14.6 (13.4)	0.96	1.0	CT1-5

TABLE 5.1: **H.E.S.S. data sets for RS Oph**
T_{obs} denotes the start time of observations for each night. For the live time, the values outside the brackets are for the CT1-4 stereo analysis and the numbers in brackets are for the CT5 mono analysis. The atmospheric transparency is described by the ATC. The NSB noise level is quoted relative to the typical Galactic level for the different telescope types.

5.1 RS Ophiuchi as seen by H.E.S.S. and Fermi-LAT

The first reports by amateur astronomers of a sudden brightening of the known recurrent nova RS Oph, appeared on August 8, 2021, at 22:20 UTC[1]. Until the next morning follow-up alerts by several observatories were issued. Therefore, it became evident that the outburst of RS Oph satisfied all three trigger conditions. It was detected with a significance of $6\,\sigma$ by Fermi-LAT (Cheung et al., 2021), had a measured ejecta velocity of $\gtrsim 2600\,\mathrm{km\,s^{-1}}$ (Taguchi et al., 2021; Munari and Valisa, 2021) and an optical magnitude of $m_V \sim 5.0$. Because of that, H.E.S.S. observations were started on August 9 at 18:17 UTC, less than 20 hours after the initial reports.

5.1.1 Observation campaign

In each of the 5 subsequent nights, several hours of observations were taken. The basic properties of the individual data sets are summarized in Table 5.1. After bright moonlight prevented any further observation after August 13, 2021, an additional 32.9 hours of observations were obtained in the next observation period from August 25 to September 7. Applying a data quality selection on this data set for good atmospheric conditions and zenith angles $\lesssim 35^\circ$, resulted in 14.6 hours of this late phase data to be considered. All observations were by default taken with the full array, but unfortunately, during night 4 no CT5 observations were possible due to a hardware issue.

The early phase data set was taken under varying atmospheric conditions, which is quantified by the Atmospheric Transparency Coefficient (ATC) (Hahn et al., 2014). Especially during nights 2 and 3 a high aerosol content led to poor atmospheric conditions. Hence, this needs to be treated carefully in the H.E.S.S. analysis, which is described in more detail in Section 5.1.3. RS Oph is situated in an average FoV in

[1]The alert was issued by the American Association of Variable Star Observers (AAVSO) and can be found under `https://www.aavso.org/aavso-alert-notice-752`

terms of NSB but during nights 4 and 5 observations were taken under moonlight conditions, increasing the NSB level in these nights up to 2.5 times the galactic dark sky conditions. The analysis of the H.E.S.S. data was done separately with the stereo reconstruction for CT1-4 and the mono reconstruction for CT5.

5.1.2 Mono analysis results

The CT5 mono analysis was carried out following the steps described in Section 3.2 using the HAP software. The reconstruction, gamma-hadron separation and cuts employed were the results of the MC validation effort (Section 4.1) and the subsequently derived safe mono analysis configuration (Section 4.2.1). For the derivation of significance maps the ring background method was used, as introduced in Section 3.2.5.

The mono analysis reveals a significant detection of RS Oph with significances between 6.4 σ and 9.6 σ in each night with data separately (see Table 5.2). The combined map for nights 1-3 and 5 is presented in Figure 5.1a. In this combined map, RS Oph is clearly detected with an overall significance of 17.4 σ at the position of its known optical counterpart. Furthermore, the radial excess distribution in Figure 5.1c shows the point-like nature of the signal matching well with the PSF derived from simulations. The background estimate is well normalized deviating only slightly from an ideal background description (see Figure 5.1b). No clear signal is found in the CT5 mono analysis in the combined late observation phase. This is shown in Figure 5.1a, in which a small $\sim 2\,\sigma$ excess at the position of RS Oph can be seen. However, it peaks at $\sim 0.1^\circ$ angular offset from RS Oph making it likely a background fluctuation.

Spectral properties for the individual nights were derived using the reflected regions background technique (see Section 3.2.5). Different analysis configurations and IRFs were employed to take the varying atmospheric conditions into account. The data taken in nights 1, 5 and in the late phase were acquired under good atmospheric conditions (ATC $\geq$ 0.9). For these datasets, the safe mono configuration and IRFs as described in Section 4.2.1 were applied, as they include a simulated atmosphere and mirror reflectivity matched to good atmospheric conditions. For the analysis of data from nights 2 and 3 taken with poorer atmospheric conditions, the mono configuration and IRFs as derived before the MC validation effort were employed. As described in Section 4.1 (see summary in Table 4.1), these were based on simulations with higher aerosol content and a lower mirror reflectivity. With the trigger rates derived from these simulations, one can calculate an $ATC \approx 0.7$ for the simulation set. This is hence well suited for the analysis of both these nights. The other changes made during the validation concern mostly low amplitude images close to the trigger threshold and can therefore be neglected with the high amplitude cut for the analysis at 250 p.e.

The lower energy threshold for the analysis was defined as the energy at which the effective area reaches 10 % of its maximum value. For nights 1 and 5, this value is

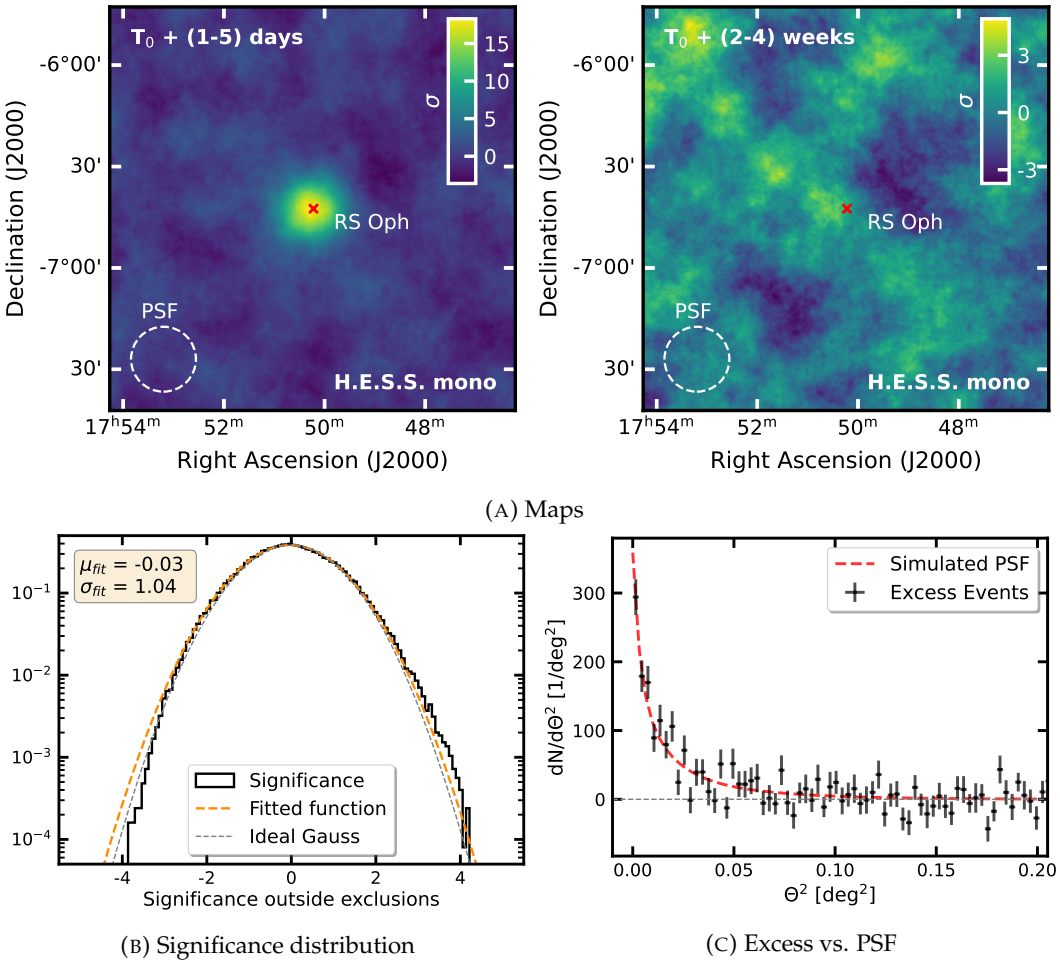

(A) Maps

(B) Significance distribution

(C) Excess vs. PSF

FIGURE 5.1: **RS Oph CT5 mono significance maps**
In **A** the significance maps derived from the H.E.S.S. mono analysis of the first 5 nights and the late phase of observations up to 4 weeks after the outburst are presented with correlation radii of 0.13°. The size of the PSF is indicated by the white dashed circle. In **B** the resulting histogram of significance values outside of the exclusion mask is drawn together with a fitted Gaussian. The Gaussian is close to an ideal background description with a width of 1. **C** compares the radial excess distribution centered at RS Oph with the PSF derived from simulations. The PSF is described by Equation 4.2.

Data set	Sign. $[\sigma]$	ϕ_0 [10^{-11} TeV^{-1} cm^{-2} s^{-1}]	E_0 [TeV]	Index Γ
Aug. 09	6.4	$14.9 \pm (2.7) \pm (3.0)$	0.18	$3.22 \pm (0.38) \pm (0.20)$
Aug. 10	7.1	$25.2 \pm (4.7) \pm (5.0)$	0.18	$4.01 \pm (0.48) \pm (0.20)$
Aug. 11	9.6	$28.5 \pm (3.3) \pm (5.7)$	0.18	$3.15 \pm (0.23) \pm (0.20)$
Aug. 13	9.4	$23.3 \pm (3.3) \pm (4.7)$	0.18	$3.77 \pm (0.32) \pm (0.20)$
Aug. 25 - Sep. 07	2.3	6.3 (upper limit)	0.18	3.5 (fixed)

TABLE 5.2: **Nightly mono significance and spectral parameters of RS Oph**
The results from the monoscopic analysis are shown. The quoted detection significances are derived with the ring background method. The best-fitting nightly spectral parameters from the H.E.S.S. reflected regions analysis are assuming a power-law model (Equation 3.17). For comparison purposes, the flux normalization ϕ_0 in this table is derived at the same reference energy E_0. The shown uncertainties are always first the statistical and then the systematic uncertainties. The derived systematic uncertainties are discussed in the text (Section 5.1.3). For the late phase data set no spectral result was calculated but only a differential upper limit was derived, which is quoted here.

100 GeV. Due to the different IRFs used, the corresponding value for nights 2 and 3 is slightly higher, at 110 GeV. The spectral fits were made for each night individually assuming a power-law spectral model as defined in Equation 3.17. The results of the spectral fits are summarized in Table 5.2. The best-fit values of the spectral indices are all, within statistical and systematic errors, consistent with a value of 3.5. These values are also in agreement with those derived in the stereo analysis (see Table 5.3). The flux, quoted at an energy of 180 GeV, increased until night 3 and then decreased again towards night 5. As it is shown in Figure 5.2 the spectral results agree within uncertainties with those derived in the stereo analysis. The mono analysis has a reduced energy threshold, probing a different energy range than the stereo datasets. Through the combination of both, a wider range of the source spectra is studied, highlighting the synergy between the mono and stereo analysis approaches.

For the late phase only a flux upper limit was obtained. Assuming a spectral index of 3.5 for the full safe energy range a differential upper limit at 95 % confidence level was derived, for which the normalization value at 0.18 TeV is also quoted in Table 5.2. Integrating between 250 GeV and 2.5 TeV for a comparison with the stereo results yielded a flux upper limit of $F_{UL,mono}(E > 250\,\mathrm{GeV}) = 1.3 \times 10^{-12}\,\mathrm{erg\,cm^{-2}\,s^{-1}}$ consistent with the derived stereo flux as presented in Table 5.3 and Figure 5.7.

Using an integration interval between 0.11 TeV and 1.1 TeV, better suited to the mono results, one can compute energy flux measurements for each night. These are summarized as a light curve relative to T_0 = Modified Julian Days (MJD) 59435.25, which is the time of peak optical emission (Kafka, 2021). This is presented in Figure 5.3, where it is compared to the decay fit that was obtained on the H.E.S.S. stereo light curve (see Section 5.1.4). Both the comparison with the fitted decay slope and

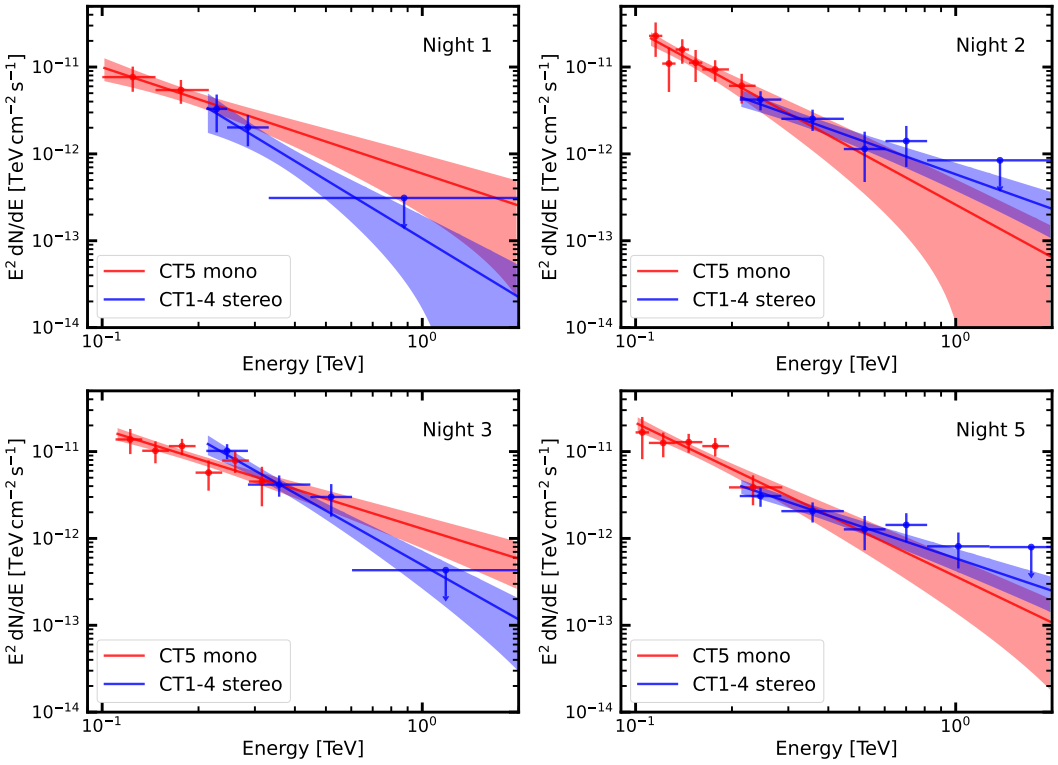

FIGURE 5.2: **Night-wise mono & stereo spectra for RS Oph**
The CT5 mono spectra and flux points have been derived with the choice of IRF as discussed in the text. For comparison, the derived CT1-4 stereo spectra after applying the atmospheric correction and flux points are shown. Upper limits are only shown for the stereo spectra. For night 4, CT5 was not active and hence the SED is not shown. The best-fit spectral parameters can be found in Table 5.2.

the actual stereo light curve above 250 GeV (Figure 5.7) show a matching flux evolution. The emission peaks on night three in both cases and the flux decays afterward consistent with the derived upper limit for the late observation phase.

5.1.3 Validation and systematics of H.E.S.S. mono results

To validate the spectral results with the two different sets of IRFs, three sets of Crab Nebula runs with different atmospheric conditions were defined. Each set consisted of 1.5 h to 2 h of observations with default wobble offset (see Section 3.1.3). All runs were taken within a few months in the year prior to the RS Oph campaign. The first data set had ATC values of $\sim 0.6 - 0.65$, the second data set an average of ~ 0.78 and the third one ≥ 0.9. Hence, the first set is a well-suited test set for night 3 of the RS Oph observations, the second for night 2 and the third one for the other nights. The spectral properties were derived for each of the test data sets using the same method as for the RS Oph analysis. This means that for the first two Crab data sets the IRFs used for nights 2 and 3 were employed and for the third one, the IRFs used for the other nights. The spectral parameters were derived using a power-law spectral model and are presented in Figure 5.4. The results show good agreement with the

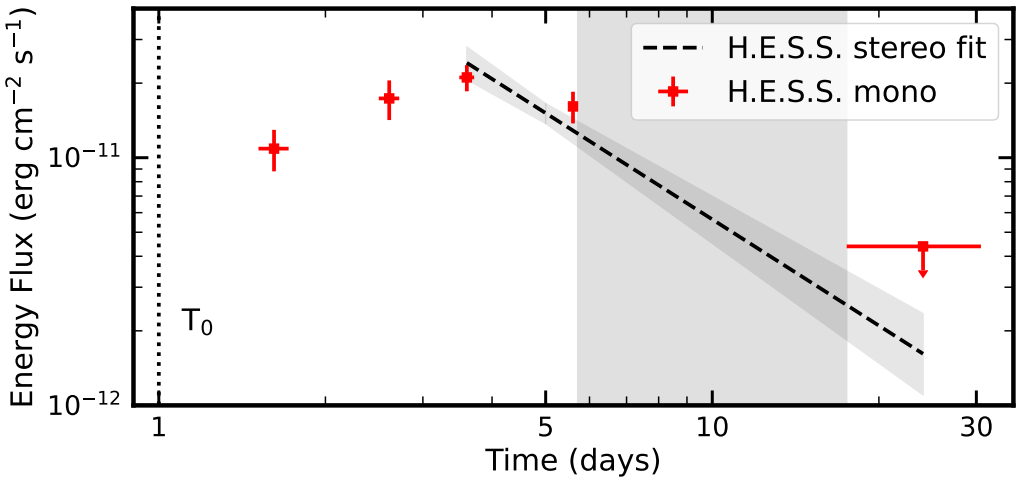

FIGURE 5.3: **Light curve of the mono analysis of RS Oph**
The CT5 mono flux was integrated between 0.11 TeV and 1.1 TeV. For comparison, the derived power-law decay for the CT1-4 stereo flux has been rescaled to the mono flux level and added. More details on this can be found in Figure 5.7 and Section 5.1.4. The observation break due to bright moonlight is indicated by the shaded grey band and T_0 by the dashed black line.

H.E.S.S. Crab reference spectrum from H.E.S.S. Collaboration et al. (2006b). Deviations in the flux normalization are below 15 % for all atmospheric conditions. The spectral indices show a systematic shift by $\sim$0.15 that can be explained by the observed deviation from a power-law description of the Crab spectrum towards lower energies and is also consistent with the derived mono spectrum of the Crab Nebula in Section 4.2.2.

There are several factors that contribute to the total systematic uncertainties in the mono analysis. Systematic uncertainties originating from the MC hadronic interaction models and the live time of the data set have an impact of $\sim$1 % on the flux normalization. The number of broken pixels for CT5 in the RS Oph runs is $\lesssim$ 1 % and therefore the effect of broken pixels contributes $\leq$ 5 % to the systematic uncertainty of the flux normalization (H.E.S.S. Collaboration et al., 2006b; H.E.S.S. Collaboration et al., 2017). To account for the different choices of IRFs and the potential remaining mismatch between simulation and observing conditions, a systematic uncertainty of up to 15 % on the flux normalization was derived. This is based on the remaining deviation of the reconstructed mono Crab flux from the reference flux. For the spectral index similarly a systematic uncertainty of 0.15 was estimated. To approximate the systematic uncertainty based on an imperfect background normalization, the background normalization α was varied following the method described in H.E.S.S. Collaboration et al. (2006a). It was varied by $\pm$5 % and the spectral fit was rerun afterward. This is a rather conservative estimate as the actual background normalization level is well described over the whole FoV(see Figure 5.1b). As a result, the systematic contribution from the background description was estimated to be

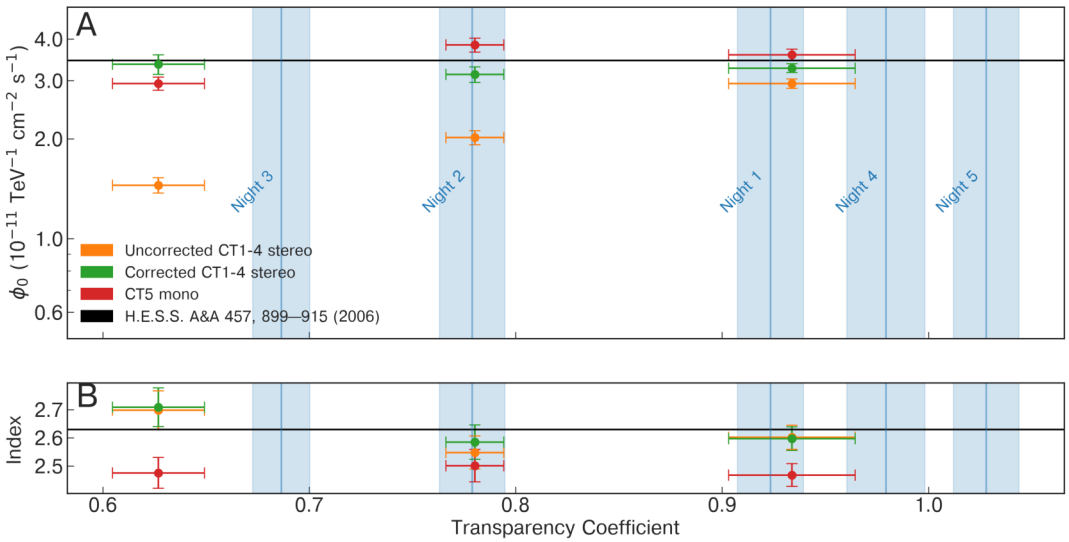

FIGURE 5.4: **Atmospheric transparency correction and validation of results with Crab Nebula observations**
The Crab Nebula observations were grouped into 3 data sets depending on their atmospheric transparency conditions quantified by the ATC. The CT5 mono analyses were derived employing different sets of IRFs matching the actual observing conditions, whereas the CT1-4 stereo results were afterward corrected for the effect of differing atmospheric transparency. The top panel illustrates the resulting normalization ϕ_0 of the reconstructed flux at an energy of 1 TeV assuming a power-law spectral model and the bottom panel shows the reconstructed index Γ. As a reference, the spectral fit from H.E.S.S. Collaboration et al. (2006b) is added. Vertical blue lines indicate the atmospheric transparency conditions during the RS Oph observations. Taken from H.E.S.S. Collaboration et al. (2022).

15 % on the flux and 0.15 on the spectral index. The total estimate for the systematic errors in the mono analysis is thus 20 % on the flux normalization and 0.2 on the spectral index. These systematic errors are also shown in Table 5.2. The overall energy scale uncertainty of H.E.S.S. observations can be assumed to be ∼15 % based on multi-instrument studies of the Crab Nebula (Nigro et al., 2019).

The effect of bright moonlight on the mono analysis and the uncertainties introduced by applying reconstruction algorithms and IRFs based on simulations with the default trigger settings to observations with moonlight trigger settings (for details see Bi et al., 2022) did not yield a firm conclusion by the time of writing. Hence the mono flux points derived in night 5 were not used for the fit of the combined Fermi-LAT and H.E.S.S. spectra and the theoretical modeling as discussed in the next chapter. Nevertheless, as the mono spectral results represent a well-matching continuation of the stereo spectrum towards lower energies in night 5, no significant change on the results would be expected.

Data set	Sign. $[\sigma]$	ϕ_0 $[10^{-11}$ TeV^{-1} cm^{-2} s$^{-1}]$	E_0 [TeV]	Index Γ
Aug. 09	5.8	$0.91 \pm (0.28) \pm (0.14)$	0.35	$4.24 \pm (0.75) \pm (0.15)$
Aug. 10	9.0	$1.90 \pm (0.32) \pm (0.38)$	0.35	$3.32 \pm (0.30) \pm (0.15)$
Aug. 11	9.8	$3.57 \pm (0.54) \pm (0.54)$	0.35	$4.08 \pm (0.42) \pm (0.20)$
Aug. 12	13.6	$3.00 \pm (0.33) \pm (0.45)$	0.35	$3.27 \pm (0.21) \pm (0.15)$
Aug. 13	10.5	$1.77 \pm (0.25) \pm (0.35)$	0.35	$3.24 \pm (0.24) \pm (0.15)$
Aug. 25- Sep. 07	3.3	$0.24 \pm (0.08) \pm (0.04)$	0.35	$3.33 \pm (0.45) \pm (0.15)$

TABLE 5.3: **Nightly stereo significance and spectral parameters of RS Oph**
The stereoscopic results are shown. The quoted detection significances are derived with the ring background method. The best-fitting nightly spectral parameters from the H.E.S.S. likelihood-based "3D" analysis are assuming a power-law model of the form Equation 3.17 and have been corrected for different atmospheric conditions. The shown uncertainties are always first the statistical and then the systematical uncertainties. The correction scheme and systematic uncertainties (Section 5.1.3) are discussed in the text.

5.1.4 Summary of stereo and combined results

The stereo analysis was run with the ImPACT reconstruction and using the likelihood-based fitting to derive the spectral properties. Similarly to the mono analysis, RS Oph was detected with high significance in each of the first 5 nights as summarized in Table 5.3. The combined data exhibits a $\sim 20\,\sigma$ point-like signal from the position of RS Oph. For the late phase, a weaker $3.3\,\sigma$ signal consistent with the position of RS Oph is found. The two maps for the early and late phases are shown in Figure 5.5. The spectral results in Table 5.3 show a spectral index > 3 for all nights consistent with the mono spectra. The spectral results were corrected for the varying atmospheric conditions by scaling the energy scale of the energy migration matrix and the effective areas taking the measured ATC into account. This correction was also validated on the same Crab Nebula data sets, which is presented as well in Figure 5.4. The systematics have been derived following a similar approach to H.E.S.S. Collaboration et al. (2006b) and further taking into account the remaining differences in the Crab Nebula spectra.

To derive a multiwavelength spectrum, simultaneous data between 60 MeV and 500 GeV from Fermi-LAT were analyzed. More details are discussed in H.E.S.S. Collaboration et al. (2022). From this, combined fits to the Fermi-LAT, H.E.S.S. mono and stereo flux points, ranging over several orders of magnitude in energy, could be obtained. These are derived with log-parabola models that are presented for each night in Table 5.4. The best-fit models show good consistency with the flux points. As it is also evident in Figure 5.6, there exists a general trend that the flux normalization decreases and the parabola widens over time. This is also accompanied by an increase in the maximum energy visible in the VHE spectrum. The smooth spectral behavior over the whole energy range indicates a common origin of the gamma-rays.

Data set	ϕ_0 [10^{-4} TeV^{-1} cm^{-2} s^{-1}]	E_0 [GeV]	α	β
Aug. 09	7.06 ± 0.58	1.0	1.98 ± 0.04	0.19 ± 0.01
Aug. 10	4.27 ± 0.43	1.0	2.12 ± 0.05	0.13 ± 0.01
Aug. 11	3.69 ± 0.42	1.0	2.01 ± 0.06	0.13 ± 0.01
Aug. 12	1.79 ± 0.32	1.0	2.02 ± 0.09	0.11 ± 0.02
Aug. 13	1.94 ± 0.32	1.0	2.05 ± 0.07	0.12 ± 0.02

TABLE 5.4: **Combined Fermi-LAT and H.E.S.S. log-parabola fits for RS Oph**
The spectral parameters are derived from a joint fit of the Fermi-LAT and H.E.S.S. mono and stereo flux points with a log-parabola model (see Equation 3.19).

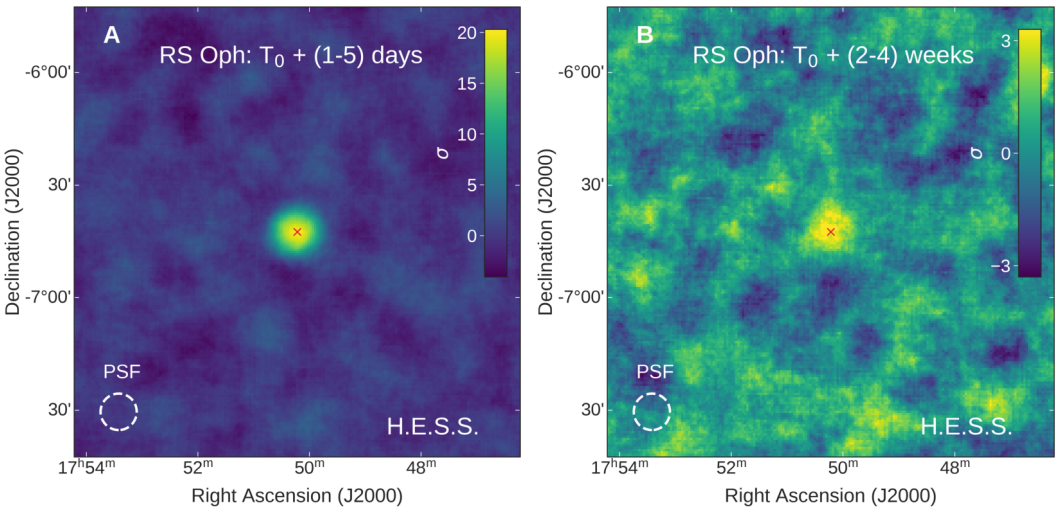

FIGURE 5.5: **RS Oph stereo significance maps**
Significance maps derived from the H.E.S.S. stereo analysis of the first 5 nights and the late phase of observations. The size of the PSF is indicated by the white dashed circle. Taken from H.E.S.S. Collaboration et al. (2022).

The time evolution of both the Fermi-LAT flux integrated between 60 MeV and 500 GeV and the H.E.S.S. flux integrated between 250 GeV and 2.5 TeV are shown in Figure 5.7. Similarly to the H.E.S.S. mono light curve, the H.E.S.S. stereo gamma-ray flux rises smoothly from T_0 until a peak is reached on the third night. Afterward, the VHE gamma-ray flux decays and is an order of magnitude smaller in the late phase observations about 2 weeks later. The Fermi-LAT flux also shows a similar behavior but peaks already at $T_0 + 1$ day, 2 days prior to the H.E.S.S. peak. A power-law of the form $t^{-\alpha}$ was employed to fit the decay after the peak. Choosing T_0 = 1 day, the best-fitting values are $\alpha_{LAT} = 1.31 \pm 0.07$ and $\alpha_{HESS} = 1.43 \pm 0.18$ for Fermi-LAT and H.E.S.S. respectively. These values are consistent with each other within the statistical uncertainties. This similar behavior of the light curve strengthens the point that indeed the whole HE to VHE emission is stemming from a common origin.

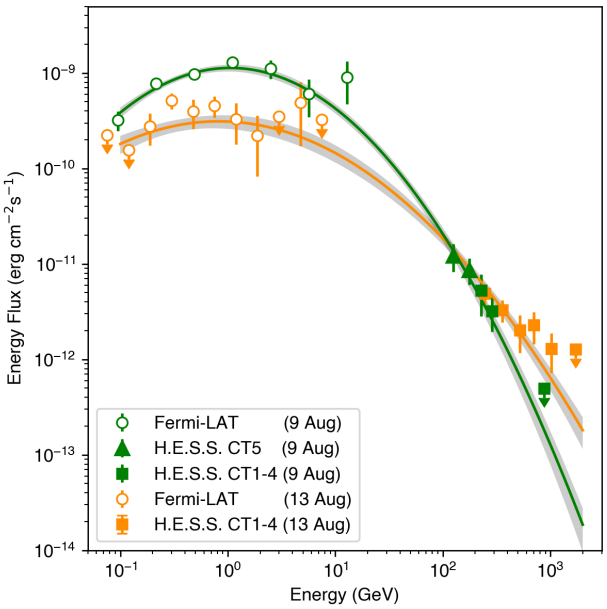

FIGURE 5.6: **RS Oph combined H.E.S.S. and Fermi-LAT spectra** The H.E.S.S. mono and stereo and Fermi-LAT spectra for night 1 (green) and night 5 (orange) were fitted jointly with a log-parabola model. For night 5 the mono flux points were not taken into account due to larger uncertainties connected with bright moonlight. The Fermi-LAT spectral points are derived over 24 h time bins centered at the H.E.S.S. observation times. Taken from H.E.S.S. Collaboration et al. (2022).

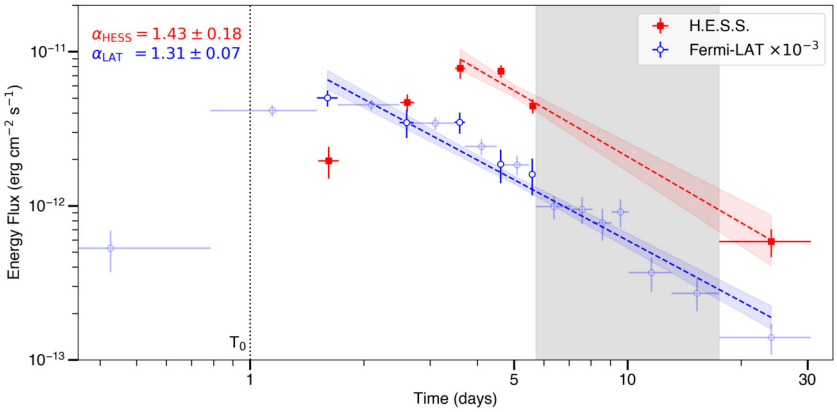

FIGURE 5.7: **H.E.S.S. and Fermi-LAT light curves of RS Oph** The light curves for RS Oph are on data from Fermi-LAT and H.E.S.S. observations. The H.E.S.S. data are based on the stereo reconstruction results and cover a period of five nights. Afterward, observations paused for ten days due to bright moonlight, which is indicated by the shaded grey band. Later, they continued for another 14 days. Fermi-LAT data was binned in 6-hour intervals (blue circles) simultaneous to the H.E.S.S. observations. The data outside of these times is presented with transparent markers. The results of fitting a power-law slope model to the temporal decay after the time of peak flux are shown for both instruments. T_0 (black dashed line) marks the peak of the outburst in the optical waveband. Taken from H.E.S.S. Collaboration et al. (2022).

5.2 Summary of theoretical modeling & interpretation

The basic underlying idea as introduced in Section 2.4.3 and schematically drawn in Figure 2.15 is that particles are accelerated at the external shock as it propagates into the wind of the red giant and subsequently generate the observed gamma-rays. Shock velocities retrieved from optical spectroscopic measurements of the 2021 eruption are in the range $u_{\rm sh} = 4000 - 5000$ km s^{-1} (Mikolajewska et al., 2021). The previous 2006 outburst exhibited an hourglass shape (O'Brien et al., 2006; Bode et al., 2007) also drawn in Figure 2.15. Whereas the pinching can be explained by the denser gas close to the orbital plane, orthogonal to it, the assumed shock expands unhindered into the wind of the red giant (Booth et al., 2016; Walder et al., 2008). This showed compatible shock velocities (Bode et al., 2006; Sokoloski et al., 2006; Bode et al., 2007) to the 2021 outburst lasting over the first 5 months in the polar regions. Hence, it can be assumed that during the early phase of the 2021 nova, the shock velocity was at least several thousand kilometers per second.

At these high-velocity shocks, particles can experience diffusive shock acceleration. For this, two scenarios as introduced in more detail in Section 2.2, need to be considered, on the one hand, a hadronic origin producing gamma-rays via π^0-decay and on the other hand, a leptonic origin producing gamma-rays via inverse Compton processes.

The predictions for the spectrum and time-dependent behavior of these two scenarios are derived using a 1D hydrodynamical model describing the motion of the ejecta and the dynamics of the forward shock. The environment is adapted to the actual time-dependent conditions, e.g. a decreasing upstream density is included. Within this description electrons and protons are induced in a single zone. More details on the model and its parameters can be found in H.E.S.S. Collaboration et al. (2022). The result is then compared to the data and used to discern between the two cases.

To produce gamma-rays with energies up to 1 TeV as observed with H.E.S.S., the accelerated particles need to reach even higher energies. Following Bell et al. (2013) the confinement limit on the maximum energy for a charged particle (with atomic number Z) and assuming a wind-like density profile, while neglecting radiative losses, is

$$E_{\rm max} = 1.5|Z| \left(\frac{\xi_{\rm esc}}{0.01}\right) \left(\frac{\dot{M}/v_{\rm wind}}{10^{11}\ {\rm kg\ m^{-1}}}\right)^{1/2} \left(\frac{u_{\rm sh}}{5000\ {\rm km\ s^{-1}}}\right)^2 {\rm TeV}\ , \qquad (5.1)$$

with $\dot{M}$ and $v_{\rm wind}$ the mass-loss rate and the wind velocity of the red giant, respectively. The efficiency parameter $\xi_{\rm esc}$ describing the fraction of energy density flux processed by the shock and lost to the upstream escaping energetic particles is predicted to be about 1 % for high Mach-number shocks (Bell et al., 2013). Particularly, for RS Oph $\dot{M}/v_{\rm wind} = 6 \times 10^{11}$ kg m^{-1} (O'Brien et al., 2006) and the shock velocity as already described above can be adopted. This results in a maximum energy

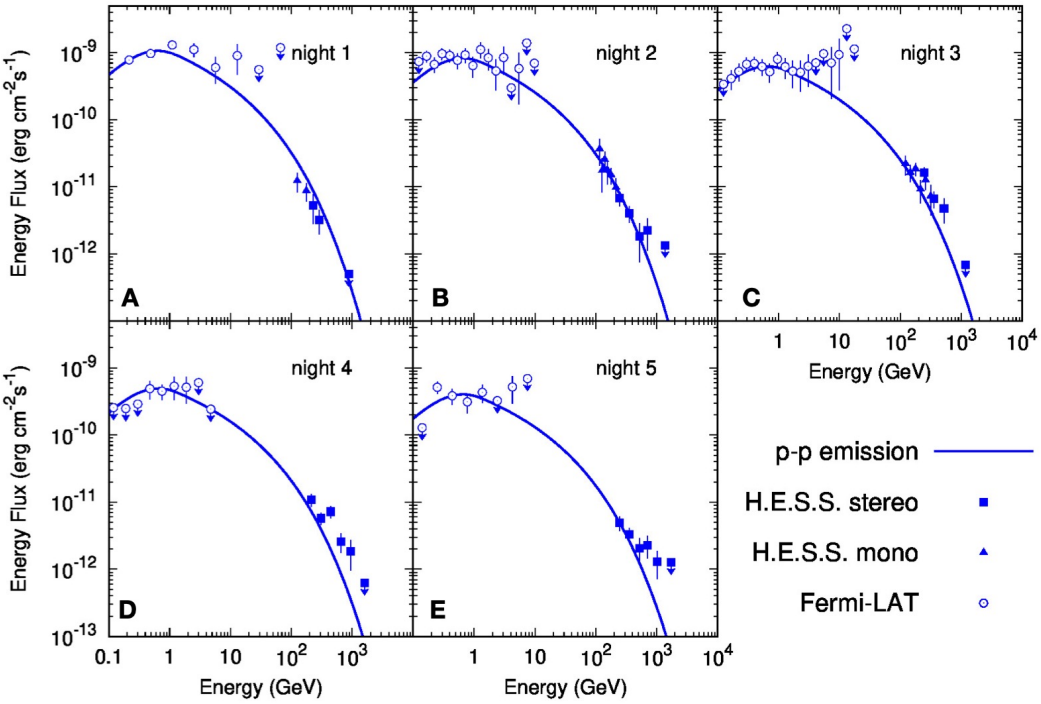

FIGURE 5.8: **Night-wise combined SEDs compared to a hadronic model**
For each night the Fermi-LAT and H.E.S.S. flux points are shown together with the modeled gamma-ray emission. The model is based on injected protons with an index of 2.2 into a time-dependent model. Taken from H.E.S.S. Collaboration et al. (2022), where also the exact model parameters can be found.

$E_{\mathrm{max}} \approx 10$ TeV compatible with the measured maximum gamma-ray energies.

In the hadronic scenario, this confinement limit is the dominating constraint for the acceleration of protons. Applying the single-zone model and matching it to the data requires that $> 10\,\%$ of the internal energy of the shocked gas is transferred to the acceleration of protons. The 2-day delay between the peaks in the Fermi-LAT and H.E.S.S. light curve is then caused by the finite acceleration time, that is needed to accelerate protons to energies > 1 TeV and fill this high energy part of the proton distribution. The hadronic model is also able to self-consistently reproduce the spectral evolution between night 1 and 5 shown in Figure 5.8.

In the leptonic scenario, the acceleration needs to overcome the strong radiative losses caused by inverse Compton and synchrotron cooling. This requires the acceleration of electrons close to the maximum acceleration rate, set by Bohm diffusion. But this would, in turn, also suggest the existence of an energetic hadronic component. The difference in the Fermi-LAT and H.E.S.S. spectral slopes could in this scenario be explained by energy-dependent cooling rates. The delay in the light curve would be caused by the changing photon target field in the Fermi-LAT regime and the full radiative emission of the fast cooling high-energy electrons in the H.E.S.S. regime. After the peak, all electrons would start to be slowly cooling due to the decreased photon energy density. To match the observed gamma-ray fluxes for the

leptonic scenario efficiencies $> 1\,\%$ are needed, which is significantly higher than theories of injection at high-Mach number shocks predict (Malkov and Drury, 2001). Hence the hadronic scenario is favored, which is in line with the acceleration efficiencies and maximum energy predictions from theory and can also naturally match and trace the observed time-dependent signal. This is further in line with former models of gamma-ray emission in novae (Metzger et al., 2016; Li et al., 2017; Aydi et al., 2020).

The contribution to the cosmic ray sea of RS Oph can be approximated by taking into account the total kinetic energy from each outburst of RS Oph of $\sim 10^{43}$ erg, which is to large parts converted to relativistic protons. Even though the repeated outbursts of RS Oph could be the source of a local cosmic ray enhancement depending on the assumed diffusion coefficient, the contribution of novae is sub-dominant to the average Galactic cosmic ray population. Furthermore, the fact that nova explosions reach maximum energies and acceleration efficiencies close to their theoretical limit, can have important implications for supernovae. If extrapolated to supernova conditions with denser winds and faster shocks, this could explain the origin of PeV cosmic rays stemming from within our galaxy.

5.3 Summary and conclusion

RS Oph is the first nova detected in the VHE regime and became the first member of a new class of TeV transients. Due to the strong observed signal H.E.S.S. could detect it, both, in its CT5 mono and CT1-4 stereo analysis on each of the first nights individually. This allowed for a time-resolved tracking of the outburst. The CT5 mono analysis was based on the previous successful validation and verification efforts and was hence the first published result with the FlashCam camera installed on CT5. It extended the VHE signal to lower energies > 100 GeV, showing a good connection to the simultaneous Fermi-LAT data. The combined HE and VHE spectrum exhibits a smooth spectral behavior over several orders of magnitude. The signal shows a clear variability over time with both the H.E.S.S. mono and stereo flux increasing until night 3 and decaying afterward. Whereas the peak of emission happens for the Fermi-LAT light curve 2 days earlier, the decay profile is consistent with the H.E.S.S. results. These findings imply a common origin of the HE and VHE emission and the delay reflects the expected finite acceleration time.

Time-dependent modeling of the combined Fermi-LAT and H.E.S.S. data favored a hadronic origin of the gamma-ray emission. This demands efficient cosmic ray acceleration to occur at the fast shock driven by the thermonuclear explosion as it propagates into the dense wind of the red giant companion. The maximum photon energy of ~ 1 TeV closely matches theoretical limits for such systems. This has important implications for supernova explosions, strongly supporting the hypothesis, that the primary component of galactic cosmic rays originates in core-collapse supernova remnants.

Naturally, the outburst of RS Oph was observed by a variety of other instruments. Observations by MAGIC showed a consistent spectral behavior but no clear time variability over its first 4 days (Acciari et al., 2022). The lack of time variability could be explained by the missing data on night 5 and a different integration range for the light curve. Furthermore, for the late phase, no signal but only an upper limit was derived which clearly shows a similar flux decay. Both, Acciari et al. (2022) and Cheung et al. (2022) favor a hadronic origin of the emission similar to the H.E.S.S. findings, strengthening the evidence provided by previous models of hadronic gamma-ray emission in novae.

RS Oph was the brightest detected Fermi-LAT nova up to date, making it a unique event so far. Nevertheless, it remains an open question if VHE emission of novae is limited to recurrent symbiotic novae or can also be detected in classical novae, which are known emitters in the HE regime (Chomiuk et al., 2021). Especially the improvement in sensitivity provided by the future CTA should result in a larger collection of potentially detectable novae and help in better understanding the gamma-ray emission from different kinds of novae.

Chapter 6

Gamma-ray emission from Eta Carinae

Situated in the Carina Nebula Complex (CNC), the enigmatic binary system Eta Carinae has been studied in detail in several wavebands over periods up to several centuries. This chapter will focus on the recent gamma-ray observation campaigns and the subsequent analysis of η Car, which properties and multiwavelength observational history are described in Section 2.3. η Car has been identified as a source of HE (Abdo et al., 2010) and VHE (H.E.S.S. Collaboration et al., 2020) emission by Fermi-LAT and H.E.S.S., respectively only in recent years. The system can be tracked with current instruments over its full 5.5-year orbit. The periastron passage, at which the stars are separated only on $\sim$1 au scales, has shown strong variability in other wavelengths (see Section 2.3.3) and is hence of special importance.

The 2009, 2014 and the recent 2020 periastron passages were already followed by Fermi-LAT and have been discussed in several works (see e.g. Reitberger et al., 2012; Reitberger et al., 2015; Balbo and Walter, 2017; White et al., 2020; Martí-Devesa and Reimer, 2021). H.E.S.S. observed the 2009 periastron passage with only limited exposure yielding no detection (H.E.S.S. Collaboration et al., 2012). Unfortunately, the 2014 periastron passage happened outside the visibility season for H.E.S.S. allowing only for observations at phases 0.96 and 1.09 for which nevertheless a significant VHE gamma-ray signal from η Car was reported (H.E.S.S. Collaboration et al., 2020). The 2020 periastron was the first periastron passage visible for H.E.S.S. in its final 5-telescope array state. Thus, a dedicated and in-depth observation campaign was planned and carried out.

In this chapter, I will report on the outline of the H.E.S.S. observation campaign in the years 2020 and 2021. Additionally, I will discuss the caveats and difficulties of an IACT observation and analysis in this special FoV with extreme NSB conditions. Subsequently, the thorough analysis and checks of the H.E.S.S. data with both monoscopic and stereoscopic reconstruction are presented. Together with unpublished data from previous years the first light curve spanning a full orbit of η Car in the VHE regime is provided. Special emphasis is laid on the data set taken around the periastron passage, which is combined with an analysis of contemporaneous HE data from the Fermi-LAT to build a multiwavelength SED.

I have planned, proposed and followed closely the 2020 and 2021 H.E.S.S. campaigns as the principal investigator and checked the data quality as described in Section 6.1. The data-taking settings were derived primarily by Felix Werner and the H.E.S.S. 1U camera team. I have carried out all steps in the derivation of the analysis configuration (Section 6.2). The technical implementation of the emulation scheme described in Section 6.2.3 was mostly done by Vincent Marandon. I have afterward performed all steps in the H.E.S.S. mono and stereo analysis (Section 6.2 and Section 6.3). Further, I have carried out the Fermi-LAT analysis described in Section 6.4 and combined and interpreted the results in Section 6.5 using model curves provided by Mischa Breuhaus.

6.1 Observation campaign

The observation strategy for IACT observations of η Car has to be selected carefully due to the unique field of view. As discussed in more detail in Section 2.3, η Car lies at the heart of the CNC. The CNC is described in optical wavelengths as a region of large-scale diffuse emission. It's total apparent visual brightness is around 1 mag stretched over an area of about 2° diameter on the sky[1]. Even though this bright region is spread over many pixels for the H.E.S.S. cameras, it still represents quite extraordinary levels of NSB. Furthermore, several bright stars with brightness $m_V < 5$ mag exist in and around the CNC illuminating single pixels. For IACTs, the NSB will lead to noise-only triggers without any actual air shower. Usually, the trigger settings are set to avoid frequent noise triggers but with increasing sky brightness the so-called NSB-wall is hit. This means, that the number of accidental triggers will increase drastically and dominate the trigger rate, especially if several adjacent pixels are influenced. This will cause fake events and also dead time, both harmful for further analysis. Individual illuminated pixels can also suffer from high currents from the large p.e. rate, potentially damaging the PMTs. Hence it is of crucial importance to adapt the trigger settings to this special FoV, as otherwise no stable, trustable and safe data-taking would be possible.

To estimate the NSB rates and patterns for the new FlashCam camera a small study was performed. Firstly, the NSB rate from previous observations (H.E.S.S. Collaboration et al., 2020) with the predecessor camera already projected into sky coordinates was taken. This is a good first estimate but difficult to directly scale to the new camera as up to $\sim$10 % of the pixels were switched off during data acquisition due to bright sky regions. Hence in these pixels no measurement of the NSB was obtained. To better constrain the sky brightness in the blue waveband, where the PMTs are the most sensitive, the DSS2-blue[2] survey at 395 nm to 540 nm for the CNC region was considered. With these two maps, a conversion factor from

[1] More on the optical characteristics of the Carina Nebula (NGC 3372) can be found at e.g. `http://www.messier.seds.org/xtra/ngc/n3372.html` .

[2] More details can be found on `https://archive.eso.org/dss/dss`

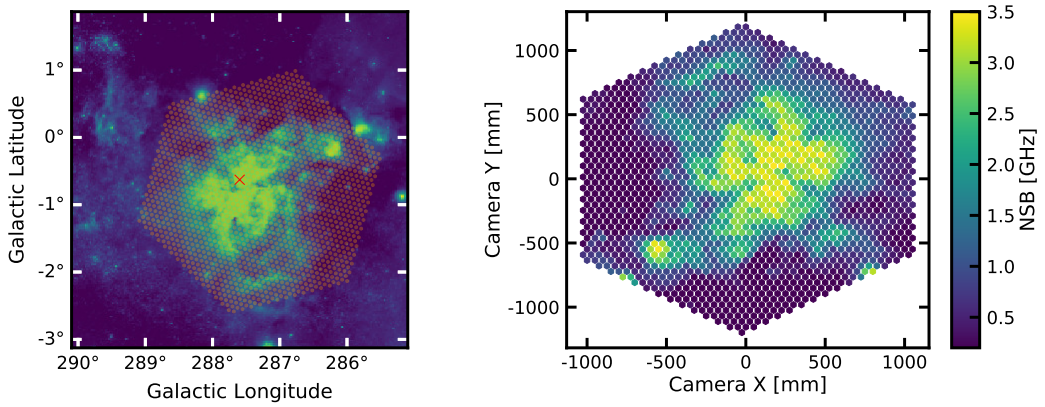

FIGURE 6.1: **Estimation of NSB rate for η Car observations with FlashCam**
On the left, the CNC region is depicted in the blue waveband as imaged by the DSS2-Blue survey. Overlaid are the pixels of the FlashCam camera with pointing and time equal to the start of the H.E.S.S. observation run 158426. This run had a wobble offset of $-0.7°$ in right ascension. The red cross denotes the position of η Car. On the right, the estimated NSB value for each pixel of the camera is shown.

the DSS2 intensity to the measured previous NSB rate was calculated. For a specific observation time and pointing, FlashCam, as mounted in CT5, was projected onto the sky and the FlashCam NSB rate in each pixel was estimated. The estimate was derived from the DSS2 intensity applying the calculated conversion factor and the scaling in NSB sensitivity from the old to the FlashCam camera. The scaling factor included the different pixel sizes and quantum efficiencies. The derived estimate per pixel can be seen in Figure 6.1. Here, the camera pointing and observation time is selected to match the beginning of observation run 158426, which will be further used for reference low-level studies in this chapter. It becomes clear that a large fraction of the camera has to deal with large NSB rates many times the galactic average of $\sim$0.25 GHz. Furthermore, individual pixels might be affected by rates of several GHz, forcing the camera server to switch them off.

To keep the number of switched-off pixels as small as possible for FlashCam a reduced gain setting of 4.6 LSB/p.e. is used, the same as for observation runs under bright moonlight. This tolerates NSB values of up to $\sim$6 GHz in a single pixel before it is switched off. Switched-off pixels will repeatedly be tested to be switched on again because e.g. bright stars will appear in different pixels over time as the telescopes are slewing. The NSB limit at which a pixel is excluded from the trigger is raised to 2.7 GHz. Pointing on the CNC region, a trigger rate scan was obtained. This resulted in an increased trigger threshold of 91 p.e. for a 9-pixel sum to allow stable trigger rates. For CT1-4 the trigger threshold was increased to 6.5 p.e. after a trigger rate scan but the default gain was kept. The final settings are described in Table 6.1 and compared to the default values for nominal observations.

These settings allow stable data taking with only a minor impact on the sensitivity. The measured NSB values show reasonable consistency with the estimated

Parameter	Gain	Trigger thresh.	NSB limit Trigger	NSB limit Switch Off
CT5 - default	9.3 LSB/p.e.	69 p.e.	1.1 GHz	∼3 GHz
CT5 - η Car	4.6 LSB/p.e.	91 p.e.	2.7 GHz	∼6 GHz
CT1-4 - default	60/80 ADC/p.e.	5.5 p.e.	/	∼1.5 GHz
CT1-4 - η Car	60/80 ADC/p.e.	6.5 p.e.	/	∼1.5 GHz

TABLE 6.1: **Observation settings for η Car runs**
Both the default and the η Car specific settings are shown. The η Car settings are sometimes also referred to as bright-source region settings (Bi et al., 2022) as they should in principle be valid for other bright source regions as well. The CT1-4 gain was kept at its default value, which was 80 ADC/p.e. until June 2020 and 60 ADC/p.e. afterward. No NSB limit for the trigger exists for CT1-4 as they are directly switched off in case of high NSB .

features and overall scale derived in Figure 6.1, as it is shown for the example run in Figure 6.2. However, the diffuse bright CNC region is less pronounced, whereas individual bright stars have a stronger effect. The median NSB level over the FoV is, averaged over the full run, 0.19 GHz and 0.66 GHz for CT1 and CT5, respectively, which is a factor 2 or more compared with typical average galactic conditions (0.10 GHz for CT1 and 0.25 GHz for CT5). As expected from the irregular features within the FoV, the distribution of NSB values is highly inhomogeneous with a prominent tail towards high NSB values. Individual pixel-wise values will indeed reach up to the pixel switch-off point.

Consequently, this means that about 10-15 and 30-40 pixels are switched off for CT1-4 and CT5, respectively. While a few pixels are not active or switched for every run, e.g. the 3 structure pixels in FlashCam, typical broken pixel numbers for other targets are < 5 for CT1-4 and ∼10 for CT5. Hence the number of broken pixels is increased but still < 3 % of all pixels, shown for the example run in Figure 6.3, where also the clear connection of switched-off pixels with high NSB can be noticed. For CT5, 30 additional pixels are excluded from the trigger but still record data. Using these settings and the increased trigger thresholds, the trigger rate is evaluated as its shown in Figure 6.4. The rate is stable over the course of one run for the CT5 mono, the CT1-4 stereo and the system rate. Also, the mean rate is similar for all runs with the usual dependence on the zenith angle. The variability of the trigger rate described by the RMS is also within the expected range slightly above Poisson fluctuations.

η Car is visible for H.E.S.S. during the winter and spring months starting from December until the beginning of June. The minimum zenith angle under which it can be observed is 36.4°. The observation strategy was selected to obtain as priority observations around culmination at zenith angles $\leq 40°$ for the full observation

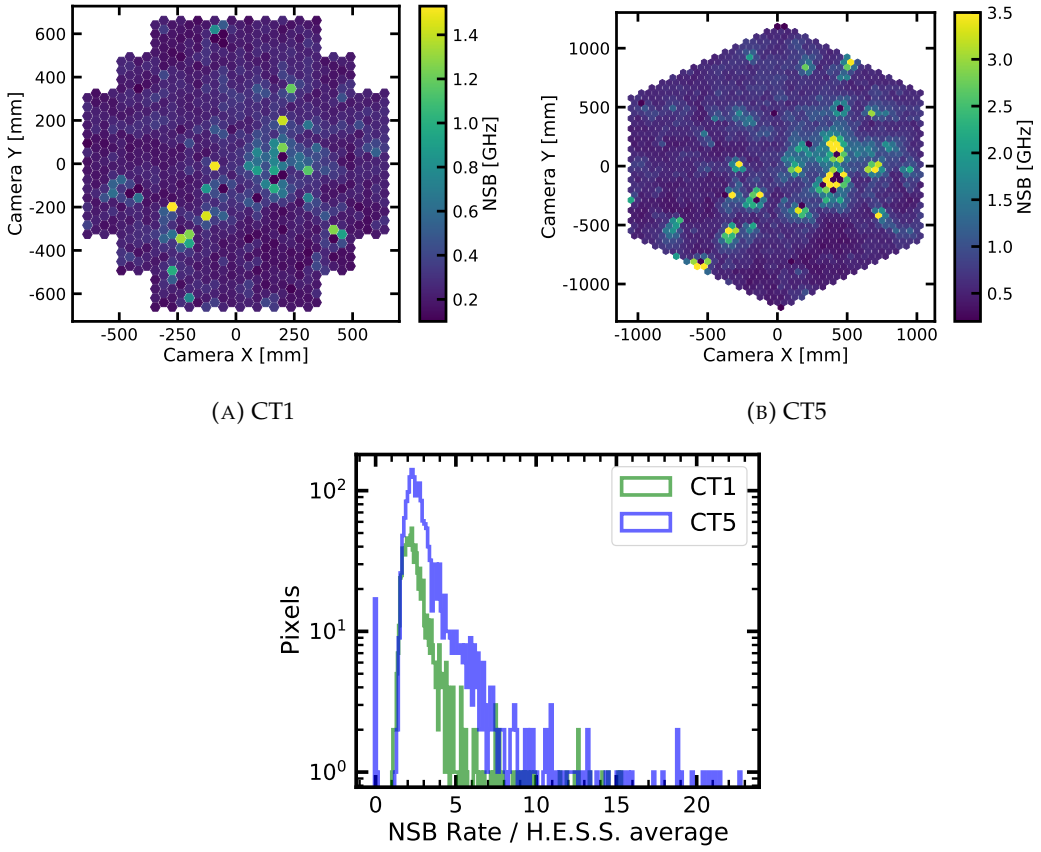

(A) CT1

(B) CT5

(C) Distributions

FIGURE 6.2: **Measured pixel-wise NSB for an examplary η Car run** In **A** the NSB averaged over a few ten seconds for run 158426 is shown for the CT1 camera. **B** presents the same as **A** but for CT5. The color scale is cropped at 3.5 GHz to allow for comparison with the estimation presented in Figure 6.1. In **C** the distributions of the NSB over the camera are compared between CT1 and CT5. For both, the values are computed relative to the average galactic NSB (0.10 GHz for CT1 and 0.25 GHz for CT5). Pixels with NSB values of 0 are switched off.

season. During the period closely around the actual periastron passage in February[3] a loosened zenith angle requirement with a possible extension up to 60° was considered, to maximize the exposure during this period. Unfortunately, the available observation time, especially in February, was limited due to the Namibian rainy season. Further data was acquired in spring 2021 corresponding to an orbital phase of ∼0.2 assuring sufficient coverage over the entire 5.5-year orbital period together with the existing data from previous years.

Applying a run selection on trigger rate RMS ($\leq$ 50 Hz), run duration ($\geq$ 1500 s) and maximum zenith angle ($\leq$ 60°), this yielded a final data set of 97.8 hours during the 2020 periastron campaign and 31.5 hours in 2021. The combined observation campaigns of 2017 to 2019 had a live time of 63.3 h after selection, whereas for the

[3]Using the ephemeris from Teodoro et al. (2016) the 2020 periastron passage was expected for February 17, 2020.

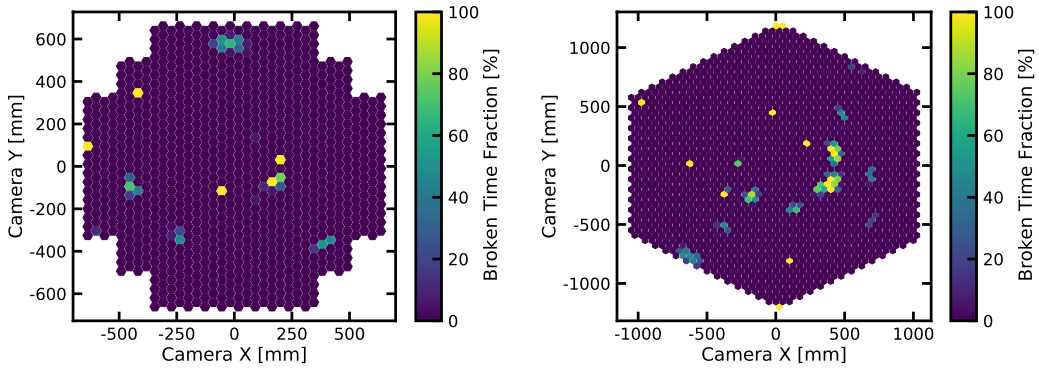

(A) CT1 (B) CT5

FIGURE 6.3: **Broken pixel fraction for an example η Car run**
In **A** and **B** the fraction of the run for which individual pixels are switched off is shown for CT1 and CT5, respectively. The average number of broken pixels is 13 and 36 respectively. For CT1 only the high gain channel is shown, but the low gain fraction looks quite similar, whereas CT5 has only one gain channel. The rotation of the cameras and hence the movement of bright stars over the course of one run is clearly visible.

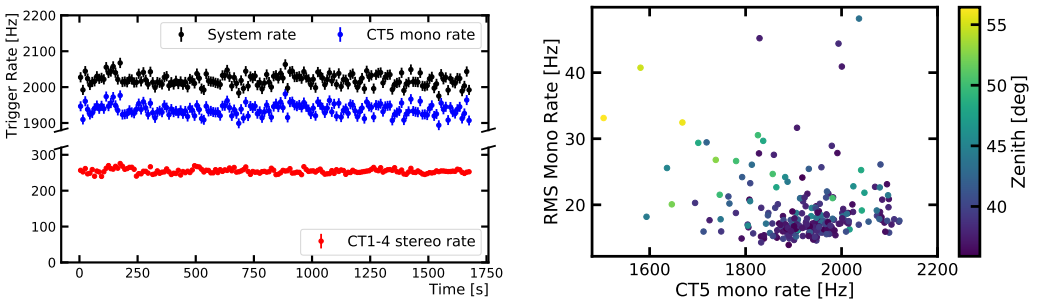

FIGURE 6.4: **Trigger rate stability for η Car observations**
In **A** the CT5 mono, CT1-4 stereo and system rate are compared over the duration of the example run 158426. Trigger rates are estimated in 10s time intervals. In **B** the mean CT5 mono trigger rates, as well as their RMS, are shown for the 2020 η Car data-set after a run selection on RMS $\leq$ 50Hz and a minimum duration of 1500 s. The marker color shows the zenith angle of the observation.

Data set	Start Date	End Date	Live Time [h]	Mean zenith [°]
H.E.S.S. 1 2013-2016	Jan 13,2013	May 30,2016	20.6	39.2
H.E.S.S. 1U 2017-2019	Jan 29, 2017	Apr 7, 2019	63.3	39.2
Periastron 2020	Dec 23, 2019	May 24, 2020	97.8	39.9
"Phase 0.2" 2021	Feb 15, 2021	Apr 10, 2021	31.5	37.2

TABLE 6.2: **Basic properties of η Car data sets**
H.E.S.S. 1 refers to the period with the original cameras in CT1-4, whereas H.E.S.S. 1U denotes the updated CT1-4 cameras. The 2020 & 2021 datasets were taken with FlashCam installed at CT5. The live time is given for the stereo observation time and is corrected for dead time.

2013-16 time period 20.6 h of good-quality data was obtained. The basic properties are summarized in Table 6.2.

6.2 Mono analysis results

Due to the steep spectrum of η Car with spectral indeces of 3.9 and 3.5 derived for the two data sets around the 2014 periastron passage in H.E.S.S. Collaboration et al. (2020), the lower energy threshold of CT5 and the corresponding mono analysis is of particular interest. Nevertheless, the reconstruction of images with unusually high and inhomogeneous noise based on data from only one telescope needs to be done very carefully.

6.2.1 Special simulations set

The exceptional noise levels in the η Car analysis result in a mismatch when simulations that assume a standard NSB, such as those run for Section 4.2.1, are used. The reconstruction and gamma-hadron separation and also the corresponding IRFs rely fully on simulations. Hence a special set of simulations based on the same software setup as described in more detail in Section 3.2.2 and Section 4.2.1 was computed. This special set includes the change in camera settings for η Car runs as summarized in Table 6.1 and uses measured NSB maps in the simulations. For these, the NSB maps derived from the full 2020 data set were combined and averaged for each telescope. The maps, shown in Figure 6.5, were then converted to the corresponding altitude and azimuth frame to be included for a simulation at a specific zenith angle. Subsequently, a set of point source gamma simulations including the NSB maps was run for each combination of zenith angle and offset angle (see Table 6.3). The wobble offset was altered in different directions. Hence applying this simulation set ensured matching noise effects on camera pixels between simulations and data. Diffuse proton and gamma simulations were computed with the same settings for test purposes as well.

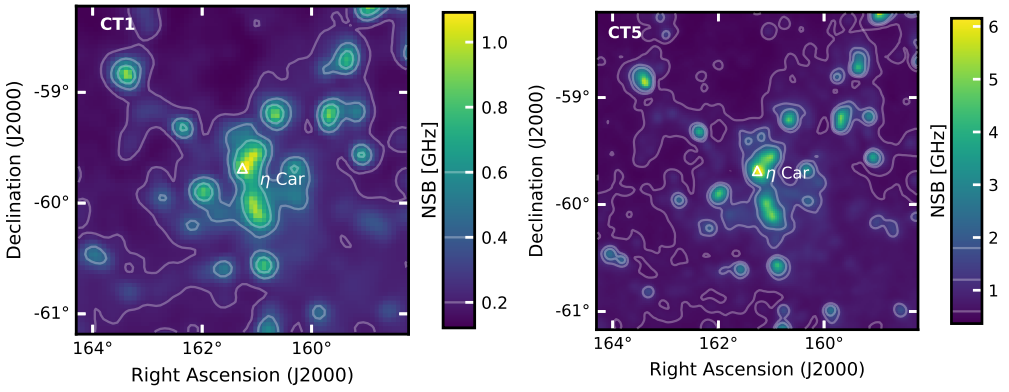

(A) CT1 (B) CT5

FIGURE 6.5: **Average NSB maps for the η Car field**
Both maps have been derived by averaging the NSB maps from all runs of the 2020 dataset. The position of η Car is shown with a white triangle. Contour levels for better visualization have been added at 0.2, 0.4 and 0.6 GHz for CT1 and 0.6, 1.2 and 1.8 GHz for CT5. Both maps are zoomed in for better visibility of the main features and have been used in an extended version for the simulations.

Settings	Zenith [°]	Offset [°]	Azimuth [°]	Primary
Specific	37, 40, 45, 50, 55, 60	0, 0.5, 0.7, 1.0	180	Gamma - point source
Specific	37, 40, 45, 50, 55, 60	/	180	Proton diffuse
Specific	37, 40, 45, 50, 55, 60	/	180	Gamma diffuse

TABLE 6.3: **Specific simulation set for η Car**
The simulation settings were used according to the validated settings derived in Section 4.1 but changing the camera settings according to Table 6.1 and using the NSB maps shown in Figure 6.5.

6.2.2 Special configuration

Based on the special simulation set a designated mono analysis configuration could be derived. This will further be labeled "safe_mono_etacar". The time cleaning method was chosen (see Section 4.3) to utilize its enhanced cleaning performance keeping more shower information. The larger noise level corresponding to an average pedestal width of $2.7 - 2.8$ p.e. raises the precut, as defined in Section 4.3.2, much higher. However, it is still advantageous with respect to the default tail cut cleaning, keeping ∼20 to 30 % more shower intensity for 250 p.e. showers. This is evaluated on the diffuse simulation set and shown in Figure 6.6a for the TimingN5 (see Table 4.4 for details) cleaning comparing it with the TimingN3 cleaning. TimingN5 performs slightly better in retaining more image intensity and is hence chosen.

The fraction of secondary and multiple clusters on gamma images is shown in Figure 6.6b, depicting clearly that the probability of images being split due to the high noise cut is still rather low, at a 1 % level for 300 GeV gammas. Furthermore, no

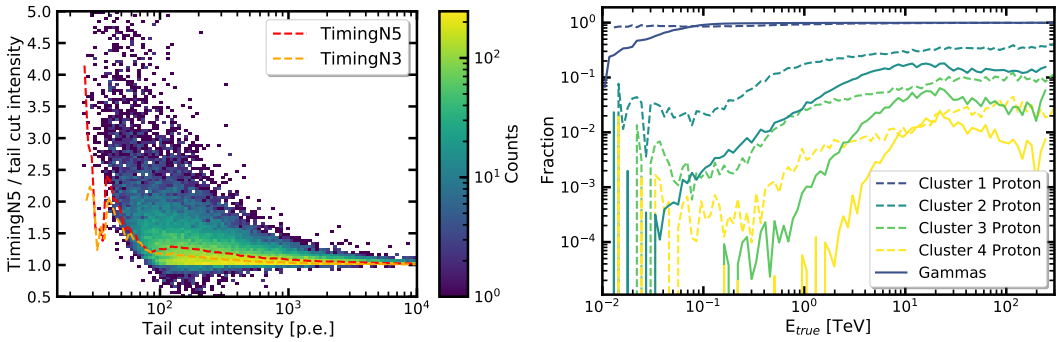

(A) Ratio of image amplitudes

(B) Fraction of clusters

FIGURE 6.6: **Ratio of image amplitudes and cluster fraction for the η Car diffuse simulations**
For **A** the ratios were derived from a set of diffuse gamma simulations as described in Table 6.3 at 40° zenith. Tail-cut cleaning corresponds to the default cleaning used for FlashCam at CT5. The plot shows the amplitude ratio for the TimingN5 cleaning as a 2D histogram, as well as its mean value for each bin along the x-axis. For comparison the bin-wise mean value for TimingN3 is shown. In **B** the fraction of images with at least one, two, three or four clusters are compared between the diffuse gamma and diffuse proton simulations at 40° zenith as a function of simulated energy. Dashed lines correspond to protons simulations and solid lines to gamma simulations with the colors depicting the cluster ID.

triggered images are cleaned away completely at energies above 100 GeV. For protons, the rate of secondary clusters is much higher due to the expected sub-showers in proton induced EAS but the number of images being cleaned away completely is also minimal above 100 GeV.

The harder precut also implies that the default energy and direction reconstruction can't be used, as cleaned shower images will look different than those derived from the default simulations with the same cleaning. Therefore, the direction and energy reconstruction neural networks were trained with the designated gamma point source simulations, following the approach already used for the mono configuration presented in Section 4.2.1. The gamma-hadron separation was trained with the designated simulations. To provide well-suited off events as a counterpart, a higher overall pedestal width value of 2.7 p.e. matching the mean of the η Car field was applied to several off runs. This means that the cleaning of the off events has on average a similar noise pre-cut as it is used for the gamma simulations and as it will be the case for the η Car data set.

As described in Table 6.4, the same cuts as for the safe_mono configuration were used for the preselection. The postselection cuts were optimized on simulation and off events for a source with a steep spectral index of 3.7 and a flux of 2 % of the Crab Nebula at 1 TeV similar to the η Car spectrum derived in H.E.S.S. Collaboration et al. (2020). The performance is described in Figure 6.7 with an angular resolution of $\sim$0.15°, a large effective area ($\geq 10^4\,\mathrm{m}^2$) and decent energy reconstruction (energy bias $\leq 20\,\%$) above $\sim$150 GeV for runs close to the culmination of η Car.

Image Intensity	Image Pixels	Local Distance	ζ_{BDT}	Θ
250 p.e.	10	0.8 m	0.85	0.134°

TABLE 6.4: **Cuts of the safe_mono_etacar analysis configuration**
Both preselection and postselection cuts are shown. Preselection cuts are based on the properties of the cleaned images and postselection cuts on the neural-network-based reconstruction and separation.

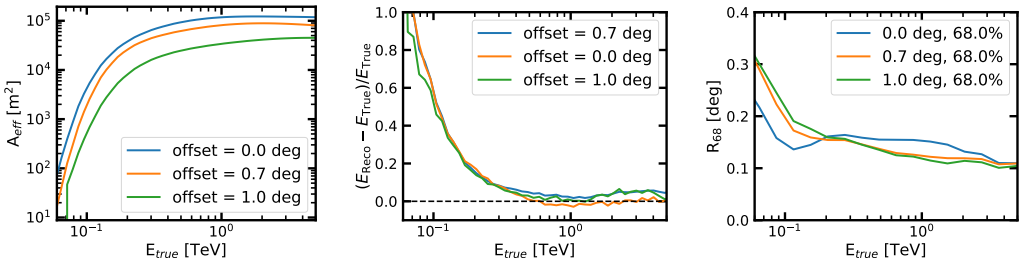

FIGURE 6.7: **IRFs and performance for the safe_mono_etacar analysis configuration**
The effective area A_{eff} is shown for a specific pointing position of an example observation run at 38° zenith as a function of true energy. The offset denotes the source offset from the camera center. The energy bias in the middle is shown for the same zenith angle. In the right panel, the PSF is parametrized by its 68 % containment radius R_{68} for several offsets with again the same zenith angle.

6.2.3 Method to emulate η Car observation conditions for other runs

To validate the analysis configuration and get a proper description of the background and its acceptance, test runs targeted at other sources were transformed to represent a run within the η Car field. The transformation scheme is described in the following:

1. The target position and time of the test run are shifted to the observation position and time of the η Car run.

2. Each event is offset by a constant value that corresponds to the difference of time between the first event of the η Car run and the first event of the current run.

3. For each pixel, the pedestal width of the test run is enlarged to match the one of the targeted η Car run or the current value is kept if the value from the test run for a given pixel is greater. This is done because the pedestal width is linked with the NSB in the pixel. The pedestal bias is already subtracted after the calibration as discussed in Section 3.2.1 and hence does not need to be transformed.

4. The "broken pixels" information of the two runs is merged ensuring the deactivation of invalid pixels from both runs for the analysis.

5. Noise is added in each pixel such that the distribution of noise will match the merged pedestal width. This is done by dicing an additional number of p.e. assuming that the noise in both runs (test and η Car) is following a Gaussian distribution.

6. All steps after the calibration level, including image cleaning and the derivation of Hillas parameters, are rerun to properly use the emulated conditions. Corresponding event images should hence be as close as possible to an event image observed pointing at the η Car field.

The different trigger thresholds of the reference run and the η Car run will not have an influence on the event selection as long as the analysis preselection cuts are higher than the trigger thresholds. This is clearly the case for the safe_mono_etacar configuration with an image amplitude cut of 250 p.e.

6.2.4 Validation of configuration

To validate the safe_mono_etacar configuration and IRFs it is not possible to use standard Crab observations, as the reconstruction and separation steps were already trained on simulations with high and inhomogeneous NSB. Hence steps 3 to 6 of the emulation scheme described above were applied to a small subset of four Crab Nebula runs with different η Car reference runs. Afterward, the resulting spectrum after running an analysis with the safe_mono_etacar configuration was derived. For this, the reflected regions background method (Section 3.2.5) was utilized. This resulted in a power-law fit with an index of 2.58 ± 0.04, slightly softer but within the systematics consistent with the derived mono spectrum in Section 4.2.2. The flux normalization at 1 TeV is $(4.54 \pm 0.16) \times 10^{-11}\,\mathrm{TeV}^{-1}\,\mathrm{cm}^{-2}\,\mathrm{s}^{-1}$, which is 17 % higher than the flux normalization in Section 4.2.2. The difference might be partly explained by the contamination of badly reconstructed off events and noise artifacts that could be reduced by better-suited background methods. Nevertheless, it will be treated as an additional systematic uncertainty on the flux that needs to be taken into account for the spectral results derived with this configuration.

6.2.5 Derivation of background model

Ring background result Using the previously derived analysis configuration, the 2020 periastron data set was analyzed with a ring background method (Section 3.2.5). As it is discussed in more detail in Section 2.3.4 and Chapter 7 the wind region and even the Homunculus region are at scales smaller than 0.1 pc, which is not resolvable by H.E.S.S. Hence the emission linked to η Car and its close surroundings should appear point-like in any H.E.S.S. analysis. To take into account field-specific characteristics the acceptance curve was derived from the η Car runs themselves outside the exclusion regions assuming radial symmetry of the background acceptance. Applying this analysis a highly significant excess at the position of η Car with 38 σ was

found, as shown in Figure 6.8a. However, the results show clear problems, depicting a very large extended excess strongly deviating from the size of the PSF. Furthermore, the background normalization is very poor with obvious features in the significance map outside the exclusion regions up to $\pm 12\,\sigma$. A Gaussian fit to the distribution of these significance values yielded a width of 2.4 deviating strongly from a good background description with width 1. These findings are summarized in Figure 6.8b. From this, it is very obvious that the assumption of a radially symmetric acceptance does not hold for this particular FoV. The effects of noise and broken pixels, that will e.g. crop or enlargen images, are not negligible and not homogeneously distributed. Hence any detected excess at the target position and outside of it might be a noise artifact. This is also supported by the strong deviation from the expected point-like signal as shown in Figure 6.8c. In Figure 6.8d slices along the same axis with a width of 1° across both the excess and the NSB maps are drawn. The axis is roughly diagonal from the lower left to the upper right in the maps. The integrated excess profile and NSB profile show a good resemblance to each other strengthening the point that the excess derived with the ring background method is indeed mostly a noise artifact. Nevertheless, a point-like signal could still be present, but a better background description is needed to potentially recover it.

On/Off background derivation The effects of NSB and broken pixels, which are mostly turned off due to NSB, are strongly related to the actual sky coordinates the telescopes are pointing at. Therefore, an On/Off background method should be well suited to also mimic these effects for the background. As the CNC is a very unique field, off observations targeted at other empty fields are processed with the emulation scheme described in Section 6.2.3. With this the resulting shifted off runs will appear as if they had been taken pointing at the η Car field but without a gamma-ray source. For each reference η Car run in the 2020 data set, a list of 10 off runs is shifted accordingly. The 10 off runs were taken at similar zenith conditions and during a similar time as the η Car data set. Furthermore, they were selected based on good atmospheric conditions, a full run duration and no obvious issues in their low-level diagnostics. From these shifted off runs also the typical Hillas parameters can be retrieved and compared to events from actual η Car observations. This shows good agreement as it can be seen in Figure 6.9.

To the off event lists safe thresholds were applied. These were the energy at which 10 % of the maximum effective area is reached and a maximum offset of 1.6°. Subsequently, an off map was filled, which will be used as the background map.

Cut on displacement variable The direction of shower images severely influenced by high noise levels and especially broken pixels is hard to reconstruct with a single image. The resulting displacement parameter δ_{RECO} (see Section 3.2.3) might thus be poorly constrained. Especially in the high NSB region with many broken pixels around η Car (see Figure 6.5), the shower direction might be reconstructed rather

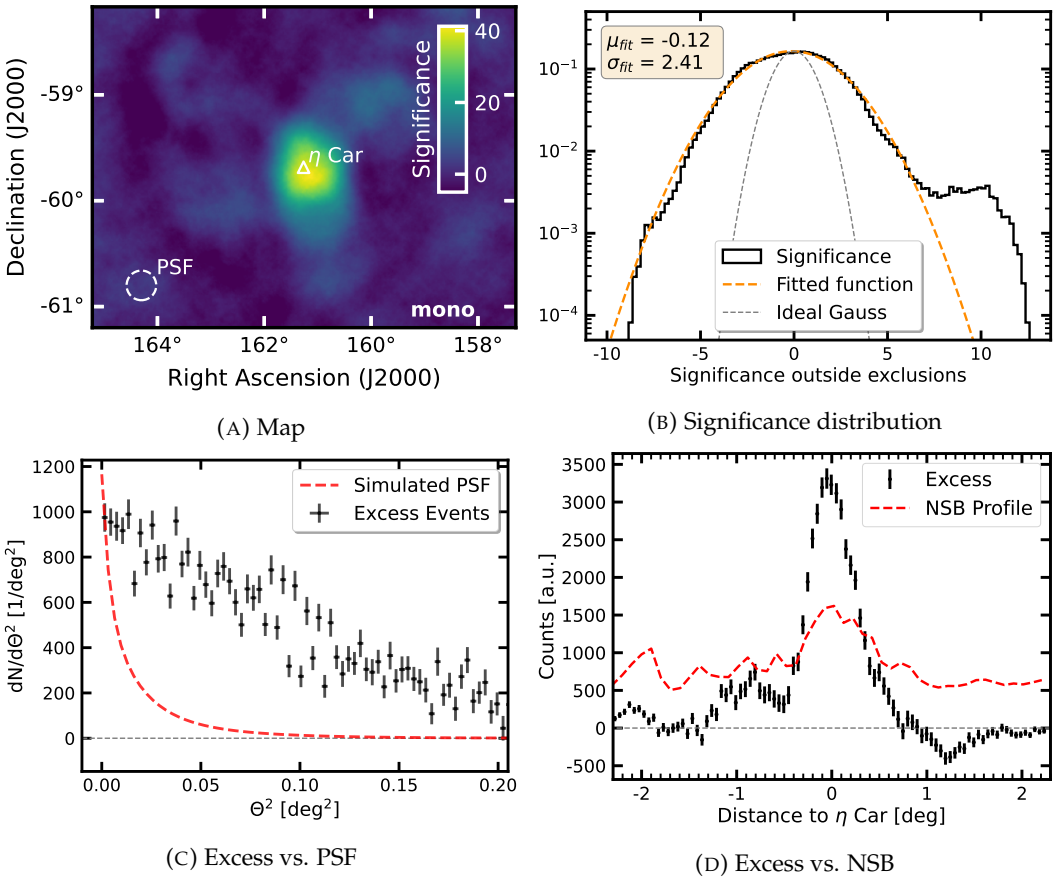

(A) Map

(B) Significance distribution

(C) Excess vs. PSF

(D) Excess vs. NSB

FIGURE 6.8: **Results of ring background mono analysis for η Car** In **A** the resulting significance map is shown. The size of the PSF is denoted by a dashed circle and the position of η Car is highlighted by a white triangle. In **B** the resulting histogram of significance values outside of the exclusion mask is drawn together with a fitted Gaussian. The Gaussian is strongly deviating from an ideal background description with width 1. **C** compares the radial excess distribution centered at η Car with the PSF derived from simulations. The PSF is described by Equation 4.2. **D** compares the excess distribution along a rectangular slice with a width of 1° across the FoV with the NSB profile derived along the same axis. The orientation of the axis is roughly diagonal from the lower left to the upper right in the significance map. The NSB profile is arbitrarily scaled.

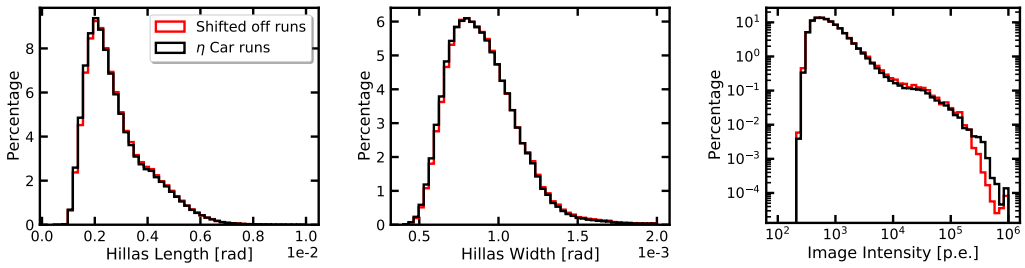

FIGURE 6.9: **Comparison of shifted off events and η Car observation events**
The off events were shifted with the method described in Section 6.2.3. All distributions are derived after preselection and gamma-hadron separation cuts and normalized relative to the total number of events after cuts. In **A** the Hillas length, in **B** the Hillas width and in **C** the image intensities after cleaning are compared.

close to the image itself, having a small δ_{RECO}. This would contribute to an excess in the region, which is not stemming from η Car or another gamma-ray source. To check the influence of that, the δ_{RECO} distribution was derived from the point source gamma simulations with 0.7° wobble offset, which were weighted to represent a source with a spectral index of 3.5. This was compared to the excess in the η Car on region, which has a radius of 0.134° as stated in Table 6.1. The excess in the on region was derived by subtracting the normalized distribution found in the shifted off runs from the distribution found in the on runs. The normalization α was derived to have equal counts in the on and off maps outside of the exclusion mask. As visualized in Figure 6.10 the distribution from gamma simulations is well constrained, whereas the excess events exhibit some excess at smaller δ_{RECO} values. Consequently, a cut on $\delta_{RECO} \geq 0.009$ was introduced, which keeps 80 % of the gammas but minimizes the number of closely reconstructed background events. The resulting distribution after applying this cut to the full 2020 data set and the corresponding off data set yields a better match. To account for the loss in gamma efficiency the IRFs were again derived including the cut on δ_{RECO}. The final analysis configuration for the mono analysis is thus the on/off background method described above with the addition of this cut.

6.2.6 Mono analysis results

Employing the previously described methods and applying the same safe cuts, on and off counts maps were produced (see Figure 6.11). A conservative exclusion mask was set to mask the inner bright CNC region as well as the brightest additional stars. Afterward, the normalization factor α from the ratio of on and off counts outside the exclusion mask was derived allowing the calculation of a significance map following the approach described in Section 3.2.4. The resulting significance map with a correlation radius on the size of the Θ-cut is shown in Figure 6.12a. At the η Car position, a peak significance of 7.4 σ can be found with its maximum value at an

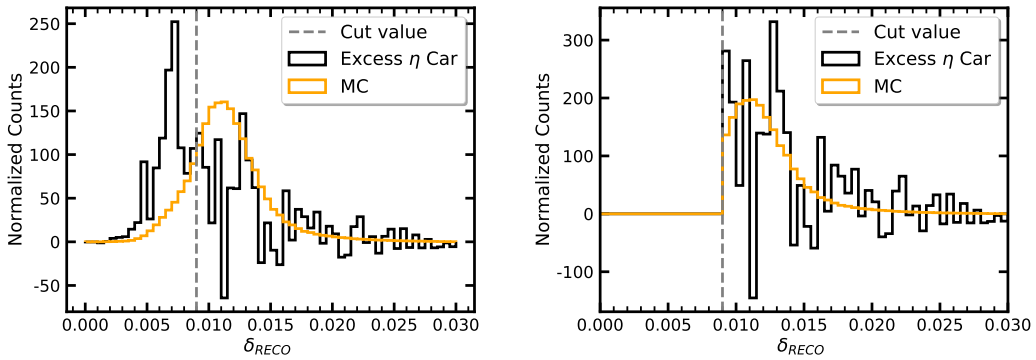

(A) Without δ_{RECO} cut (B) With δ_{RECO} cut

FIGURE 6.10: **Derivation and application of δ_{RECO} cut**
In **A** the distributions of the displacement variable δ_{RECO} are compared between gamma simulations and excess events from the on region. The gamma simulations are point-like simulations as defined in Table 6.3 at 40° zenith and 0.7° offset. A spectral index of 3.5 is assumed. The excess distribution is derived by subtracting the α times off distribution from the on distribution. On and off events are both taken within the on region with the off events derived from the off map obtained in the previous section. The normalization α was set to have equal counts in the on and off maps outside of the exclusion mask. After applying a cut of $\delta_{RECO} \geq 0.009$ the distributions, as well as α have been derived again and are compared in **B**. Both the MC and excess distribution are normalized to an area under the curve of 1.

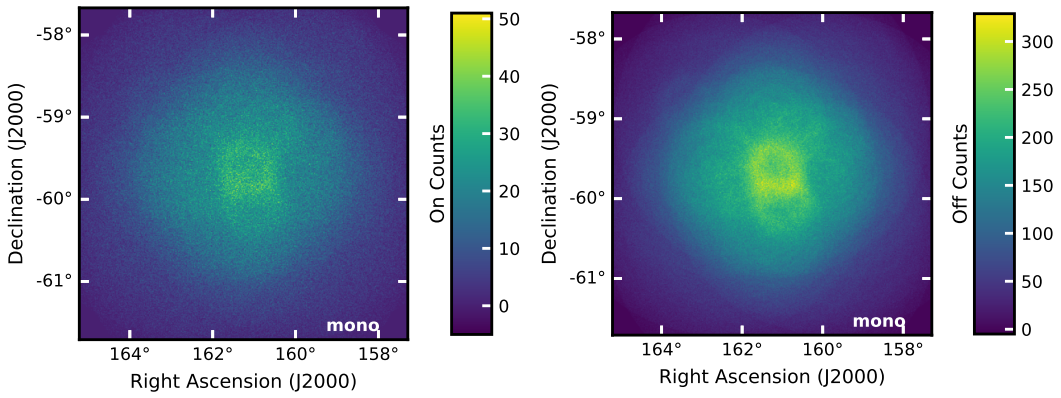

(A) On counts map (B) Off counts map

FIGURE 6.11: **On and off counts map for the ON/Off background mono analysis of the η Car periastron data set**
The on counts map (**A**) is derived from all runs of the periastron data set after applying all cuts including the δ_{RECO} cut. The off counts map (**B**) is similarly derived from the shifted off runs as described in more detail in the text. For both maps, a safe cut on energy at which 10 % of the maximum effective area is reached has been applied. Further, a cut on the maximum offset for reconstructed events from the camera pointing center of 1.6° was used.

offset of 0.03° from η Car, which is much smaller than the PSF. Comparing the radial excess distribution to the PSF derived from simulations shows a good match to a point-like signal (see Figure 6.12b). However, as it is evident from the map and the radial excess distributions there are still several non-point-like features reaching up to 6 σ visible within the inner CNC region. Even though an astrophysical origin, e.g. a connection to other unknown gamma-ray sources, can not be explicitly ruled out, there is no clear association to known Fermi-LAT sources and open clusters, which could act as potential gamma-ray sources within the CNC region. Hence it is assumed that these are remaining noise and background artifacts. Outside of the exclusion region, the background normalization tested by the significance distribution is described by a Gaussian with a width of 1.3, a bit wider than the ideal case (see Figure 6.12c). Nevertheless, compared to the results obtained with the ring background method a drastic improvement could be achieved, which actually allows for spectral modeling of the η Car excess even though large systematics need to still be taken into account.

To derive the spectral properties a circular region with size $\Theta = 0.134°$ centered at η Car was chosen. The spectral properties were modeled with a power law as described in Equation 3.17. To account for potential differences in the energy scale due to e.g. biases in the muon estimation, α was derived in each energy bin separately. This is shown in Figure 6.13a together with the derived excess counts per energy bin and the predicted counts from the fitted spectral model showing generally good agreement between fit and data. The lower energy threshold of the analysis is 0.14 TeV. The fit resulted in a spectral index of $\Gamma = 3.3 \pm 0.4$ and a flux normalization at a fixed reference energy of 0.2 TeV of $\phi_0 = (4.5 \pm 1.0) \times 10^{-11}\,\mathrm{TeV}^{-1}\,\mathrm{cm}^{-2}\,\mathrm{s}^{-1}$. The resulting SED with two flux points and two upper limits derived in 4 bins between 0.14 TeV and 1.88 TeV is shown in Figure 6.13b. The two flux points have significances of 3.7 σ each. The resulting spectral model is compared to the spectral models derived around the 2014 periastron, which were published in H.E.S.S. Collaboration et al. (2020). Additionally, the spectral model as obtained without the On/Off background method but with a reflected regions method using the safe_etacar_mono configuration is presented. Comparing these spectral models, one can clearly see that the careful consideration of noise artifacts reduces the flux drastically compared to both the reflected regions analysis and the published SED. Those are actually in agreement within errors, whereas even within systematics the derived 2020 periastron flux is not consistent.

The 2020 periastron is not extraordinary compared with previous periastron passages in X-rays (Hamaguchi et al., 2020; Kashi et al., 2021) and especially not in the Fermi-LAT HE data (Martí-Devesa and Reimer, 2021). Hence a drastic flux reduction due to strong orbit-to-orbit variability of η Car can be almost certainly ruled out. The reduced flux is just a result of the more careful treatment of noise factors in the analysis. This is further indicated by the good match of the spectrum derived without careful noise treatment compared to the published spectra.

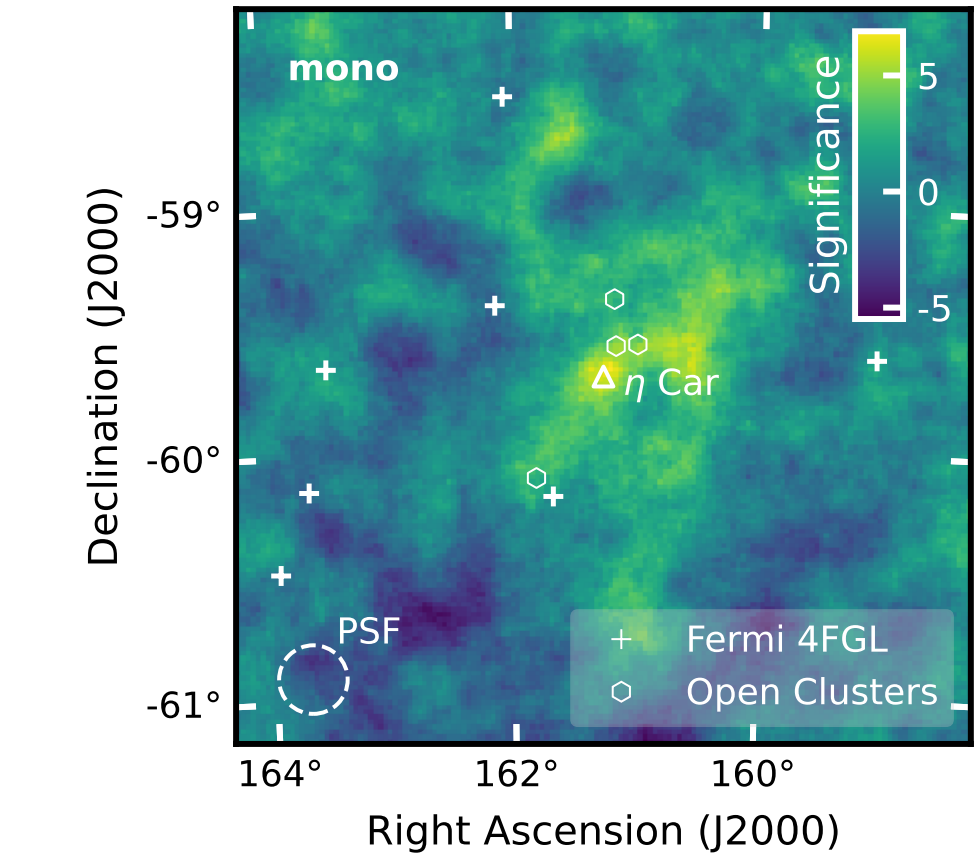

(A) Significance map

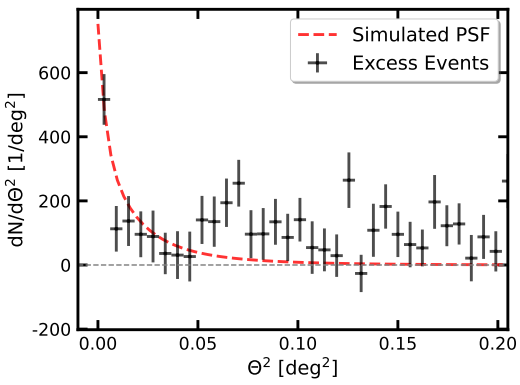

(B) Excess vs. PSF

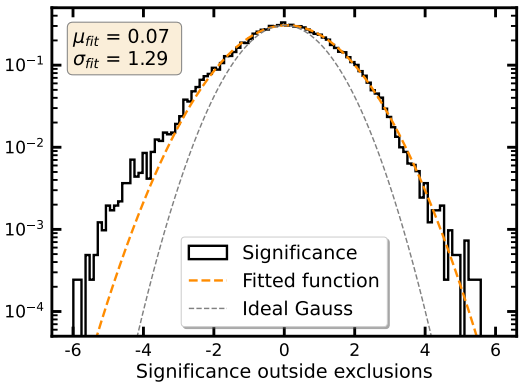

(C) Significance distribution

FIGURE 6.12: **Results of the ON/Off background mono analysis of the η Car periastron data set**
In **A** the resulting significance map with a correlation radius of 0.134° is shown. The position of η Car is marked with a white triangle. Additionally, all other 4FGL sources in the FoV are marked together with open clusters from Preibisch et al. (2011). The radial excess distribution centered on the η Car position is compared in **B** to the PSF derived from simulations for a source with assumed index 3.4. The scale of the PSF function was matched to the first bin. In **C** the significance distribution outside of the exclusion mask is fitted with a Gaussian. For reference also an ideal description of a Gaussian with a width of 1 and a mean of 0 is drawn.

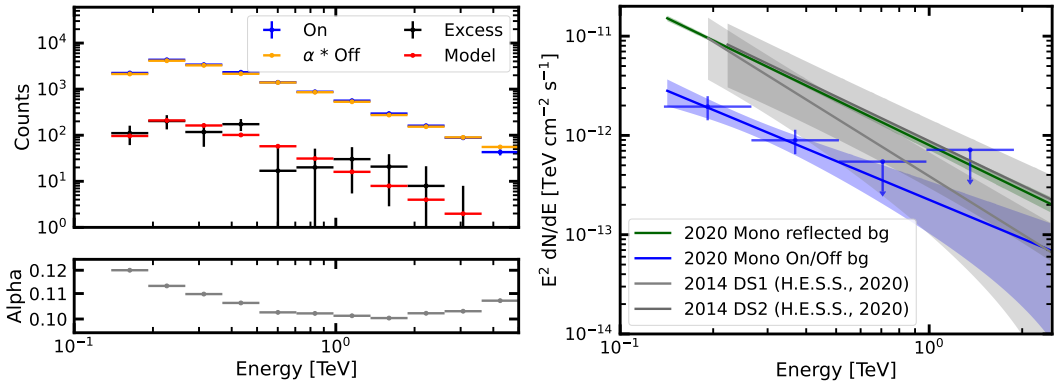

(A) Predicted and measured excess counts (B) Mono SED

FIGURE 6.13: **Spectral results of the η Car mono analysis**
In **A** the on and normalized off counts in the on region are presented for each energy bin together with the accordingly derived excess counts. The normalization α was derived independently in each energy bin, which is shown in the lower panel. The number of predicted counts of the best-fit power-law spectral model is compared to the excess counts. In **B** the resulting SED from the On/Off approach with flux points is compared to the spectral model derived from a reflected regions analysis without any special treatment to model the noise influence. The spectra taken around the 2014 periastron passage from H.E.S.S. Collaboration et al. (2020) are also shown for comparison. The spectral models for the 2020 data set only include statistical errors, whereas the 2014 spectra also include systematic errors as discussed in the paper.

The systematics of the spectral parameters, especially the flux normalization, have to be treated quite conservatively. The systematic uncertainty can be assumed to be asymmetric, potentially biasing the result towards a higher flux. Therefore, from the remaining features in the significance map a relative negative systematic uncertainty of at least ∼50 % can be assumed.

The 2021 dataset was not analyzed in mono with the On/Off method. Still, the variability of the mono signal was tested by obtaining a relative excess map between the 2020 and 2021 data sets. As the influence by noise should be the same in both data sets, an positive or negative excess at the position of η Car would hint at a time variability of the gamma-ray signal. No significant excess was found constraining the variability of the signal. However, due to the high systematics of the mono analysis, more elaborated constraints on the variability are discussed only for the stereo analysis in the next section.

6.3 Stereo analysis results

For the CT1-4 stereo analysis, the ImPACT reconstruction technique as described in Section 3.2.3 with standard cuts (see Table 3.2) was chosen. As the stereo direction reconstruction is more robust against the effects of noise and the noise level is

taken into account for the ImPACT based reconstruction, no custom analysis configuration and background modeling method had to be employed. Instead, the ring background method and the reflected regions background method were chosen for the derivation of maps and spectra, respectively. The data sets described in Table 6.2 were analyzed individually. The maximum offset considered was 2° and the safe energy threshold was determined by the energy at which the effective area reaches 10 % of its maximum value.

2020 periastron data set For the 2020 periastron data set the resulting significance map with a correlation radius on the size of the PSF is shown in Figure 6.14a. At the η Car position a significance of 8.5 σ can be found. If compared to other 4FGL sources and known open clusters no other sources are significantly detected. In general, no clear features outside the source region are visible. Comparing the radial excess distribution to the PSF derived from simulations shows a good match to a point-like signal (see Figure 6.14b). A second extended component with a radius of $\sim$0.3° might be visible that could contribute up to 20 % of the flux in the on region. This will be treated as an additional systematic. The background outside of the exclusion region is described reasonably well with the significance distribution fitted by a Gaussian with a width of 1.17 and a mean of -0.02 (see Figure 6.14c).

For deriving the SED once again the spectrum was modeled as a power-law (see Equation 3.17). The lower energy threshold is 0.31 TeV and the reference energy was fixed at 1 TeV. The best fit result yielded a spectral index of $\Gamma = 3.3 \pm 0.2$ and a flux normalization of $\phi_0 = (2.0 \pm 0.3) \times 10^{-13}\,\mathrm{TeV}^{-1}\,\mathrm{cm}^{-2}\,\mathrm{s}^{-1}$. The resulting SED with four flux points and three upper limits derived in 7 bins between 0.31 TeV and 4.48 TeV is shown in Figure 6.15. The four flux points have significances of 3.8, 5.7, 5.3 and 3.1 σ respectively. The derived spectral properties are within the statistical uncertainties consistent with the derived mono spectrum on the same data set. This further strengthens the point, that the mono result derived with the On/Off method is indeed a robust result and the actual flux of η Car is lower than derived in H.E.S.S. Collaboration et al. (2020). The highest significant flux point has a reference energy of 1.18 TeV and a maximum energy of 1.43 TeV. Hence this will be adopted further as an estimate of the maximum photon energy.

2021 data set The 2021 data set taken at a phase of $\sim$0.2 was analyzed with the same methods as the 2020 data set. The derived significance map yields a significant detection of η Car with 5.1 σ. The map with corresponding significance distribution is shown in Figure 6.16. The background is well normalized similar to the analysis of the 2020 data set. Deriving the SED in the same energy range as for the periastron data set yielded a spectral index of $\Gamma = 3.7 \pm 0.5$ and a flux normalization of $\phi_0 = (1.3 \pm 0.6) \times 10^{-13}\,\mathrm{TeV}^{-1}\,\mathrm{cm}^{-2}\,\mathrm{s}^{-1}$ at a reference energy of 1 TeV. The resulting best-fit power-law model and the flux points are shown in Figure 6.15. The spectral parameters show a slightly softer spectrum but match within uncertainties with the

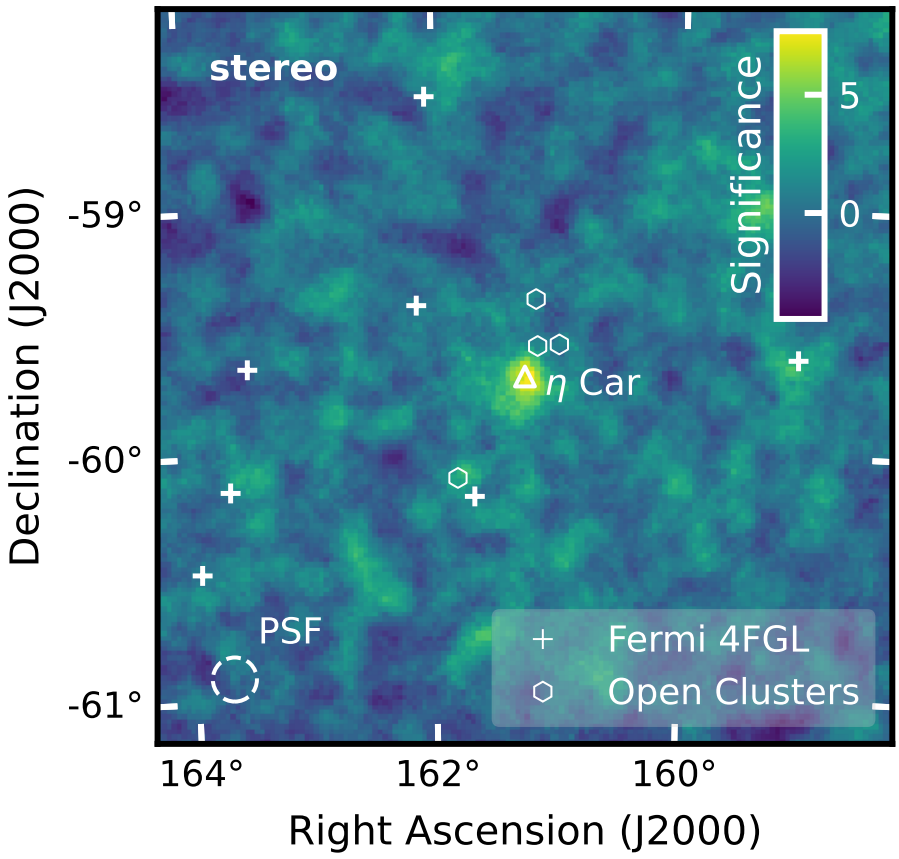

(A) Significance map

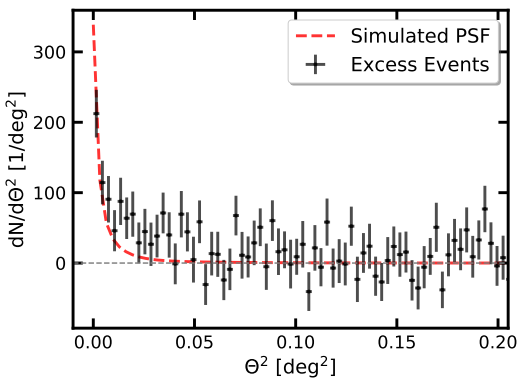

(B) Excess vs. PSF

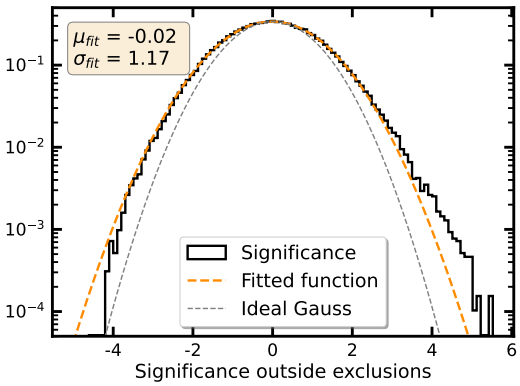

(C) Significance distribution

FIGURE 6.14: **Results of the stereo analysis of the η Car periastron data set**

In **A** the resulting significance map with a correlation radius of 0.09° is shown. The position of η Car is marked with a white triangle. Additionally, all other 4FGL sources in the FoV are marked together with open clusters from Preibisch et al. (2011). The radial excess distribution centered on the η Car position is compared in **B** to the PSF derived from simulations for a source with assumed index 3.5. The scale of the PSF function was matched to the first bin. In **C** the significance distribution outside of the exclusion mask is fitted with a Gaussian. For reference also an ideal description of a Gaussian with a width of 1 and a mean of 0 is drawn.

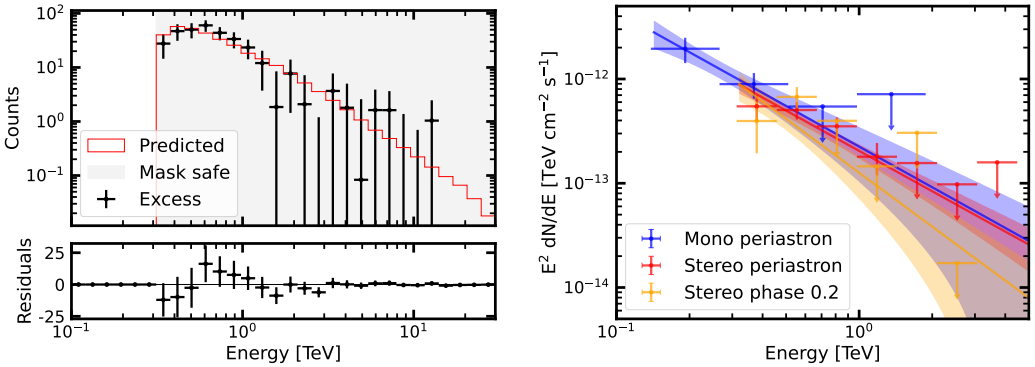

(A) Predicted and measured excess counts (B) SEDs

FIGURE 6.15: **Spectral results of the η Car stereo analysis**
In **A** the number of predicted counts of the best-fit power-law spectral model is compared to the excess counts with the resulting residuals. In **B** the resulting SED from the stereo analysis of the periastron data set is compared to the spectral model derived in the mono analysis of the same dataset. Furthermore, the best-fit spectral model for the 2021 phase 0.2 dataset is shown. Additionally, also the derived flux points are compared.

2020 spectral parameters. Only the first two flux points in the same bins as above are significant with values of 2.0 and 4.8 σ, whereas for higher energies only upper limits are derived. Hence the maximum energy is only 0.67 TeV. The rather constraining high-energy upper limits are further hints for a softer spectrum and earlier cut-off, but due to the large uncertainties no clear conclusion can be drawn from this.

Long-term light curve The data sets for the years from 2013 to 2019 (see Table 6.2) were also analyzed with the reflected regions background method to derive a long-term light curve. Stereoscopic data sets from the years before 2012 are already published in H.E.S.S. Collaboration et al. (2012). The run selection was done using the spectral selection cuts (H.E.S.S. Collaboration et al., 2018) and requiring a minimum number of 2 small telescopes passing these cuts. The data taking stability during the early years of η Car observations was rather poor and during some observation phases only CT5 mono observations were taken. Therefore, the available data set is rather limited, especially for the years 2013 to 2016. The stereo data taken around the last periastron was not considered in H.E.S.S. Collaboration et al. (2020) but is taken into account in this thesis. However, only a few runs pass the selection cuts. The data were analyzed individually for the H.E.S.S. 1 and 1U data sets. In the combined H.E.S.S. 1 data set the total significance at the η Car position was below 2σ. Hence only upper limits for a light curve could be derived. For this, the time bins were chosen according to the observation campaigns in the different years. The energy flux for the light curve in general was derived between 0.31 and 3.1 TeV.

The H.E.S.S. 1U 2017-19 data set resulted in a total excess of 3.4σ. For this a spectrum with a spectral index of $\Gamma = 3.6 \pm 0.5$ and a flux normalization of $\phi_0 =$

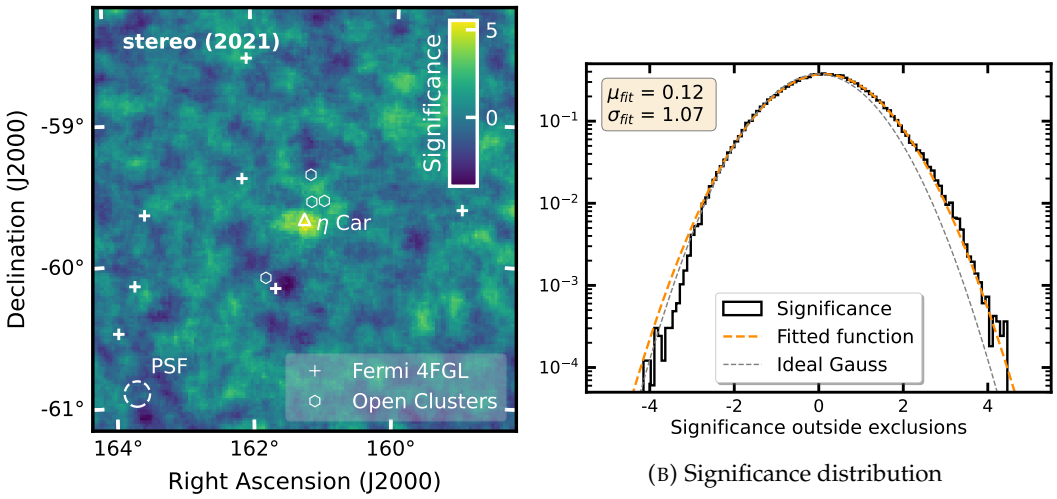

(A) Significance map

(B) Significance distribution

FIGURE 6.16: **Results of the stereo analysis of the η Car 2021 data set**
In **A** the resulting significance map with a correlation radius of 0.09° is shown. The position of η Car is marked with a white triangle. Additionally, all other 4FGL sources in the FoV are marked together with open clusters from Preibisch et al. (2011). In **B** the significance distribution outside of the exclusion mask is fitted with a Gaussian. For reference also an ideal description of a Gaussian with a width of 1 and a mean of 0 is drawn.

$(0.7 \pm 0.3) \times 10^{-13}\,\mathrm{TeV}^{-1}\,\mathrm{cm}^{-2}\,\mathrm{s}^{-1}$ at a reference energy of 1 TeV was retrieved. To obtain light curve points the time bins were again chosen according to the observation campaigns in the different years. With this, only the 2019 campaign yielded a flux point above the 2σ threshold with 2.3σ.

For the light curve the periastron data set was also split up into the different observation periods between the observation breaks in H.E.S.S. due to bright moon. Flux points for each period could be retrieved with significances of 4.2, 4.0, 2.6, 3.8 and 5.1 σ. The 2021 data set was not further split up. The resulting light curve as a function of time and phase can be seen in Figure 6.17. There, a reduction of the flux in the off phases around phase 0.5 and later becomes evident, whereas the flux rises towards periastron. During the periastron passage no clear variability on short time scales of roughly a month is present. At phase 0.2 the flux is still comparable to the periastron flux. The general behavior of the long term light curve is rather similar to the Fermi-LAT component above 10 GeV as derived by Martí-Devesa and Reimer (2021).

In Figure 6.18 the phase interval around the periastron passage is compared in the multiwavelength context. The gamma-ray components show similar behavior, both in the HE regime using the Fermi-LAT light curves around the previous two periastron passages (White et al., 2020) and in the VHE regime using the light curve derived in this work. Within the large uncertainties, the gamma-ray flux shows no significant variability on these time scales. This is in contrast to the large variability

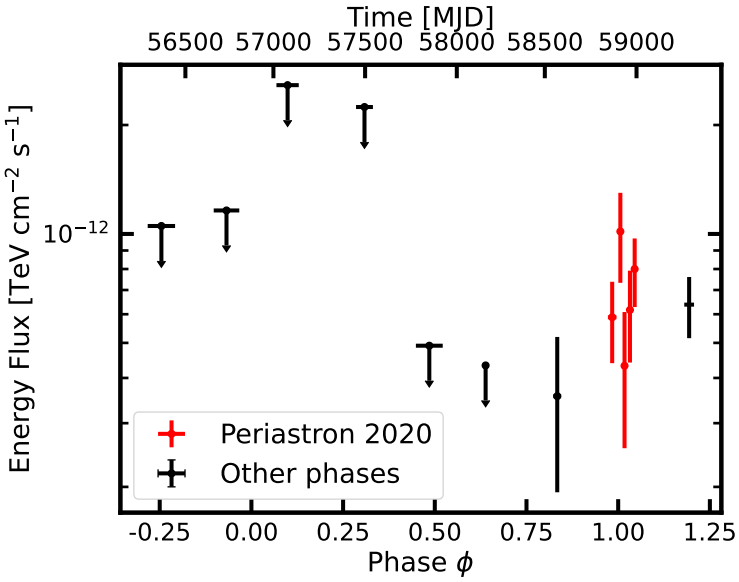

FIGURE 6.17: **Light curve of η Car**
All flux points are based on stereo reconstruction results and integrated between 0.31 and 3.1 TeV. The data taken during the H.E.S.S. periastron campaign is highlighted and split into time bins according to the observation periods between full moon breaks. The other data sets are split up by year. Both the observation time in MJD and the corresponding phase are given. The phase has been derived following the ephemeris from Teodoro et al. (2016) with phase $\phi = 0$ corresponding to the 2014 periastron.

in the X-ray regime, which is discussed in more detail in Section 2.3.3. For the X-ray regime also the 2020 light curve obtained with NICER[4] from Kashi et al. (2021) is shown, which shows a shorter recovery time but otherwise similar characteristics compared to previous passages. The different behavior of the gamma-ray and X-ray light curves is a clear sign, that the gamma-ray emission is caused by different particle populations than the thermal and non-thermal X-ray components (White et al., 2020).

6.4 Fermi-LAT analysis results

Fermi-LAT data was additionally analyzed to retrieve a multiwavelength SED for the periastron data set. In the first iteration, the full data set from the launch of Fermi up to October 2022 was taken into account. The data selection and modeling were done with the same approach as described in detail in Chapter 7. The only difference is that the lower energy threshold chosen for this analysis was 60 MeV to obtain a result for the full available energy range. To have an accurate background model for the Fermi-LAT analysis the CO cloud templates as discussed in Chapter 7 were also taken into account. After running the optimization and fitting steps, the

[4]The Neutron star Interior Composition Explorer (NICER; Gendreau et al., 2016) is an X-ray instrument on board of the International Space Station.

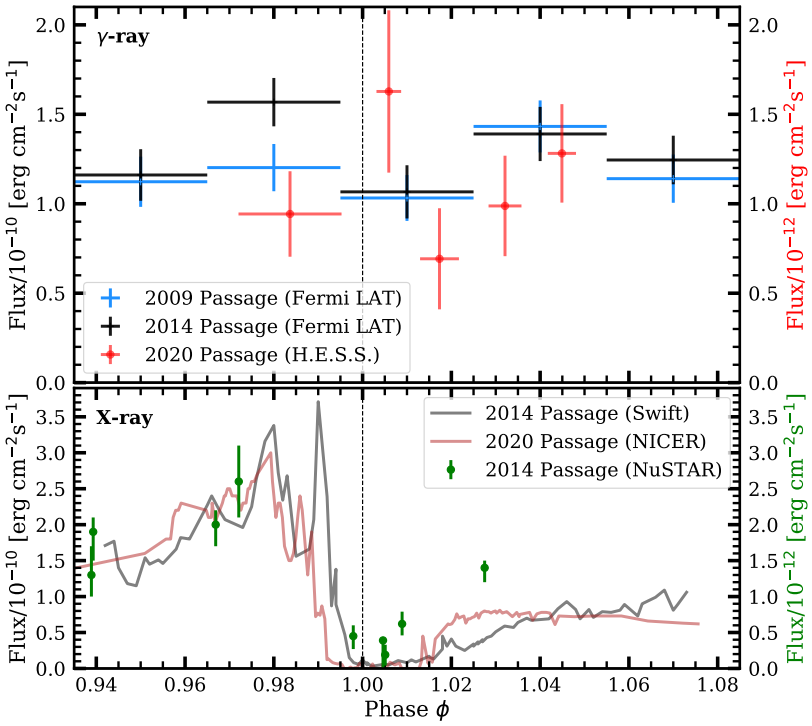

FIGURE 6.18: **Light curve of periastron passage compared with multiwavelength data**
In the upper panel the H.E.S.S. light curve points for the 2020 periastron passage derived in this work are compared to the Fermi-LAT light curve presented in White et al. (2020). In the lower panel the X-ray data between 2 keV and 10 keV from Swift (from Corcoran et al., 2017) around the 2014 periastron passage and the NICER flux (Kashi et al., 2021) obtained in the same energy range around the 2020 passage is presented. Additionally, the NuSTAR observations between 30 and 50 keV from Hamaguchi et al. (2018) taken around the 2014 periastron are shown. The y-axes on the left denote the Fermi and Swift/NICER flux, respectively. The y-axes on the right the H.E.S.S. (red) and NuSTAR (green) flux. The dashed line represents the periastron passage at phase $\phi = 0$.

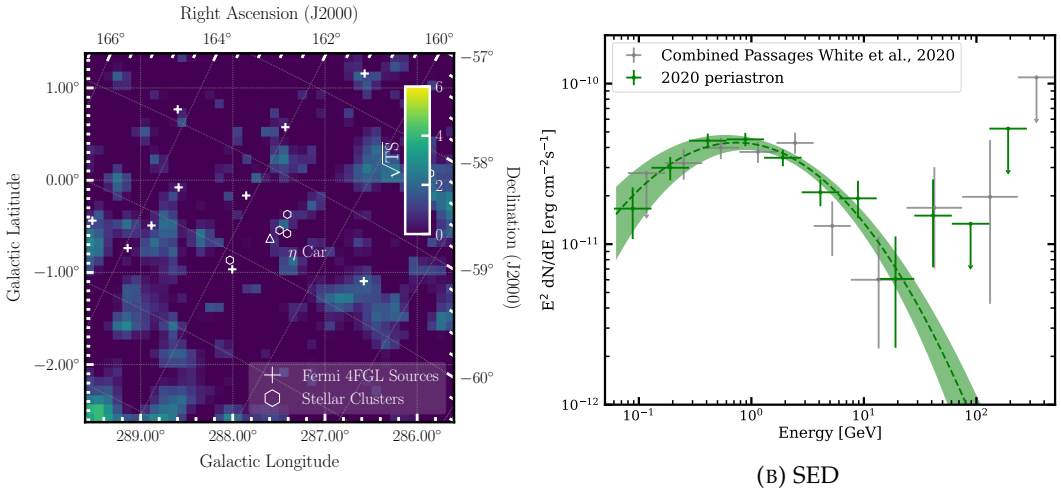

(A) Residual map

(B) SED

FIGURE 6.19: **Results of the contemporaneous Fermi-LAT analysis of the η Car 2020 periastron**
In **A** the residual TS map is shown after all fitted model components have been subtracted. The position of η Car is marked with a white triangle. Additionally, all other 4FGL sources in the FoV are marked together with open clusters from Preibisch et al. (2011). In **B** the resulting η Car SED above 60 MeV fitted as a log-parabola with flux points is compared to the flux points derived from White et al. (2020) for the previous periastron passages.

resulting background and source model was fixed. A data set contemporaneous to the H.E.S.S. periastron data set was defined, lasting from Mission Elapsed Time (MET) 598755697 to MET 612045512. The model derived from the full data set was used for the analysis of the contemporaneous data set, only allowing the spectral model of η Car to vary. As suggested by the 4FGL catalog and previous analysis of the region (e.g. White et al., 2020; Martí-Devesa and Reimer, 2021), η Car, in the 4FGL catalog labeled 4FGL J1045-5940, was modeled as a point source with a log-parabola spectral model (see Equation 3.19). In the contemporaneous data set, η Car was detected with a TS value of 580. The resulting residual map after subtraction of all model components including η Car is shown in Figure 6.19a. The resulting best fit model has a spectral index of $\alpha = 2.34 \pm 0.07$, a curvature of $\beta = 0.17 \pm 0.03$ and a flux normalization at $E_0 = 2.01$ GeV of $\phi_0 = (3.5 \pm 0.2) \times 10^{-6}\,\mathrm{erg}^{-1}\,\mathrm{cm}^{-2}\,\mathrm{s}^{-1}$. In Figure 6.19b it is compared to the combined SED from the previous periastron passages as derived by White et al. (2020). The general flux level and shape are rather similar even though one has to note the smaller phase interval used in White et al. (2020).

6.5 Combined results and interpretation

The combined spectral result for the H.E.S.S. periastron observation corresponds to the phase interval from 0.97 to 1.05. Overall the H.E.S.S. result shows a good extension of the Fermi-LAT spectrum building a combined SED starting at 60 MeV up to

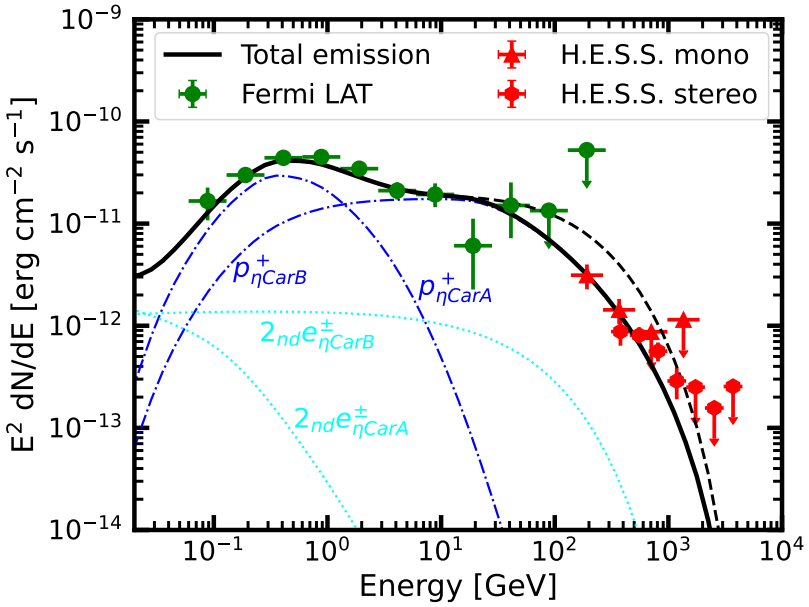

FIGURE 6.20: **Combined periastron spectrum of η Car**
The flux points for the periastron period are combined as derived in the previous sections. The total periastron model as well as the individual components from White et al. (2020) assuming an increased radial distance of 10 au is shown. The individual components denote the hadronic and secondary leptonic components from both winds. The dashed line denotes the unabsorbed model.

TeV energies (see Figure 6.20). The model from Ohm et al. (2015), which was further developed in White et al. (2020) was employed in order to constrain the acceleration processes responsible for the detected gamma-ray emission. It takes into account the formation of the two shocks associated with the two winds as described in Section 2.3.2. At each shock, both protons and electrons are injected, for which then a resulting gamma-ray spectrum is derived. The authors concluded, that for the HE and VHE regimes, only the contributions from protons from the two shocks play a significant role, with only a minor contribution from secondary electrons.

For this thesis, the predicted gamma-ray spectra before absorption of the periastron phase (phase 0.995 to 1.025) were taken from White et al. (2020). In their model, gamma-ray emission from the ballistic region right outside the shock cap is assumed. This results in a rather high absorption during the periastron passage as presented in their paper due to the close proximity of the two stars. This would imply a strong reduction of the H.E.S.S. flux around periastron, which is not in line with the findings in this thesis. Hence a reduced gamma-gamma absorption during periastron with respect to their model needs to be assumed. To effectively reduce the absorption the emission region of gamma-rays can be moved further out leading to a larger mixing region in the model. Hence transparency curves were calculated for spheres at several distances with respect to the center of mass of the binary system. The emission was assumed to be spherically symmetric and the geometry of the system adapted

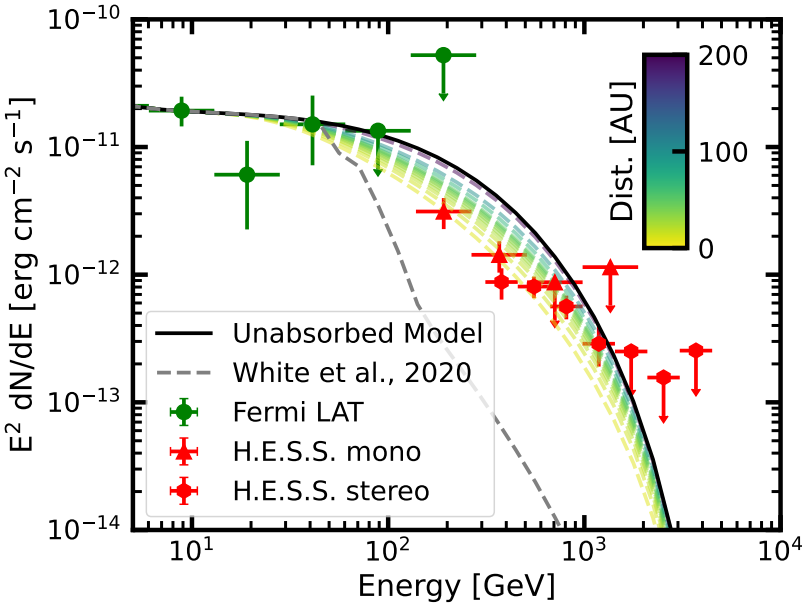

FIGURE 6.21: **Model spectrum for different emission regions compared to the combined SED**
The total predicted model flux from the periastron phase in White et al. (2020) is compared to the data assuming different absorption curves. The gamma-gamma absorption curves provided by Mischa Breuhaus were calculated assuming emission from different radial distances between 10 au and 200 au from the center of mass of the binary system. For comparison, also the absorbed and unabsorbed model from White et al. (2020) is shown.

to periastron assuming the stellar and orbital parameters described in Section 2.3.1. As a result, the total gamma-ray emission assuming the different absorption curves is presented in Figure 6.21.

From this, one can conclude that indeed the emission needs to originate from further out in the system compared to the assumptions in White et al. (2020), where no H.E.S.S. data was available. The H.E.S.S. flux level is well matched if the emission takes place at scales of 10 au to 20 au from the binary. In Figure 6.20 the individual components of the model are shown compared to the data assuming a radial distance of 10 au for the gamma emission. For this, the normalization of the flux from η Car A was slightly increased with regards to White et al. (2020) to better match the observed Fermi-LAT flux during the 2020 periastron. The H.E.S.S. emission can be explained by the hadronic emission from the side of η Car B and the secondary leptonic component plays only a negligible role for the full energy range.

Even though the adapted model matches the overall H.E.S.S. flux points well, the H.E.S.S. spectrum implies a harder spectral behavior than suggested by the model. To account for that as well, the cut-off energy of the proton spectrum can be varied. In order to derive the properties of the underlying proton spectrum the unabsorbed model spectrum of η Car B was fitted assuming an exponential cut-off power law (see Equation 3.18) proton spectrum using the Gamera package (Hahn et al., 2022).

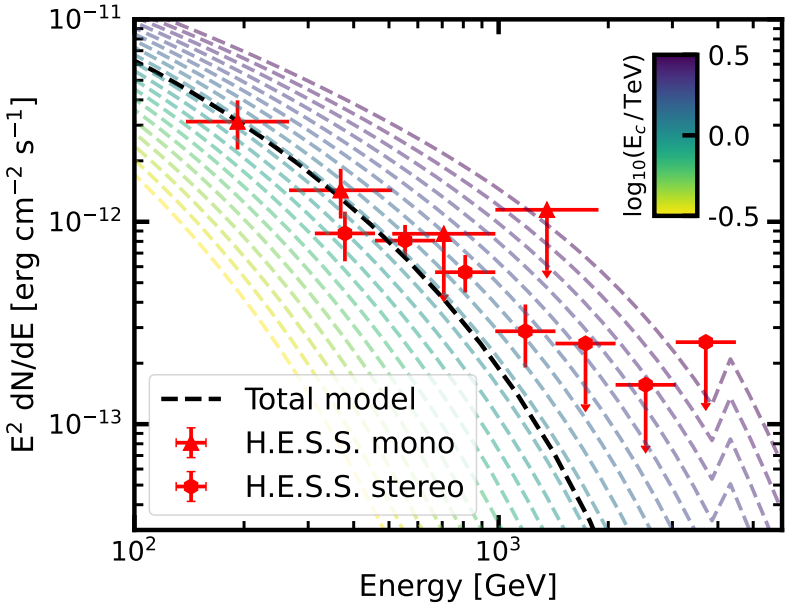

FIGURE 6.22: **Varying the cutoff energy for the hadronic component of η Car B**
The cut-off energy E_c is varied, keeping the index and normalization fixed. The cutoff energy was varied in 20 logarithmic bins between 0.32 and 3.2 TeV. The emission region was assumed to be at a distance of 10 au and the resulting absorption curve was used. The total model refers to the total emission from the original model without adapting E_c.

The normalization was fixed to be equal to the model spectrum at 1 GeV and the fit was run between 1 GeV and 3 TeV, resulting in an index of 1.8 and a cut-off at 1.1 TeV. Afterward, the cut-off energy was varied between 0.32 TeV and 3.2 TeV, keeping the index and normalization fixed. The resulting gamma-ray SEDs assuming emission from a radial distance of 10 au are compared to the high energy Fermi-LAT and H.E.S.S. flux points in Figure 6.22. As expected, a higher cut-off energy ∼1.5 TeV describes the shape of the H.E.S.S. SED better. Such a gradual increase in the cut-off energy for the protons accelerated at the shock of η Car B is still in line with the Hillas limit of 30 TeV (White et al., 2020) and the otherwise not precisely constrained model parameters.

With these estimates, it can be concluded that the model from White et al. (2020) describes the spectrum of the 2020 periastron passage well if the absorption region is moved out to a distance of ∼10 au, e.g. through a longer mixing length, and a higher cut-off for the hadronic component accelerated in η Car B is assumed. These findings are also in line with the light curve of η Car that shows no flux reduction for the periastron passage which would be expected for a strong gamma-gamma absorption during periastron. The increase of flux towards periastron yielding also higher maximum photon energies in the periastron SED can be explained by the higher density in the ballistic region during that period making p-p interactions more likely (Ohm et al., 2015; White et al., 2020).

6.6 Summary and conclusion

In this chapter the VHE gamma-ray emission of η Car was presented with special emphasis on the 2020 periastron passage. η Car is situated in a special FoV characterized by high and inhomogeneous NSB, testing the observational limits for IACTs. Therefore, special settings were needed to achieve stable data taking. This generated a large data set especially during the 2020 periastron passage for the phase interval from 0.98 to 1.05. For the mono analysis, a very careful treatment of noise factors had to be set up and applied to retrieve trustworthy results. This yielded a detection of η Car during the 2020 periastron passage above energies of 130 GeV complementary to the detection in the stereo analysis. Both, mono and stereo analysis were carried out independently and agree in the spectral shape and flux normalization, resulting in a periastron SED described as a steep power law with an index $\Gamma \approx 3.3$. However, the resulting spectra show a clear miss-match with the mono spectra published in H.E.S.S. Collaboration et al. (2020). This strongly hints at severe noise contamination in the published spectrum, which is not properly accounted for in the uncertainties.

The spectrum based on data taken at a phase of $\sim$0.2 matches the periastron spectrum with a slightly lower flux. The long-term light curve shows some variability over the orbit with a suppression of flux away from periastron and a small rise towards periastron. This is in line with light curves of the high energy Fermi-LAT component (Martí-Devesa and Reimer, 2021) and predictions from the model by Ohm et al. (2015). On shorter time scales during the periastron passage itself though no significant variability could be observed.

Using simultaneous Fermi-LAT data a multiwavelength SED was derived for the 2020 periastron passage. The combined spectrum was compared to the multi-component model by White et al. (2020). With modifications of the position of the emission region and the cutoff energy of the hadronic component, the model matches the observed flux points well. The H.E.S.S. data suggests, that the emission originates further out in the system at distances of $\sim$10 to $\sim$20 au and that the proton spectrum has a higher cutoff energy at $\sim$1.5 TeV. The good match of the resulting model is further evidence for the dominantly hadronic origin of the gamma-ray emission from η Car, with the H.E.S.S. detection tracing the protons accelerated on the side of η Car B.

A more precise measurement of upcoming periastron passages by CTA employing stereo analysis techniques for the full energy range can provide further evidence on that in the future. Nevertheless, H.E.S.S. can already constrain the VHE variability with observations around the 2025 periastron passage.

Chapter 7

Escape from Eta Carinae

Having established η Car as a potential proton accelerator to TeV energies in the previous chapter, the escape of CRs from it can be further investigated. In the model by White et al. (2020), already discussed in Section 2.3.3 and Section 6.5, a non-negligible amount of accelerated protons escapes the wind collision region, and could potentially interact with the surrounding material further out. The environment around η Car as introduced in Section 2.3 is extraordinary with many interesting features and structures. Therefore, some of them could play a role for gamma-ray emission associated to η Car acting as a target material for the escaping cosmic rays. On large scales, White et al. (2020) found already significant emission above the expectations from the 'sea' of diffuse cosmic rays associated with the molecular clouds in the CNC but did not provide further details. Recently, Ge et al. (2022) published the first analysis of the excess gamma-ray emission around η Car considering two Gaussian regions, for which significant emission of likely hadronic origin was found. They conclude that the emission could be connected to young massive stellar clusters in the region, such as Trumpler 14 and 16. Nevertheless, the authors were not able to rule out, that η Car or yet unknown cosmic ray sources are the acceleration sites of the cosmic rays producing the gamma-ray emission.

Following up on these papers a more detailed analysis of the emission from η Car and the surrounding excess emission is performed considering not only two but four different regions. These regions correspond to specific nearby molecular cloud structures connected to the Carina Nebula-Gum 31 complex. On smaller scales unresolvable by Fermi-LAT the Homunculus Nebula could also provide a target to produce gamma-rays. Therefore, a systematic analysis of cosmic ray transport escaping from η Car through surrounding features on hugely varying scales is attempted in the following.

My contribution to this work includes carrying out and interpreting the Fermi-LAT analysis presented in Section 7.2. Further, I evaluated the cosmic ray transport within the clouds and subsequently the feasibility of its origin from η Car (see Section 7.3.2). The discussion of the transport and radiative signatures from the wind region and Homunculus Nebula (see Section 7.3.1) was done by Mischa Breuhaus. The content has been submitted under the title "Escape from η Carinae" to A&A (Steinmassl et al., 2023).

7.1 Environment around η Car

The environment outside the orbit of the η Car system and up to ISM scales is highly complex and structured as introduced in Section 2.3. The following zones are considered:

- **The shock cap/wind collision region** – the region between the stars where the stellar winds collide and shocks are forming.
- **The pinwheel/wind region** – a high-velocity outflow with gradual mixing of the high and low-density winds of the two stars, ending on the scale of the cool molecular torus observed using ALMA (Smith et al., 2018).
- **The Homunculus** – the expanding shell associated to the great eruption of 1843 with an estimated total mass up to a few ten $M_\odot$ (Smith, 2008).
- **The Carina Nebula** – the star formation region containing several massive stellar clusters and 10^3–10^5 solar mass molecular clouds (see e.g. Rebolledo et al. (2015)).

Figure 7.1 illustrates these different scales graphically. The picture for the shock cap stems from the simulations of Parkin et al. (2011) and the one for the wind region from simulations from Clementel et al. (2014). The other three pictures are images from the paper of Smith (2005) in the case of the little Homunculus and observed by the Hubble Space Telescope (HST) and the VLT Survey Telescope in the case of the Homunculus and the Carina Nebula, respectively. Also shown are the approximate spatial scales associated to gamma-ray absorption in the radiation fields of η Car. Similar to Section 6.5, a spherical geometry of the γ-ray emission region was assumed. The two stars were taken to be at their maximum separation, the apastron position. The black line at the uppermost part of the figure shows the radii, at which more than 50 % of gamma-rays with an energy of 200 GeV are absorbed before reaching Earth. The peak absorption occurs close to 600 GeV, and the gray line shows the radial distances until which more than 10 % of these 600 GeV gamma-rays are absorbed (see also Figure 6.21). Therefore, gamma-ray absorption has to be taken into account for any gamma-ray emission within ∼200 au to the stars.

Protons and nuclei accelerated in η Car may interact in each of these regions and produce detectable gamma-ray emission. In the thin-target approximation, the expected fluxes are proportional to the product of the residence time and average density. All of these regions can potentially produce detectable gamma-ray signatures if the transport conditions are appropriate - as discussed in Section 7.3.1 and Section 7.3.2. For the largest scales of the Carina Nebula, additional CR sources may also contribute significantly, as discussed in Section 7.4.

As detailed in Rebolledo et al., 2015 and in Section 2.3.4, four clouds with masses of $\approx 10^4 - 10^5\,M_\odot$ are detected in CO maps and also dust measurements. These are labeled Southern Cloud, Northern Cloud, Southern Pillars, and Gum 31. From

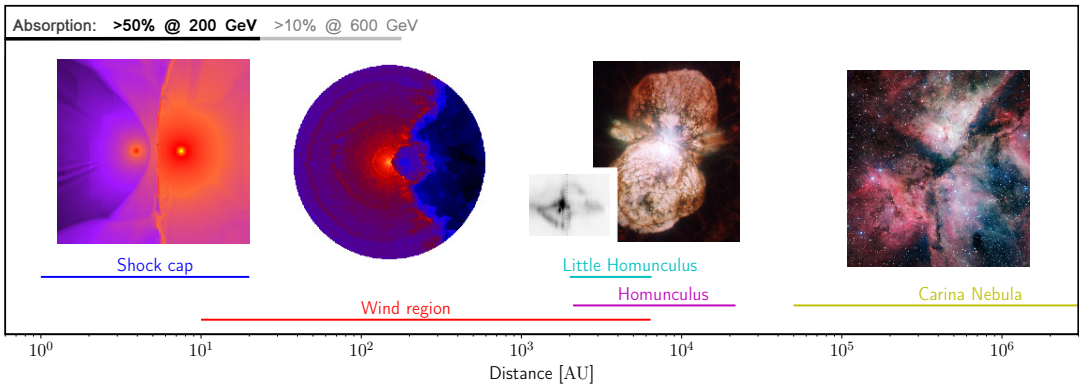

FIGURE 7.1: **Distances of different possible emission regions around Eta Carinae**
Because some regions such as the large or the little Homunculus Nebula are asymmetric, or their size can change over time such as for the shock cap, the sizes shown cover a large range of values. The different extensions are: 1 to 20 au (shock cap), 10 to 6.4×10^3 au (wind region), 2×10^3 to 6.5×10^3 au (little Homunculus), 2.1×10^3 to 21.7×10^3 au (Homunculus) and $> 50 \times 10^3$ au (Carina Nebula). Also shown are the zones corresponding to significant gamma-ray absorption. The 600 GeV case corresponds to the maximum absorption. The individual images are taken from Parkin et al. (2011), Clementel et al. (2014), Smith (2005), HST, ESO. Figure provided by Mischa Breuhaus and Jim Hinton.

the velocity maps presented in that paper, a clear connection to the CNC-Gum 31 complex is evident. Whilst the emission of the binary system up to the scale of the Homunculus is unresolvable with Fermi-LAT, these clouds are resolvable. Hence with these, the cosmic ray density around η Car can be probed as discussed in Section 7.2 and Section 7.3.2.

7.2 Fermi analysis results

The approach to Fermi data analysis follows closely that of White et al. (2020). The data selection was based on the latest Fermi-LAT Pass 8 data starting from Aug 4th, 2008 (MET 239557417) to Oct 26th, 2022 (MET 688521600). Events over an energy range of 500 MeV (chosen to avoid poorly reconstructed events at lower energies) and 500 GeV were included from a region of interest (ROI) of 10° by 10°, centered at the nominal position of η Car and aligned in galactic coordinates. Data were chosen according to the SOURCE event class (*evclass=128*) with FRONT+BACK event types (*evtype=3*). Time periods in which the ROI was observed at zenith angle greater than 90° were excluded to minimize contamination from atmospheric gamma-rays from the Earth. The lifetime and exposure were corrected accordingly. Further, the time interval between MET 542144904 and 550885992 was excluded due to potential contamination by the bright nova ASASSN-18fv, detected with Fermi-LAT about 1° away from η Car in that time period (Aydi et al., 2020).

Parameter	Value
Data release	P8R3
IRFs	P8R3_SOURCE_V3
ROI data width	10°
ROI model width	15°
Bin size	0.1°
zmax	90°
Coordinate system	GAL
Minimum energy	500 MeV
Maximum Energy	500 GeV
MET start	239557417
MET stop	688521600
MET excluded (ASASSN-18fv)	542144904 – 550885992
evclass	128
evtype	3
Galactic diffuse template	gll_iem_v07.fits
Isotropic background component	iso_P8R3_SOURCE_V3_v1.txt
Fermi-LAT catalogue	4FGL-DR3 (gll_psc_v29.fit)

TABLE 7.1: **Configuration used for the Fermi-LAT analysis**

Data were analysed utilising *Fermitools* (version 2.2.0) and *FermiPy* (version 1.2) (Wood et al., 2017). The model of sources surrounding η Car was taken similar to White et al. (2020), which includes all sources in the ROI from the *Fermi*-LAT 12-year source catalog, the third data release of 4FGL (Abdollahi et al., 2022b), with the exception of the unidentified source 4FGL J1046.7-6010. Further, the up-to-date Galactic diffuse background template and isotropic component files together with the IRFs matching the event selection were employed. The exact details of the analysis are summarized in Table 7.1.

In White et al. (2020) an additional diffuse source was added to the model based on the CO survey of Dame et al. (2001). In this work, the model is split into four individual clouds, following the region definitions as outlined in Rebolledo et al. (2015) and described in the previous section and in Section 2.3.4. The four templates are accordingly labeled Southern Cloud, Northern Cloud, Southern Pillars and Gum 31 and can be seen as an overlay in Figure 7.2. Each cloud is included in the model as a diffuse component with a power-law spectral shape.

Optimization of the model was performed in an iterative fashion. First, the normalization of the list of the up to 5 brightest sources with a predicted number of counts amounting to 95 % of the total predicted counts of the model are freed and a simultaneous fit is performed. Next, the normalization of the sources with more than 1 predicted count and not included in the first step was performed individually. Finally, the shape and normalization of all sources with a TS exceeding 25 in the previous fits were freed and a simultaneous fit was performed. The same process was repeated but allowing up to ten sources for the first optimization step. After optimizing the model, the cloud component spectral shapes were fixed in a

Cloud Name	Spectral Index	Energy Flux [$\mathrm{erg\,cm^{-2}\,s^{-1}}$]	TS
Southern Cloud	2.31 ± 0.05	$(2.4 \pm 0.3) \times 10^{-11}$	277
Northern Cloud	2.25 ± 0.06	$(2.0 \pm 0.2) \times 10^{-11}$	211
Southern Pillars	2.54 ± 0.06	$(1.8 \pm 0.2) \times 10^{-11}$	326
Gum 31	2.25 ± 0.06	$(2.3 \pm 0.3) \times 10^{-11}$	250

TABLE 7.2: **TS values and power-law spectral properties of the molecular clouds**
The resulting best-fit spectral properties assume a power-law spectral model. The energy flux is derived by integrating from 500 MeV to 100 GeV.

first fitting iteration freeing η Car (4FGL J1045.1-5940) and the normalization of all sources within a 3° radius. As suggested by the 4FGL catalog, and previous analysis of the region (White et al., 2020; Martí-Devesa and Reimer, 2021), η Car was modeled as a point source with a log-parabola spectrum (see Equation 3.19). This yielded a best fit log parabola model for η Car with $\alpha = 2.30 \pm 0.02$, $\beta = 0.11 \pm 0.01$, $\phi_0 = (2.43 \pm 0.07) \times 10^{-6}$ $\mathrm{cm^{-2}\,erg^{-1}\,s^{-1}}$ and $E_0 = 2.11$ GeV.

In a second fitting iteration η Car and all other previously free sources were fixed and the normalization and spectral shape of all four clouds were freed. Hence any miss-association of flux between the close Southern and Northern Clouds and the bright η Car could be minimized. Following the fitting for η Car and the clouds, a SED was generated for the source of interest. Whereas a similar event selection approach was taken in Ge et al. (2022), their main result is based on the addition of two Gaussian disks in the fit instead of the cloud templates employed in this work.

The four clouds were each detected with significant excesses and TS values of > 200. The exact values are summarised in Table 7.2. The residual emission in the ROI could be clearly reduced with the addition of the cloud templates, as shown in Figure 7.2. Here, all Fermi 4FGL sources and selected massive stellar clusters from Preibisch et al. (2011) are also indicated.

The resulting best-fit spectral parameters can be seen in Table 7.2. The flux points of the four individual clouds are shown in Figure 7.3 comparing it to the derived spectrum of η Car. The spectral shapes and normalizations determined for the Southern Cloud, Northern Cloud and Gum 31 regions show a reasonable level of consistency, with a spectral index between 2.2 and 2.3. In contrast, the Southern Pillars are described by a slightly softer spectrum, mostly caused by an apparent cutoff above 20 GeV. Below that energy, the derived flux points are quite consistent with the other three clouds. Different spectral models for each cloud (broken power law and log-parabola) were tested by fitting the SEDs of each cloud. This yielded up to 10 % difference on the integrated energy flux, which can be considered as a contribution to the systematic uncertainty of the analysis.

The inner regions introduced in Section 7.1 are not resolvable in gamma-rays. With the 68 % containment radius of the Fermi-LAT PSF above 20 GeV being $\sim 0.1°$

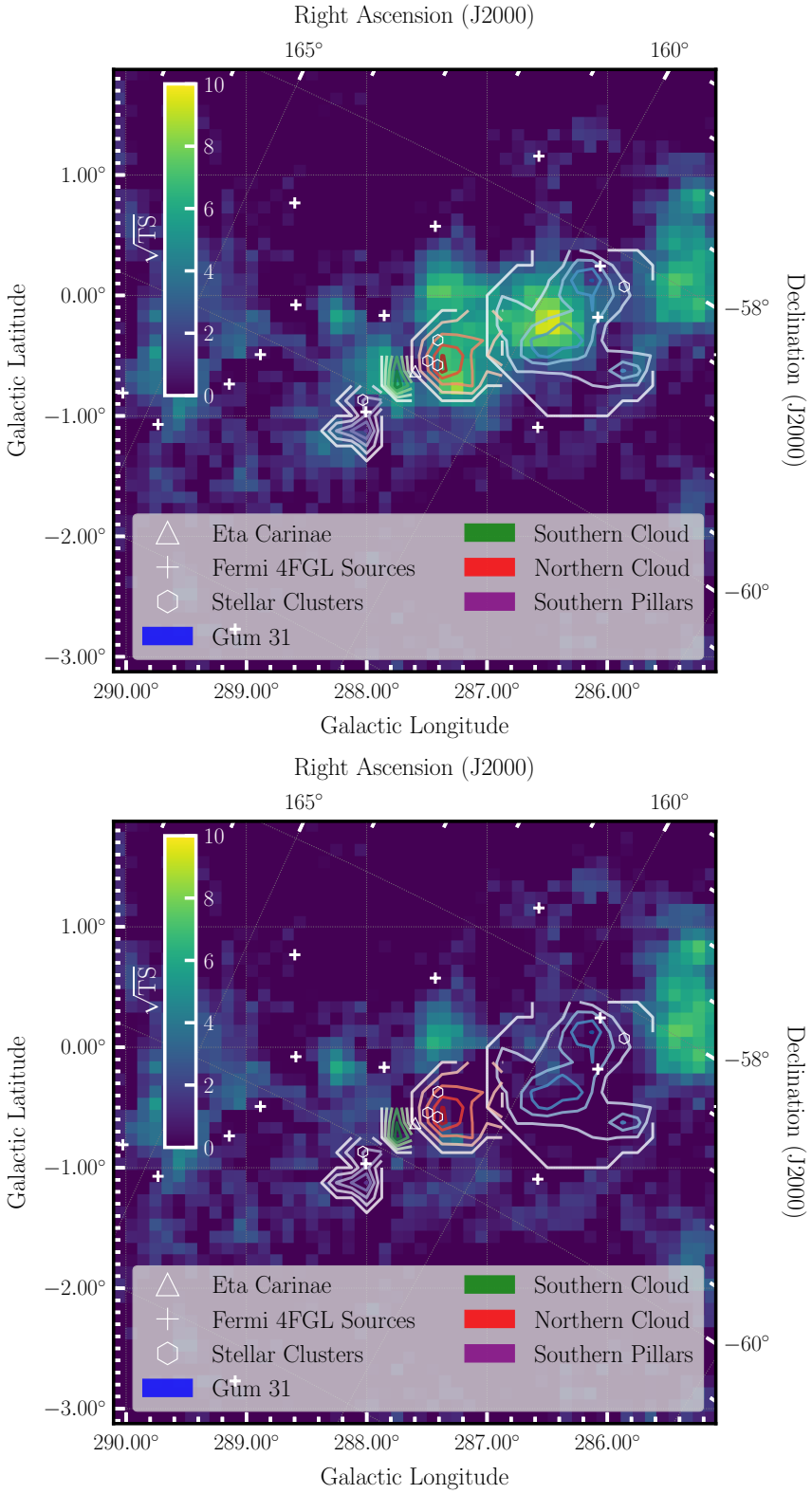

FIGURE 7.2: **Residual significance maps of the Fermi analysis** The significance is here calculated as $\sqrt{TS}$. In the upper panel, the map without the addition of the cloud templates to the model is shown, whereas they are included in the lower panel. In each plot the cloud templates are overlaid by colored contours, also depicting the gas density distribution. Additionally, all other 4FGL sources highlighting η Car are marked together with massive stellar clusters from Preibisch et al. (2011).

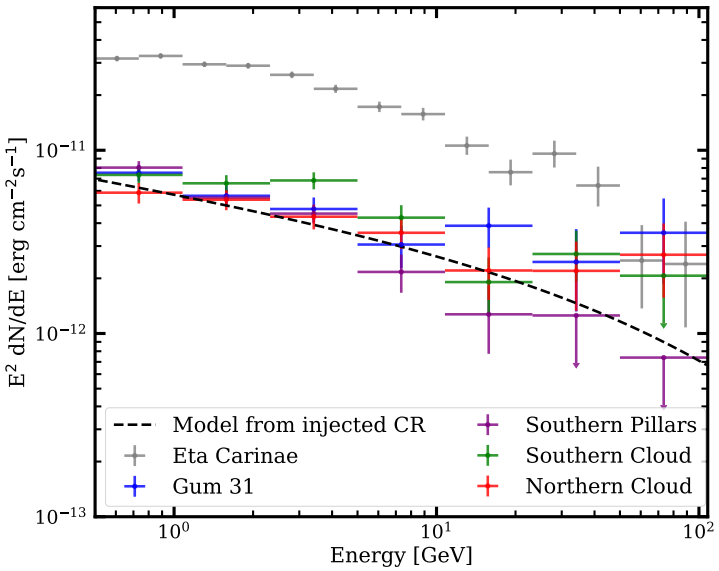

FIGURE 7.3: **Spectra of the four clouds as derived by the Fermi LAT analysis.**
For comparison, the spectrum derived for η Car is also shown in grey. Additionally, a model derived from an injected cosmic ray (CR) spectrum is shown. The cosmic ray spectrum is modeled as a power law with index 2 and an exponential cutoff at 2 TeV. The normalization has been scaled arbitrarily.

(Abdollahi et al., 2020), the physical size of this region is at least ∼4 pc or larger depending on the energy. An upper limit on the gamma-ray flux originating from this inner region can hence be only estimated from the quiescent baseline component of the η Car gamma-ray flux. Long-term light curves show only mild variability (e.g. White et al., 2020; Martí-Devesa and Reimer, 2021), with the gamma-ray flux never dropping below 60 % of the mean integrated flux level. This gives a baseline energy flux of $(5.6 \pm 0.3) \times 10^{-11}\,\mathrm{erg\,cm^{-2}\,s^{-1}}$ integrated from 500 MeV to 100 GeV.

7.3 Interpretation

7.3.1 Propagation of CRs around η Car and expected emission

Propagation in the wind region Simulations by Madura et al. (2012) (see also Parkin et al. (2011)) find that the fast wind from η Car B carves out a low-density channel with a large opening angle in the direction of the apastron position. Only particles that find themselves in this channel can expect to escape the system since any particle which gets captured by the wind of η Car A will be destroyed in collisions with the dense wind material due to the high energy losses. The large low-density opening is only interrupted shortly by the periastron passage by material from the high-density wind of η Car A. This might lead to enhanced mixing between the two winds and to enhanced emission during the periastron phase.

After the CRs are accelerated in the shock at the side of the companion star η Car B, they will be dragged by the ballistic outflow. This is the so-called ballistic region. Eventually, the flow will be dominated by the wind from the stars and the CRs and follow the flow from the wind of η Car B. Potentially, some fraction of particles might migrate into the high-density wind of η Car A. For particles advected by the low-density wind of η Car-B, the advective energy losses are the dominant loss mechanism. Although the magnetic fields are toroidal at large distances, a sufficient amount of turbulence could be created to allow the particles to start diffusing after some distance from the stars. If and at which distances the transition from advective to diffusive transport occurs depends on the details of the plasma flow. The adiabatic losses suffered by the accelerated CRs during the advective transport phase will have an impact on the resulting gamma-ray emission from escaping particles.

The maximum particle energy due to the Hillas limit at the shock of η Car B is ∼30 TeV (White et al., 2020). The detection of the system by H.E.S.S. (H.E.S.S. Collaboration et al., 2020) could therefore restrict the spatial extent of the emission region, but the details depend crucially on where the transition from the ballistic outflow to advective and from advective to diffusive transport takes place. Due to the eccentricity of the orbit, the extent of the shock cap varies from ∼1 au at periastron to ∼20 au at apastron. If the transport at radial distances above $r_0 = 20$ au is advective, e.g. protons of 30 TeV will cool down to between 1.4 TeV and 630 GeV when they reach the little Homunculus. For a larger value of $r_0 = 40$ au, these numbers are 2.2 TeV and 1 TeV, respectively. Therefore, completely adiabatic transport is an issue for maximum particle energies as well as the energetics of escaping particles. The transport in the wind region has to be diffusive already at short distances for the escaping particles to be important for potential gamma-ray emission further out.

For the production of ∼1 TeV gamma-rays, CR protons of several TeV are needed. This implies that the emission has to be produced within 100 au or 200 au if the transport is dominantly advective until such distances. Additionally, any observation of time variability of the TeV gamma-rays can put limits on the size of the emission region.

In the wind region close to the stars, the absorption of gamma-rays due to pair production plays an important role. In this work, only the assumption of spherically symmetric emission is discussed. Due to the change in the stellar position, there is an orbital variation in the absorption. It is strongest between phases 0.9 and 0.2, however, for a radial distance of 20 au, the differences are already below 7 % and they decrease quickly moving outwards. The small phase dependence of the absorption and an emission region at a distance of ∼20 au is in line with the conclusions based on the H.E.S.S. data discussed in Section 6.5. Therefore, the phase dependence of the absorption is ignored and the representative case for phase 0.5 is used as an average value.

In Figure 7.1 the absorption for spherically symmetric emission at phase 0.5 for

two different energies is shown. The case of 600 GeV corresponds roughly to maximum absorption. Whereas at 20 au, close to half of the emission is absorbed, at 200 au more than 90 % of the gamma-rays reach Earth.

The Homunculus nebula When the CRs leave the wind region, they encounter the little Homunculus nebula. The total mass of the little Homunculus is likely $\sim$0.1 $M_\odot$ (Smith, 2005). However, the by far more massive structure in the close vicinity of η Car is the large Homunculus nebula, with more than 10 $M_\odot$ (Smith et al., 2003) and likely between 15 $M_\odot$ and 35 $M_\odot$ (Smith and Ferland, 2007). This huge amount of mass could lead to a significant amount of gamma-ray emission when the escaping CRs interact with the high-density shell.

To model emission from the Homunculus, the escaping CR spectrum from the model of White et al. (2020) was used. For simplicity, possible spectral changes caused by the propagation through the wind region are ignored, because the exact propagation properties are unknown and are impossible to separate observationally from spectral changes by the propagation through the Homunculus itself. After leaving the little Homunculus nebula, the CRs are expected to simply pass through the hollow space until reaching the Homunculus shell. Because the shell is only $\sim$600 au thick, the total emission is below $10^{13}\,\mathrm{erg\,cm^{-2}\,s^{-1}}$ at all energies if the CRs directly pass through the thin shell. This is negligible compared to the emission detected by Fermi-LAT. However, the produced emission in the Homunculus can be much larger if the particles diffuse more slowly through the shell. A lower limit on the diffusion coefficient can be derived by assuming Bohm diffusion. Unfortunately, the magnetic field in the shell is unknown and difficult to constrain and values of 100 µG or even higher could be possible (Aitken et al., 1995). The energy dependence of the diffusion coefficient is considered to have the following form:

$$D(E) = D_0 \times \left(\frac{E}{1\,\mathrm{GeV}}\right)^{\alpha}. \tag{7.1}$$

The dotted blue curve in Figure 7.4 shows the emission produced in the Homunculus for $D_0 = 9 \times 10^{22}\,\mathrm{cm^2\,s^{-1}}$ and $\alpha = 0.5$. As can be seen, interactions in the Homunculus nebula of escaping CRs could account for a significant amount of steady-state gamma-ray emission. Even models, where the low energy gamma-ray emission is to very large parts produced in the Homunculus are possible. This would imply that no particle acceleration occurs at the shock of η Car A due to, e.g. low Mach numbers. Figure 7.4 shows the emission produced by particles accelerated at the shock of η Car B from the model of White et al. (2020), with and without absorption. Additionally, the emission from the Homunculus is derived for $D_0 = 9 \times 10^{21}\,\mathrm{cm^2\,s^{-1}}$, $\alpha = 1$ and a factor of 1.1 more escaping CRs compared to the model of White et al. (2020). The combined emission matches very well the whole Fermi-LAT data. In such a scenario, the weak phase-dependent variability is entirely

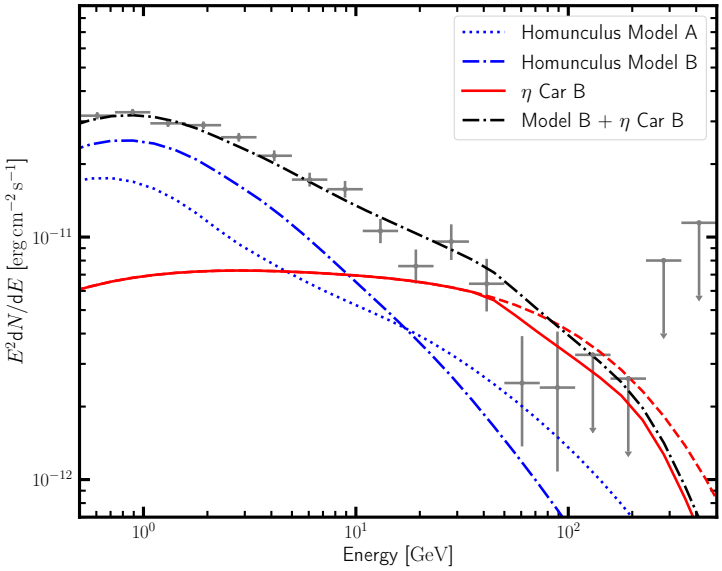

FIGURE 7.4: **Possible emission from η Car and the Homunculus together with Fermi-LAT data**
The blue curves show emission from the Homunculus for different diffusion properties of the escaping CRs. The dotted curve (Model A) is for $D_0 = 9 \times 10^{22}\,\mathrm{cm^2\,s^{-1}}$ and $\alpha = 0.5$. The dashed-dotted curve (Model B) is for $D_0 = 9 \times 10^{21}\,\mathrm{cm^2\,s^{-1}}$, $\alpha = 1$ and a factor of 1.1 more escaping CRs compared to the model from White et al. (2020). The red solid line shows the emission from η Car produced by particles accelerated at the shock towards η Car B from White et al. (2020) (the red dashed line is without absorption). The dashed-dotted black curve shows the combined emission from η Car B and Model B. Figure provided by Mischa Breuhaus.

produced by changes in the red curve. The assumed diffusion coefficient in the Homunculus is well above the case of Bohm diffusion for a magnetic field of 100 µG. CRs below a few tens of GeV interact entirely in the nebula.

A model for particle acceleration solely at the companion shock together with steady emission from the Homunculus by the escaping CRs can also account for the hard non-thermal X-ray emission because in the model from White et al. (2020) the hard X-rays are nearly exclusively accounted for by electrons accelerated at the shock from η Car-B. Since the variability in the Fermi-LAT energy regime is only moderate, at least ∼60 % of the emission can be produced by a steady state source. This also includes CRs potentially accelerated at the outgoing blast wave of 1843 (Ohm et al., 2010; Skilton et al., 2012). Disentangling these different components is impossible from the gamma-ray data alone and more information, for example about the propagation through the different regions, is required.

7.3.2 Propagation in the Carina Nebula

Cosmic rays escaping from η Car and its close neighborhood eventually propagate into the Carina Nebula. There they encounter the molecular clouds described in

Section 2.3.4 as a potential target material to produce gamma-rays. The main large cloud structures of the Carina Nebula show indeed significant gamma-ray emission (see Section 7.2) which could be a clear signature of this.

In Figure 7.3 additionally, a model gamma-ray spectrum derived from an injected cosmic ray spectrum following a power-law with exponential cutoff is shown. The assumed cosmic ray spectrum has an index of 2 and an exponential cutoff at 2 TeV similar to the proton spectrum derived for η Car in White et al. (2020). To compute a gamma-ray spectrum the parametrizations from Kappes et al. (2007) were employed and energy-dependent transport leading to a softening of $-1/3$ was assumed. The resulting gamma-ray spectrum shows a similar spectral behavior as it is observed from the 4 clouds themselves.

To further probe the point, if the gamma-ray emission could be caused by cosmic rays escaping from η Car the cosmic ray density for these four clouds is estimated. The cosmic ray density in a certain region can be calculated from the gamma-ray luminosity and cloud mass following Aharonian et al. (2019) as

$$w_{CR}(\geq 10E_\gamma) = 1.8 \times 10^{-2} \left(\frac{\eta}{1.5}\right)^{-1} \left(\frac{L_\gamma(\geq E_\gamma)}{10^{34}\,\mathrm{erg\,s^{-1}}}\right) \left(\frac{M}{10^6 M_\odot}\right)^{-1} \mathrm{eV\,cm^{-3}}\,. \quad (7.2)$$

Here, the parameter η accounting for the presence of heavier nuclei is assumed to be 1.5 and the gamma-ray luminosity L_γ above 500 MeV is derived from integrating the gamma-ray flux and assuming the typical distance to the Carina Nebula of 2.3 kpc. The minimum gamma-ray energy of 500 MeV translates approximately to CR energies above 5 GeV. The masses are assumed to follow the dust mass estimate from Rebolledo et al. (2015), Table 2 based on Herschel infrared Galactic Plane Survey (HiGAL, Molinari et al. (2010)) data. The mass uncertainty derived from dust maps is mostly dominated by uncertainties in temperature derivation (∼10 %) (Urquhart et al., 2018), the HiGal survey flux (∼5 %) (Molinari et al., 2016) and the local gas-to-dust mass ratio assumption. According to Giannetti et al. (2017) the local variation of this can be estimated to be on the order of 20 %. Hence an assumed uncertainty of 25 % on the mass is adopted, not reflecting systematic uncertainties. Systematic uncertainties especially from the gas-to-dust mass ratio could be up to a factor of a few.

The resulting CR density profile can be seen in Figure 7.5. The physical extent is visualized by the error bars as the minimum and maximum distance from η Car. The conversion to a physical distance scale assumes that all clouds are located in a plane at the same distance.

Assuming η Car as the origin of the CRs, this would imply a $1/r$ profile similar to what is observed within massive stellar clusters (Aharonian et al., 2019),

$$w(r) = w_0(r/r_o)^{-1}. \quad (7.3)$$

The profile is normalized at $r_0 = 10$ pc and a value of $w_0 = 0.48 \pm 0.09\,\mathrm{eVcm^{-3}}$ can

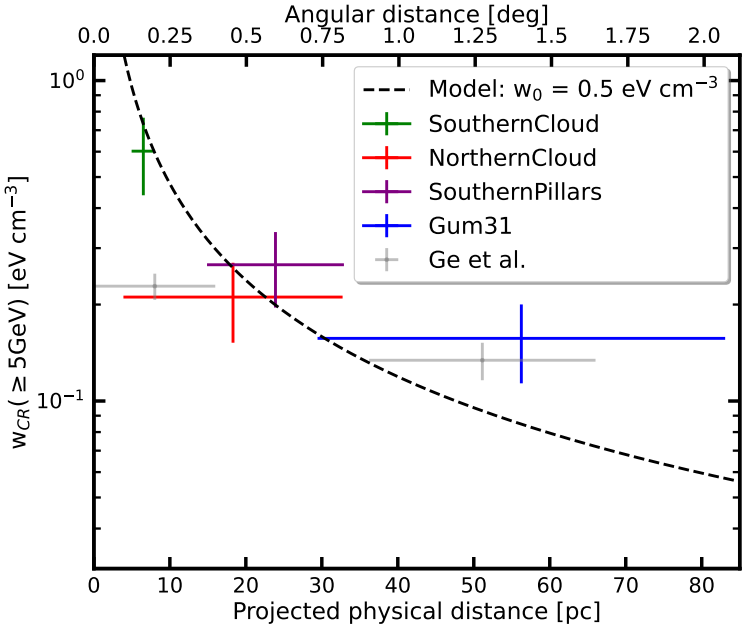

FIGURE 7.5: **The CR density for each of the 4 clouds as function of distance to η Car**

The angular distance has been transformed to a physical using a distance of 2.3 kpc. Distance errors depict the maximum extent of the cloud templates. A $1/r$ type profile as described in Equation 7.3 has been fitted to the data points and is shown by the dashed line. For comparison, the CR densities as derived in Ge et al. (2022) for their regions A & B are shown in light grey.

be derived from a fit to the CR density profile of the clouds. Using the derived maximum energy flux and mass for the Homunculus gives an upper limit on the cosmic ray energy density of $\sim 10^3$ eVcm^{-3}. At a distance of $\lesssim 0.1$ pc, this does not constrain the derived 1/r behavior. Assuming an integration radius of 60 pc, corresponding to the outer edge of the emission seen in the CNC-Gum 31 complex, this would imply a total energy of CR protons of $W_p = 5 \times 10^{48}$ erg. The diffusion time can be calculated from the maximum distance R_{max} cosmic rays have propagated and the diffusion coefficient. For the emission associated to the molecular clouds, R_{max} is at least 60 pc and the energy-dependent diffusion is assumed to follow Equation 7.1.

Taking a typical galactic diffusion coefficient of $D_0 = 3 \times 10^{28}\,\mathrm{cm^2\,s^{-1}}$ at 1 GeV (Strong et al., 2007) and $\alpha = 0.4$, the diffusion time for 5 GeV cosmic rays is $\sim 5 \times 10^3$ yr. This would imply a cosmic ray power of $\sim 3 \times 10^{37}\,\mathrm{erg\,s^{-1}}$ escaping from η Car. A more realistic value of $\sim 5 \times 10^{35}\,\mathrm{erg\,s^{-1}}$, derived from the escaping cosmic ray flux produced in η Car, would suggest slower diffusion with $D_0 = 5 \times 10^{26}\,\mathrm{cm^2\,s^{-1}}$.

The lower limit on the diffusion coefficient at $D_0 = 5 \times 10^{25}\,\mathrm{cm^2\,s^{-1}}$ is set by the age of the system, $\sim 2 - 3 \times 10^6$ years (Mehner et al., 2010). Nevertheless, if assuming diffusion with $D_0 = 5 \times 10^{26}\,\mathrm{cm^2\,s^{-1}}$, the diffusion time through the northern cloud with a diameter of 30 pc is $\sim 1.4 \times 10^5$ yr. On the other hand, the life time τ_{pp} of the diffusing protons is following Hinton and Hofmann (2009) depending on the

number density n in cm^{-3}, roughly $\tau_{\mathrm{pp}} = 3 \times 10^7 n^{-1}\,\mathrm{yr}$ (see also Equation 2.14). This results for the Northern Cloud in $\tau_{\mathrm{pp}} \approx 1.0 \times 10^5\,\mathrm{yr}$, assuming a mass of the Northern cloud of $1 \times 10^5\,\mathrm{M}_\odot$ (Rebolledo et al., 2015) and if the cloud volume is approximated as a sphere. Consequently, the thin target approximation does not hold anymore. Hence faster diffusion would be needed, leading to a higher total cosmic ray power, that can hardly be purely produced by η Car in its current state.

Therefore, either a higher cosmic ray output from η Car in the past is needed or additional contribution from other sources in the CNC. Good candidate sources would be massive stellar clusters, such as the close-by Trumpler 14 or other massive binaries situated in the star-forming regions of the CNC.

7.4 Summary and conclusion

The η Car system and its surroundings are extremely complex, with the wind region, the little and large Homunculus nebulae, and molecular clouds nearby. For a significant amount of particles to escape from the system, the CRs have to diffuse in the low-density region carved by the wind from η Car B, otherwise, they will either interact in the wind region or lose their energy via adiabatic losses. Particles diffusing into the high-density region can lead to an additional contribution to the total gamma-ray spectrum. Depending on the propagation properties, the interaction of escaping particles in the Homunculus nebula can account for a very large fraction of the total gamma-rays.

The observed emission of η Car on scales not resolvable by Fermi-LAT can be explained well by a variety of different models. Additionally to the model described in White et al. (2020), this also includes models solely accelerating particles at the shock towards η Car-B, with the lower energy Fermi-LAT emission dominantly produced in the Homunculus (see Section 7.3.1). Therefore, it seems likely that contributions from several zones account to the overall emission, which has to be included in any future model. However, the determination of the exact amount of emission produced in each region depends on the details of the CR transport and remains a challenge.

Escaping CRs from η Car can also interact in the molecular clouds of the Carina Nebula. As shown in Section 7.3.2, the derived radial profile of the cosmic ray densities seems to be indicative of an origin of cosmic rays from η Car . However, η Car would have had to be more powerful in the past to account for the whole emission or additional CR sources are needed. The problem for assessing this is the long propagation time of particles since η Car is highly variable on short timescales of $\sim$100 yr. The properties of the system before the great eruption in the 19th century are completely unknown, but the CR output from the binary system depends on the stellar parameters and could hence have been different in the past. Potential

other CR sources are Trumpler 14, Trumpler 16, or other massive binaries. However, escaped CRs from η Car could still provide a non-negligible contribution to the gamma-ray emission from the clouds.

The observations of η Car at several hundreds of GeV and TeV energies by Imaging Atmospheric Cherenkov Telescopes as presented in Chapter 6 are also of great interest. This part of the spectrum is affected by absorption and potential adiabatic losses. Accurate, potentially time-dependent observations around periastron, therefore help to investigate the propagation properties close to the stars and to constrain the emission regions, as discussed in some detail in Section 6.5. Additional observations with H.E.S.S. and more sensitive observations with the future CTA observatory might provide crucial information to help unravel the physics of the fascinating binary system η Car.

Chapter 8

Summary of results

In this thesis, the reconstruction pipeline of H.E.S.S. within the HAP framework was validated in an end-to-end approach. Subsequently, the scientific results from the FlashCam camera installed at the 28 m telescope in the autumn of 2019 could be successfully verified. A monoscopic analysis configuration for data from FlashCam was set up and expanded by a novel sensitive cleaning approach. The mono analysis was, together with stereo and Fermi-LAT analysis approaches, applied to data of two special binary systems, the recurrent nova RS Oph and the colliding wind binary η Car. The gamma-ray emission detected from these two systems gave strong evidence for their nature as powerful hadronic accelerators. The main findings of this thesis will be summarized in the following:

- The first end-to-end validation effort of the full 5-telescope H.E.S.S. array within the HAP chain revealed significant mismatches between the simulations and the observed data. The validation effort had the goal to resolve these mismatches systematically using a bottom-up approach. It was focused on the hardware phase after the installation of FlashCam at CT5 in autumn 2019. The main parameters which needed to be adapted in the simulations were the aerosol level of the atmosphere, the trigger threshold of the telescopes, the mirror reflectivity and the optical PSF. By matching these to the measured observation conditions and the derived realistic hardware settings, a good level of consistency could be achieved for the low-level trigger behavior as well as the image properties after cleaning.

- After the validation of the simulations, an analysis configuration for the mono analysis was derived. With this configuration, the FlashCam camera installed at CT5 could be scientifically validated making use of known gamma-ray sources. This yielded a validation of the reconstruction and gamma-hadron separation methods and high-level scientific products. Most notably, the flux of the standard candle of TeV astronomy, the Crab Nebula, matched the reference flux (H.E.S.S. Collaboration et al., 2006b) within 12 %, a good match taking into account the systematic uncertainties inherent to IACT analysis. Furthermore, tests on the bright AGN PKS 2155-304 showed a good description of the PSF with respect to the data. Consequently, scientific results obtained with FlashCam can be deemed validated.

◊ A novel cleaning approach based on the timing information in showers was introduced for H.E.S.S. It made use of the well-tested clustering algorithm DBSCAN. The time-based cleaning was optimized with the goal to keep as much shower information as possible, while not being susceptible to noise. The derived best settings increase the shower information after cleaning significantly. Therefore, this cleaning method shows a lot of potential to improve the reconstruction and gamma-hadron separation of low-energetic showers.

◊ The recurrent nova RS Oph became the first nova with detected TeV emission during its outburst and the subsequent follow-up campaign with H.E.S.S. in August 2021. The analysis with both the validated mono and stereo chain returned a strong signal, allowing for a time-resolved tracing of the outburst. In this thesis special emphasis was laid on the mono analysis. The VHE light curve showed an increasing flux until night 3 and a power-law decay afterward. Whereas the behavior is similar in the HE light curve, the H.E.S.S. emission peaks about two days after the Fermi-LAT emission. The similar shape of the H.E.S.S. and Fermi light curves implies a common origin of the emission over the whole MeV to TeV regime, with the delay reflecting the expected finite acceleration time.

◊ The broadband SED of RS Oph combining Fermi-LAT, H.E.S.S. mono and stereo measurements presents a smooth spectral behavior over several orders of magnitude. Time-dependent modeling of the combined SED favored a hadronic origin of the gamma-ray emission, naturally explaining the observed spectral shape. This strongly supports previous claims of novae as proton accelerators. The maximum photon energy of $\sim$1 TeV closely matches theoretical limits for such systems. Therefore, efficient cosmic ray acceleration at the fast shock driven by the thermonuclear explosion is needed. Furthermore, this has important implications for supernova explosions, strongly supporting the hypothesis, that the primary component of galactic cosmic rays originates in core-collapse supernova remnants.

◊ The CWB η Car was extensively monitored with H.E.S.S. over the past years with special emphasis on the 2020 periastron passage. Situated in a FoV heavily influenced by bright and inhomogeneous NSB, the analysis had to be done with special care, especially for the mono reconstruction. This tested the limits of the mono reconstruction technique for IACTs. Nevertheless, it eventually yielded a detection of η Car during the 2020 periastron passage above energies of 130 GeV complementary to a detection with the stereo analysis.

◊ The resulting SED of η Car during periastron from mono and stereo analysis is described as a steep power law with an index $\Gamma \approx 3.3$. In comparison with the mono spectra published in H.E.S.S. Collaboration et al. (2020), the spectra derived in this work show a considerably lower flux, strongly hinting at severe

noise contamination in the published spectra. The VHE long-term light curve showed some variability over the orbit with a suppression of flux away from periastron and a small rise towards periastron.

◊ The broadband SED of η Car including simultaneous Fermi-LAT and H.E.S.S. data was compared to the multicomponent model by White et al. (2020). The H.E.S.S. data suggests, that the emission originates further out in the system at distances of ∼10 to ∼20 au and that the spectrum of protons accelerated in the wind of η Car B has a higher cutoff energy at ∼1.5 TeV. The good match of the resulting adapted model is further evidence for the dominantly hadronic origin of the gamma-ray emission from η Car, with the H.E.S.S. detection tracing the protons accelerated at the shock associated with the wind from η Car B.

◊ A significant diffuse excess associated with the 4 large molecular cloud structures in the region was detected in a Fermi-LAT analysis of the Carina Nebula-Gum 31 complex. The analysis utilized spatial templates based on CO measurements to model the molecular clouds. The clouds exhibit a resulting power-law spectrum with index ∼2.3 consistent with the expected model from escaping CRs of η Car.

◊ The derived radial profile of the cosmic ray densities of these clouds with respect to η Car seems to be indicative of an origin of cosmic rays from there. However, η Car would have had to be more powerful in the past to account for the whole emission or additional CR sources are needed.

The validation results of this thesis are crucial for the ongoing analysis efforts within the H.E.S.S. collaboration. Especially for soft extragalactic sources, heavily influenced by absorption through extragalactic background light, a robust CT5 mono analysis can be important. The validation of the analysis chain is part of an ongoing effort to provide verified DL3 level data products to the H.E.S.S. collaboration and as a legacy archive to the community, once H.E.S.S. is not operated anymore. All verification steps and the improvements seen with time-based cleaning are also important for the CTA project, for which the middle-sized telescopes will be equipped with FlashCam cameras as well. CTA will improve the sensitivity over the full VHE energy range, giving rise to an increased potential to detect nova outbursts in this regime. Hence it will help further in answering the questions related to the nature of non-thermal emission of nova outbursts and will help to understand whether the efficient hadronic acceleration seen from RS Oph is unique among novae or not. For η Car, a precise measurement of upcoming periastron passages by CTA, employing stereo analysis techniques for the full energy range, can provide further clues about the VHE variability and constraints on the acceleration properties.

Acronyms

η Car Eta Carinae. iii, v, vii, ix, 1, 2, 5, 18–28, 32, 45, 127–149, 151–155, 157–173, 199, 201–203

4FGL fourth Fermi Large Area Telescope catalog. 70, 143, 145, 146, 148, 151, 160–162

ADC analogue to digital converter. 47, 75

AERONET Aerosol Robotic Network. 81–83, 86

AGN active galactic nuclei. 17, 96, 171

ATC Atmospheric Transparency Coefficient. 112, 113, 116, 118, 119

BDT Boosted Decision Tree. 52

CNC Carina Nebula Complex. 27, 28, 127–130, 138, 140, 142, 157, 169, 199

CORSIKA COsmic Ray SImulations for KAscade. 49, 75, 86, 87

CR cosmic ray. 1–7, 10–12, 28, 81, 84, 157, 158, 163, 167, 173

CTA Cherenkov Telescope Array. 4, 35, 36, 43, 46, 71, 86, 98, 125, 155, 170, 173

CWB colliding wind binary. 18, 172

DAQ Data Aquisition System. 45, 46

DBSCAN Density-Based Spatial Clustering of Applications with Noise. viii, 99–102, 109, 172, 200

DL data level. 45, 46, 48, 49, 52, 54, 57, 59, 67, 68, 75, 87, 173

EAS extensive air shower. 36, 39–42, 49, 135

EGRET Energetic Gamma Ray Experiment Telescope. 65

FITS Flexible Image Transport System. 57

FoV field of view. 35, 43, 44, 59–61, 67, 112, 117, 127, 128, 130, 138, 139, 143, 146, 148, 151, 155, 172

GBM Gamma-ray Burst Monitor. 65

H.E.S.S. High Energy Stereoscopic System. iii, v, vii, viii, 1, 2, 24, 26, 27, 30, 35, 36, 43–49, 51, 53, 55, 57, 59–61, 63, 64, 70, 71, 73–76, 78–84, 86, 88, 90, 92–94, 96, 98–109, 111–113, 115–125, 127–130, 133, 137, 147–155, 164, 170–173, 197, 199–201, 203

HAP H.E.S.S. Analysis Package. 46, 49, 57, 63, 64, 73–75, 78, 79, 85, 86, 88, 101, 113, 171, 200

HAWC High Altitude Water Cherenkov. 35, 36

HE high energy. 4, 12, 13, 16, 25, 26, 28, 30, 31, 35, 65, 71, 120, 124, 125, 127, 142, 148, 152, 172

HEGRA High Energy Gamma Ray Astronomy. 43

IACT Imaging Atmospheric Cherenkov Telescope. iii, vii, 1, 35–39, 41–43, 45–47, 49, 51, 53, 55–57, 59, 61, 63, 67, 68, 71, 73, 99, 127, 128, 155, 171, 172, 199, 203

ID identification label. 101, 102, 135, 200

ImPACT Image Pixel-wise fit for Atmospheric Cherenkov Telescopes. 48, 52, 53, 55, 56, 89, 90, 106–108, 119, 144, 145, 199, 201, 203

IRF instrument response function. 46, 55–57, 59, 68, 70, 73, 74, 86, 89, 105, 109, 113, 116–118, 133, 136, 140, 160, 200, 201

LAT Large Area Telescope. iii, v, viii, ix, 2, 24–26, 30, 31, 35, 36, 65–71, 96, 111–113, 115, 117–121, 123–125, 127, 128, 142, 148–151, 153–155, 157, 159–161, 169, 171–173, 199–201, 203

LED light emitting diode. 47

LHAASO Large High Altitude Air Shower Observatory. 35, 96

LSB least significant bit. 75, 129, 130

MAGIC Major Atmospheric Gamma-Ray Imaging Cherenkov. 43, 98, 111, 125

MC Monte Carlo. viii, 48, 49, 51, 52, 55, 59, 67, 74, 78, 83, 85, 86, 90, 92, 95, 98, 101, 107, 113, 117

MET Mission Elapsed Time. 151, 159, 160

MJD Modified Julian Days. 21, 115

NASA National Aeronautics and Space Administration. 65, 66

NSB night sky background. 45, 47–49, 59, 80–83, 86, 87, 101, 107, 109, 112, 113, 127–131, 133, 134, 136, 138, 139, 155, 172, 201

p.e. photo-electron. 45, 47, 48, 50, 52, 56, 75, 76, 78–80, 83, 84, 87, 100–105, 107, 109, 113, 128–130, 134–137

PMT photomultiplier tube. 42, 44, 79, 128

PSF point spread function. 56, 59, 61, 69, 77, 81, 82, 86, 94–96, 113, 114, 120, 136, 138, 139, 142, 143, 145, 146, 161, 171, 200

RG red giant. 28, 29, 32

RMS root mean square. 47, 52, 79, 130–132

ROI region of interest. 159–161

RS Oph RS Ophiuchi. iii, v, 1, 2, 18, 29, 30, 32, 33, 111–122, 124, 125, 171–173, 201, 203

SED spectral energy distribution. 15, 63, 64, 74, 93, 96, 116, 123, 127, 142, 144, 145, 147, 149, 151, 153–155, 161, 172, 173, 200, 201

TS test statistic. 57, 58, 70, 151, 161, 162, 203

UHE ultra-high energy. 35

VERITAS Very Energetic Radiation Imaging Telescope Array System. 43

VHE very-high energy. iii, 4, 12, 14, 16–18, 26, 27, 30, 35, 36, 43, 71, 74, 90, 111, 119, 120, 124, 125, 127, 148, 152, 155, 172, 173, 199

WCR wind collision region. 21, 23, 25

WD white dwarf. 5, 18, 28, 29, 32

Bibliography

Aab, A., P. Abreu, M. Aglietta, I. Al Samarai, et al. (Dec. 2017). "Inferences on mass composition and tests of hadronic interactions from 0.3 to 100 EeV using the water-Cherenkov detectors of the Pierre Auger Observatory". In: Phys. Rev. D 96.12, 122003, p. 122003. DOI: 10.1103/PhysRevD.96.122003.

Aab, A., P. Abreu, M. Aglietta, I. F. M. Albuquerque, et al. (Feb. 2018). "An Indication of Anisotropy in Arrival Directions of Ultra-high-energy Cosmic Rays through Comparison to the Flux Pattern of Extragalactic Gamma-Ray Sources". In: ApJ 853.2, L29, p. L29. DOI: 10.3847/2041-8213/aaa66d.

Abdo, A. A., M. Ackermann, M. Ajello, A. Allafort, et al. (Nov. 2010). "Fermi Large Area Telescope Observation of a Gamma-ray Source at the Position of Eta Carinae". In: ApJ 723.1, pp. 649–657. DOI: 10.1088/0004-637X/723/1/649.

Abdo, A. A., M. Ackermann, M. Ajello, W. B. Atwood, et al. (Dec. 2009). "Fermi Observations of TeV-Selected Active Galactic Nuclei". In: ApJ 707.2, pp. 1310–1333. DOI: 10.1088/0004-637X/707/2/1310.

Abdollahi, S., F. Acero, M. Ackermann, M. Ajello, et al. (Mar. 2020). "Fermi Large Area Telescope Fourth Source Catalog". In: *The Astrophysical Journal Supplement Series* 247.1, p. 33. DOI: 10.3847/1538-4365/ab6bcb.

Abdollahi, S., F. Acero, M. Ackermann, L. Baldini, et al. (July 2022a). "Search for New Cosmic-Ray Acceleration Sites within the 4FGL Catalog Galactic Plane Sources". In: ApJ 933.2, 204, p. 204. DOI: 10.3847/1538-4357/ac704f.

Abdollahi, S., F. Acero, L. Baldini, J. Ballet, et al. (June 2022b). "Incremental Fermi Large Area Telescope Fourth Source Catalog". In: ApJS 260.2, 53, p. 53. DOI: 10.3847/1538-4365/ac6751.

Abeysekara, A. U., A. Albert, R. Alfaro, C. Alvarez, et al. (Oct. 2018a). "Very-high-energy particle acceleration powered by the jets of the microquasar SS 433". In: Nature 562.7725, pp. 82–85. DOI: 10.1038/s41586-018-0565-5.

Abeysekara, A. U., W. Benbow, R. Bird, A. Brill, et al. (Nov. 2018b). "Periastron Observations of TeV Gamma-Ray Emission from a Binary System with a 50-year Period". In: ApJ 867.1, L19, p. L19. DOI: 10.3847/2041-8213/aae70e.

Acciari, V. A., S. Ansoldi, L. A. Antonelli, A. Arbet Engels, et al. (Apr. 2022). "Proton acceleration in thermonuclear nova explosions revealed by gamma rays". In: *Nature Astronomy* 6, pp. 689–697. DOI: 10.1038/s41550-022-01640-z.

Ackermann, M., M. Ajello, A. Albert, A. Allafort, et al. (Nov. 2012). "The Fermi Large Area Telescope on Orbit: Event Classification, Instrument Response Functions, and Calibration". In: ApJS 203.1, 4, p. 4. DOI: 10.1088/0067-0049/203/1/4.

Aharonian, Felix, Ruizhi Yang, and Emma de Oña Wilhelmi (Mar. 2019). "Massive stars as major factories of Galactic cosmic rays". In: *Nature Astronomy* 3, pp. 561–567. DOI: 10.1038/s41550-019-0724-0.

Aharonian, Felix A. (2004). *Very high energy cosmic gamma radiation : a crucial window on the extreme Universe*. DOI: 10.1142/4657.

Aitken, David K., Craig H. Smith, Toby J. T. Moore, and Patrick F. Roche (Mar. 1995). "Mid-infrared studies of eta Carinae-II. Polarimetric imaging at 12.5 μm and the magnetic field structure". In: MNRAS 273.2, pp. 359–366. DOI: 10.1093/mnras/273.2.359.

Akashi, Muhammad, Noam Soker, and Ehud Behar (June 2006). "Accretion onto the Companion of η Carinae during the Spectroscopic Event. II. X-Ray Emission Cycle". In: ApJ 644.1, pp. 451–463. DOI: 10.1086/503317.

Aleksić, J., S. Ansoldi, L. A. Antonelli, P. Antoranz, et al. (Mar. 2015). "Measurement of the Crab Nebula spectrum over three decades in energy with the MAGIC telescopes". In: *Journal of High Energy Astrophysics* 5, pp. 30–38. DOI: 10.1016/j.jheap.2015.01.002.

Aleksić, J., S. Ansoldi, L. A. Antonelli, P. Antoranz, et al. (Jan. 2016). "The major upgrade of the MAGIC telescopes, Part I: The hardware improvements and the commissioning of the system". In: *Astroparticle Physics* 72, pp. 61–75. DOI: 10.1016/j.astropartphys.2015.04.004.

Aliu, E., H. Anderhub, L. A. Antonelli, P. Antoranz, et al. (Jan. 2009). "Improving the performance of the single-dish Cherenkov telescope MAGIC through the use of signal timing". In: *Astroparticle Physics* 30.6, pp. 293–305. DOI: 10.1016/j.astropartphys.2008.10.003.

AMS Collaboration, M. Aguilar, J. Alcaraz, J. Allaby, et al. (Aug. 2002). "The Alpha Magnetic Spectrometer (AMS) on the International Space Station: Part I - results from the test flight on the space shuttle". In: Phys. Rep. 366.6, pp. 331–405. DOI: 10.1016/S0370-1573(02)00013-3.

Atwood, W., A. Albert, L. Baldini, M. Tinivella, et al. (Mar. 2013). "Pass 8: Toward the Full Realization of the Fermi-LAT Scientific Potential". In: *arXiv e-prints*, arXiv:1303.3514, arXiv:1303.3514. DOI: 10.48550/arXiv.1303.3514.

Atwood, W. B., A. A. Abdo, M. Ackermann, W. Althouse, et al. (June 2009). "The Large Area Telescope on the Fermi Gamma-Ray Space Telescope Mission". In: ApJ 697.2, pp. 1071–1102. DOI: 10.1088/0004-637X/697/2/1071.

Aydi, Elias, Kirill V. Sokolovsky, Laura Chomiuk, Elad Steinberg, et al. (Apr. 2020). "Direct evidence for shock-powered optical emission in a nova". In: *Nature Astronomy* 4, pp. 776–780. DOI: 10.1038/s41550-020-1070-y.

Balbo, M. and R. Walter (July 2017). "Fermi acceleration along the orbit of η Carinae". In: A&A 603, A111, A111. DOI: 10.1051/0004-6361/201629640.

Barnes, Peter J., Yoshinori Yonekura, Stuart D. Ryder, Andrew M. Hopkins, et al. (Feb. 2010). "Discovery of large-scale gravitational infall in a massive protostellar

cluster". In: MNRAS 402.1, pp. 73–86. DOI: 10.1111/j.1365-2966.2009.15890.x.

Barry, R. K., K. Mukai, J. L. Sokoloski, W. C. Danchi, et al. (Dec. 2008). "On the Distance of RS Ophiuchi". In: *RS Ophiuchi (2006) and the Recurrent Nova Phenomenon*. Ed. by A. Evans, M. F. Bode, T. J. O'Brien, and M. J. Darnley. Vol. 401. Astronomical Society of the Pacific Conference Series, p. 52.

Bednarek, W. and J. Pabich (June 2011). "High-energy radiation from the massive binary system Eta Carinae". In: A&A 530, A49, A49. DOI: 10.1051/0004-6361/201116549.

Bell, A. R. (Jan. 1978a). "The acceleration of cosmic rays in shock fronts - I." In: MNRAS 182, pp. 147–156. DOI: 10.1093/mnras/182.2.147.

— (Feb. 1978b). "The acceleration of cosmic rays in shock fronts - II." In: MNRAS 182, pp. 443–455. DOI: 10.1093/mnras/182.3.443.

Bell, A. R., K. M. Schure, B. Reville, and G. Giacinti (May 2013). "Cosmic-ray acceleration and escape from supernova remnants". In: MNRAS 431.1, pp. 415–429. DOI: 10.1093/mnras/stt179.

Bell, A.R. (2013). "Cosmic ray acceleration". In: *Astroparticle Physics* 43. Seeing the High-Energy Universe with the Cherenkov Telescope Array - The Science Explored with the CTA, pp. 56–70. ISSN: 0927-6505. DOI: https://doi.org/10.1016/j.astropartphys.2012.05.022.

Berge, D., S. Funk, and J. Hinton (May 2007). "Background modelling in very-high-energy γ-ray astronomy". In: A&A 466.3, pp. 1219–1229. DOI: 10.1051/0004-6361:20066674.

Berlanas, S. R., J. Maíz Apellániz, A. Herrero, L. Mahy, et al. (Jan. 2023). "Gaia-ESO Survey: massive stars in the Carina Nebula. A new census of OB stars". In: *arXiv e-prints*, arXiv:2301.08310, arXiv:2301.08310. DOI: 10.48550/arXiv.2301.08310.

Bernlöhr, K., A. Barnacka, Y. Becherini, O. Blanch Bigas, et al. (Mar. 2013). "Monte Carlo design studies for the Cherenkov Telescope Array". In: *Astroparticle Physics* 43, pp. 171–188. DOI: 10.1016/j.astropartphys.2012.10.002.

Bernlöhr, Konrad (2008). "Simulation of imaging atmospheric Cherenkov telescopes with CORSIKA and sim_telarray". In: *Astroparticle Physics* 30.3, pp. 149–158. ISSN: 0927-6505. DOI: https://doi.org/10.1016/j.astropartphys.2008.07.009.

Bethe, H. and W. Heitler (Aug. 1934). "On the Stopping of Fast Particles and on the Creation of Positive Electrons". In: *Proceedings of the Royal Society of London Series A* 146.856, pp. 83–112. DOI: 10.1098/rspa.1934.0140.

Bi, B., M. Barcelo, C. Bauer, F. A. Benkhali, et al. (Mar. 2022). "Performance of the new FlashCam-based camera in the 28m telescope of H.E.S.S." In: *37th International Cosmic Ray Conference*, 743, p. 743. DOI: 10.22323/1.395.0743.

Bird, D. J., S. C. Corbato, H. Y. Dai, J. W. Elbert, et al. (Mar. 1995). "Detection of a Cosmic Ray with Measured Energy Well beyond the Expected Spectral Cutoff due to Cosmic Microwave Radiation". In: ApJ 441, p. 144. DOI: 10.1086/175344.

Blandford, R. D. and J. P. Ostriker (Apr. 1978). "Particle acceleration by astrophysical shocks." In: ApJ 221, pp. L29–L32. DOI: 10.1086/182658.

Blumenthal, George R. and Robert J. Gould (Jan. 1970). "Bremsstrahlung, Synchrotron Radiation, and Compton Scattering of High-Energy Electrons Traversing Dilute Gases". In: *Reviews of Modern Physics* 42.2, pp. 237–271. DOI: 10.1103/RevModPhys.42.237.

Bode, M. F., D. J. Harman, T. J. O'Brien, Howard E. Bond, et al. (Aug. 2007). "Hubble Space Telescope Imaging of the Expanding Nebular Remnant of the 2006 Outburst of the Recurrent Nova RS Ophiuchi". In: ApJ 665.1, pp. L63–L66. DOI: 10.1086/520929.

Bode, M. F., T. J. O'Brien, J. P. Osborne, K. L. Page, et al. (Nov. 2006). "Swift Observations of the 2006 Outburst of the Recurrent Nova RS Ophiuchi. I. Early X-Ray Emission from the Shocked Ejecta and Red Giant Wind". In: ApJ 652.1, pp. 629–635. DOI: 10.1086/507980.

Bode, Michael F. and Aneurin Evans (2008). *Classical Novae*. Vol. 43.

Booth, R. A., S. Mohamed, and Ph. Podsiadlowski (Mar. 2016). "Modelling the circumstellar medium in RS Ophiuchi and its link to Type Ia supernovae". In: MNRAS 457.1, pp. 822–835. DOI: 10.1093/mnras/stw001.

Brandi, E., C. Quiroga, J. Mikołajewska, O. E. Ferrer, and L. G. García (Apr. 2009). "Spectroscopic orbits and variations of RS Ophiuchi". In: A&A 497.3, pp. 815–825. DOI: 10.1051/0004-6361/200811417.

Castellina, A. (May 2017). "Ground-based cosmic ray experiments: A review". In: *Nuovo Cimento C Geophysics Space Physics C* 40.3, 143, p. 143. DOI: 10.1393/ncc/i2017-17143-1.

Cherenkov, P.A. (1934). "Visible emission of clean liquids by action of γ radiation". In: *Dok. Akad. Nauk SSSR* 2, 451–454.

Chernyakova, M., D. Malyshev, A. Paizis, N. La Palombara, et al. (Nov. 2019). "Overview of non-transient γ-ray binaries and prospects for the Cherenkov Telescope Array". In: A&A 631, A177, A177. DOI: 10.1051/0004-6361/201936501.

Cheung, C. C., S. Ciprini, and T. J. Johnson (Aug. 2021). "Fermi-LAT Gamma-ray Detection of the Recurrent Nova RS Oph". In: *The Astronomer's Telegram* 14834, p. 1.

Cheung, C. C., T. J. Johnson, P. Jean, M. Kerr, et al. (Aug. 2022). "Fermi LAT Gamma-ray Detection of the Recurrent Nova RS Ophiuchi during its 2021 Outburst". In: ApJ 935.1, 44, p. 44. DOI: 10.3847/1538-4357/ac7eb7.

Chomiuk, Laura, Brian D. Metzger, and Ken J. Shen (Sept. 2021). "New Insights into Classical Novae". In: ARA&A 59, pp. 391–444. DOI: 10.1146/annurev-astro-112420-114502.

Clementel, N., T. I. Madura, C. J. H. Kruip, V. Icke, and T. R. Gull (Sept. 2014). "3D radiative transfer in η Carinae: application of the SIMPLEX algorithm to 3D SPH simulations of binary colliding winds". In: MNRAS 443.3, pp. 2475–2491. DOI: 10.1093/mnras/stu1287.

Corcoran, M. F. and K. Hamaguchi (Aug. 2007). "Eta Car and Its Surroundings: the X-ray Diagnosis". In: *Revista Mexicana de Astronomia y Astrofisica Conference Series*. Vol. 30. Revista Mexicana de Astronomia y Astrofisica Conference Series, pp. 29–34. DOI: 10.48550/arXiv.astro-ph/0703039.

Corcoran, M. F., J. Liburd, D. Morris, C. M. P. Russell, et al. (Mar. 2017). "The 2014 X-Ray Minimum of η Carinae as Seen by Swift". In: ApJ 838.1, 45, p. 45. DOI: 10.3847/1538-4357/aa6347.

Cornils, R., S. Gillessen, I. Jung, W. Hofmann, et al. (2003). "The optical system of the H.E.S.S. imaging atmospheric Cherenkov telescopes. Part II: mirror alignment and point spread function". In: *Astroparticle Physics* 20.2, pp. 129–143. ISSN: 0927-6505. DOI: https://doi.org/10.1016/S0927-6505(03)00172-5.

Dame, T. M., Dap Hartmann, and P. Thaddeus (Feb. 2001). "The Milky Way in Molecular Clouds: A New Complete CO Survey". In: ApJ 547.2, pp. 792–813. DOI: 10.1086/318388.

Damineli, A., D. J. Hillier, M. F. Corcoran, O. Stahl, et al. (Feb. 2008). "The periodicity of the η Carinae events". In: *Monthly Notices of the Royal Astronomical Society* 384.4, pp. 1649–1656. ISSN: 0035-8711. DOI: 10.1111/j.1365-2966.2007.12815.x.

Daum, A., G. Hermann, and HEGRA Collaboration (Jan. 1997). "The Stereoscopic System of Imaging Atmospheric Cherenkov Telescopes of the HEGRA-Collaboration". In: *International Cosmic Ray Conference*. Vol. 5. International Cosmic Ray Conference, p. 117.

Davidson, Kris and Roberta M. Humphreys (Jan. 1997). "Eta Carinae and Its Environment". In: ARA&A 35, pp. 1–32. DOI: 10.1146/annurev.astro.35.1.1.

Davidson, Kris and Roberta M. Humphreys (Jan. 2012). *Eta Carinae and the Supernova Impostors*. Vol. 384. Astrophysics and Space Science Library. DOI: 10.1007/978-1-4614-2275-4.

Davies, John M. and Eugene S. Cotton (1957). "Design of the quartermaster solar furnace". In: *Solar Energy* 1.2, pp. 16–22. ISSN: 0038-092X. DOI: https://doi.org/10.1016/0038-092X(57)90116-0.

De Angelis, A. and M. Mallamaci (Aug. 2018). "Gamma-ray astrophysics". In: *European Physical Journal Plus* 133.8, 324, p. 324. DOI: 10.1140/epjp/i2018-12181-0.

De Angelis, Alessandro, Vincent Tatischeff, Andrea Argan, Søren Brandt, et al. (June 2021). "Gamma-ray astrophysics in the MeV range". In: *Experimental Astronomy* 51.3, pp. 1225–1254. DOI: 10.1007/s10686-021-09706-y.

de Groot, M., C. Sterken, and A. M. van Genderen (Sept. 2001). "Cyclicities in the light variations of S Doradus stars III. P Cygni". In: A&A 376, pp. 224–231. DOI: 10.1051/0004-6361:20010960.

de Naurois, Mathieu (Nov. 2021). "The Making of Catalogues of Very-High-Energy γ-ray Sources". In: *Universe* 7.11, p. 421. DOI: 10.3390/universe7110421.

de Naurois, Mathieu and Loïc Rolland (2009). "A high performance likelihood reconstruction of γ-rays for imaging atmospheric Cherenkov telescopes". In: *Astroparticle Physics* 32.5, pp. 231–252. ISSN: 0927-6505. DOI: https://doi.org/10.1016/j.astropartphys.2009.09.001.

Deil, C., R. Zanin, J. Lefaucheur, C. Boisson, et al. (July 2017). "Gammapy - A prototype for the CTA science tools". In: *35th International Cosmic Ray Conference (ICRC2017)*. Vol. 301. International Cosmic Ray Conference, 766, p. 766. DOI: 10.22323/1.301.0766.

Deil, Christoph (Jan. 2011). "HESS and Fermi surveys of the galactic gamma-ray source population". PhD thesis. Ruprecht-Karls University of Heidelberg, Germany.

Dembinski, H., R. Engel, A. Fedynitch, T. K. Gaisser, et al. (July 2017). "Data-driven model of the cosmic-ray flux and mass composition from 10 GeV to 10^{11} GeV". In: *35th International Cosmic Ray Conference (ICRC2017)*. Vol. 301. International Cosmic Ray Conference, 533, p. 533. DOI: 10.22323/1.301.0533.

Dirson, Ludmilla and Dieter Horns (Mar. 2022). "Phenomenological modelling of the Crab Nebula's broad band energy spectrum and its apparent extension". In: *arXiv e-prints*, arXiv:2203.11502, arXiv:2203.11502. DOI: 10.48550/arXiv.2203.11502.

Duchêne, Gaspard and Adam Kraus (Aug. 2013). "Stellar Multiplicity". In: ARA&A 51.1, pp. 269–310. DOI: 10.1146/annurev-astro-081710-102602.

Eichler, D. and V. Usov (Jan. 1993). "Particle Acceleration and Nonthermal Radio Emission in Binaries of Early-Type Stars". In: ApJ 402, p. 271. DOI: 10.1086/172130.

Engel, Ralph, Dieter Heck, and Tanguy Pierog (2011). "Extensive Air Showers and Hadronic Interactions at High Energy". In: *Annual Review of Nuclear and Particle Science* 61.1, pp. 467–489. DOI: 10.1146/annurev.nucl.012809.104544.

Ester, Martin, Hans-Peter Kriegel, Jörg Sander, and Xiaowei Xu (1996). "A Density-Based Algorithm for Discovering Clusters in Large Spatial Databases with Noise". In: *Proc. of 2nd International Conference on Knowledge Discovery and*, pp. 226–231.

Evoli, Carmelo (Dec. 2020). *The Cosmic-Ray Energy Spectrum*. DOI: 10.5281/zenodo.4396125.

Fermi, Enrico (Apr. 1949). "On the Origin of the Cosmic Radiation". In: *Physical Review* 75.8, pp. 1169–1174. DOI: 10.1103/PhysRev.75.1169.

Franckowiak, A., P. Jean, M. Wood, C. C. Cheung, and S. Buson (Feb. 2018). "Search for gamma-ray emission from Galactic novae with the Fermi -LAT". In: A&A 609, A120, A120. DOI: 10.1051/0004-6361/201731516.

Funk, S., G. Hermann, J. Hinton, D. Berge, et al. (Nov. 2004). "The trigger system of the H.E.S.S. telescope array". In: *Astroparticle Physics* 22.3-4, pp. 285–296. DOI: 10.1016/j.astropartphys.2004.08.001.

Funk, Stefan (2005). "A new population of very high-energy γ-ray sources detected with H.E.S.S. in the inner part of the Milky Way". PhD thesis. Ruprecht-Karls-Universität Heidelberg.

— (2015). "Ground- and Space-Based Gamma-Ray Astronomy". In: *Annual Review of Nuclear and Particle Science* 65.1, pp. 245–277. DOI: 10.1146/annurev-nucl-102014-022036.

Gabici, Stefano, Felix A. Aharonian, and Pasquale Blasi (June 2007). "Gamma rays from molecular clouds". In: Ap&SS 309.1-4, pp. 365–371. DOI: 10.1007/s10509-007-9427-6.

Gaia Collaboration, A. G. A. Brown, A. Vallenari, T. Prusti, et al. (Aug. 2018). "Gaia Data Release 2. Summary of the contents and survey properties". In: A&A 616, A1, A1. DOI: 10.1051/0004-6361/201833051.

Gaisser, T. K., Todor Staney, F. Halzen, W. F. Long, and E. Zas (Jan. 1991). "Gamma-ray astronomy above 50 TeV with muon-poor showers". In: *Phys. Rev. D* 43 (2), pp. 314–318. DOI: 10.1103/PhysRevD.43.314.

Gaisser, Thomas K., Ralph Engel, and Elisa Resconi (2016). *Cosmic Rays and Particle Physics*.

Gallagher, J. S. and S. Starrfield (Jan. 1978). "Theory and observations of classical novae." In: ARA&A 16, pp. 171–214. DOI: 10.1146/annurev.aa.16.090178.001131.

Ge, Ting-Ting, Xiao-Na Sun, Rui-Zhi Yang, Yun-Feng Liang, and En-Wei Liang (Dec. 2022). "Diffuse γ-ray emission around the massive star forming region of Carina Nebula Complex". In: MNRAS 517.4, pp. 5121–5128. DOI: 10.1093/mnras/stac2885.

Gehrels, N., G. Chincarini, P. Giommi, K. O. Mason, et al. (Aug. 2004). "The Swift Gamma-Ray Burst Mission". In: ApJ 611.2, pp. 1005–1020. DOI: 10.1086/422091.

Gendreau, Keith C., Zaven Arzoumanian, Phillip W. Adkins, Cheryl L. Albert, et al. (July 2016). "The Neutron star Interior Composition Explorer (NICER): design and development". In: *Space Telescopes and Instrumentation 2016: Ultraviolet to Gamma Ray*. Vol. 9905. Society of Photo-Optical Instrumentation Engineers (SPIE) Conference Series, 99051H, 99051H. DOI: 10.1117/12.2231304.

Giannetti, A., S. Leurini, C. König, J. S. Urquhart, et al. (Oct. 2017). "Galactocentric variation of the gas-to-dust ratio and its relation with metallicity". In: A&A 606, L12, p. L12. DOI: 10.1051/0004-6361/201731728.

Giavitto, Gianluca, Simon Bonnefoy, Terry Ashton, Michael Backes, et al. (2018). "Performance of the upgraded H.E.S.S. cameras". In: *Proceedings of 35th International Cosmic Ray Conference — PoS(ICRC2017)*. Vol. 301, p. 805. DOI: 10.22323/1.301.0805.

Greisen, Kenneth (Apr. 1966). "End to the Cosmic-Ray Spectrum?" In: Phys. Rev. Lett. 16.17, pp. 748–750. DOI: 10.1103/PhysRevLett.16.748.

Hahn, J., R. de los Reyes, K. Bernlöhr, P. Krüger, et al. (2014). "Impact of aerosols and adverse atmospheric conditions on the data quality for spectral analysis of

the H.E.S.S. telescopes". In: *Astroparticle Physics* 54, pp. 25–32. ISSN: 0927-6505. DOI: https://doi.org/10.1016/j.astropartphys.2013.10.003.

Hahn, Joachim, Carlo Romoli, and Mischa Breuhaus (Mar. 2022). *GAMERA: Source modeling in gamma astronomy*. Astrophysics Source Code Library, record ascl:2203.007.

Haino, S., T. Sanuki, K. Abe, K. Anraku, et al. (July 2004). "Measurements of primary and atmospheric cosmic-ray spectra with the BESS-TeV spectrometer". In: *Physics Letters B* 594.1-2, pp. 35–46. DOI: 10.1016/j.physletb.2004.05.019.

Hamaguchi, Kenji, Michael F. Corcoran, Julian M. Pittard, Neetika Sharma, et al. (July 2018). "Non-thermal X-rays from colliding wind shock acceleration in the massive binary Eta Carinae". In: *Nature Astronomy* 2, pp. 731–736. DOI: 10.1038/s41550-018-0505-1.

Hamaguchi, Kenji, David A. Espinoza-Galeas, Michael Francis Corcoran, Christopher Russell, et al. (May 2020). "Brightest Non-Thermal X-ray Emission Observed from Eta Carinae". In: *The Astronomer's Telegram* 13738, p. 1.

Harrison, Fiona A., William W. Craig, Finn E. Christensen, Charles J. Hailey, et al. (June 2013). "The Nuclear Spectroscopic Telescope Array (NuSTAR) High-energy X-Ray Mission". In: ApJ 770.2, 103, p. 103. DOI: 10.1088/0004-637X/770/2/103.

Hartman, R. C., D. L. Bertsch, S. D. Bloom, A. W. Chen, et al. (July 1999). "The Third EGRET Catalog of High-Energy Gamma-Ray Sources". In: ApJS 123.1, pp. 79–202. DOI: 10.1086/313231.

Heck, D., J. Knapp, J. N. Capdevielle, G. Schatz, and T. Thouw (1998). *CORSIKA: a Monte Carlo code to simulate extensive air showers.*

Heitler, W. (1954). *Quantum theory of radiation*.

Hess, Victor F. (1912). "Über Beobachtungen der durchdringenden Strahlung bei sieben Freiballonfahrten". In: *Phys. Z.* 13, pp. 1084–1091.

H.E.S.S. Collaboration (2023). "Constraints on the high-energy γ-ray emission from the Crab nebula from a Fermi-LAT and H.E.S.S. multi-instrument analysis". in prep.

H.E.S.S. Collaboration, H. Abdalla, A. Abramowski, F. Aharonian, et al. (Apr. 2017). "Gamma-ray blazar spectra with H.E.S.S. II mono analysis: The case of PKS 2155-304 and PG 1553+113". In: A&A 600, A89, A89. DOI: 10.1051/0004-6361/201629427.

H.E.S.S. Collaboration, H. Abdalla, A. Abramowski, F. Aharonian, et al. (Apr. 2018). "The H.E.S.S. Galactic plane survey". In: A&A 612, A1, A1. DOI: 10.1051/0004-6361/201732098.

H.E.S.S. Collaboration, H. Abdalla, R. Adam, F. Aharonian, et al. (Nov. 2019). "A very-high-energy component deep in the γ-ray burst afterglow". In: Nature 575.7783, pp. 464–467. DOI: 10.1038/s41586-019-1743-9.

H.E.S.S. Collaboration, H. Abdalla, R. Adam, F. Aharonian, et al. (Mar. 2020). "Detection of very-high-energy γ-ray emission from the colliding wind binary η Car with H.E.S.S." In: A&A 635, A167, A167. DOI: 10.1051/0004-6361/201936761.

H.E.S.S. Collaboration, H. Abdalla, F. Aharonian, F. Ait Benkhali, et al. (June 2021). "Revealing x-ray and gamma ray temporal and spectral similarities in the GRB 190829A afterglow". In: *Science* 372.6546, pp. 1081–1085. DOI: 10.1126/science.abe8560.

H.E.S.S. Collaboration, A. Abramowski, F. Acero, F. Aharonian, et al. (Sept. 2010a). "VHE γ-ray emission of PKS 2155-304: spectral and temporal variability". In: A&A 520, A83, A83. DOI: 10.1051/0004-6361/201014484.

H.E.S.S. Collaboration, A. Abramowski, F. Acero, F. Aharonian, et al. (July 2012). "HESS observations of the Carina nebula and its enigmatic colliding wind binary Eta Carinae". In: *Monthly Notices of the Royal Astronomical Society* 424.1, pp. 128–135. ISSN: 0035-8711. DOI: 10.1111/j.1365-2966.2012.21180.x.

H.E.S.S. Collaboration, A. Abramowski, F. Acero, F. Aharonian, et al. (Mar. 2013). "H.E.S.S. observations of the binary system PSR B1259-63/LS 2883 around the 2010/2011 periastron passage". In: A&A 551, A94, A94. DOI: 10.1051/0004-6361/201220612.

H.E.S.S. Collaboration, F. Acero, F. Aharonian, A. G. Akhperjanian, et al. (Mar. 2010b). "Localizing the VHE γ-ray source at the Galactic Centre". In: MNRAS 402.3, pp. 1877–1882. DOI: 10.1111/j.1365-2966.2009.16014.x.

H.E.S.S. Collaboration, F. Aharonian, F. Ait Benkhali, E. O. Angüner, et al. (Apr. 2022). "Time-resolved hadronic particle acceleration in the recurrent nova RS Ophiuchi". In: *Science* 376.6588, pp. 77–80. DOI: 10.1126/science.abn0567.

H.E.S.S. Collaboration, F. Aharonian, A. G. Akhperjanian, K. M. Aye, et al. (Nov. 2004). "Calibration of cameras of the H.E.S.S. detector". In: *Astroparticle Physics* 22.2, pp. 109–125. DOI: 10.1016/j.astropartphys.2004.06.006.

H.E.S.S. Collaboration, F. Aharonian, A. G. Akhperjanian, A. R. Bazer-Bachi, et al. (Apr. 2006a). "A detailed spectral and morphological study of the gamma-ray supernova remnant RX J1713.7-3946 with HESS". In: A&A 449.1, pp. 223–242. DOI: 10.1051/0004-6361:20054279.

H.E.S.S. Collaboration, F. Aharonian, A. G. Akhperjanian, A. R. Bazer-Bachi, et al. (Oct. 2006b). "Observations of the Crab nebula with HESS". In: A&A 457.3, pp. 899–915. DOI: 10.1051/0004-6361:20065351.

Hillas, A. M. (Jan. 1984). "The Origin of Ultra-High-Energy Cosmic Rays". In: ARA&A 22, pp. 425–444. DOI: 10.1146/annurev.aa.22.090184.002233.

— (Aug. 1985). "Cerenkov Light Images of EAS Produced by Primary Gamma Rays and by Nuclei". In: *19th International Cosmic Ray Conference (ICRC19), Volume 3*. Vol. 3. International Cosmic Ray Conference, p. 445.

Hillier, D. John, K. Davidson, K. Ishibashi, and T. Gull (June 2001). "On the Nature of the Central Source in η Carinae". In: ApJ 553.2, pp. 837–860. DOI: 10.1086/320948.

Hinton, J. A. and W. Hofmann (Sept. 2009). "Teraelectronvolt Astronomy". In: ARA&A 47.1, pp. 523–565. DOI: 10.1146/annurev-astro-082708-101816.

Hofmann, W., I. Jung, A. Konopelko, H. Krawczynski, et al. (Nov. 1999). "Comparison of techniques to reconstruct VHE gamma-ray showers from multiple stereoscopic Cherenkov images". In: *Astroparticle Physics* 12.3, pp. 135–143. DOI: 10.1016/S0927-6505(99)00084-5.

Holben, B.N., T.F. Eck, I. Slutsker, D. Tanré, et al. (1998). "AERONET—A Federated Instrument Network and Data Archive for Aerosol Characterization". In: *Remote Sensing of Environment* 66.1, pp. 1–16. ISSN: 0034-4257. DOI: https://doi.org/10.1016/S0034-4257(98)00031-5.

Holch, Tim Lukas, Fabian Leuschner, Johannes Schäfer, and Simon Steinmassl (Dec. 2022). "Assessing aerosol induced errors in Monte Carlo based air-shower reconstruction for atmospheric Cherenkov detectors". In: *Journal of Physics: Conference Series* 2398.1, p. 012017. DOI: 10.1088/1742-6596/2398/1/012017.

Hoppe, Stefan (Dec. 2008). "Emitters of VHE γ-radiation as revealed by the H.E.S.S. Galactic plane survey". PhD thesis. Ruprecht-Karls University of Heidelberg, Germany.

IceCube Collaboration, M. G. Aartsen, M. Ackermann, J. Adams, et al. (July 2018). "Multimessenger observations of a flaring blazar coincident with high-energy neutrino IceCube-170922A". In: *Science* 361.6398, eaat1378, eaat1378. DOI: 10.1126/science.aat1378.

IceCube Collaboration, R. Abbasi, M. Ackermann, J. Adams, et al. (Nov. 2022). "Evidence for neutrino emission from the nearby active galaxy NGC 1068". In: *Science* 378.6619, pp. 538–543. DOI: 10.1126/science.abg3395.

Iping, Rosina C., George Sonneborn, Theodore R. Gull, Derck L. Massa, and D. John Hillier (Nov. 2005). "Detection of a Hot Binary Companion of η Carinae". In: ApJ 633.1, pp. L37–L40. DOI: 10.1086/498268.

James, F. and M. Roos (1975). "Minuit - a system for function minimization and analysis of the parameter errors and correlations". In: *Computer Physics Communications* 10.6, pp. 343–367. ISSN: 0010-4655. DOI: https://doi.org/10.1016/0010-4655(75)90039-9.

Jardin-Blicq, Armelle (2019). "The TeV γ-ray emission of the Galactic Plane. HAWC and H.E.S.S. observations of the Galactic Plane and detailed study of the region surrounding 2HWC J1928+177". PhD thesis. Ruprecht-Karls University of Heidelberg, Germany.

Kafexhiu, Ervin, Felix Aharonian, Andrew M. Taylor, and Gabriela S. Vila (Dec. 2014). "Parametrization of gamma-ray production cross sections for p p interactions in a broad proton energy range from the kinematic threshold to PeV energies". In: Phys. Rev. D 90.12, 123014, p. 123014. DOI: 10.1103/PhysRevD.90.123014.

Kafka, S. (2021). *Observations from the AAVSO International Database*. https://www.aavso.org.

Kappes, Alexander, Jim Hinton, Christian Stegmann, and Felix A. Aharonian (Feb. 2007). "Potential Neutrino Signals from Galactic γ-Ray Sources". In: ApJ 656.2, pp. 870–878. DOI: 10.1086/508936.

Kashi, Amit, David A. Principe, Noam Soker, and Joel H. Kastner (June 2021). "The X-Ray Properties of Eta Carinae During Its 2020 X-Ray Minimum". In: ApJ 914.1, 47, p. 47. DOI: 10.3847/1538-4357/abfa9c.

Kelner, S. R. and F. A. Aharonian (Aug. 2008). "Energy spectra of gamma rays, electrons, and neutrinos produced at interactions of relativistic protons with low energy radiation". In: Phys. Rev. D 78.3, 034013, p. 034013. DOI: 10.1103/PhysRevD.78.034013.

Kelner, S. R., F. A. Aharonian, and V. V. Bugayov (Aug. 2006). "Energy spectra of gamma rays, electrons, and neutrinos produced at proton-proton interactions in the very high energy regime". In: Phys. Rev. D 74.3, 034018, p. 034018. DOI: 10.1103/PhysRevD.74.034018.

Leuschner, Fabian (2023). in preparation. PhD thesis. Eberhard Karls Universitüt Tübingen.

Leuschner, Fabian, Johannes Schäfer, Simon Steinmassl, Tim Holch, et al. (Mar. 2023). "Validating Monte Carlo simulations for an analysis chain in H.E.S.S". In: arXiv:2303.00412, arXiv:2303.00412.

Levine, Alan M., Hale Bradt, Wei Cui, J. G. Jernigan, et al. (Sept. 1996). "First Results from the All-Sky Monitor on the Rossi X-Ray Timing Explorer". In: ApJ 469, p. L33. DOI: 10.1086/310260.

Lhaaso Collaboration, Zhen Cao, F. Aharonian, Q. An, et al. (July 2021). "Peta-electron volt gamma-ray emission from the Crab Nebula". In: *Science* 373, pp. 425–430. DOI: 10.1126/science.abg5137.

Li, Kwan-Lok, Brian D. Metzger, Laura Chomiuk, Indrek Vurm, et al. (Sept. 2017). "A nova outburst powered by shocks". In: *Nature Astronomy* 1, pp. 697–702. DOI: 10.1038/s41550-017-0222-1.

Li, T. P. and Y. Q. Ma (Sept. 1983). "Analysis methods for results in gamma-ray astronomy." In: ApJ 272, pp. 317–324. DOI: 10.1086/161295.

Lindegren, L., U. Bastian, M. Biermann, A. Bombrun, et al. (May 2021). "Gaia Early Data Release 3. Parallax bias versus magnitude, colour, and position". In: A&A 649, A4, A4. DOI: 10.1051/0004-6361/202039653.

Longair, Malcolm S. (2011). *High Energy Astrophysics*.

Madura, T. I., T. R. Gull, S. P. Owocki, J. H. Groh, et al. (Mar. 2012). "Constraining the absolute orientation of η Carinae's binary orbit: a 3D dynamical model for the broad [Fe III] emission". In: MNRAS 420.3, pp. 2064–2086. DOI: 10.1111/j.1365-2966.2011.20165.x.

MAGIC Collaboration, V. A. Acciari, S. Ansoldi, L. A. Antonelli, et al. (Nov. 2019). "Teraelectronvolt emission from the γ-ray burst GRB 190114C". In: Nature 575.7783, pp. 455–458. DOI: 10.1038/s41586-019-1750-x.

Maier, Gernot (Feb. 2022). *Hillas Plot*. Version v1.0.0. DOI: 10.5281/zenodo.6037985.

Malkov, M. A. and L. O'C. Drury (Apr. 2001). "Nonlinear theory of diffusive acceleration of particles by shock waves". In: *Reports on Progress in Physics* 64.4, pp. 429–481. DOI: 10.1088/0034-4885/64/4/201.

Marandon, Vincent (Nov. 2010). "TeV observations of pulsar wind nebulae". PhD thesis. Astroparticle and Cosmology Laboratory, Paris.

Marrocchesi, Pier Simone (Apr. 2017). "Charged Cosmic Rays: a Review of Balloon and Space Borne Measurements". In: *arXiv e-prints*, arXiv:1704.00304, arXiv:1704.00304. DOI: 10.48550/arXiv.1704.00304.

Martí-Devesa, G. and O. Reimer (Oct. 2021). "η Carinae with Fermi-LAT: two full orbits and the third periastron". In: A&A 654, A44, A44. DOI: 10.1051/0004-6361/202140451.

Martí-Devesa, G., O. Reimer, J. Li, and D. F. Torres (Mar. 2020). "Hints of γ-ray orbital variability from γ^2 Velorum". In: A&A 635, A141, A141. DOI: 10.1051/0004-6361/202037462.

Matthews, J. (2005). "A Heitler model of extensive air showers". In: *Astroparticle Physics* 22.5, pp. 387–397. ISSN: 0927-6505. DOI: https://doi.org/10.1016/j.astropartphys.2004.09.003.

Mattox, J. R., D. L. Bertsch, J. Chiang, B. L. Dingus, et al. (Apr. 1996). "The Likelihood Analysis of EGRET Data". In: ApJ 461, p. 396. DOI: 10.1086/177068.

Mehle, Andraž, Boštjan Likar, and Dejan Tomaževič (2017). "In-line recognition of agglomerated pharmaceutical pellets with density-based clustering and convolutional neural network". In: *2017 Fifteenth IAPR International Conference on Machine Vision Applications (MVA)*, pp. 9–12. DOI: 10.23919/MVA.2017.7986760.

Mehner, A., K. Davidson, R. M. Humphreys, F. M. Walter, et al. (June 2015). "Eta Carinae's 2014.6 spectroscopic event: Clues to the long-term recovery from its Great Eruption". In: A&A 578, A122, A122. DOI: 10.1051/0004-6361/201425522.

Mehner, Andrea, Kris Davidson, Gary J. Ferland, and Roberta M. Humphreys (Feb. 2010). "High-excitation Emission Lines near Eta Carinae, and Its Likely Companion Star". In: ApJ 710.1, pp. 729–742. DOI: 10.1088/0004-637X/710/1/729.

Metzger, B. D., D. Caprioli, I. Vurm, A. M. Beloborodov, et al. (Apr. 2016). "Novae as Tevatrons: prospects for CTA and IceCube". In: MNRAS 457.2, pp. 1786–1795. DOI: 10.1093/mnras/stw123.

Meyer, M., D. Horns, and H. S. Zechlin (Nov. 2010). "The Crab Nebula as a standard candle in very high-energy astrophysics". In: A&A 523, A2, A2. DOI: 10.1051/0004-6361/201014108.

Mikolajewska, Joanna, Elias Aydi, David Buckley, Cezary Galan, and Marina Orio (Aug. 2021). "SALT high resolution spectroscopy of RS Oph: evidence for acceleration of the nova ejecta". In: *The Astronomer's Telegram* 14852, p. 1.

Mikołajewska, Joanna and Michael M. Shara (Oct. 2017). "The Massive CO White Dwarf in the Symbiotic Recurrent Nova RS Ophiuchi". In: ApJ 847.2, 99, p. 99. DOI: 10.3847/1538-4357/aa87b6.

Mitchell, Alison, Vincent Marandon, and Robert Daniel Parsons (2016). "A Generic Algorithm for IACT Optical Efficiency Calibration using Muons ". In: *Proceedings of The 34th International Cosmic Ray Conference — PoS(ICRC2015)*. Vol. 236, p. 756. DOI: 10.22323/1.236.0756.

Mohrmann, L., A. Specovius, D. Tiziani, S. Funk, et al. (Dec. 2019). "Validation of open-source science tools and background model construction in γ-ray astronomy". In: A&A 632, A72, A72. DOI: 10.1051/0004-6361/201936452.

Moliere, Gert (1948). "Theorie der Streuung schneller geladener Teilchen II Mehrfach- und Vielfachstreuung". In: *Zeitschrift für Naturforschung A* 3.2, pp. 78–97. DOI: doi:10.1515/zna-1948-0203.

Molinari, S., E. Schisano, D. Elia, M. Pestalozzi, et al. (July 2016). "Hi-GAL, the Herschel infrared Galactic Plane Survey: photometric maps and compact source catalogues. First data release for the inner Milky Way: +68° $\geq$ l $\geq$ -70°". In: A&A 591, A149, A149. DOI: 10.1051/0004-6361/201526380.

Molinari, S., B. Swinyard, J. Bally, M. Barlow, et al. (Mar. 2010). "Hi-GAL: The Herschel Infrared Galactic Plane Survey". In: PASP 122.889, p. 314. DOI: 10.1086/651314.

Munari, U. and P. Valisa (Aug. 2021). "Echelle spectroscopy of RS Oph at day +0.87 from optical discovery". In: *The Astronomer's Telegram* 14840, p. 1.

Murach, T., M. Gajdus, and R. Parsons (July 2015). "A Neural Network-based Reconstruction Algorithm for monoscopically detected Air Showers observed with the H.E.S.S. Experiment". In: *34th International Cosmic Ray Conference (ICRC2015)*. Vol. 34. International Cosmic Ray Conference, 1022, p. 1022. DOI: 10.22323/1.236.01022.

Murach, Thomas (Jan. 2017). "Monoscopic analysis of H.E.S.S. Phase II data on PSR B1259–63/LS 2883". PhD thesis. Humboldt University of Berlin, Germany.

NASA (Oct. 1976). *U.S. standard atmosphere, 1976*.

Nigro, C., C. Deil, R. Zanin, T. Hassan, et al. (May 2019). "Towards open and reproducible multi-instrument analysis in gamma-ray astronomy". In: A&A 625, A10, A10. DOI: 10.1051/0004-6361/201834938.

Nigro, Cosimo, Tarek Hassan, and Laura Olivera-Nieto (Oct. 2021). "Evolution of Data Formats in Very-High-Energy Gamma-Ray Astronomy". In: *Universe* 7.10, p. 374. DOI: 10.3390/universe7100374.

O'Brien, T. J., M. F. Bode, R. W. Porcas, T. W. B. Muxlow, et al. (July 2006). "An asymmetric shock wave in the 2006 outburst of the recurrent nova RS Ophiuchi". In: Nature 442.7100, pp. 279–281. DOI: 10.1038/nature04949.

Ohm, S., J. A. Hinton, and W. Domainko (Aug. 2010). "Particle Acceleration in the Expanding Blast Wave of η Carina's Great Eruption of 1843". In: ApJ 718, pp. L161–L165. DOI: 10.1088/2041-8205/718/2/L161.

Ohm, S., C. van Eldik, and K. Egberts (June 2009). "γ/hadron separation in very-high-energy γ-ray astronomy using a multivariate analysis method". In: *Astroparticle Physics* 31.5, pp. 383–391. ISSN: 0927-6505. DOI: https://doi.org/10.1016/j.astropartphys.2009.04.001.

Ohm, S., V. Zabalza, J. A. Hinton, and E. R. Parkin (Mar. 2015). "On the origin of γ-ray emission in η Carina". In: *Monthly Notices of the Royal Astronomical Society: Letters* 449.1, pp. L132–L136. ISSN: 1745-3925. DOI: 10.1093/mnrasl/slv032.

Ohm, Stefan (2010). "Development of an Advanced gamma/hadron separation technique and application to particular gamma-ray sources with H.E.S.S." PhD thesis. Ruprecht-Karls University of Heidelberg, Germany.

Olivera-Nieto, L., A. M. W. Mitchell, K. Bernlöhr, and J. A. Hinton (Dec. 2021). "Muons as a tool for background rejection in imaging atmospheric Cherenkov telescope arrays". In: *European Physical Journal C* 81.12, 1101, p. 1101. DOI: 10.1140/epjc/s10052-021-09869-0.

Olivera-Nieto, L., H. X. Ren, A. M. W. Mitchell, V. Marandon, and J. A. Hinton (Dec. 2022). "Background rejection using image residuals from large telescopes in imaging atmospheric Cherenkov telescope arrays". In: *European Physical Journal C* 82.12, 1118, p. 1118. DOI: 10.1140/epjc/s10052-022-11067-5.

Olivera-Nieto, Laura (2023). "Resolving particle acceleration and transport in the jets of the microquasar SS 433 with H.E.S.S. and HAWC". PhD thesis. Ruprecht-Karls University of Heidelberg, Germany.

Ostapchenko, S. (Jan. 2006). "QGSJET-II: towards reliable description of very high energy hadronic interactions". In: *Nuclear Physics B Proceedings Supplements* 151, pp. 143–146. DOI: 10.1016/j.nuclphysbps.2005.07.026.

Parkin, E. R. and J. M. Pittard (Aug. 2008). "A 3D dynamical model of the colliding winds in binary systems". In: MNRAS 388.3, pp. 1047–1061. DOI: 10.1111/j.1365-2966.2008.13511.x.

Parkin, E. R., J. M. Pittard, M. F. Corcoran, and K. Hamaguchi (Jan. 2011). "Spiraling Out of Control: Three-dimensional Hydrodynamical Modeling of the Colliding Winds in η Carinae". In: ApJ 726.2, 105, p. 105. DOI: 10.1088/0004-637X/726/2/105.

Parkin, E. R., J. M. Pittard, M. F. Corcoran, K. Hamaguchi, and I. R. Stevens (Apr. 2009). "3D modelling of the colliding winds in η Carinae - evidence for radiative inhibition". In: MNRAS 394.4, pp. 1758–1774. DOI: 10.1111/j.1365-2966.2009.14475.x.

Parsons, R. D. and J. A. Hinton (Apr. 2014). "A Monte Carlo template based analysis for air-Cherenkov arrays". In: *Astroparticle Physics* 56, pp. 26–34. DOI: 10.1016/j.astropartphys.2014.03.002.

Particle Data Group, R L Workman, V D Burkert, V Crede, et al. (Aug. 2022). "Review of Particle Physics". In: *Progress of Theoretical and Experimental Physics* 2022.8. 083C01. ISSN: 2050-3911. DOI: 10.1093/ptep/ptac097.

Peron, G. and F. Aharonian (Mar. 2022). "Probing the galactic cosmic-ray density with current and future γ-ray instruments". In: A&A 659, A57, A57. DOI: 10.1051/0004-6361/202142416.

Pittard, J. M. and M. F. Corcoran (Feb. 2002). "In hot pursuit of the hidden companion of eta Carinae: An X-ray determination of the wind parameters". In: A&A 383, pp. 636–647. DOI: 10.1051/0004-6361:20020025.

Preibisch, T., T. Ratzka, B. Kuderna, H. Ohlendorf, et al. (June 2011). "Deep wide-field near-infrared survey of the Carina Nebula". In: A&A 530, A34, A34. DOI: 10.1051/0004-6361/201116781.

Puehlhofer, G., K. Bernlöhr, B. Bi, G. Hermann, et al. (Mar. 2022). "Science verification of the new FlashCam-based camera in the 28m telescope of H.E.S.S." In: *37th International Cosmic Ray Conference*, 764, p. 764. DOI: 10.22323/1.395.0764.

Pühlhofer, G., M. Barcelo, C. Bauer, B. Bi, et al. (Sept. 2019). "FlashCam: a fully digital camera for the Cherenkov telescope array medium-sized telescopes". In: *Optics for EUV, X-Ray, and Gamma-Ray Astronomy IX*. Ed. by Stephen L. O'Dell and Giovanni Pareschi. Vol. 11119. Society of Photo-Optical Instrumentation Engineers (SPIE) Conference Series, 111191V, p. 111191V. DOI: 10.1117/12.2531025.

Rebolledo, David, Michael Burton, Anne Green, Catherine Braiding, et al. (Dec. 2015). "The Carina Nebula and Gum 31 molecular complex – I. Molecular gas distribution, column densities, and dust temperatures". In: *Monthly Notices of the Royal Astronomical Society* 456.3, pp. 2406–2424. ISSN: 0035-8711. DOI: 10.1093/mnras/stv2776.

Reitberger, K., A. Reimer, O. Reimer, and H. Takahashi (May 2015). "The first full orbit of η Carinae seen by Fermi". In: A&A 577, A100, A100. DOI: 10.1051/0004-6361/201525726.

Reitberger, K., O. Reimer, A. Reimer, M. Werner, et al. (Aug. 2012). "Gamma-ray follow-up studies on η Carinae". In: A&A 544, A98, A98. DOI: 10.1051/0004-6361/201219249.

Rochester, Leon, Tracy Usher, Robert P. Johnson, and Bill Atwood (Jan. 2010). "Upgrades to the Event Simulation and Reconstruction for the Fermi Large Area Telescope". In: *arXiv e-prints*, arXiv:1001.5005, arXiv:1001.5005. DOI: 10.48550/arXiv.1001.5005.

Rolke, Wolfgang A., Angel M. López, and Jan Conrad (Oct. 2005). "Limits and confidence intervals in the presence of nuisance parameters". In: *Nuclear Instruments and Methods in Physics Research A* 551.2-3, pp. 493–503. DOI: 10.1016/j.nima.2005.05.068.

Ruiz Velasco, Edna (2021). "Search and first detection of very-high-energy photons in gamma-ray bursts: an analysis with HAWC and H.E.S.S." PhD thesis. Ruprecht-Karls University of Heidelberg, Germany. DOI: 10.11588/heidok.00029603.

Sailer, S., F. Werner, G. Hermann, M. Barcelo, et al. (Aug. 2019). "Trigger performance verification of the FlashCam prototype camera". In: *Nuclear Instruments*

and Methods in Physics Research A 936, pp. 392–393. DOI: 10.1016/j.nima.2018.08.104.

Schaefer, Bradley E. (Apr. 2010). "Comprehensive Photometric Histories of All Known Galactic Recurrent Novae". In: ApJS 187.2, pp. 275–373. DOI: 10.1088/0067-0049/187/2/275.

Schäfer, J. (2023). "A Novel Simulation for the IceAct Demonstrator Telescope with TARGET-Trigger Electronics, Monte Carlo Validation of the H.E.S.S. Simulation Chain and a 3D Analysis of the Crab Nebula Using the ABRIR Method for Background Rejection Based on H.E.S.S. Data". In preparation. PhD thesis. Friedrich-Alexander-Universität Erlangen-Nürnberg.

Shayduk, M. and CTA Consortium (Jan. 2013). "Optimized Next-neighbour Image Cleaning Method for Cherenkov Telescopes". In: *International Cosmic Ray Conference*. Vol. 33. International Cosmic Ray Conference, p. 3000. DOI: 10.48550/arXiv.1307.4939.

Skilton, J. L., W. Domainko, J. A. Hinton, D. I. Jones, et al. (Mar. 2012). "Constraints on the non-thermal emission from η Carinae's blast wave of 1843". In: A&A 539, A101, A101. DOI: 10.1051/0004-6361/201118434.

Smith, N., R. D. Gehrz, P. M. Hinz, W. F. Hoffmann, et al. (Mar. 2003). "Mass and Kinetic Energy of the Homunculus Nebula around η Carinae". In: AJ 125, pp. 1458–1466. DOI: 10.1086/346278.

Smith, N., A. Ginsburg, and J. Bally (Mar. 2018). "A disrupted molecular torus around Eta Carinae as seen in ^{12}CO with ALMA". In: MNRAS 474, pp. 4988–4996. DOI: 10.1093/mnras/stx3050.

Smith, Nathan (Mar. 2005). "Doppler tomography of the Little Homunculus: high-resolution spectra of [FeII]λ16435 around Eta Carinae*". In: MNRAS 357.4, pp. 1330–1336. DOI: 10.1111/j.1365-2966.2005.08750.x.

Smith, Nathan (Apr. 2006). "A census of the Carina Nebula - I. Cumulative energy input from massive stars". In: MNRAS 367.2, pp. 763–772. DOI: 10.1111/j.1365-2966.2006.10007.x.

Smith, Nathan (Sept. 2008). "A blast wave from the 1843 eruption of η Carinae". In: *Nature* 455.7210, 201–203. ISSN: 1476-4687. DOI: 10.1038/nature07269.

Smith, Nathan, Michael P. Egan, Sean Carey, Stephan D. Price, et al. (Apr. 2000). "Large-Scale Structure of the Carina Nebula". In: ApJ 532.2, pp. L145–L148. DOI: 10.1086/312578.

Smith, Nathan and Gary J. Ferland (Feb. 2007). "The Structure of the Homunculus. II. Modeling the Physical Conditions in η Carinae's Molecular Shell*". In: *The Astrophysical Journal* 655.2, p. 911. DOI: 10.1086/510328.

Sokoloski, J. L., G. J. M. Luna, K. Mukai, and Scott J. Kenyon (July 2006). "An X-ray-emitting blast wave from the recurrent nova RS Ophiuchi". In: Nature 442.7100, pp. 276–278. DOI: 10.1038/nature04893.

Stecker, F. W. (Mar. 1970). "The Cosmic γ-Ray Spectrum from Secondary Particle Production in Cosmic-Ray Interactions". In: Ap&SS 6.3, pp. 377–389. DOI: 10.1007/BF00653856.

Steinmassl, S., M. Breuhaus, R. White, B. Reville, and J.A. Hinton (2023). "Escape from η Carinae". In: A&A. in preparation.

Strong, Andrew W., Igor V. Moskalenko, and Vladimir S. Ptuskin (2007). "Cosmic-Ray Propagation and Interactions in the Galaxy". In: *Annual Review of Nuclear and Particle Science* 57.1, pp. 285–327. DOI: 10.1146/annurev.nucl.57.090506.123011.

Taguchi, Kenta, Toshiya Ueta, and Keisuke Isogai (Aug. 2021). "Spectroscopic Follow-up Observation of the 2021 outburst of the recurrent nova RS Ophiuchi". In: *The Astronomer's Telegram* 14838, p. 1.

Tamm, IE and IM Frank (1937). "Coherent radiation of fast electrons in a medium". In: *Dokl. Akad. Nauk SSSR*. Vol. 14. 3, pp. 107–112.

Tatischeff, V. and M. Hernanz (July 2007). "Evidence for Nonlinear Diffusive Shock Acceleration of Cosmic Rays in the 2006 Outburst of the Recurrent Nova RS Ophiuchi". In: ApJ 663.2, pp. L101–L104. DOI: 10.1086/520049.

Teodoro, M., A. Damineli, B. Heathcote, N. D. Richardson, et al. (Mar. 2016). "He II λ4686 Emission from the Massive Binary System in η Car: Constraints to the Orbital Elements and the Nature of the Periodic Minima". In: ApJ 819.2, 131, p. 131. DOI: 10.3847/0004-637X/819/2/131.

Urquhart, J. S., C. König, A. Giannetti, S. Leurini, et al. (Jan. 2018). "ATLASGAL - properties of a complete sample of Galactic clumps". In: MNRAS 473.1, pp. 1059–1102. DOI: 10.1093/mnras/stx2258.

Vieu, T., S. Gabici, V. Tatischeff, and S. Ravikularaman (May 2022). "Cosmic ray production in superbubbles". In: MNRAS 512.1, pp. 1275–1293. DOI: 10.1093/mnras/stac543.

Wakely, S. P. and D. Horan (Jan. 2008). "TeVCat: An online catalog for Very High Energy Gamma-Ray Astronomy". In: *International Cosmic Ray Conference*. Vol. 3. International Cosmic Ray Conference, pp. 1341–1344.

Walder, R., D. Folini, and S. N. Shore (June 2008). "3D simulations of RS Ophiuchi: from accretion to nova blast". In: A&A 484.1, pp. L9–L12. DOI: 10.1051/0004-6361:200809703.

Walter, M. and A. W. Wolfendale (Aug. 2012). "Early history of cosmic particle physics". In: *European Physical Journal H* 37.3, pp. 323–358. DOI: 10.1140/epjh/e2012-30020-1.

Weekes, T. C., M. F. Cawley, D. J. Fegan, K. G. Gibbs, et al. (July 1989). "Observation of TeV Gamma Rays from the Crab Nebula Using the Atmospheric Cerenkov Imaging Technique". In: ApJ 342, p. 379. DOI: 10.1086/167599.

Werner, F., C. Bauer, S. Bernhard, M. Capasso, et al. (Dec. 2017). "Performance verification of the FlashCam prototype camera for the Cherenkov Telescope Array".

In: *Nuclear Instruments and Methods in Physics Research A* 876, pp. 31–34. DOI: 10.1016/j.nima.2016.12.056.

Werner, M., O. Reimer, A. Reimer, and K. Egberts (July 2013). "Fermi-LAT upper limits on gamma-ray emission from colliding wind binaries". In: A&A 555, A102, A102. DOI: 10.1051/0004-6361/201220502.

White, R., M. Breuhaus, R. Konno, S. Ohm, et al. (Mar. 2020). "Gamma-ray and X-ray constraints on non-thermal processes in η Carinae". In: A&A 635, A144, A144. DOI: 10.1051/0004-6361/201937031.

Wolf, William M., Lars Bildsten, Jared Brooks, and Bill Paxton (Nov. 2013). "Hydrogen Burning on Accreting White Dwarfs: Stability, Recurrent Novae, and the Post-nova Supersoft Phase". In: ApJ 777.2, 136, p. 136. DOI: 10.1088/0004-637X/777/2/136.

Wood, M., R. Caputo, E. Charles, M. Di Mauro, et al. (July 2017). "Fermipy: An open-source Python package for analysis of Fermi-LAT Data". In: *35th International Cosmic Ray Conference (ICRC2017)*. Vol. 301. International Cosmic Ray Conference, 824, p. 824. DOI: 10.22323/1.301.0824.

Yaron, O., D. Prialnik, M. M. Shara, and A. Kovetz (Apr. 2005). "An Extended Grid of Nova Models. II. The Parameter Space of Nova Outbursts". In: ApJ 623.1, pp. 398–410. DOI: 10.1086/428435.

Zanin, R., H. Abdalla, H. Abe, S. Abe, et al. (Mar. 2022). "CTA – the World's largest ground-based gamma-ray observatory". In: *37th International Cosmic Ray Conference*, 5, p. 5. DOI: 10.22323/1.395.0005.

Zatsepin, G. T. and V. A. Kuzmin (Aug. 1966). "Upper Limit of the Spectrum of Cosmic Rays". In: *Soviet Journal of Experimental and Theoretical Physics Letters* 4, p. 78.

Zhu, S. J., T. Murach, S. Ohm, M. Fuessling, et al. (Mar. 2022). "The upgraded Data Acquisition System of the H.E.S.S. telescope array". In: *37th International Cosmic Ray Conference*, 759, p. 759. DOI: 10.22323/1.395.0759.

Zorn, Justus (Jan. 2020). "Cherenkov camera and analysis development for highest-energy gamma-ray astronomy". PhD thesis. Ruprecht-Karls University of Heidelberg, Germany.

Personal Bibliography

Publications

Listed are publications, to which I made major contributions. As part of the H.E.S.S. collaboration I have been an author of 18 published journal articles as of March 2023. A full and up-to-date list can be found at `https://orcid.org/0000-0002-2865-8563`.

- H.E.S.S. Collaboration, ..., S. Steinmassl, et al. (Apr. 2022). “Time-resolved hadronic particle acceleration in the recurrent nova RS Ophiuchi”. In: Science 376.6588, pp. 77–80. DOI: `https://doi.org/10.1126/science.abn0567`.

In preparation

- Steinmassl, S., M. Breuhaus, R. White, B. Reville and J. A. Hinton. (2023). "Escape from η Carinae". submitted to A&A.
- H.E.S.S. Collaboration, ..., S. Steinmassl, et al. "The Eta Carinae 2020 periastron passage as seen by H.E.S.S.", in preparation.

Conference proceedings

Listed are proceedings, to which I made major contributions.

- Pühlhofer, G, ..., S. Steinmassl, ... for the H.E.S.S. collaboration. (2021). "Science verification of the new FlashCam-based camera in the 28m telescope of H.E.S.S." In: 37th International Cosmic Ray Conference, p. 764. DOI: `https://doi.org/10.22323/1.395.0764`.
- Leuschner, F., J. Schäfer, S. Steinmassl, T. Holch, et al. (2023). “Validating Monte Carlo simulations for an analysis chain in H.E.S.S.” In: 7th Heidelberg International Symposium on High-Energy Gamma-Ray Astronomy. DOI: `10.48550/arXiv.2303.00412`.

Conference contributions

- Steinmassl, Simon. March 2022. "Science verification and highlights of the new FlashCam-based camera in the 28m telescope of H.E.S.S.". DPG Spring Meeting. Heidelberg, Germany.

- Steinmassl, Simon. July 2022. "Efficient cosmic-ray acceleration in the recurrent nova RS Ophuichi revealed by H.E.S.S.". 7th Heidelberg International Symposium on High-Energy Gamma-Ray Astronomy, Barcelona, Spain.

List of Figures

List of Tables

Acknowledgements

First and foremost I would like to thank my supervisor Prof. Jim Hinton for giving me the chance to work in the fascinating field of high-energy astrophysics. Jim supported me constantly through the challenges of the Ph.D. project, helped with his expertise and great ideas and also his kind and encouraging character.

I would also like to thank Prof. Stefan Wagner for following the project as part of my thesis committee and already in advance for reading and evaluating this thesis. I am grateful to the other examination committee members, Prof. Röpke and Prof. Schultz-Coulon, for agreeing to take part in the final exam.

Many people helped me by proofreading parts of this thesis, for which I am very grateful. Thanks to all of you!

I appreciated the unique working atmosphere at MPIK very much, giving plenty of room for detailed discussions, and getting advice and help. I am very grateful to all people at MPIK, who helped in the projects for this thesis. Particularly, the members of the Eta Car team (Mischa, Rich, Brian and Jim) and the (former) MPIK H.E.S.S. members involved in my projects (Jim, Vincent, Lars, Laura, Quentin, Konrad, Brian, Dan, Felix, German). Especially, I would like to mention Dr. Felix Werner, who was also part of my thesis committee and helped me throughout the thesis, and Dr. Vincent Marandon, who could answer every, sometimes annoying or stupid, question about H.E.S.S. and beyond. Vincent was further always very helpful with coding advise or contribution of code and I also enjoyed the many discussions over coffee or beer.

Additionally, I would like to thank Dr. Laura for being such a good company over the course of our PhDs, for sharing all the small rants and jokes at work, accompanying me on the trips to meetings and schools and especially for becoming a very good friend. I would like to thank my former and present (Justus, Simon, Hazal, Georg, Clara) office mates for the relaxed atmosphere and all the small chats and jokes in between. Of course, many other people from MPIK also contributed with help and advice but also with creating such a pleasant and social atmosphere at work.

Furthermore, I would like to thank all the members within H.E.S.S., who support the instrument, take the data, run the calibration or do any other service task. I would like to thank all the H.E.S.S. colleagues, who contributed directly or indirectly to the collaborative efforts discussed in this work and without whom the results would not have been possible.

Natürlich waren auch Erholungspausen und Unterstützung von außerhalb des Arbeitsplatzes unabdingbar für das Gelingen dieser Arbeit. Ich möchte allen meinen Volleyballteamkollegen und allen Beachern füer die unzähligen Stunden in der Halle oder im Sand danken. Besonderer Dank natürlich auch an alle anderen Freund*innen, die mich auf dem Weg unterstützt und immer wieder abgelenkt haben. Ganz vielen Dank an meine Geschwister, Konstantin und Marlene, und meine Eltern, Alfred und Maren, dafür, dass heimkommen immer wie Urlaub ist. Und natürlich für die dauerhafte Unterstützung über die letzten 28 Jahre und dass ihr mir immer alles ermöglicht habt, was ich erreichen wollte.

Zu guter Letzt noch ganz lieben Dank an Vanessa. Für alles und v.a. dafür dass du Teil meines Lebens geworden bist!